学位論文

Evolution of polycyclic aromatic hydrocarbons (PAHs) in the interstellar medium revealed by AKARI

(あかりで探る星間空間における PAH の進化)

平成 27 年 12 月博士 (理学) 申請

東京大学大学院理学系研究科
天文学専攻

森 珠実

Abstract

We present the results of observational studies of the processing of polycyclic aromatic hydrocarbons (PAHs) in the interstellar medium (ISM) based on infrared (IR) slit spectroscopy of the Infrared Camera (IRC) on board *AKARI* and laboratory work on deuterated hydrocarbon materials motivated by these studies. The IR wavelength region contains many emission and/or absorption features associated with various kinds of gaseous and solid materials in the ISM. The diffuse IR light coming from the ISM tells us much about interstellar matters and thus much about the interstellar environment and the evolution of materials in the universe. Among these IR features, we focus on a series of prominent emission bands, called the unidentified infrared (UIR) bands, whose carrier is generally thought to be PAHs and/or their relative compounds. *AKARI*'s unique advantages are the unprecedented sensitivity in the 2–5 μm near-infrared (NIR) wavelength range, especially for diffuse sources, and the simultaneous coverage of 2-13 μm in the same slit area. We take advantage of these characteristics while demonstrating that NIR spectroscopy is important for exploring the evolution of PAHs in the ISM.

In the 2–5 μm spectrum of astronomical objects, a prominent emission band appears at 3.3 μm. The relative intensity of the 3.3 μm band to the UIR bands at longer wavelengths, especially the 11.3 μm band, is considered to be the most robust PAH size distribution indicator. Although size distribution is one of the most important factors of PAH processing, the ratio of the 3.3 to 11.3 μm band, $I_{3.3\,\mu\mathrm{m}}/I_{11.3\,\mu\mathrm{m}}$, has not yet been carefully investigated, due to the difficulty of simultaneous observations at these largely separated wavelengths. Here, from simultaneous slit spectroscopy at 2–5 μm NIR and 5–13 μm MIR wavelengths of the diffuse light of the Large Magellanic Cloud (LMC) by the *AKARI*/IRC, we systematically investigated the intensity ratios of the UIR bands appearing from 2 to 13 μm for the first time. The observations were performed toward nine positions of the LMC. In order to cover a wide range of radiation conditions, the target positions are chosen such that each has different *IRAS* 25 to 12 μm and 60 to 100 μm color, which are sensitive to massive star-forming activities. Among the regions without ionized gas signatures, the ratio of the 3.3 to 11.3 μm band shows a positive correlation with the *IRAS* 25 to 12 μm and *AKARI* 24 to 11 μm band colors, whereas the other H II region-like targets do not follow this sequence. In the latter targets, the ratio of the 3.3 to 11.3 μm band is much smaller than extrapolation from the correlation. This difference is successfully accounted for in terms of the paucity of very small PAHs ($n_{\mathrm{C}} < 100$) in H II region-like targets, which is possibly due to preferential

destruction of very small PAHs in ionized gas-dominated regions. This result clearly demonstrates that the diagram of the ratio of the 3.3 to 11.3 μm band v.s. the ratio of the 7.7 to 11.3 μm band can be a good probe for local star-forming activity.

The intensity ratio of the 3.4–3.6 μm bands to the 3.3 μm band can also indicate PAH alteration. The sub-features that commonly appear at approximately 3.4–3.6 μm, next to the PAH 3.3 μm band, are associated with the vibration modes of aliphatic C-H bonds such as branched alkyl groups and chain structures. On the other hand, the 3.3 μm band is assigned to aromatic C-H bonds. The intensity ratio of the 3.4–3.6 μm bands to the 3.3 μm band can therefore be used as a tracer of the structure of interstellar PAHs. Using a large collection of high-quality NIR spectra (2.5–5.4 μm) of galactic H II regions and H II region-like objects, we investigated the UIR bands at NIR wavelengths. Thirty-six objects were observed by the *AKARI*/IRC as a part of a director's time program. The analysis shows that the aliphatic to aromatic ratio of $I_{3.4-3.6\,\mu\mathrm{m}}/I_{3.3\,\mu\mathrm{m}}$ decreases against the ratio of the 3.7 μm continuum intensity to the 3.3 μm band, $I_{\mathrm{cont},3.7\,\mu\mathrm{m}}/I_{3.3\,\mu\mathrm{m}}$, which is an indicator of the ionization fraction of PAHs. The *AKARI* MIR color of $I_{9\,\mu\mathrm{m}}/I_{18\,\mu\mathrm{m}}$ also decreases steeply against the ratio of the hydrogen recombination line Brα at 4.05 μm to the 3.3 μm band, $I_{\mathrm{Br}\alpha}/I_{3.3\,\mu\mathrm{m}}$. These facts indicate possible dust processing inside or at the boundary of ionized gas. In addition to the 3.3–3.6 μm band complex, most spectra show a relatively weak emission feature at 5.22 μm with sufficient signal-to-noise ratios, which we identify as the PAH 5.25 μm band previously reported. By careful analysis, we found good correlation between the 5.25 μm band and both the aromatic hydrocarbon feature at 3.3 μm and the aliphatic ones at approximately 3.4–3.6 μm. The present results provide us convincing evidence that the astronomical 5.25 μm band is associated with C-H vibrations of PAHs, as suggested by previous studies, showing its potential to probe the PAH size distribution.

It is also known that deuterated PAHs (PADs) exhibit emission features at approximately 4.3–4.8 μm instead of 3.3–3.5 μm because of the difference in the reduced mass between the C–H and C–D oscillators. PAHs are thought to be a possible reservoir of missing deuterium (D) in the ISM. However, the latest results of *AKARI* NIR slit spectroscopy suggest that there is no significant signature at 4.3–4.8 μm showing the incorporation of deuterium into PAHs. There still remains a mystery about the refuge of deuterium in the ISM. To investigate a possible effect on the cross-section by deuteration quantitatively, we generated deuterated hydrocarbon materials in the laboratory in a similar way to the synthesis of quenched carbonaceous composites (QCCs). We then measured their 2–25 μm IR spectra and hydrogen isotope ratios, using a Fourier transform infrared spectrometer (FT-IR) and a nanoscale secondary ion mass spectrometer (NanoSIMS). By using a mixture of methane and perdeuterated methane gas with five different mixing ratios as the starting material, we investigated the spectral transitions from non-deuterated to perdeuterated hydrocarbon materials. Deuteration does not change the cross-section at NIR wavelengths significantly, which supports our interpretation of the *AKARI* results that

PAHs are not the dominant carrier of deuterium in the ISM. Furthermore, we found a new feature peaking at 20.4 μm, which is possibly due to combination of C-C-C out-of-plane and C-D out-of-plane vibration modes. We suggest that this feature can be a PAD tracer at MIR wavelengths.

As described above, we investigated the evolution of PAHs in the ISM in terms of size distribution, chemical structure, and hydrogen isotope ratio. These ISM properties are revealed in the NIR spectroscopic range, via *AKARI* observations and subsequent laboratory experiments. In particular, the size distribution and chemical structure of PAHs vary according to the host environment, suggesting that PAHs can be a useful diagnostic tool for interstellar environments.

Contents

Chapter 1

General introduction

1.1 Background and present problems in studies on the interstellar matter

Space between stars seems barren and empty at a glance, but is actually filled with gas and dust particles, which are called the interstellar medium (ISM). Dust plays an important role in the metempsychosis of materials in the universe. Stars synthesize heavy elements in their interior, and eject them to the ISM by stellar mass-loss and/or explosion at the end of their lives. Dust is a substantial reservoir of these heavy elements in the ISM, and is also materials for forming new-generation stars (see Figure1.1, Onaka 2012). Such "recycling" in the universe is one of the primary issues in present-day astronomy, which leads to understanding of the chemical evolution of the universe and the formation of planetary systems like our Solar system. In order to tackle this problem, we have to correctly understand the formation and evolution of dust in the ISM (Dwek & Scalo 1980). Thanks to the recent progress in many different branches of astronomy and planetary science; laboratory astrophysics, meteoritics, as well as observational and theoretical astronomy, the properties of cosmic dust have gradually become clear (e.g., Jones 2004; Tielens 2005; Meixner et al. 2006). However, several issues still remain open questions; "Where and how are they formed?", "How are they processed and destroyed?", and so on.

1–1000 μm infrared (IR) observations have played an important role in the study of the ISM, since the ISM emits its absorbed energy predominantly at IR wavelengths. IR emissions coming from dust are generally considered to be divided into three parts [see Figure 2 of Compiègne et al. (2011)]. One is thermal emission from sub-micron size amorphous carbon or silicate dust grains peaking at approximately 100–300 μm far-infrared (FIR) wavelengths (Boulanger et al. 1985). These grains are called big grains (BGs). Another one is excess emission at approximately 20–100 μm mid-infrared (MIR) wavelengths, which is accounted for by stochastic heating of nanometer size amorphous carbon dust grains named very small grains (VSGs). The last one is a series of prominent emission bands appearing at 3.3, 6.2, 7.7, 8.6, 11.3, and 12.7 μm associated with faint features at 3.4, 5.2, 5.7, 10.8, 11.0,13.5, 14.2, 16.4 and 17.4 μm, which are called the unidentified infrared (UIR) bands (see also Figure 1.3). These emission bands are commonly attributed to the IR fluorescence of polycyclic

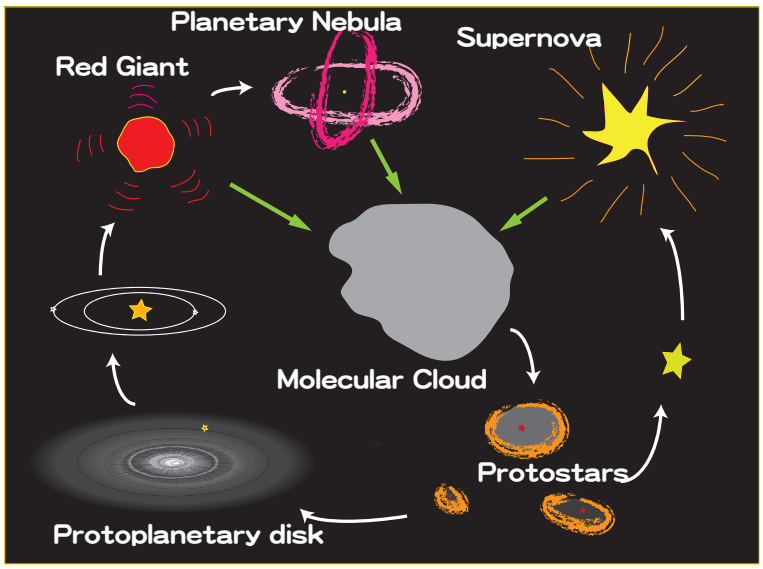

Figure 1.1: Schematic drawing of the lifecycle of dust in the ISM. Quoted from Onaka (2012).

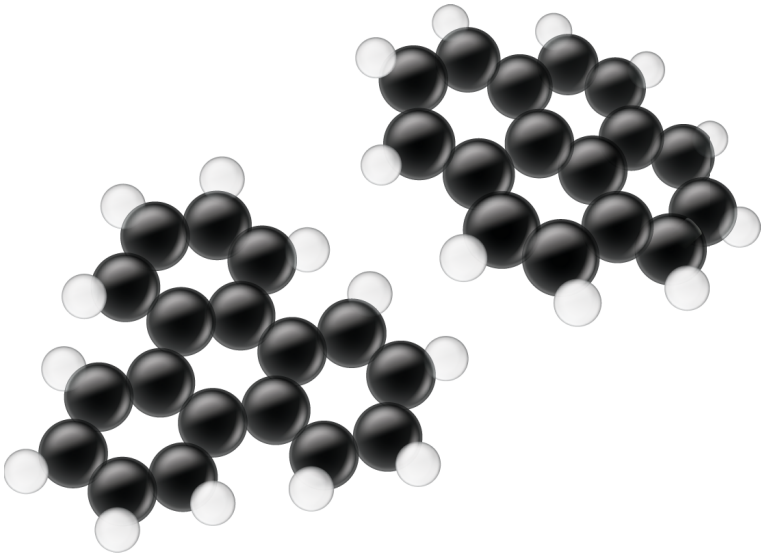

Figure 1.2: Typical structure of PAHs (Hammonds 2015). White and black spheres indicate hydrogen and carbon atoms, respectively.

aromatic hydrocarbons (PAHs) or PAH-containing carbonaceous compounds in the ISM (e.g., Sakata et al. 1984; Puget & Leger 1989; Papoular et al. 1989; Allamandola et al. 1989b). PAH is a general term referring to aromatic hydrocarbons that consist of fused aromatic rings without any of heteroatoms or substitutes. Figure 1.2 illustrates a typical structure of PAHs (Hammonds et al. 2015). PAHs were also discovered in comets and meteorites, and their close connection to the origin of life is expected. PAHs also attract a lot of attention as a carrier of anomalous microwave emission (AME; Draine & Lazarian 1998; Bell et al. 2015; Hensley et al. 2015) and missing deuterium in the ISM (see Chapter 5 for more detailed discussion; Peeters et al. 2004b; Draine 2006; Buragohain et al. 2015; Doney et al. 2016). Details of the UIR bands and their possible carriers, PAHs, are described in §1.2.

In addition to the UIR bands, 2–15 μm near infrared (NIR) and MIR spectra of astronomical objects show many emission and/or absorption features associated with gaseous and solid materials in the ISM, depending on their interstellar environment. Thanks to the advent of IR astronomical satellites such as *Infrared Space Observatory* (*ISO*), *Spitzer Space Telescope*, and *AKARI*, which explored the universe at IR wavelengths without being disturbed by Earth's atmosphere, the wealth of the 2–15 μm wavelength region has come under the spotlight. Table 1.1 summarizes the major ISM features between 2 and 15 μm. There are absorption features due to various ice species (e.g., H_2O at 3.05 μm and 6.02 μm and CO_2 at 4.25 μm and 15.2 μm; Gibb et al. 2004; Shimonishi et al. 2010), fundamental vibrational transitions of CO gas (e.g., Rho et al. 2012), several molecular hydrogen lines (e.g., Lee et al. 2011), and a number of hydrogen and helium recombination lines. There are also forbidden lines of several heavy elements like Ar, Ne, and Si at MIR wavelengths, from which we can infer the hardness of the incident radiation field (e.g., Dale et al. 2006). As for carbon compounds beside PAHs, fullerenes are known to have active vibrational modes at MIR wavelengths (e.g., C_{60} at 7.0, 8.5, 17.4, and 18.9 μm). Fullerenes have been proposed as an alternative carbon form in the interstellar environment for several decades (Kroto et al. 1985). Recently, Cami et al. (2010) reported the discovery of active vibrational modes of C_{60} and C_{70} in a young planetary nebula, Tc 1, by MIR spectroscopy with the Infrared Spectrograph (IRS) onboard *Spitzer*. Since then, similar features were also detected in several astronomical objects (e.g., Sellgren et al. 2010). Diamonds also show spectral features at 3.4 and 3.5 μm (e.g., Van Kerckhoven et al. 2002; Goto et al. 2009). Furthermore, deuterated PAHs (PADs) are expected to have vibration modes in this wavelength range (see Table 5.1; Bauschlicher et al. 1997; Hudgins et al. 2004; Buragohain et al. 2015; Doney et al. 2016). Absorption features due to large carbonaceous dust are detected at 3.29–3.52 μm, which are attributed either aromatic or aliphatic C-H vibrations (Dartois et al. 2004; Chiar et al. 2013). 6.0-6.4 μm, 6.85 and 7.24 μm absorption features are also attributed to carbonaceous dust (Dartois & Muñoz-Caro 2007; Chiar et al. 2013). They are relatively weak and thus only seen in large column density regions, such as toward the galactic center or duty torus around AGNs. The 2–15 μm wavelength range thus contains significant pieces of information about the ISM, helping us to cultivate a better understanding of the ISM.

Table 1.1: Major features appearing at 2–15 μm wavelengths

Name	Wavelength [μm]	
Hydrogen Recombination Lines		
Brackett ($n \rightarrow 4$) serieas		
HI Brβ	2.63	
HI Brα	4.05	
Pfundt ($n \rightarrow 5$) series		
HI Pf12	2.76	
HI Pfη	2.88	
HI Pfϵ	3.03	
HI Pfδ	3.29	contribute to the UIR 3.3 μm band
HI Pfγ	3.75	
HI Pfβ	4.65	
HI Pfα	7.46	contribute to the UIR 7.7 μm band
Humphreys ($n \rightarrow 6$) serieas		
HI Hu15	3.91	
HI Hu14	4.02	
HI Hu13	4.18	
HI Huη	4.38	
HI Huϵ	4.67	
HI Huδ	5.12	
Helium Recombination Lines		
HeI ($^3D_1 - -^3F_0$)	4.30	
Hydrogen Molecular Lines		
H_2 1–0 O(3)	2.80	
H_2 1–0 O(5)	3.24	
H_2 1–0 O(6)	3.50	
H_2 1–0 O(7)	3.81	
H_2 0–0 S(14)	3.72	
H_2 0–0 S(13)	3.85	
H_2 0–0 S(12)	4.00	
H_2 0–0 S(11)	4.19	
H_2 0–0 S(10)	4.41	
H_2 0–0 S(9)	4.69	
Forbidden Lines of Heavy Elements		
[Ar II] ($^2P_{1/2} - -^2P_{3/2}$)	6.98	
[Ar III] ($^3P_1 - -^3P_2$)	8.99	
[S IV] ($^2P_{3/2} - -^2P_{1/2}$)	10.51	
[Ne II] ($^2P_{1/2} - -^2P_{3/2}$)	12.81	
The UIR Bands		
the 3.3 μm band[a]	3.3	aromatic C-H stretch
the 3.4-3.6 μm sub-features[a]	3.4–3.6	aliphatic C-H stretch or overtone band of aromatic C-H stretch
the 5.25 μm band[a,b]	5.25	blending of overtone, difference, and combination bands of C-H stretch and C-H bend
the 5.7 μm band[a,b]	5.7	blending of overtone, difference, and combination bands of C-H stretch and C-H bend
the 6.2 μm band[a]	6.2	C-C stretching mode
the 7.7 μm band[a]	7.7	blending of C-C stretch and C-H in-plane bend
the 8.6 μm band[a]	8.6	C-H in-plane bend
the 11.3 μm band[a]	11.3	solo C-H out-of-plane bend
the 12.6 μm band[a]	12.6	trio C-H out-of-plane bend
Ice Absorption Features		
NH_3 ice[c]	2.96	-N-H stretch
H_2O ice[c,d]	3.05	O-H stretch
CH_3OH ice[c]	3.53	C-H stretch
CH_3OH ice[c]	3.95	C-H stretch
CO_2 ice[d]	4.27	C-O stretch
$^{13}CO_2$ ice[d]	4.38	^{13}C-O stretch
XCN ice[e]	4.62	CN stretch
CO ice[d]	4.67	^{12}CO stretch
^{13}CO ice[d]	4.78	^{13}CO stretch
H_2O ice[c]	6.02	H-O-H bend
CH_4 ice[g]	7.70	C-H (ν_4) deformation
CH_3OH ice[c]	8.9	C-H_3 rock
NH_3 ice[h]	9.35	Umbrella
H_3OH ice[c]	9.75	C-O strech
H_2O ice[f]	13.3	Libration
CO_2 ice[d]	15.2	O-C-O bend

[a] From Allamandola et al. (1989b).
[b] From Boersma et al. (2009).
[c] From D'Hendecourt & Allamandola (1986).
[d] From Gerakines et al. (1995).
[e] From Schutte & Greenberg (1997).
[f] From Hudgins et al. (1993).
[g] From Boogert et al. (1997).
[h] From Kerkhof et al. (1999).

1.2 The unidentified infrared bands

The UIR bands are one of the most interesting and ubiquitous features in the ISM. Figure 1.3 presents the spectrum of a H II region, Orion Bar H2S1, obtained with the the Short Wavelength Spectrometer (SWS) on-board *ISO* extracted from Sloan et al. (2003). The spectrum clearly exhibits the UIR bands at 3.3, 6.2, 7.7, 8.6, 11.3, and 12.7 μm. Since the discovery of the 11.3 μm band in planetary nebulae in 1973 (Gillett et al. 1973), air-borne, ground-based, and space IR observations have shown that the UIR bands appear in a wide range of astrophysical environments such as PDRs, reflection nebulae, planetary nebulae (e.g., Peeters et al. 2002), diffuse ISM (e.g., Onaka et al. 1996; Mattila et al. 1996), and various kinds of nearby galaxies (e.g., Dale et al. 2006; Kaneda et al. 2008; Smith et al. 2007). Interestingly, they are discovered even in distant galaxies (e.g., Lutz et al. 2005; Sajina et al. 2007; Riechers et al. 2014). As mentioned in §1.1, the carriers of the UIR bands are generally believed to be PAHs or related carbonaceous materials. They are the smallest member of the interstellar carbonaceous dust grains, and harbor approximately more than 20 % of carbon in the universe (Tielens 2008). By strict definition, PAHs do not contain any heteroatoms or substitutes. However, the carriers of the UIR bands are considered not to be such pure aromatic compounds. They should include partial defects, aliphatic structures such as branched alkyl groups, double hydrogens, and chain structures (Kwok & Zhang 2011; Li & Draine 2012, see Chapter 4 for more detailed discussion;), and substituents (e.g., C replaced by N; Hudgins et al. 2005). In some cases, they may possibly be dehydrogenated. Kwok & Zhang (2011) suggested that mixed aromatic-aliphatic organic nano-particles are more appropriate as the carries of the UIR bands than PAHs. On the other side, Li & Draine (2012) pointed out the inconsistency of this hypothesis with observations, arguing that the carriers of UIR bands are predominantly aromatic. Recently possible inclusion of oxygen and magnesium-containing molecules is also discussed (Sadjadi et al. 2015). The carriers of the UIR bands (hereafter symbolically called PAHs) are excited by absorbing a single ultraviolet (UV) photon and emit a number of photons corresponding to vibration modes of C-C and C-H bonds at IR wavelengths. The 3.3 μm band is assigned to an aromatic C-H stretching, the 6.2 μm band to a C-C stretching, the 7.7 μm band to blending of several C-C stretching modes and C-H in-plane bending modes, the 8.6 μm band to a C-H in-plane bending, the 11.3 μm band to a solo C-H out-of-plane bending, and the 12.6 μm band to a trio C-H out-of-plane bending mode, respectively (see Table 1.1; Allamandola et al. 1989b). The "solo", "duo", and "trio" denote the number of adjacent H atoms. Besides, the minor band complex between 3.4 and 3.6 μm and the weak bands peaking at 5.25 and 5.7 μm are associated with aliphatic C-H stretching or overtone of aromatic C-H stretching and blending of overtone, difference, and combination of C-H stretching and C-H bending, respectively. Because of their weakness, few studies have focused on these minor features. In particular, little has been reported on the 5.25 and 5.7 μm bands (see Chapter 4 for more detailed discussion).

The profile and strength of the UIR bands are thought to reflect the chemical and physical characteristics

of PAHs such as molecular structure, size distribution, and ionization state, which may be altered according to dust processing in the ISM (Tielens 2008). PAHs are vulnerable to harsh conditions in the ISM. They should manifest the effects of dust processing most clearly. Because of such expected sensitivity to dust processing, its brightness, and ubiquitousness in astrophysical environments, the UIR bands are expected to be an efficient probe for not only dust processing in the ISM but also interstellar environments in the nearby and far universe. Latest *Spitzer* and *AKARI* observations have demonstrated that there are regional differences in the UIR band appearance, especially at MIR wavelengths. However, few studies have investigated the correlation between the properties of PAHs derived from the UIR bands and physical conditions of the ISM quantitatively. The evolution of PAHs is poorly understood, although several mechanisms have been suggested. It is one of the current important issues in the ISM physics to connect theoretical, experimental, and observational studies, and clarify the process of formation and destruction of PAHs in the ISM.

Laboratory experiments and theoretical calculations predict several mechanisms for formation and destruction of PAHs (e.g., Chiar et al. 2013). Following three mechanisms are thought to be the major supply sources of carbonaceous grains like PAHs; (1) formation in the ejecta of mass-losing C-rich AGB stars, (2) fragmentation of larger carbonaceous grains induced by grain-grain collision (shattering) in shocks, and (3) condensation in dense molecular clouds. Paradis et al. (2009) suggested that PAHs should originate in molecular clouds, as well as stellar mass-loss process, unlike VSGs and BGs, based on the observations of the Large Magellanic Cloud (LMC) performed as a part of Surveying the Agents of a Galaxy's Evolution (SAGE) legacy survey with *Spitzer*. With respect to the destruction process, two mechanisms are proposed; (1) photodissociation by high UV radiation (e.g., Buch 1989; Allain et al. 1996b,a), and (2) sputtering in shock waves or hot plasma (e.g., Jones et al. 1996; Micelotta et al. 2010b,a). Recently, Seok et al. (2012) reported the detection of the 3.3 μm band at the supernova remnant (SNR) N49 in the LMC, suggesting significant processing of PAHs in SNR shocks. Yamagishi et al. (2012) also pointed out that shattering of large carbonaceous grains is responsible for the presence of very small PAHs ($n_{\rm C} < 100$, where $n_{\rm C}$ is the number of carbon atoms in the PAH) in the halo of M82. As recent theoretical studies, Micelotta et al. (2010a,b) investigated PAH destruction processes in hot gas and interstellar shocks. They suggested that small PAHs are more efficiently destroyed than larger ones by sputtering in hot gas at temperature below 10^6 K like H II regions.

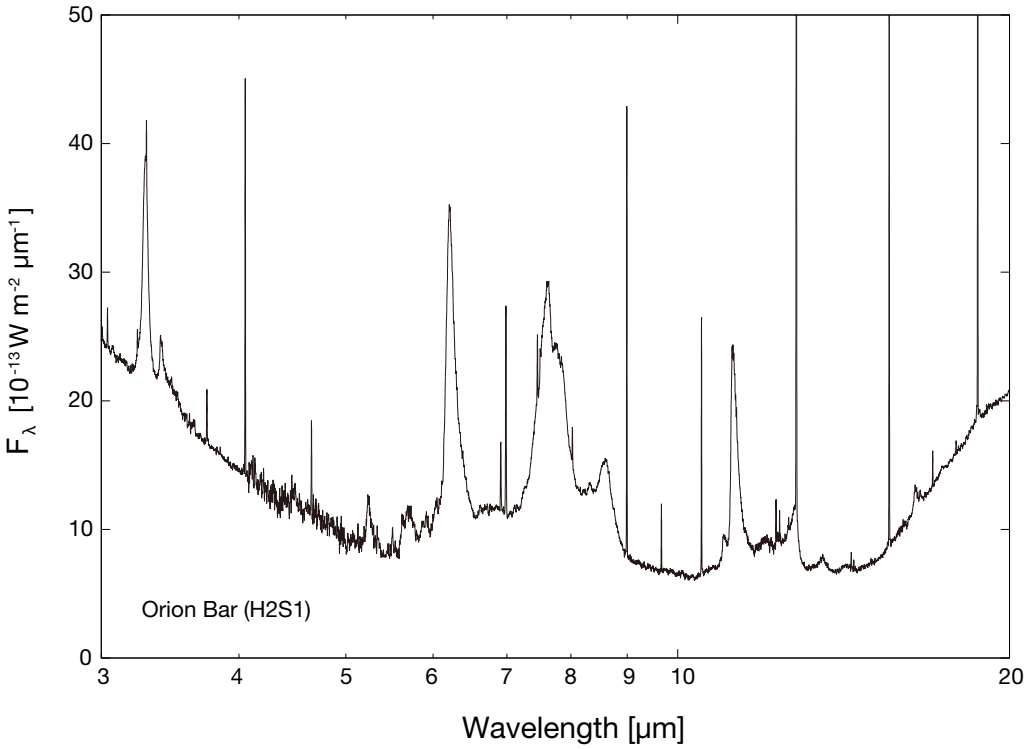

Figure 1.3: *ISO*/SWS spectrum of the PDR at the Orion Bar (Sloan et al. 2003).

1.3 Contents

Here, we report the observational results of IR slit spectroscopy with the the Infrared Camera (IRC) onboard *AKARI*, which covers the spectral range of 2–13 μm. The main subject of this thesis is the characteristics and processing of interstellar PAHs. The UIR bands have been extensively investigated at MIR wavelengths with the *Spitzer*/IRS and other facilities (e.g., Smith et al. 2007). They revealed that the UIR bands at MIR wavelengths have close connection to the PAH ionization degree, and can be a good probe for local star-formation activities. On the other hand, although the UIR bands at NIR wavelengths can be a key to understand the size distribution and chemical structures of PAHs, which are thought to drastically change according to their local host environments, the spectral range shorter than 5.5 μm has not come under the spotlight over the past few decades until the advent of *AKARI*. The SWS onboard *ISO* provides spectroscopic information on this range, but they are limited only for very bright sources. The *AKARI*/IRC has a higher sensitivity at 2–5 μm wavelengths by factor of ten than the *ISO*/SWS. Taking advantage of this unique characteristics of the *AKARI*/IRC, we performed careful analysis on the UIR bands at NIR wavelengths, and cut through a new phase of the study of interstellar PAHs. The contents are roughly divided into three parts, Chapter 3, 4, and 5. Chapter 2 describes the detail of the *AKARI*/IRC.

Chapter 3 presents the results of 2.5–13 μm NIR and MIR slit spectroscopic observations toward the LMC with the *AKARI*/IRC (Mori et al. 2012). Although a number of dedicated studies have so far been made on the UIR band ratios in various astronomical objects, none of them have careful discussion on the UIR band ratios including the 3.3 μm band. Here, thanks to the unique characteristic of the *AKARI*/IRC, we are able to investigate continuous spectra from 2.5 to 13 μm of diffuse regions for the first time.

Chapter 4 introduces the results of 2.5–5.4 μm NIR slit spectroscopic observations of thirty-six H II regions in our Galaxy with the *AKARI*/IRC (Mori et al. 2014). Not only the 3.3–3.6 μm PAH band complex, the spectra shows a variety of ISM features such as hydrogen combination lines and a H_2O ice absorption band. The unique wavelength coverage and high sensitivity of the *AKARI*/IRC enables us to study these ISM features based on a larger quantity of astronomical spectra than ever before.

Chapter 5 shows the results of experimental study on PADs in the ISM. We synthesize deuterated hydrocarbon materials in the laboratory, and investigate the effect of deuteration upon their IR spectra to reconsider the results of *AKARI*/IRC NIR slit spectroscopy reported in Onaka et al. (2014).

A summary is given in Chapter 6.

Chapter 2

AKARI observations

2.1 AKARI mission

AKARI, also known as *ASTRO-F* or *Infrared Imaging Surveyor*, is the second-generation Japanese IR astronomical satellite, developed and managed by Institute of Space and Astronautical Science (ISAS)/Japan Aerospace eXploration Agency (JAXA) and the collaborators with the participation of European Space Agency (ESA, Murakami et al. 2007). *AKARI* has a 68.5 cm cooled telescope, and two on-board instruments, the IRC (Onaka et al. 2007b) and Far-infrared Surveyor (FIS, Kawada et al. 2007), covering the NIR to FIR wavelength range of 1.7–180 μm. The FIS is designed for an all-sky survey at FIR wavelengths of 65, 90, 140, and 160 μm together with FIR spectroscopy by a Fourier transform spectrometer, while the IRC is for pointed observations in imaging and spectroscopy at NIR and MIR wavelengths and for an all-survey at 9 and 18 μm performed simultaneously with the FIS all-sky survey. *AKARI* was launched with 170 liter of liquid helium and threw on a sun-synchronous orbit at an altitude of 700 km by a JAXA M-V rocket in February, 2006. MIR and FIR observations were carried out as well as NIR observations until August, 2007, when the liquid helium boiled off, as the telescope and the instruments were kept lower than 7 K by the assistance of the on-board mechanical coolers (Nakagawa et al. 2007). In the first half year after the performance verification (PV) phase, called Phase 1, the all-sky survey were executed intensively with the highest priority. In this period, some pointed observations at high ecliptic latitudes, and a part of large-area surveys in North Ecliptic Pole (NEP) region and the LMC, were also performed. Phase 1 started in May, 2006 and ended in November, 2006. After the end of the Phase 1 period, *AKARI* performed pointed observations for Mission Programs and Open Time proposals, and the all-sky survey observations to fill the scan gaps, until the exhaustion of liquid helium in August, 2007. This phase is called Phase 2. In Phase 1 and Phase 2, *AKARI* surveyed more than 96% of the whole sky at MIR and FIR wavelengths (Ishihara et al. 2010; Doi et al. 2015), and performed more than five thousand pointed observations. After the exhaustion of liquid helium, NIR observations continued with the NIR channel of the IRC till the end of its scientific operation in May, 2011. This phase is called Phase 3. *AKARI* completed its

mission life in November, 2011, leaving a huge amount of significant astronomical data. The all-sky survey at IR wavelengths is one of the main scientific goals of *AKARI*. Most of the *AKARI* data have been placed in public data archives, which include point source catalogues of the all-sky survey at six bands. The legacy of *AKARI* covers a wide range of astronomical objects, and are utilized even now.

Table 2.1: Band characteristics of the IRC (Onaka et al. 2007b)

Channel	Band	Reference wavelength [μm]	Wavelength [μm]	Isophotal wavelength [μm]	Effective Bandwidth [μm]
NIR	*N2*	2.4	1.9–2.8	2.34	0.71
	N3	3.2	2.7–3.8	3.19	0.87
	N4	4.1	3.6–5.3	4.33	1.53
MIR-S	*S7*	7.0	5.9–8.4	7.12	1.75
	S9W	9.0	6.7–11.6	8.61	4.10
	S11	11.0	8.5–13.1	10.45	4.12
MIR-L	*L15*	15.0	12.6–19.4	15.58	5.98
	L18W	18.0	13.9–25.6	18.39	9.97
	L24	24.0	20.3–26.5	22.89	5.34

[a] In NP mode, the spectral resolution depends on the wavelength.

2.2 Overview of slit spectroscopy with the AKARI Infrared Camera

This thesis mainly deals with NIR and MIR slit spectroscopic data, obtained by pointed observations with the *AKARI*/IRC. In the following, we briefly describe the IRC in particular its spectroscopic part. See Onaka et al. (2007b) for full description.

2.2.1 Instrument

A panoramic view and a photograph of the IRC are displayed in Figure 2.1. As shown in this figure, the IRC consists of three IR channels, the NIR, MIR-S, and MIR-L channel, which are designed to cover the NIR wavelength range of 1.7–5.5 μm, the shorter MIR wavelength range of 5.8–14.1 μm, and the longer MIR wavelength range of 12.4–26.5 μm, respectively. They are equipped with nine imaging filters: *N2*, *N3*, *S7*, *S11*, *S9W*, *S11*, *L15*, *L18W*, and *L24* (see Table 2.1 for details), and a prism and grisms as the dispersers, which offer five spectroscopic modes, *NP*, *NG*, *SG1*, *SG2*, and *LG2*. The first and second letters indicate the relevant channel and the disperser employed, the prism or the grism, respectively. For instance, the NIR channel has two options for the NIR disperser: the prism and the grism, which severally provide different wavelength coverages and different spectral resolutions (1.7–5.3 μm, $\lambda/\Delta\lambda \sim 20$–40 for the *NP* and 2.5–5.0 μm, $\lambda/\Delta\lambda \sim 100$ for the *NG*). The performance of each spectroscopic mode is summarized in Table 2.2.

Figure 2.2 illustrates the field of view (FoV) of each channel of the IRC, which is about $10' \times 10'$. A small window of $1' \times 1'$ ("Np" window) is commonly used for spectroscopy of point sources to avoid confusion from surrounding objects, $3'' \times 1'$ and $5'' \times 0.8'$ slits ("Ns" and "Nh" slits) are used for diffuse sources. As one of the unique advantages of the IRC, the NIR and MIR-S channels share the same FoV, which is composed of a large window of $10' \times 10'$, "Nc" window, and the "Ns" slit, by virtue of the beam splitter. Thus, by using the "Ns" slit, we can obtain continuous spectra from 2 to 13 μm simultaneously for diffuse regions. In addition to the "Ns" slit, the NIR channel has other choices for the slit, "Nh" slit or "Np" window. We note that the spectral resolution also depends on the choice for the slit, since the slit width is slightly different between "Ns" and "Nh".

Table 2.2: Wavelength overages and the spectral resolutions of the IRC spectroscopy (Onaka et al. 2007b)

Channel	Mode	Wavelength coverage [μm]	Spectral resolution [μm/pixel]
NIR	*NP*	1.7–5.3	0.06 (at 3.5 μm)[a]
	NG	2.5–5.0	0.0097
MIR-S	*SG1*	5.4–8.4	0.057
	SG2	7.5–12.9	0.099
MIR-L	*LG2*	17.5–25.7	0.175

[a]In NP mode, the spectral resolution depends on the wavelength.

2.2.2 Observation program

In a pointed observation, the telescope and the instruments of *AKARI* set to follow a fixed observational sequence, which is composed of the exposure, filter switch, and dithering operations. There are several patterns of the combination of those operations, which are referred to Astronomical Observation Templates (AOTs). The IRC AOTs in Phase 2 are represented as IRC#, and those in Phase 3 as IRCZ#, where # is the AOT number. Figure 2.3 (c) describes the outline of four major IRC AOTs, AOT02 (two-filter mode), AOT03 (three-filter mode), AOT04 (spectroscopic mode) and AOT05 (one-filter mode). In each AOT, filters, dispersers, location, and use of the slit can be additionally customized according to the purpose of the observation. As shown in Figure 2.3, except for AOT05, one standard frame of the NIR channel consists of one short exposure (4.675 sec) and one long exposure (44.41 sec), and that of the MIR-S and MIR-L channels consists of one short exposure (0.5844 sec) and three long exposures (16.36 sec). In all AOTs, except for AOT11 (slow-scan mode), dark current is measured at the first and last parts of the observation.

AOT04 is designed for spectroscopic observations, and thus does not include dithering operations. A single imaging frame is inserted at the middle of the observation to obtain the reference image. Dispersers can be exchanged between the former part and the latter part of the observation. The dataset presented in Chapter 3 were taken with "IRC04", the spectroscopic mode in Phase 2, and covered the NIR to MIR wavelength range of 2.5–13 μm, while those in Chapter 4 were obtained with "IRCZ04", the spectroscopic mode in Phase 3, and covered only the NIR wavelength range of 2–5.4 μm.

2.2.3 Detector anomaly

It is known that the IRC array gives artifacts such as "multiplexer bleed", "column pull down", and, "banding", which also appears in the array of the Infrared Array Camera (IRAC) onboard *Spitzer* (Fazio et al. 2004). See Hora et al. (2000, 2003a,b, 2004); Pipher et al. (2004) for details of those effects. Particularly, we must be careful in the reduction of Phase 2 NIR data, since the column pull down has a serious impact on the NIR array detectors during Phase 2 period (See details in 3.2.3). However, its effect mostly diminishes in Phase 3 NIR data, because of the different conditions of the array operation during Phase 3 period. Ghosts are also known to be present in the NIR and MIR observations due to reflection in the beam splitter. In the present study, we removed those which showed apparent ghosts from the analysis. Besides, intense scattered light emerges at

the edge of the MIR array detectors (e.g., Sakon et al. 2007). In Chapter 3, we can subtract them by using off-images.

A recent detailed study shows that in the case of NIR grism spectroscopy, there is a contribution of the second-order light at wavelengths longer than 4.9 μm. A small dispersion effect affects the wavelength calibration at 3.2–3.7 μm (Baba et al. 2015; Hammonds et al. 2015). In the present analysis, we do not use the spectra obtained with the *NG* mode at wavelengths longer than 4.9 μm. The small shift in the 3 μm region does not affect the present results either.

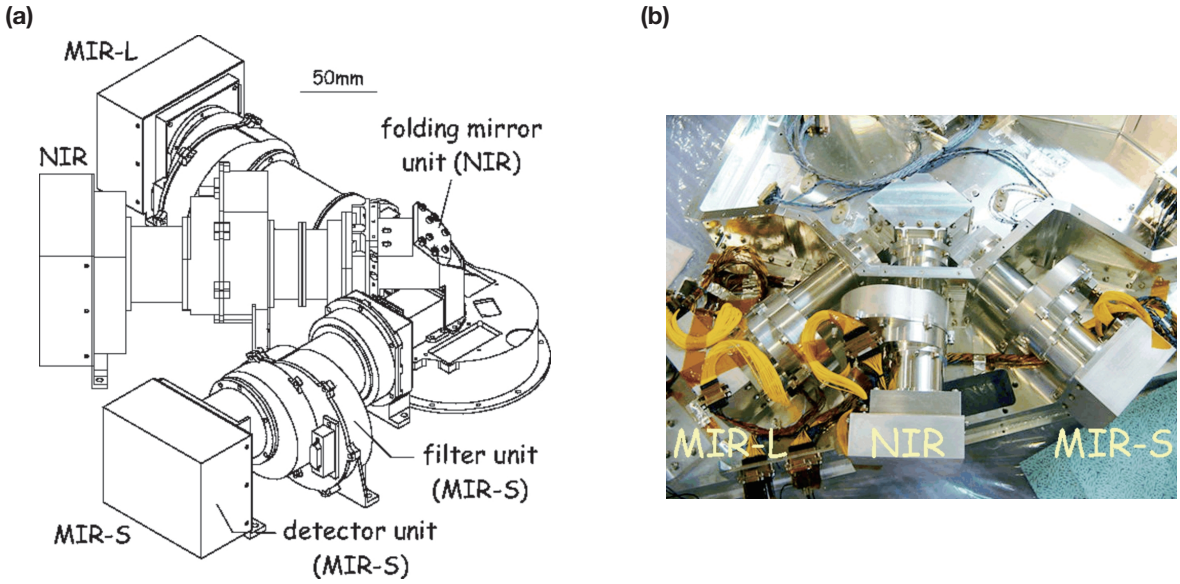

Figure 2.1: **(a)** Panoramic view and **(b)** photograph of the IRC. Quoted from Onaka et al. (2007b).

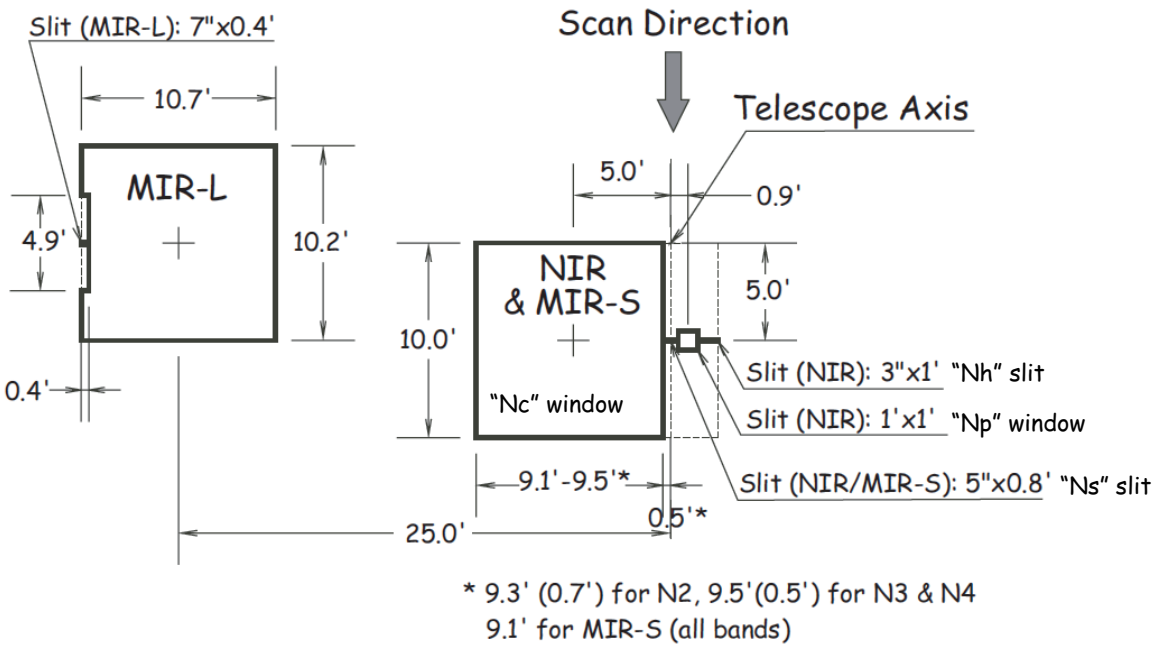

Figure 2.2: FoV of the three IRC channels. Quoted from Onaka et al. (2007b).

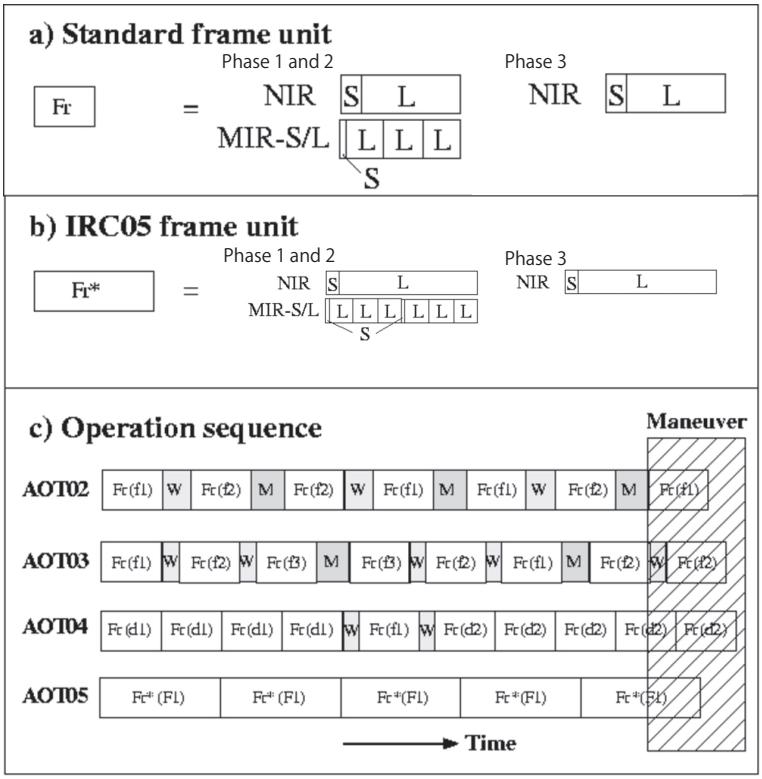

Figure 2.3: Outline of the frame units and four major IRC AOTs. Quoted from Onaka et al. (2007b).

Chapter 3

2-13 μm unidentified infrared band ratio analysis of the Large Magellanic Cloud

3.1 Introduction

In this chapter, we present the results of NIR and MIR slit-spectroscopy observations of the diffuse ISM with different radiation conditions in the LMC by the IRC onboard *AKARI* (Mori et al. 2012).

The LMC is a nearby irregular galaxy and is located at the distance of 50 kpc from the Milky Way (Feast 1999; Keller & Wood 2006). At the LMC distance, $1''$ corresponds to 0.24 pc. In addition to its proximity, the almost face-on orientation (i $\sim$35°; van der Marel & Cioni 2001; Olsen & Salyk 2002; Nikolaev et al. 2004) provides us a unique opportunity to investigate various physical environments without confusion with the spatial resolution of the *AKARI*/IRC ($\sim5''$ in the MIR).

As described in §1.2, the profile and strength of the UIR bands reflect the chemical and physical characteristics of PAHs, and is expected to be a good probe for physical conditions of the ISM, in particular local star-formation activity (e.g., Peeters et al. 2004b). Among them, the intensity ratios of the UIR bands contain a great deal of information about PAHs such as the size distribution and ionization fraction of PAHs. The size distribution of PAHs are considered to be one of the most important factors related to processing of PAHs, accordingly the physical conditions of the environment where they are emitted, such as local star-formation activity and presence of AGNs. The 3.3 μm band is at the shortest wavelength and requires the highest excitation among the UIR bands. Due to the correlation between heat capacity and size, the 3.3 μm band is most sensitive to the processing of the smallest PAHs ($n_{\rm C} < 100$; Schutte et al. 1993). Its relative intensity to the UIR bands at longer wavelengths, such as the 11.3 μm band, provides us with significant information on the average temperature of PAHs, which depends on the size distribution and/or the excitation condition of PAHs. However, due to the difficulty of simultaneous observations at NIR and MIR wavelengths systematic investigation on the ratio of the 3.3 to 11.3 μm bands has not been performed so far, although it is the most robust estimator of the

size distribution of PAHs. Here, we present a systematic study of the intensity ratios of the UIR bands between 2 and 13 μm including the ratio of the 3.3 to 11.3 μm bands, based on continuous spectra of the diffuse regions of the LMC obtained with the AKARI/IRC.

As mentioned in Chapter 2, the IRC can uniquely obtain a spectrum from 2.5 to 13 μm simultaneously with the same slit. This is advantageous when observing extended objects over other space instruments. The SWS onboard the *ISO* had different diaphragms from the NIR to MIR (de Graauw et al. 1996). The IRS on *Spitzer* lacked a channel in the NIR (Houck et al. 2004). Vermeij et al. (2002) investigated the UIR band ratios of H II regions in the LMC based on observations with the ISOPHOT/PHT-S instrument on board *ISO*, but they did not include the 3.3 μm band in their analysis because of the low sensitivity in the short wavelength channel. This work is the first analysis of the UIR band ratios including $I_{3.3\,\mu\mathrm{m}}/I_{11.3\,\mu\mathrm{m}}$ extracted from exactly the same area. It shows that $I_{3.3\,\mu\mathrm{m}}/I_{11.3\,\mu\mathrm{m}}$ can trace the history of PAH destruction from the perspective of PAH size distribution including small ones, which is difficult only with MIR observations.

In §3.2, the observations and the data reduction are illustrated together with the selection of the target positions. The obtained spectra are presented in §3.3. In §3.4, the observed variations in the UIR band ratios in different radiation field conditions are examined in terms of the PAH model. Diagnostic of the physical conditions of the observed regions is also discussed based on the UIR band ratios.

Table 3.1: Observation log and parameters

Position ID	Date	Obs.ID	AOT	Disperser	Center position of the slit		A_V[a]
					$\alpha_{\rm J2000}$	$\delta_{\rm J2000}$	
Position 1	2006 October 14	1400318.1	IRC04 b:Ns	NG, *SG1* and *SG2*	$05^{\rm h}38^{\rm m}20.^{\rm s}78$	-70°07′19.05″	1.89
Position 2	2006 October 19	1400330.1	IRC04 b:Ns	NG, *SG1* and *SG2*	$05^{\rm h}39^{\rm m}45.^{\rm s}62$	-70°00′34.30″	0.72
Position 3	2006 October 2	1400346.1	IRC04 b:Ns	NG, *SG1* and *SG2*	$05^{\rm h}48^{\rm m}09.^{\rm s}94$	-69°52′51.60″	1.90
Position 4	2007 May 15	1402426.1	IRC04 b:Ns	NG, *SG1* and *SG2*	$05^{\rm h}25^{\rm m}54.^{\rm s}98$	-66°10′30.15″	0.04
Position 5	2006 October 16	1400324.1	IRC04 b:Ns	NG, *SG1* and *SG2*	$05^{\rm h}43^{\rm m}42.^{\rm s}55$	-69°22′31.85″	0.83
Position 6	2007 May 18	1402422.1	IRC04 b:Ns	NG, *SG1* and *SG2*	$05^{\rm h}26^{\rm m}06.^{\rm s}05$	-68°36′02.20″	0.63
Position 7	2006 October 16	1400334.1	IRC04 b:Ns	NG, *SG1* and *SG2*	$05^{\rm h}39^{\rm m}17.^{\rm s}67$	-69°30′14.25″	0.54
Position 8	2006 October 16	1400320.1	IRC04 b:Ns	NG, *SG1* and *SG2*	$05^{\rm h}40^{\rm m}00.^{\rm s}17$	-69°45′26.25″	2.11
LMC-off	2006 November 10	1500719.1	IRC04 a:Ns	*NP*, *SG1* and *SG2*	$06^{\rm h}00^{\rm m}00.^{\rm s}0$	-66°36′30″	-
LMC-off	2006 November 10	1500720.1	IRC04 a:Ns	*NP*, *SG1* and *SG2*	$06^{\rm h}00^{\rm m}00.^{\rm s}0$	-66°36′30″	-

[a]From Dobashi et al. (2008).

3.2 Observations and data reduction

3.2.1 Observations

This study employs datasets of eight pointed observations (observation IDs: 1400330, 1400346, 1400318, 1402426, 1400324, 1402422, 1400334 and 1400320) collected as part of the *AKARI* mission program "ISM in our Galaxy and Nearby Galaxies" (ISMGN; Kaneda et al. 2009). All of the observations were performed with the slit spectroscopic mode, using "Ns" slit ($0.8' \times 5''$, see Figure 2.2), and the grism for the NIR disperser. Details of IRC spectroscopy are summarized in Ohyama et al. (2007). The AOT is "IRC04 b:Ns". The NIR spectrum was taken with the *NG* mode (2.5–5.0 μm, $\lambda/\Delta\lambda \sim 100$), and the MIR spectra were taken with the *SG1* and *SG2* modes (4.6–9.2 μm, $\lambda/\Delta\lambda \sim 50$ and 7.2–13.4 μm, $\lambda/\Delta\lambda \sim 50$; see Chapter 2 for more detailed information on the instrument). As mentioned in §2.2.1, the NIR and MIR observations were done for the same position simultaneously by means of a beam splitter, enabling us to acquire a continuous spectrum from 2.5 to 13.4 μm of the same slit area of $0.8'$ length by $5''$ width. The observation parameters are summarized in Table 3.1. The accurate slit position was determined from the *N3* band image taken during each pointed observation (see §3.2.3), by referring to the positions of point sources in the 2MASS catalog.

3.2.2 Target selection

The targets were selected by taking account of the CO mapping data (Mizuno et al. 2001) and IR colors of $I_{25\,\mu{\rm m}}/I_{12\,\mu{\rm m}}$ and $I_{60\,\mu{\rm m}}/I_{100\,\mu{\rm m}}$, which were derived from Infrared Astronomical Satellite (*IRAS*) all-sky survey data. They were originally selected from the catalogue of star clusters in the LMC compiled by Bica et al. (1996), but there are no available further information than the *IRAS* colors. The *IRAS* colors are considered to be sensitive to local star-formation activities (Boulanger et al. 1988; Onaka et al. 2007a). Sakon et al. (2006) have shown that extremely large *IRAS* colors of $I_{25\,\mu{\rm m}}/I_{12\,\mu{\rm m}}$ and $I_{60\,\mu{\rm m}}/I_{100\,\mu{\rm m}}$ ($\sim$3 and $\sim$0.6, respectively) in the diffuse emission in the LMC can be accounted for by a large contribution from nearby young ($< 30\,{\rm Myr}$) clusters to the incident interstellar radiation field and that small *IRAS* colors of $I_{25\,\mu{\rm m}}/I_{12\,\mu{\rm m}}$ and $I_{60\,\mu{\rm m}}/I_{100\,\mu{\rm m}}$

Table 3.2: *IRAS* and *AKARI* colors

Position ID	$I_{25\mu m}/I_{12\mu m}$	$I_{60\mu m}/I_{100\mu m}$	$I_{24\,\mu m}/I_{11\,\mu m}$
Position 1	1.00 ± 0.04	0.329 ± 0.008	0.58 ± 0.04
Position 2	1.09 ± 0.07	0.361 ± 0.017	0.78 ± 0.06
Position 3	1.63 ± 0.11	0.352 ± 0.024	1.34 ± 0.10
Position 4	1.42 ± 0.10	0.433 ± 0.025	1.50 ± 0.11
Position 5	1.54 ± 0.13	0.432 ± 0.026	1.53 ± 0.11
Position 6	1.88 ± 0.07	0.467 ± 0.020	1.85 ± 0.14
Position 7	4.87 ± 0.22	0.774 ± 0.019	6.56 ± 0.49
Position 8-1	4.77 ± 0.51	0.758 ± 0.056	7.92 ± 0.59
Position 8-2	4.77 ± 0.51	0.758 ± 0.056	7.37 ± 0.55

[a]The values are the ratios of the radiances in W m^{-2} Hz^{-1} $arcsec^{-2}$.

($\sim$1 and $\sim$0.3, respectively) are those expected from the heating by the incident radiation field inside quiescent molecular clouds (e.g., Miville-Deschênes et al. 2002). According to these results, we selected several infrared bright positions with different *IRAS* colors as the targets of the present study, where molecular clouds are recognized in the CO maps (Mizuno et al. 2001; Fukui et al. 2008). Since the beam size of the *IRAS* data is larger than the size of the slit of the *AKARI*/IRC, we also derived the *AKARI* color of $I_{24\,\mu m}/I_{11\,\mu m}$ from the dataset of Kato et al. (2012), where $I_{24\,\mu m}$ and $I_{11\,\mu m}$ are the flux densities at the *AKARI*/IRC *L24* and *S11* band, respectively, to obtain the local radiation field conditions. The flux density was measured over an aperture of 5″ in radius around the central position of the slit. The *IRAS* and *AKARI* colors of the present targets are summarized in Table 3.2. The trend of the *AKARI* color of $I_{24\,\mu m}/I_{11\,\mu m}$ is very similar to that of the *IRAS* $I_{25\,\mu m}/I_{12\,\mu m}$ color, whereby we confirm that the selection based on the *IRAS* colors is relevant to the purpose of the present study. Hence, the target positions cover a wide range of incident radiation field conditions including molecular clouds, PDRs and H II regions.

In Figure 3.1, the slit positions are shown over the false color image of the LMC obtained by the *AKARI*/IRC LMC survey program (Ita et al. 2008; Kato et al. 2012). The *S11* band images of a $10' \times 10'$ area including each slit position are also shown in Figures 3.2 (a)–(h). The slit is positioned at regions without apparent point sources in all the positions except for Position 8. At Position 8, a bright point-like source is recognized in part of the slit. We splitted the spectrum of Position 8 into two parts: one including the point-like source (Position 8-1) and one without (Position 8-2). For the other positions, the spectrum was extracted over almost the entire slit length of 40–50″.

The *AKARI* color of $I_{24\,\mu m}/I_{11\,\mu m}$ and the *IRAS* colors of $I_{25\,\mu m}/I_{12\,\mu m}$ and $I_{60\,\mu m}/I_{100\,\mu m}$ at Positions 1, 2, 3, 4, 5 and 6 exhibit only a limited range of 0.5–1.8, 1.0–1.9, and 0.3–0.5, respectively. These targets are not associated with SWB 0 or I type star clusters in Bica et al. (1996), indicating that they are surrounded by relatively quiescent environments (Sakon et al. 2006). The *AKARI* and *IRAS* colors at Positions 7, 8-1 and 8-2 exhibit large values. These targets are located in regions associated with OB star clusters as well as Herbig Ae/Be star clusters (N158-O1 and N158-Y1 at Position 7 and N159-Y4 at Position 8; Nakajima et al. 2005), confirming that the IR colors manifest recent star-formation activities in the ISM.

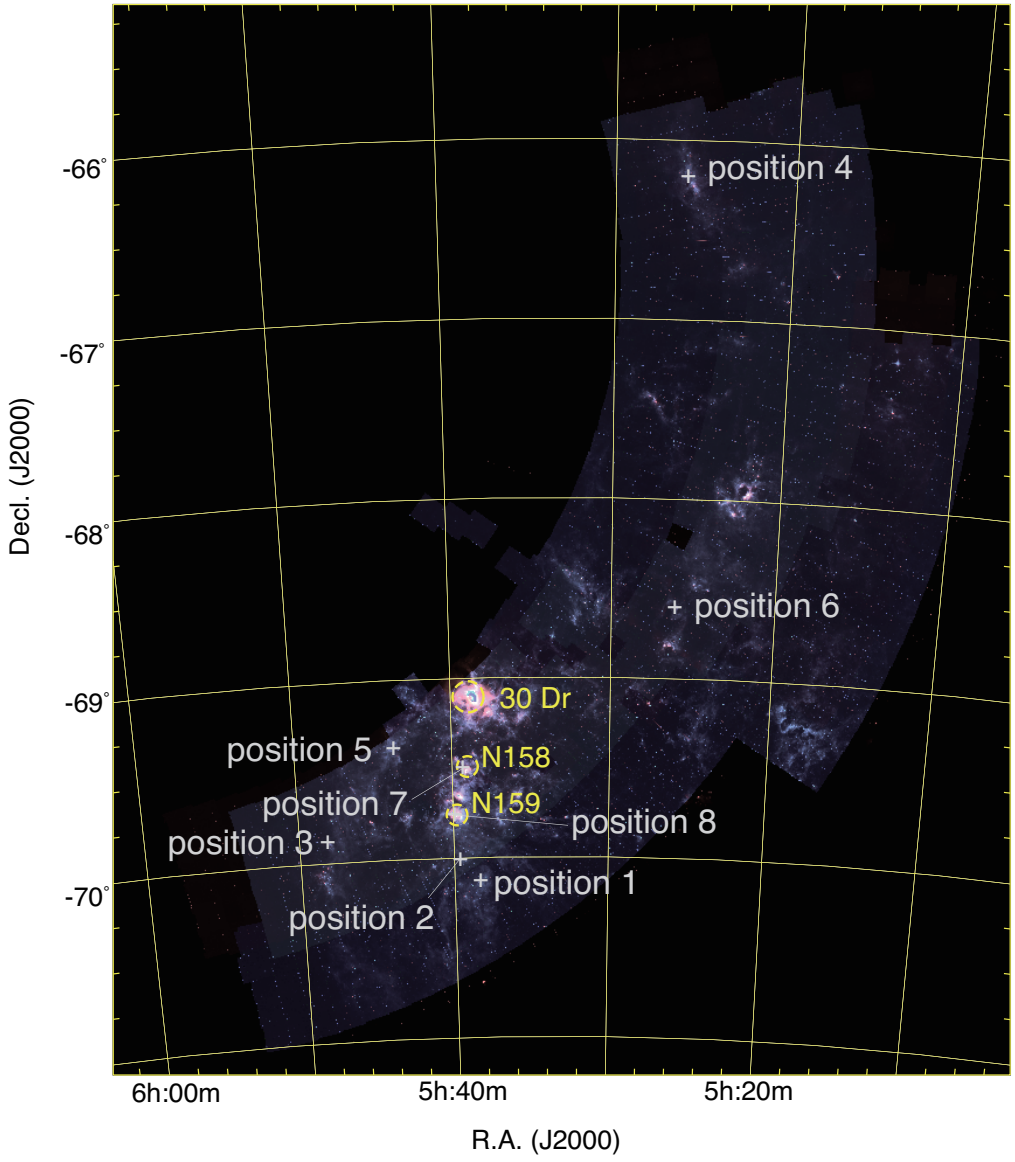

Figure 3.1: Slit positions of each pointed observation are overlain on the artificial three-color image of the LMC, where the intensities of the *AKARI*/IRC *S7*, *S11*, and *L24* bands are indicated in blue, green, and red, respectively. The white crosses indicate the center positions of the slits.

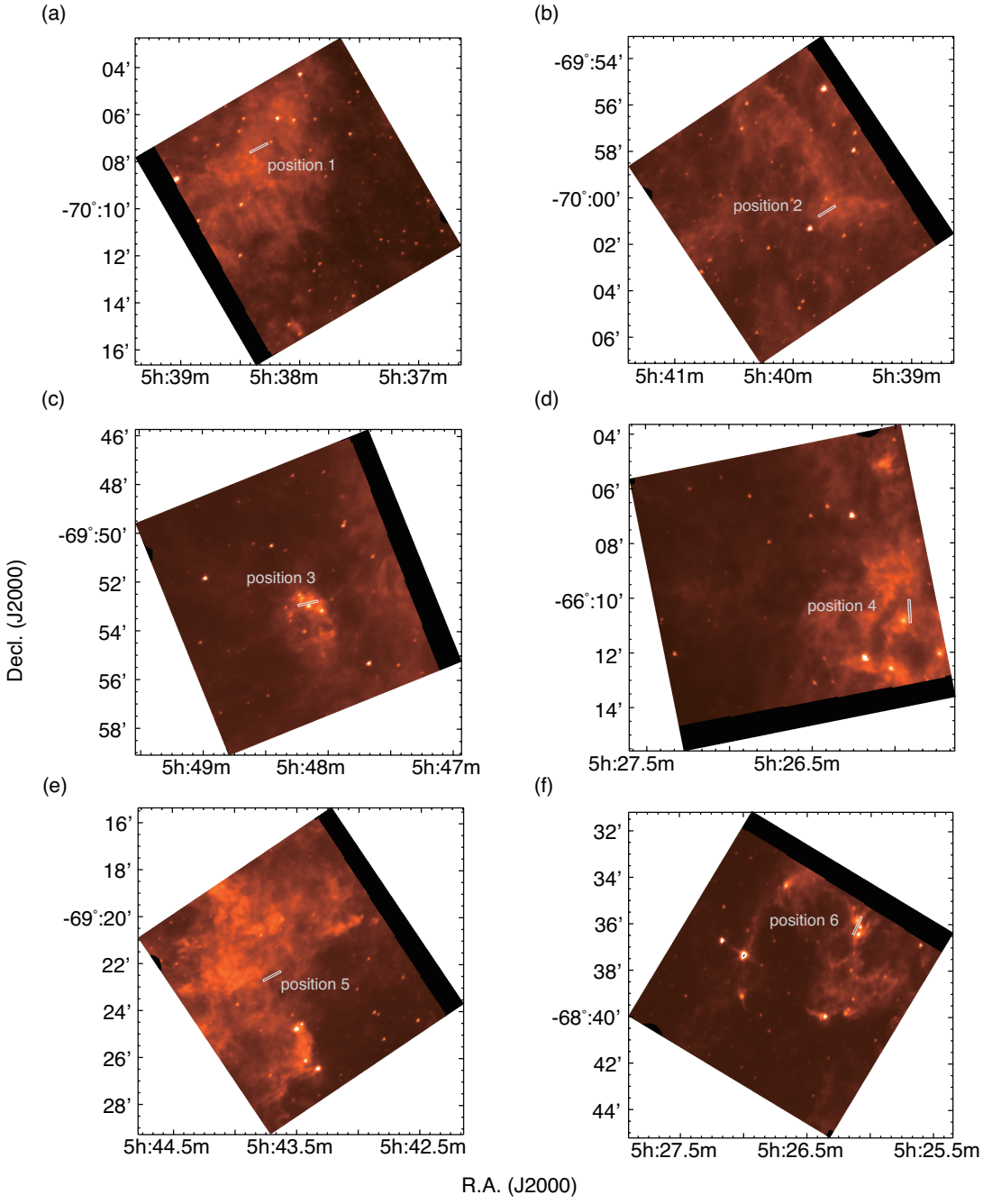

Figure 3.2: Enlarged slit position images of **(a)** Position 1, **(b)** Position 2, **(c)** Position 3, **(d)** Position 4, **(e)** Position 5, **(f)** Position 6, **(g)** Position 7, and **(h)** Position 8 are overlain on the *AKARI*/IRC *S11* band images. The white boxes indicate the slit of $0.8'$ length by $5''$ width in each observation.

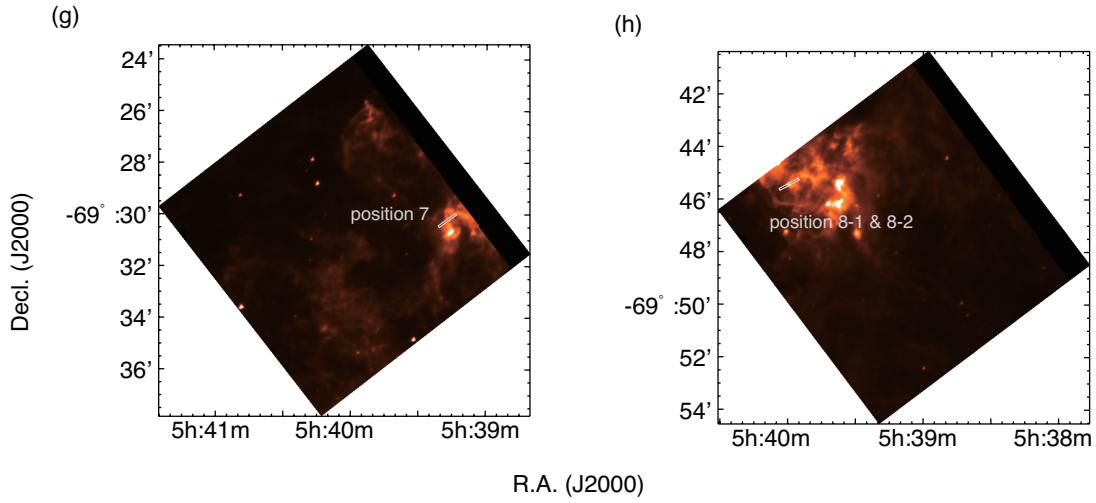

Figure 3.2: Continued.

3.2.3 Data reduction

The present data reduction basically followed the standard toolkit for the IRC spectroscopy. However, some part of the process was deviated from the toolkit with special care, since most targets are faint and require careful data processing. Details of the data reduction process are described in the following.

During a single pointed observation with AOT04 grism mode, eight to nine exposure frames of NIR grism spectroscopic data and one exposure frame of 3.2 μm imaging data were taken with the NIR channel. The dark current was measured in one frame each at the first and last parts of the pointed observation. A single exposure frame consists of one short-exposure and one long-exposure images (see Figure 2.3 for schematic view of unit frame and operation sequence). In the present study, only the long exposure data were used. The dark image for each NIR observation was obtained by averaging three long-exposure images of the dark current, which were collected from the adjacent pointed observations including itself to correct for any high-energy ionizing particle (hereafter cosmic-ray) effects by a 1.5-σ-clipping method. In the present analysis, only the dark current data measured in the first part of each pointed observation were subtracted from the observation images to avoid the latent image effects.

We recognized small shifts in position due to the pointing instability by at most $\sim 5''$ during each pointed observation except for Position 5, where an extraordinary large shift of $\sim 15''$ was found. The shift in the direction parallel to the slit was corrected so that the spectra of the same area of the sky were extracted. Because the shift in the orthogonal direction is uncorrectable, the exposure frames shifted in the direction perpendicular to the slit by more than a pixel ($\sim 1.5''$) as well as those affected by severe artifacts were discarded, except for Position 5 (see below). The remaining images were averaged taking account of the shift in positions in the direction parallel to the slit by a 1.5-σ-clipping method to remove cosmic-ray events and the artifacts.

The most critical part in the data-reduction of *NG* spectra is the removal of artificial patterns as well as the

foreground components originating from the zodiacal light and diffuse Galactic emission. In NIR observations, pixels saturated by cosmic-ray hits or extremely luminous objects often produce artificial line-like patterns in the direction parallel and orthogonal to the slit, termed as "column pull-down" and "multiplexer bleed". Particularly "column pull-down" mimics emission or absorption features in the slit spectrum. The position of the artificial line-like structure sometimes differs among different exposures even in the same pointed observation. When an artificial line structure emerges in a certain exposure image, we removed it by replacing the data of the affected pixels with those of the unaffected pixels of other exposure images at the same position. To estimate the foreground components from the zodiacal and diffuse Galactic emission, we employed the datasets obtained at positions off the LMC with AOT04 a;Ns (observation IDs:1500719 and 1500720). In these observations the NIR spectra were taken by the use of the prism instead of the grism. Because the emission at the off-LMC positions are too faint for the observations with the *NG* mode, we used the prism to obtain a reliable foreground spectrum. The slit positions of both observations are centered at $(\alpha_{\rm J2000}, \delta_{\rm J2000}) = (06^{\rm h}00^{\rm m}00.^{\rm s}0, -66^\circ36'30'')$, which is almost at the same ecliptic latitude ($\beta \sim -90^\circ$) as that of the LMC ($\sim -85^\circ$), but is at $\sim 9.7^\circ$ away from the center of the LMC. The observation log of the off-LMC position is also given in Table 3.1.

The data reduction procedures including the dark-current subtraction and the cosmic-ray correction for MIR-S spectroscopic observations were basically the same as those for NIR spectroscopic observations. During a single pointed observation with AOT04, four exposure frames of *SG1* data, four to five exposure frames of *SG2* data, and one exposure frame of *S9W* band imaging data were taken with the MIR-S channel. The dark current was measured in one frame each in the first and the last parts of the pointed observation. A single exposure frame consists of one short-exposure image and three long-exposure images(see Figure 2.3 for schematic view of unit frame and operation sequence). The dark image for each MIR-S observation was obtained by averaging three long-exposure images of the dark current by a 1.5-σ-clipping method to correct for the cosmic-ray effects. In this process, only the dark current data measured in the first part of each pointed observation sequence were used to avoid the latent image effects. Because the NIR and MIR-S channels share the same FoV, we corrected for the position shifts among the frames in the same manner as in the NIR data, taking account of the difference in the pixel FoV between the NIR and MIR-S channels. The shift in position among three long-exposure images taken in a single frame was negligible in most cases. We averaged these images by a 1.5-σ-clipping method to remove the cosmic-ray effects.

The subtraction of the foreground components (zodiacal light and diffuse Galactic emission) is a more serious problem in the data reduction of MIR spectroscopy than in NIR. In addition, the MIR detector suffers scattered light originating in the scattering within the detector array (e.g., Sakon et al. 2007). To estimate the foreground emission and the scattered light component, we used the *SG1* and *SG2* spectra collected at the position off the LMC (Observation IDs: 1500719 and 1500720). The spectrum at off-position was obtained by averaging the two observations and was subtracted from the spectra of the target positions. The MIR-S

spectra are basically dominated by the zodiacal light and thus the scattered light component of the off-position spectrum is almost the same as that in the spectra of the target. Therefore, the subtraction of the off-position spectrum works effectively not just to remove the foreground emission but also to correct for possible artifacts and greatly improves the resultant spectra.

Using the spectral response function of each module, we obtained *NG*, *SG1* and *SG2* segmental spectra at the same area of the sky except for positions 5 and 8-1 (see below). Each segmental spectrum was truncated at the wavelengths where the signal-to-noise ratio becomes low: *NG* at 2.55 μm and 4.9 μm, *SG1* at 5.5 μm and 7.9 μm and *SG2* at 7.9 μm and 13.4 μm. Then, we applied the correction for the slit efficiency for extended sources (Sakon et al. 2008) to obtain continuous spectra from 2.55 to 13.4 μm with a small gap between 4.9 and 5.5 μm. Because of the severe artifacts (column-pulldown) the *NG* spectrum was truncated at 3.8 μm and 4.5 μm for Positions 2 and 5, respectively. Note that although there is a small gap between the *NG* and *SG1* segments, all the *NG*, *SG1*, and *SG2* segmental spectra are smoothly connected to each other without scaling, suggesting that the subtraction procedure of the foreground emission and scattered light works well and reliable spectra are obtained.

The *SG1* and *SG2* observations were not carried out simultaneously during a pointed observation. A relatively large positional shift ($\sim$15$''$) during the pointed observation for Position 5 prevents us from obtaining the *SG1* and *SG2* spectra from the same region of the sky. For Position 8-1, the positional stability during the pointed observation is almost the same as the other observations. However, a small shift in the position of the point-like source in the slit of 5$''$ width between the *SG1* and *SG2* observations caused a small difference in the flux level between the *SG1* and *SG2* spectra. At both positions, we used the *NG* data taken simultaneously with the *SG2* ones only, since the positional stability was better in the *SG2* observation than that of *SG1*. Then, the *SG1* spectrum was scaled to match with the *SG2* spectra in the spectral region of 7.5 to 7.9 μm. The scaling factors are 0.9 and 0.8 for Position 5 and Position 8-1, respectively. The scaling of the *SG1* spectrum was taken into account in the derivation of the band intensity ratios (see §3.3). It does not make serious effects in the following discussion.

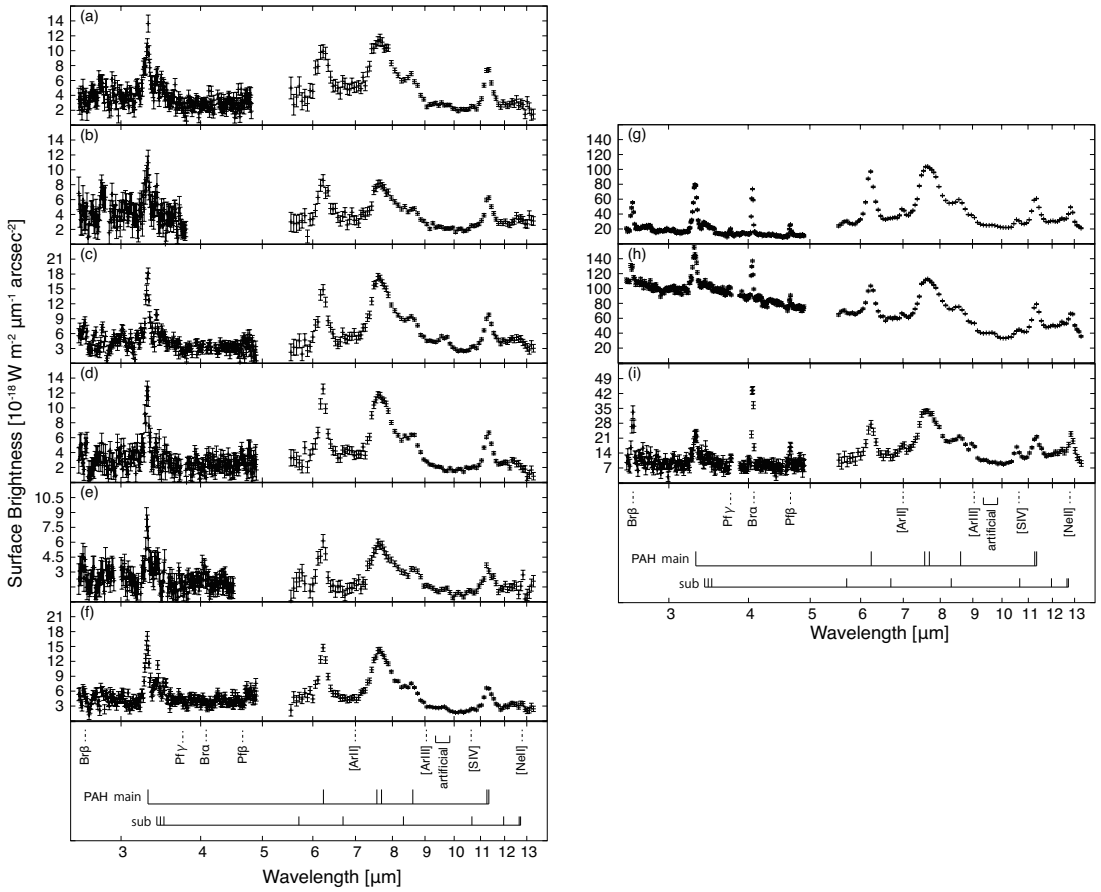

Figure 3.3: Spectra of nine regions in the LMC: **(a)** Position 1, **(b)** Position 2, **(c)** Position 3, **(d)** Position 4, **(e)** Position 5, **(f)** Position 6 **(g)** Position 7, **(h)** Position 8-1, and **(i)** Position 8-2. The bottom panel indicates the positions of the UIR bands and the emission lines.

3.3 Results

The resultant spectra toward our target positions are shown in Figure 3.3. The UIR bands are clearly seen at 3.3, 6.2, 7.7, 8.6 and 11.3 μm in every spectrum. A weak feature around 5.70 μm is also seen at Positions 7 (Boersma et al. 2009). The hydrogen recombination line of Brα 4.05 μm is detected in four of the spectra, and the hydrogen recombination lines of Brβ 2.63 μm, Pfγ 3.75 μm, and Pfβ 4.65 μm as well as the forbidden lines of [Ar II] 6.98 μm, [Ar III] 8.99 μm, [S IV] 10.51 μm, and [Ne II] 12.81 μm are detected in three of the spectra. We note that a small bump seen around at 9.6 μm is an artifact, originating from the latent of the *S9W* exposure frame taken just before the *SG2* exposure frames. Therefore, the spectral data from 9.4 to 9.8 μm are not used in the following analysis.

To derive the intensity of each UIR band and emission line, we fitted the observed spectra with

$$F_\lambda(\lambda) = \sum_{k=0}^{5} a_k \cdot \lambda^k + \sum_{k_l=1}^{14} b_{k_l} \cdot \frac{(\gamma_{k_l}/2)^2}{(\lambda-\lambda_{k_l})^2+(\gamma_{k_l}/2)^2} + \sum_{k_g=1}^{9} c_{k_g} \cdot \exp\left[-\frac{1}{2}\cdot\frac{(\lambda-\lambda_{k_g})^2}{\gamma_{k_g}^2/(8\cdot\ln 2)}\right], \quad (3.1)$$

where λ is the wavelength. The first term represents the continuum. The continuum was modeled with a polynomial function of the $5^{\rm th}$ order and was constrained to be non-negative. The second and third terms cor-

Table 3.3: UIR band parameters modeled by Lorentzian profiles

λ_{k_l} [μm]	γ_{k_l} [μm]
3.29	0.048
3.41	0.044
5.70	0.20
6.22	0.20
6.69	0.48
7.60[a]	0.34
7.85[a]	0.44
8.33	0.50
8.61	0.34
10.68	0.22
11.23[b]	0.20
11.33[b]	0.38
11.99	0.54
12.62	0.54

[a] the components of the 7.7 μm complex feature.
[b] the components of the 11.3 μm complex feature.

respond to the UIR bands and the emission lines, respectively. For the UIR bands, we included 15 components centered at 3.30, 3.41, 3.48, 5.70, 6.22, 6.69, 7.60, 7.85, 8.33, 8.61, 10.68, 11.23, 11.33, 11.99, 12.62 μm according to Smith et al. (2007). Except for the 3.48 μm component, the UIR band components were modeled with Lorentzian profiles (the second term), where λ_{k_l} is the center wavelength, γ_{k_l} is the FWHM and b_{k_l} is the height of each component. As for the 3.30, 3.41, 5.70, 6.22, 6.69, 7.60, 7.85, 8.33, 8.61, 10.68, 11.23, 11.33, 11.99, 12.62 μm components, γ_{k_l} was fixed to the best-fit value obtained for the spectrum that has the highest S/N ratio with the spectral resolution of the *AKARI*/IRC as the minimum value. The adopted value of γ_{k_l} for each component is summarized in Table 3.3. Only the height b_{kl} was left as a free parameter. The integrated intensity of each component is given as $\pi b_{k_l} \cdot \gamma_{k_l}/2$. In the following analysis, the 7.7 and 11.3 μm bands are defined as a combination of the 7.60 and 7.85 μm components and that of 11.23 and 11.33 μm components, respectively. We note that the 12.6 μm band is defined as one component of the 12.62 μm component, because the red-wing component, such as the 12.69 μm component suggested by Smith et al. (2007), is not detected at a significant level in all the spectra due to the poor S/N and the low spectral resolution.

Since the sub-features around 3.5 μm cannot be decomposed with the spectral resolution of the *AKARI*/IRC, they were modeled with one Gaussian profile (the third term), where λ_{k_g} is the center wavelength, γ_{k_g} is the FWHM and c_{kg} is the height of each component. The center wavelength λ_{k_g} and the FWHM γ_{k_g} of this component were fixed to the best-fit values obtained for the spectrum obtained with the *AKARI*/IRC (See Table 3.4). The emission lines, which have the band widths smaller than the spectral resolution of the *AKARI*/IRC, were also modeled with Gaussian profiles. The FWHM γ_{k_g} of these emission lines was fixed to match with the spectral resolution of the *AKARI*/IRC at the corresponding segment (See Table 3.5). In the fitting, only the height c_{kg} was a free parameter. The integrated intensity of each Gaussian component is given by $(\pi/\ln 2)^{1/2} \cdot \mathrm{c_{k_g}} \cdot \gamma_{\mathrm{k_g}}/2$.

We fitted 325 data-points with 29 free parameters in total as previously mentioned. The best-fit model spectra given by Eq. (3.1) are plotted together with the observed spectra in Figure 3.4. The residual spectra

Table 3.4: UIR band parameter modeled by Gaussian profile

λ_{k_g} [μm]	γ_{k_g} [μm]
3.48	0.113

Table 3.5: Emission line parameters modeled by Gaussian profiles

Line	λ_{k_g} [μm]	γ_{k_g} [μm]
Brβ	2.63	0.031
Brα	4.05	0.031
Pfγ	3.74	0.031
Pfβ	4.65	0.031
[Ar II]	6.98	0.114
[Ar III]	8.99	0.200
[S IV]	10.51	0.200
[Ne II]	12.81	0.200

are also plotted in the lower panel of each plot. The derived intensities of the major UIR bands at 3.3, 6.2, 7.7, 8.6, 11.3, and 12.6 μm and the emission lines of Brα , Brβ , Pfγ , Pfβ, [Ar II] 6.98 μm, [Ar III] 8.99 μm, [S IV] 10.51 μm, and [Ne II] 12.81 μm are summarized in Tables 3.6 and 3.7, respectively, where those detected with more than 2σ are indicated. The uncertainties in the intensity were estimated from the fitting errors taking account of the observational uncertainties.

As shown in Table 3.6, the 3.3, 6.2, 7.7, 8.6, 11.3, and 12.6 μm bands are detected at every target position except for the 12.6 μm band at Position 5, which shows the faintest emission. The 5.70 μm band are detected only at Positions 7. On the other hand, as shown in Table 3.7, all of the hydrogen recombination lines of Brα 4.05 μm, Brβ 2.63 μm, Pfγ 3.75 μm, and Pfβ 4.65 μm and the fine structure lines from the ionized gas of [Ar II] 6.98 μm, [Ar III] 8.99 μm, [S IV] 10.51 μm, and [Ne II] 12.81 μm are detected at Positions 7, 8-1 and 8-2, whereas none of them are detected at Positions 1, 2, 3, 4, 5 and 6 except for Brβ and Brα detected barely at Position 3 and Position 5. Taking account of the high ionization potentials of 27.63 eV, 34.83 eV and 21.56 eV to form Ar^{2+}, S^{3+} and Ne^{+} (Allen 1973), respectively, Positions 7, 8-1 and 8-2 are exposed to the hard incident radiation field powered by young massive stars and are associated with H II regions. This view is consistent with the radiation field conditions suggested by the *IRAS* and *AKARI* colors. Based on the characteristics of the observed spectra, we classify the targets into two groups: "Group A", which includes Positions 1, 2, 3, 4, 5 and 6 and "Group B", to which Positions 7, 8-1 and 8-2 belong. The members of Group A are supposed to be exposed to incident radiation fields of weak to moderate intensities and consist mostly of molecular clouds and PDRs. Group B members are all associated with H II regions.

We examined the effects of extinction on the spectra observed at the present target positions according to Dobashi et al. (2008). The visual extinction A_V toward the present target positions ranges from 0.0 to 2.5 as shown in the last row of Table 3.1. We assumed the "LMC avg" extinction curve provided by Weingartner & Draine (2001) to estimate the extinction at IR wavelengths. We also estimated the value of A_V from the observed ratio of Brβ to Brα at Positions 7, 8-1, and 8-2, assuming the Case B condition of $T_{\rm e} = 10^4$K and $n_{\rm e} = 10^4{\rm cm}^{-3}$ (Storey & Hummer 1995). The UIR band intensities corrected with A_V provided by Dobashi

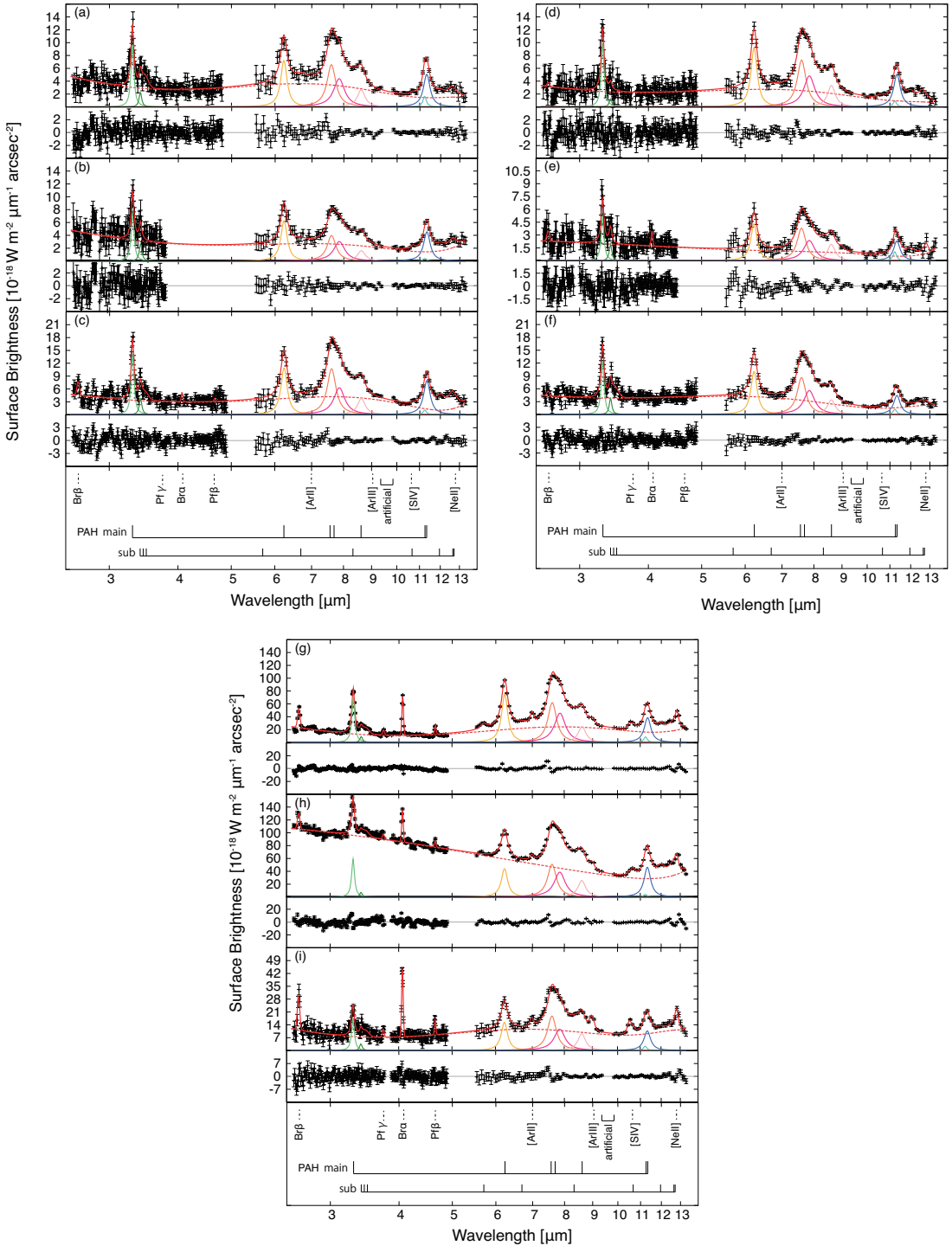

Figure 3.4: Modeled spectra are overlain on the observed spectra of nine regions in the LMC; **(a)** Position 1, **(b)** Position 2, **(c)** Position 3, **(d)** Position 4, **(e)** Position 5, **(f)** Position 6 **(g)** Position 7, **(h)** Position 8-1, and **(i)** Position 8-2. The red solid lines show the best-fit model spectra (see text). The light-red dotted lines indicate the continuum component of a quintic function. The light-green, dark-green, yellow, coral, dark-pink, pink, light-blue and dark-blue lines show the UIR 3.3 μm, 3.4 μm, 6.2 μm, 7.6 μm, 7.8 μm, 8.6 μm, 11.2 μm and 11.3 μm bands of a Lorentzian function, respectively. We cut 9.4–9.8 μm from spectra in Figure 3.3 due to the artifacts (see text). The lower panel shows a residual spectrum at each plot. The bottom panel is the same as in Figure 3.3.

Table 3.6: Observed and corrected intensity of the UIR bands

Position ID	$I_{3.3\,\mu\mathrm{m}}$	$I_{6.2\,\mu\mathrm{m}}$	$I_{7.7\,\mu\mathrm{m}}$	$I_{8.6\,\mu\mathrm{m}}$	$I_{11.3\,\mu\mathrm{m}}$	$I_{12.6\,\mu\mathrm{m}}$
Position 1	0.731 ± 0.046	2.260 ± 0.190	6.540 ± 0.320	1.421 ± 0.142	3.530 ± 0.280	1.240 ± 0.390
	0.817 ± 0.051	2.370 ± 0.200	6.940 ± 0.340	1.660 ± 0.165	4.083 ± 0.324	1.350 ± 0.430
Position 2	0.552 ± 0.068	1.970 ± 0.180	4.210 ± 0.280	0.857 ± 0.125	2.840 ± 0.250	1.070 ± 0.360
	0.575 ± 0.070	2.000 ± 0.180	4.310 ± 0.280	0.909 ± 0.132	3.000 ± 0.266	1.100 ± 0.370
Position 3	1.074 ± 0.044	3.420 ± 0.220	10.050 ± 0.350	2.020 ± 0.162	4.950 ± 0.320	2.990 ± 0.450
	1.201 ± 0.049	3.580 ± 0.230	10.680 ± 0.370	2.364 ± 0.189	5.730 ± 0.375	3.250 ± 0.490
Position 4	0.750 ± 0.052	2.880 ± 0.140	7.210 ± 0.240	1.778 ± 0.107	3.300 ± 0.210	1.390 ± 0.310
	0.751 ± 0.052	2.880 ± 0.140	7.220 ± 0.240	1.783 ± 0.107	3.310 ± 0.218	1.400 ± 0.310
Position 5	0.384 ± 0.047	1.350 ± 0.140	3.660 ± 0.240	1.022 ± 0.120	1.700 ± 0.240	$\cdots$
	0.397 ± 0.049	1.380 ± 0.140	3.740 ± 0.240	1.095 ± 0.128	1.813 ± 0.264	$\cdots$
Position 6	0.947 ± 0.038	3.150 ± 0.150	8.470 ± 0.250	1.813 ± 0.112	3.030 ± 0.220	1.000 ± 0.320
	0.982 ± 0.039	3.200 ± 0.150	8.640 ± 0.260	1.909 ± 0.117	3.178 ± 0.237	1.030 ± 0.330
Position 7	5.294 ± 0.052	23.460 ± 0.210	64.540 ± 0.350	13.195 ± 0.157	25.680 ± 0.310	11.910 ± 0.460
	5.270 ± 0.053	23.770 ± 0.210	65.020 ± 0.350	13.798 ± 0.164	26.769 ± 0.329	12.200 ± 0.470
Position 8-1	4.450 ± 0.085	13.830 ± 0.240	53.950 ± 0.470	13.703 ± 0.252	28.880 ± 0.520	15.810 ± 0.750
	4.868 ± 0.096	14.560 ± 0.260	57.150 ± 0.500	16.317 ± 0.300	33.933 ± 0.612	17.360 ± 0.820
Position 8-2	1.269 ± 0.108	4.830 ± 0.390	18.050 ± 0.610	4.850 ± 0.282	7.100 ± 0.570	3.080 ± 0.840
	1.308 ± 0.122	5.080 ± 0.410	18.890 ± 0.660	5.775 ± 0.335	8.348 ± 0.680	3.380 ± 0.920

[a]The UIR bands detected with more than $2\,\sigma$ are listed. For each position, the upper row indicates the original band intensity and the lower row shows the intensity after the correction for the extinction and the contribution from the hydrogen recombination lines (see text).

[b]In units of 10^{-18}W m^{-2} arcsec^{-2}.

et al. (2008) differ from those corrected with A_V estimated from the Case B condition by less than 10 % at Positions 7, 8-1, and 8-2. We adopted those corrected with A_V provided by Dobashi et al. (2008) at these positions for consistency with the other target positions. The effect of extinction correction on the UIR band ratios is small ($< 15\,\%$), and does not affect the following discussion.

Next, we evaluated a contribution from the unresolved emission line Pfδ at 3.30 μm to the 3.3 μm band, and that from Pfα at 7.46 μm to the 7.7 μm band. We assumed that the intensities of Pfδ and Pfα are equal to 9.3% and 30.1% of that of Brα, respectively, according to the Case B condition and subtracted them from the intensity of the 3.3 μm and 7.7 μm bands. In the present target positions, the contribution from Pfδ to the 3.3 μm band is less than 10% and that from Pfα to the 7.7 μm band is less than 3%, both of which are similar to the measurement uncertainties and thus do not affect the results. The intensity for which these corrections are applied is also listed in the lower row for each position in Tables 3.6 and 3.7. The values of the corrected UIR band ratios are listed in Table 3.8. The effect of these corrections on the values of the UIR band ratios is less than $\sim 10\%$ for all the targets. We estimated the uncertainties in $I_{6.2\,\mu\mathrm{m}}$ and $I_{7.7\,\mu\mathrm{m}}$ as the difference between the intensities with and without scaling, which dominates over the fitting errors.

Figures 3.5 (a)–(f) show the plots of the corrected UIR band ratios of the $I_{3.3\,\mu\mathrm{m}}/I_{11.3\,\mu\mathrm{m}}$, $I_{6.2\,\mu\mathrm{m}}/I_{11.3\,\mu\mathrm{m}}$, $I_{7.7\,\mu\mathrm{m}}/I_{11.3\,\mu\mathrm{m}}$, $I_{8.6\,\mu\mathrm{m}}/I_{11.3\,\mu\mathrm{m}}$, $I_{12.6\,\mu\mathrm{m}}/I_{11.3\,\mu\mathrm{m}}$, and $I_{6.2\,\mu\mathrm{m}}/I_{7.7\,\mu\mathrm{m}}$ against the *IRAS* color of $I_{25\,\mu\mathrm{m}}/I_{12\,\mu\mathrm{m}}$. Figures 3.5 (g)–(l) plot those ratios against the *AKARI* color of $I_{24\,\mu\mathrm{m}}/I_{11\,\mu\mathrm{m}}$. Group A forms a sequence with a positive slope in the plots of $I_{3.3\,\mu\mathrm{m}}/I_{11.3\,\mu\mathrm{m}}$, $I_{6.2\,\mu\mathrm{m}}/I_{11.3\,\mu\mathrm{m}}$, $I_{7.7\,\mu\mathrm{m}}/I_{11.3\,\mu\mathrm{m}}$ and $I_{8.6\,\mu\mathrm{m}}/I_{11.3\,\mu\mathrm{m}}$ against the *IRAS* and *AKARI* colors, while Group B does not follow the sequence in the plots of these band ratios. Rather $I_{3.3\,\mu\mathrm{m}}/I_{11.3\,\mu\mathrm{m}}$, $I_{6.2\,\mu\mathrm{m}}/I_{11.3\,\mu\mathrm{m}}$, and $I_{7.7\,\mu\mathrm{m}}/I_{11.3\,\mu\mathrm{m}}$ indicate a decreasing trend with the color among Group B members. However, the number of Group B data is too small to make a firm conclusion, and we will not discuss

Table 3.7: Observed and corrected intensity of the emission lines

Position ID	$I_{\mathrm{Br}\beta 2.63}$	$I_{\mathrm{Br}\alpha 4.05}$	$I_{\mathrm{Pf}\gamma 3.74}$	$I_{\mathrm{Pf}\beta 4.65}$	$I_{[\mathrm{Ar\,II}]6.98}$	$I_{[\mathrm{Ar\,III}]8.99}$	$I_{[\mathrm{S\,IV}]10.51}$	$I_{[\mathrm{Ne\,II}]12.81}$
osition 1	···	···	···	···	···	···	···	···
	···	···	···	···	···	···	···	···
Position 2	···	···	···	···	···	···	···	···
	···	···	···	···	···	···	···	···
Position 3	0.108 ± 0.027	···	···	···	···	···	···	···
	0.127 ± 0.032	···	···	···	···	···	···	···
Position 4	···	···	···	···	···	···	···	···
	···	···	···	···	···	···	···	···
Position 5	···	0.059 ± 0.016	···	···	···	···	···	···
	···	0.060 ± 0.016	···	···	···	···	···	···
Position 6	···	···	···	···	···	···	···	···
	···	···	···	···	···	···	···	···
Position 7	0.992 ± 0.032	2.057 ± 0.018	0.268 ± 0.018	0.458 ± 0.023	1.661 ± 0.080	1.500 ± 0.056	1.583 ± 0.050	3.998 ± 0.127
	1.039 ± 0.034	2.101 ± 0.017	0.275 ± 0.018	0.465 ± 0.024	1.678 ± 0.081	1.591 ± 0.059	1.675 ± 0.053	4.090 ± 0.130
Position 8-1	0.837 ± 0.053	1.711 ± 0.029	0.274 ± 0.029	0.302 ± 0.034	0.829 ± 0.091	2.051 ± 0.090	0.950 ± 0.083	3.692 ± 0.210
	1.002 ± 0.063	1.859 ± 0.031	0.302 ± 0.032	0.322 ± 0.036	0.863 ± 0.095	2.582 ± 0.113	1.183 ± 0.104	4.032 ± 0.230
Position 8-2	0.633 ± 0.067	1.281 ± 0.036	0.145 ± 0.037	0.262 ± 0.043	0.489 ± 0.147	1.411 ± 0.100	1.277 ± 0.092	1.862 ± 0.233
	0.758 ± 0.080	1.392 ± 0.039	0.160 ± 0.041	0.280 ± 0.046	0.509 ± 0.153	1.777 ± 0.126	1.591 ± 0.115	2.034 ± 0.254

[a] Emission lines detected with more than 2 σ are listed. For each position, the upper row indicates the original band intensity and the lower row shows the extinction-corrected intensity (see text).
[b] In units of 10^{-18}W m^{-2} arcsec^{-2}.

Table 3.8: UIR band intensity ratios

Position ID	$I_{3.3\,\mu\mathrm{m}}/I_{11.3\,\mu\mathrm{m}}$	$I_{6.2\,\mu\mathrm{m}}/I_{11.3\,\mu\mathrm{m}}$	$I_{7.7\,\mu\mathrm{m}}/I_{11.3\,\mu\mathrm{m}}$	$I_{8.6\,\mu\mathrm{m}}/I_{11.3\,\mu\mathrm{m}}$	$I_{12.6\,\mu\mathrm{m}}/I_{11.3\,\mu\mathrm{m}}$	$I_{6.2\,\mu\mathrm{m}}/I_{7.7\,\mu\mathrm{m}}$
Position 1	0.200 ± 0.020	0.581 ± 0.067	1.701 ± 0.159	0.406 ± 0.051	0.331 ± 0.109	0.341 ± 0.033
Position 2	0.191 ± 0.029	0.670 ± 0.085	1.438 ± 0.159	0.303 ± 0.051	0.368 ± 0.128	0.465 ± 0.052
Position 3	0.209 ± 0.016	0.625 ± 0.057	1.865 ± 0.138	0.413 ± 0.042	0.568 ± 0.094	0.335 ± 0.024
Position 4	0.227 ± 0.021	0.871 ± 0.072	2.181 ± 0.161	0.539 ± 0.048	0.423 ± 0.097	0.399 ± 0.024
Position 5	0.219 ± 0.041	0.763 ± 0.138	2.064 ± 0.380	0.604 ± 0.113	$\cdots$	0.369 ± 0.046
Position 6	0.309 ± 0.026	1.008 ± 0.090	2.718 ± 0.218	0.600 ± 0.058	0.326 ± 0.109	0.370 ± 0.021
Position 7	0.196 ± 0.003	0.888 ± 0.013	2.428 ± 0.032	0.515 ± 0.009	0.455 ± 0.018	0.365 ± 0.003
Position 8-1	0.143 ± 0.003	0.429 ± 0.096	1.684 ± 0.330	0.480 ± 0.012	0.511 ± 0.026	0.254 ± 0.005
Position 8-2	0.156 ± 0.019	0.609 ± 0.069	2.263 ± 0.200	0.691 ± 0.068	0.405 ± 0.115	0.269 ± 0.023

the trend in the following section. The $I_{12.6\,\mu\mathrm{m}}/I_{11.3\,\mu\mathrm{m}}$ and $I_{6.2\,\mu\mathrm{m}}/I_{7.7\,\mu\mathrm{m}}$ ratios do not show a systematic trend with the colors either for Groups A or B. Little variation found in the 6.2 μm to the 7.7 μm band ratio is similar to the trend seen in external galaxies (Galliano et al. 2008). The present observation shows that the 3.3 μm band is weak in Group B compared to Group A. The results are discussed in the next section.

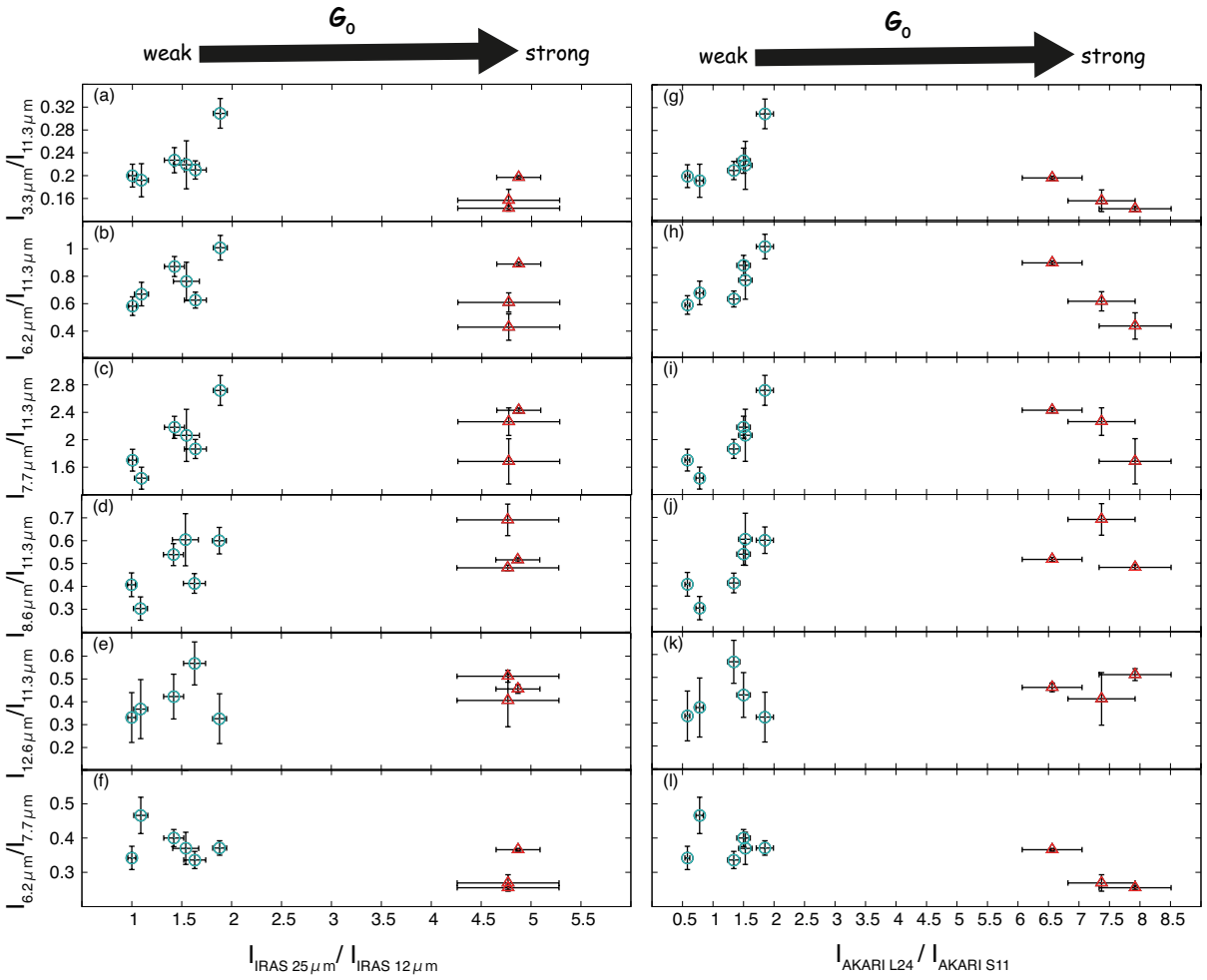

Figure 3.5: Variation of the UIR band ratios of the 3.3 μm to the 11.3 μm band [**(a)** and **(g)**], the 6.2 μm to the 11.3 μm band [**(b)** and **(h)**], the 7.7 μm to the 11.3 μm band [**(c)** and **(i)**], the 8.6 μm to the 11.3 μm band [**(d)** and **(j)**], the 12.6 μm to the 11.3 μm band [**(e)** and **(k)**], and the 6.2 μm to the 7.7 μm band [**(f)** and **(l)**] against the *IRAS* color of $I_{25\,\mu\mathrm{m}}/I_{12\,\mu\mathrm{m}}$ and the *AKARI* color of $I_{24\,\mu\mathrm{m}}/I_{11\,\mu\mathrm{m}}$. The turquoise open circles and the red open triangles with the black error-bars indicate Groups A and B, respectively. The UIR band ratios are corrected for the extinction and the contribution from the hydrogen recombination lines.

3.4 Discussion

3.4.1 Variation in the unidentified infrared band ratios

Studies based on quantum chemical calculations as well as laboratory experiments have demonstrated that the ionization fraction and the molecular size of PAHs are the primary factors to affect the relative intensity of the UIR band features (e.g., Allamandola et al. 1999; Draine & Li 2007; Tielens 2008). The ionization fraction of PAHs is determined by the balance between the photo-ionization and the recombination with ambient electrons and thus it is expected to be controlled by $G_0 \cdot T_{\rm g}^{1/2}/n_{\rm e}$, where G_0 is the intensity of the radiation field in units of the solar vicinity value ($1.6 \times 10^{-6}\,{\rm W\,m^{-2}}$, Habing 1968), $n_{\rm e}$ is the electron density, and $T_{\rm g}$ is the gas temperature (Bakes & Tielens 1994; Bakes et al. 2001). Higher $G_0/n_{\rm e}$ ratios favor larger fractions of positively ionized PAHs (Bakes et al. 2001). Laboratory experiments and theoretical studies suggested that the ionization of PAHs enhances the intensity of the band features in the 6–9 μm region relative to the features in the 11–14 μm region (DeFrees et al. 1993; Szczepanski & Vala 1993; Allamandola et al. 1999; Bakes et al. 2001). Therefore, the ionized-to-neutral band ratios (e.g. , $I_{6.2\,\mu{\rm m}}/I_{11.3\,\mu{\rm m}}$, $I_{7.7\,\mu{\rm m}}/I_{11.3\,\mu{\rm m}}$, $I_{8.6\,\mu{\rm m}}/I_{11.3\,\mu{\rm m}}$) are supposed to indicate the ionization conditions of PAHs. Observational studies reported variations in $I_{7.7\,\mu{\rm m}}/I_{11.3\,\mu{\rm m}}$ and $I_{8.6\,\mu{\rm m}}/I_{11.3\,\mu{\rm m}}$ within a reflection nebula along the distance from the central star (Bregman & Temi 2005; Joblin et al. 1996b), among Herbig Ae/Be stars with different spectral types (Sloan et al. 2005), between the inter-arm and arm regions of the star-forming galaxy NGC6949 (Sakon et al. 2007), and between the inner and outer Galaxy (Sakon et al. 2004). They are reasonably interpreted by the difference in the ionization conditions of PAHs.

Since the heat capacity is positively correlated with the size, smaller PAHs become more highly excited, if excitation source is the same. Among the UIR bands, the features at short wavelengths require a more highly excited state than those at long wavelengths. Very small PAHs ($n_{\rm C} < 100$) thus radiate intensely the 3.3 μm band, whereas large PAHs dominate the longer wavelength regions: PAHs as large as $n_{\rm C} \sim 10^2$–10^3 efficiently convert the absorbed energy into the 6.2, 7.7 and 8.6 μm bands and PAHs as large as $n_{\rm C} \sim 4000$ into the 11.3 μm band (Schutte et al. 1993; Draine & Li 2007). The 6.2 μm and 7.7 μm bands are attributed to stretching modes of C-C bonds, while the 3.3 μm, the 8.6 μm and the 11.3 μm bands are attributed to stretching modes, in-plane bending modes, and out-of-plane bending modes of C-H bonds, respectively (Allamandola et al. 1989b). Therefore the ratios of the short-to-long wavelength UIR bands from the same bonds (e.g., $I_{3.3\,\mu{\rm m}}/I_{11.3\,\mu{\rm m}}$, $I_{6.2\,\mu{\rm m}}/I_{7.7\,\mu{\rm m}}$) can be used to infer the average temperature and/or the size distribution of PAHs (e.g., Jourdain de Muizon et al. 1990; Sales et al. 2010; Boersma et al. 2010). The NIR to MIR spectra we discuss here are obtained from the same region in the sky and thus we can discuss the band intensity ratios of the major UIR bands at 3.3, 6.2, 7.7, 8.6 and 11.3 μm concurrently.

As described in §3.3, Group A forms a sequence on the diagrams of the *IRAS* and *AKARI* colors v.s.

the ionized-to-neutral UIR band ratios: $I_{6.2\,\mu\mathrm{m}}/I_{11.3\,\mu\mathrm{m}}$, $I_{7.7\,\mu\mathrm{m}}/I_{11.3\,\mu\mathrm{m}}$ and $I_{8.6\,\mu\mathrm{m}}/I_{11.3\,\mu\mathrm{m}}$. The sequence suggests that a larger fraction of PAHs is ionized as the radiation field becomes stronger. However, Group B, whose radiation fields are much stronger and harder than those of Group A, does not follow the sequence. This can be attributed to the lower ionization fraction of PAHs due to an increase in the recombination under the high electron density in H II regions relative to molecular clouds or PDRs.

There is a positive correlation between *IRAS* and *AKARI* colors and the short-to-long wavelength UIR band ratio, $I_{3.3\,\mu\mathrm{m}}/I_{11.3\,\mu\mathrm{m}}$ in Group A. This can be interpreted in terms of an increase in the excitation temperature of PAHs with the *IRAS* and *AKARI* colors in Group A. Destruction of PAHs is expected to be inefficient in environments of Group A (Micelotta et al. 2010a,b, 2011) and the size distribution of PAHs should not change considerably. Thus the excitation temperature of PAHs is mainly controlled by the hardness of the incident radiation field, but not by its intensity. On the other hand, the *IRAS* and *AKARI* colors indicate its intensity, but not the hardness directly (Sakon et al. 2006; Onaka et al. 2007b). The correlation seen in Figure 3.5 thus indicates that the incident radiation field becomes harder as the intensity becomes larger in Group A. This is a reasonable consequence of strong incident radiation fields, for which a contribution from young massive stars becomes dominant. The present observations indicate this trend explicitly based on the NIR to MIR UIR band ratios. Harder incident radiation fields also directly increase the $I_{6.2\,\mu\mathrm{m}}/I_{11.3\,\mu\mathrm{m}}$, $I_{7.7\,\mu\mathrm{m}}/I_{11.3\,\mu\mathrm{m}}$, and $I_{8.6\,\mu\mathrm{m}}/I_{11.3\,\mu\mathrm{m}}$. We show in §3.4.2 that the ionization fraction is the major factor for the increase in these ratios with a minor contribution from the hardness of the incident radiation field.

Group B does not follow the trend of Group A and shows the weaker 3.3 μm band. It can be attributed to a paucity of very small PAHs ($n_{\mathrm{C}} < 100$), which are supposed to dominantly contribute to the 3.3 μm band (Schutte et al. 1993; Draine & Li 2007), in H II regions. Micelotta et al. (2010a) suggest that electron collisions dominate in the destruction of PAHs in a hot plasma for gas temperatures between $\sim 3 \times 10^4$ and $\sim 10^6$ K, where smaller PAHs are more efficiently destroyed than larger ones. The threshold temperatures depend sensitively on the assumed electronic dissociation energy. The difference of $I_{3.3\,\mu\mathrm{m}}/I_{11.3\,\mu\mathrm{m}}$ between Group A and B may thus result from the destruction of PAHs by electron collisions in Group B. Alternatively, de-hydrogenation of small PAHs in harsh environments might also explain this trend. H-loss of small PAHs reduces the intensity of the 3.3 μm band preferentially.

3.4.2 Diagnostic diagram of the radiation field condition

The diagnostic diagram of the unidentified infrared band ratios

According to the discussion in the previous subsections and the results presented in §3.3, we explore possible diagnostic diagrams to investigate the physical conditions of the ISM by means of the UIR band ratios. The ratio of $I_{3.3\,\mu\mathrm{m}}/I_{11.3\,\mu\mathrm{m}}$ is found to be a good indicator of the size distribution of PAHs, whereas $I_{6.2\,\mu\mathrm{m}}/I_{11.3\,\mu\mathrm{m}}$, $I_{7.7\,\mu\mathrm{m}}/I_{11.3\,\mu\mathrm{m}}$, or $I_{8.6\,\mu\mathrm{m}}/I_{11.3\,\mu\mathrm{m}}$ has been indicated to be a measure of the ionized fraction of PAHs as

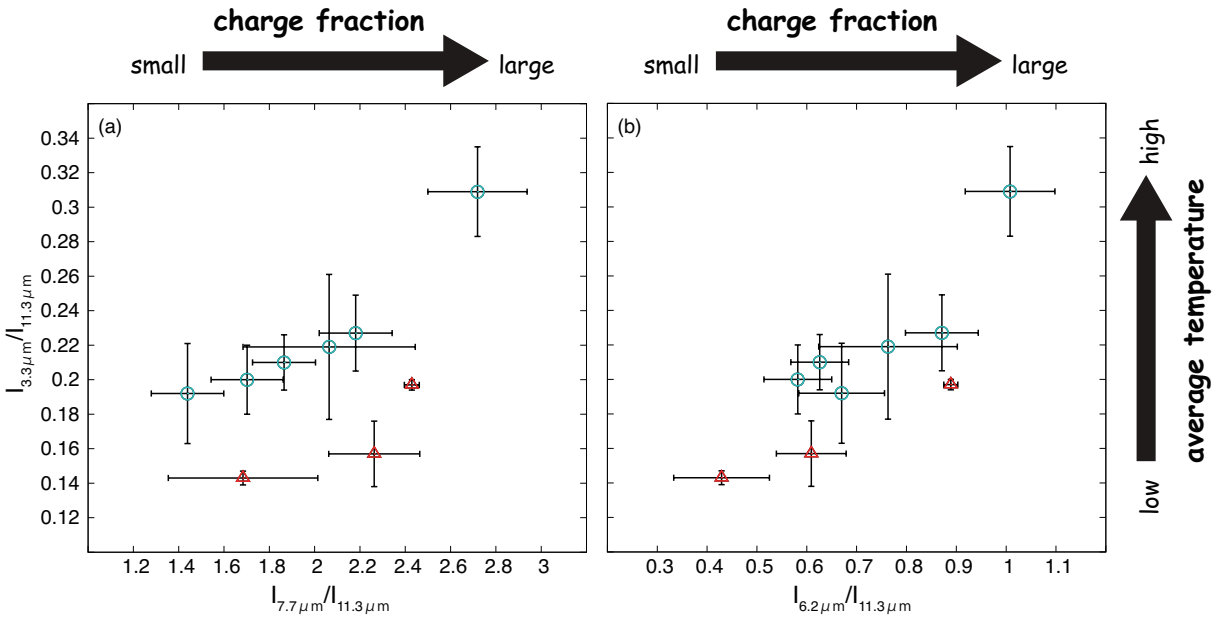

Figure 3.6: Variation of the UIR band ratios of **(a)** the 7.7 μm to the 11.3 μm band and **(b)** the 6.2 μm band the 11.3 μm band against the UIR band ratio of the 3.3 μm to the 11.3 μm band. The turquoise open circles and the red open triangles with the black error-bars indicate Groups A and B, respectively. The UIR band ratios are corrected for the extinction and the contribution from the hydrogen recombination lines.

discussed above. The 8.6 μm band is typically weak and situated on the shoulder of the strong 7.7 μm band due to the limited resolution provided by the IRC. Thus $I_{8.6\,\mu\mathrm{m}}/I_{11.3\,\mu\mathrm{m}}$ is less reliable than the other two ratios and will not be considered. Taking account of these, we investigate two-band-ratio plots of $I_{3.3\,\mu\mathrm{m}}/I_{11.3\,\mu\mathrm{m}}$ v.s. $I_{7.7\,\mu\mathrm{m}}/I_{11.3\,\mu\mathrm{m}}$ or $I_{6.2\,\mu\mathrm{m}}/I_{11.3\,\mu\mathrm{m}}$ as shown in Figures 3.6 (a) and (b).

In Figure 3.6 (a), where $I_{3.3\,\mu\mathrm{m}}/I_{11.3\,\mu\mathrm{m}}$ is plotted against $I_{7.7\,\mu\mathrm{m}}/I_{11.3\,\mu\mathrm{m}}$, Group A forms a sequence from the bottom-left to the top-right. This sequence can be interpreted in terms of the change in the spectrum of the incident radiation field together with the change in the ionization fraction of PAHs. Group B, however, does not follow the sequence and is located distinctly from Group A. Figure 3.6 (b) shows a plot of $I_{3.3\,\mu\mathrm{m}}/I_{11.3\,\mu\mathrm{m}}$ v.s. $I_{6.2\,\mu\mathrm{m}}/I_{11.3\,\mu\mathrm{m}}$. Group A forms a sequence similar to the plot of $I_{3.3\,\mu\mathrm{m}}/I_{11.3\,\mu\mathrm{m}}$ v.s. $I_{7.7\,\mu\mathrm{m}}/I_{11.3\,\mu\mathrm{m}}$ and Group B data are also separated from Group A. The separation of Group B from Group A is more distinct in Figure 3.6 (a) than in Figure 3.6 (b). Lower left points of Group B in Figure 3.6 (b) may overlap with the sequence of Group A if the sequence continues down to the lower ratios and would become difficult to be distinguished from Group A. The difference between the two plots comes from a slight decrease in the 6.2 μm band intensity relative to the 7.7 μm band in Group B, in particular in Position 8-1 and 8-2 spectra. While the $I_{6.2\,\mu\mathrm{m}}/I_{7.7\,\mu\mathrm{m}}$ ratio of Group A does not show a clear dependency on the intensity and/or hardness of the radiation field [Figures 3.5 (e) and (j)], the average value of the $I_{6.2\,\mu\mathrm{m}}/I_{7.7\,\mu\mathrm{m}}$ ratio of Group B (0.296$\pm$0.060) is slightly smaller than that of Group A (0.380$\pm$0.048). This may suggest that even medium-sized PAHs are destroyed in H II regions in Group B (Schutte et al. 1993; Draine & Li 2001; Sales et al. 2010). However, there is a large scatter in $I_{6.2\,\mu\mathrm{m}}/I_{7.7\,\mu\mathrm{m}}$ among each group. We cannot rule out a possibility that there are other

causes for the variation in $I_{6.2\,\mu\mathrm{m}}/I_{7.7\,\mu\mathrm{m}}$.

In the present results, Groups A and B can be distinguished more clearly in the diagram of $I_{3.3\,\mu\mathrm{m}}/I_{11.3\,\mu\mathrm{m}}$ v.s. $I_{7.7\,\mu\mathrm{m}}/I_{11.3\,\mu\mathrm{m}}$ than that of $I_{3.3\,\mu\mathrm{m}}/I_{11.3\,\mu\mathrm{m}}$ v.s. $I_{6.2\,\mu\mathrm{m}}/I_{11.3\,\mu\mathrm{m}}$. It suggests a potential of the diagram of $I_{3.3\,\mu\mathrm{m}}/I_{11.3\,\mu\mathrm{m}}$ v.s. $I_{7.7\,\mu\mathrm{m}}/I_{11.3\,\mu\mathrm{m}}$ as a diagnostic tool for the radiation field conditions. The 6.2 μm band is usually thought as a more reliable indicator than the 7.7 μm band, since the 6.2 μm consists of a single component, while the 7.7 μm contains more than one component (Peeters et al. 2002; Smith et al. 2007). The present results indicate that the 7.7 μm band might be a better indicator than the 6.2 μm band as far as the ionization fraction of PAHs is concerned probably because it is less sensitive to the variation in the size distribution. The number of Group B targets is small, however, and thus we need further investigations to ensure if this conclusion can be applied to the general ISM with a wide range of physical conditions.

Vermeij et al. (2002) investigated the variations in the UIR bands among the H II regions in the LMC based on ISOPHOT/PHT-S observations. They found that the $I_{6.2\,\mu\mathrm{m}}/I_{11.3\,\mu\mathrm{m}}$ and $I_{7.7\,\mu\mathrm{m}}/I_{11.3\,\mu\mathrm{m}}$ ratios are systematically smaller in H II regions in 30 Doradus and the Small Magellanic Cloud (SMC) than in galactic and non-30 Doradus regions. They suggested that the segregation may be attributed to the difference in the molecular structure of PAHs, proposing that compact PAHs may dominate in 30 Doradus regions and the SMC. The present targets do not include 30 Doradus itself. Also none of them have the incident radiation fields of the intensity similar to the 30 Doradus region. The 11.3 μm band is due to solo C-H out-of-plane bending modes and probes long straight edges, whereas the 12.6 μm band is due to trio C-H out-of-plane modes and probes corners. The contribution from compact PAHs enhances the 11.3 μm band relative to the 12.6 μm band. The different compactness of PAHs is supposed to appear more distinctly in the $I_{12.6\,\mu\mathrm{m}}/I_{11.3\,\mu\mathrm{m}}$ ratio than in the $I_{3.3\,\mu\mathrm{m}}/I_{11.3\,\mu\mathrm{m}}$. The ratio of $I_{12.6\,\mu\mathrm{m}}/I_{11.3\,\mu\mathrm{m}}$ is 0.40 ± 0.10 and 0.46 ± 0.05 for Group A and B, respectively. Although the intensity of the 12.6 μm band has a large uncertainty, the ratio does not show a distinct difference as seen in $I_{3.3\,\mu\mathrm{m}}/I_{11.3\,\mu\mathrm{m}}$, suggesting that the molecular structure does not change appreciably among the present targets and is not the major factor for the difference in $I_{3.3\,\mu\mathrm{m}}/I_{11.3\,\mu\mathrm{m}}$.

Recently Hony & SAGE-Spec Team (2011) also studied the variations of the UIR bands at MIR wavelengths in various environments across the LMC, including molecular clouds, PDRs, and H II regions, based on *Spitzer*/IRS observations. They found that the ratio $I_{7.7\,\mu\mathrm{m}}/I_{11.3\,\mu\mathrm{m}}$ is mostly controlled by the ionization fraction of PAHs and weakly correlates with the [Ne II]/[Ne III] line ratio, which they interpreted as the indicator of hardness of the incident radiation field. The present results show a similar trend, but also suggest a systematic trend with the hardness, once molecular clouds and PDRs are separated from H II regions by use of the ratio $I_{3.3\,\mu\mathrm{m}}/I_{11.3\,\mu\mathrm{m}}$. The sequence seen for Group A suggests that the excitation of PAHs as indicated by $I_{3.3\,\mu\mathrm{m}}/I_{11.3\,\mu\mathrm{m}}$ is enhanced with the ionization fraction, which is indicated by $I_{7.7\,\mu\mathrm{m}}/I_{11.3\,\mu\mathrm{m}}$ or $I_{6.2\,\mu\mathrm{m}}/I_{11.3\,\mu\mathrm{m}}$. Thus the ratio $I_{3.3\,\mu\mathrm{m}}/I_{11.3\,\mu\mathrm{m}}$ is a useful measure of the incident radiation field conditions for Group A targets. This interpretation suggests that star-forming activity of objects at the lower left is less

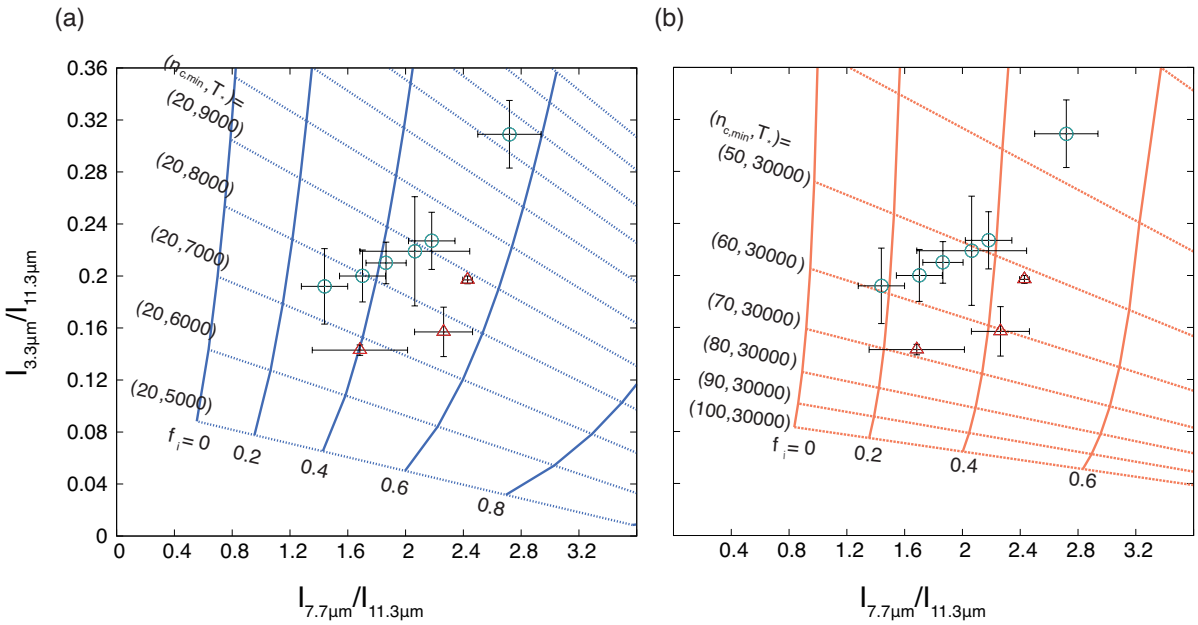

Figure 3.7: Diagnostic diagram of $I_{3.3\,\mu\mathrm{m}}/I_{11.3\,\mu\mathrm{m}}$ versus $I_{7.7\,\mu\mathrm{m}}/I_{11.3\,\mu\mathrm{m}}$. In the left panel **(a)** Case I, the model grids are calculated for a mixture of neutral and ionized PAHs with a power-law size distribution exposed to a blackbody with different temperatures T_* and various ionized fractions of PAHs f_i. The band ratios vary according to the ionization degree of PAHs, f_i, and the effective temperature of the heating source, T_*. In the right panel **(b)** Case II, the minimum PAHs is varied from those with $n_\mathrm{C} = 20$ to 100 and T_* is fixed as 30,000 K. The band ratios vary according to the ionization degree of PAHs, f_i, and the number of carbons of the smallest PAH, $n_{\mathrm{C,min}}$. The symbols of the observed points are the same as in Figure 3.6.

active than that at the upper right for Group A targets in Figure 3.6. In both plots of Figure 3.6, the ratio $I_{3.3\,\mu\mathrm{m}}/I_{11.3\,\mu\mathrm{m}}$ plays a crucial role not only to separate Group A from B, but also to estimate the incident radiation field conditions of the target in Group A.

Comparison with model

The previous subsection suggests possible diagnostic diagrams based on the UIR band ratios and qualitative interpretation is given. In this subsection we examine the diagrams quantitatively, using simple models of PAH emission.

To derive the intensity of the UIR bands emitted from a mixture of neutral and ionized PAHs of various sizes, we employed a simple theoretical model of infrared PAH emission following Schutte et al. (1993). The A-coefficients of the UIR bands in 3–20 μm were calculated from the IR cross-sections of neutral and ionized PAHs recently provided by Draine & Li (2007) and the internal energy to temperature relation provided by Draine & Li (2001) was adopted (see also Boersma et al. 2010; Bauschlicher et al. 2010). The number of carbon atoms in PAHs was assumed to be distributed between $n_\mathrm{C}^\mathrm{min}$ and $n_\mathrm{C}^\mathrm{max}$, and the size distribution of PAHs was assumed to be given by the same power-law function as graphite grains. Details on the model calculation are given in Appendix A.

The UIR band ratios of $I_{3.3\,\mu\mathrm{m}}/I_{11.3\,\mu\mathrm{m}}$ and $I_{7.7\,\mu\mathrm{m}}/I_{11.3\,\mu\mathrm{m}}$ were calculated for different temperatures of

the heating source T_*, the number of carbons of the smallest PAH $n_{\rm C,min}$, i.e., the minimum size of PAHs, and ionization fractions of PAHs $f_{\rm i}$ with different two assumptions. In the first case, Case I, we assumed a quiescent environment where the size distribution of PAHs does not change. The minimum size of PAHs was set as those with the number of carbon atoms, $n_{\rm C}$ = 20. The UIR band ratios of $I_{3.3\,\mu{\rm m}}/I_{11.3\,\mu{\rm m}}$ and $I_{7.7\,\mu{\rm m}}/I_{11.3\,\mu{\rm m}}$ calculated for various T_* and $f_{\rm i}$ are plotted in Figure 3.7 (a). Compared with the locations of the Group A data points on the plot, the bottom-left edge of the sequence corresponds to T_* ∼7500 K and $f_{\rm i}$ ∼30 %, while the top-right end of the sequence to that with T_* ∼12,000 K and $f_{\rm i}$ ∼60 %. The range of the effective temperature indicated is compatible with the effective temperature of A-type main sequence stars of 7,000–1,0000K. Thus the model calculations support the interpretation in §3.4.1 and the observed sequence of Group A can be accounted for by the increase of the effective temperature of the heating source, which increases the excitation, accompanied by the increase in the ionization fraction of PAHs without the change in the size distribution. The observed data of Group B, on the other hand, are distributed in a region corresponding to T_* ∼6,500–8,000 K and $f_{\rm i}$ ∼40–60 % for Case I, which is totally inconsistent with the fact that the radiation field of Group B should be much harder than that of Group A.

In the second case, Case II, we assumed a harsh environment such as those in Group B members. Because of the Lynman cut-off, the results of the model calculation do not depend on T_* for T_*=20,000–50,000 K, which correspond to the effective temperature of O-type main sequence stars of 30,000–50,000 K. Then, in this case, we fixed T_* to 30,000 K, and varied the minimum PAHs from those with $n_{\rm C}$ = 20 to 100. The band ratios were calculated for various $n_{\rm C,min}$ and $f_{\rm i}$ [See Figure 3.7 (b)]. As shown in Figure 3.7 (b), the observed data of Group B are distributed in a region corresponding to $n_{\rm C,min}$ ∼50–70 and $f_{\rm i}$ ∼20–40 %. The small $f_{\rm i}$ is consistent with the increase in recombination with electrons in high electron density environments of H II regions. The deviation of Group B from the sequence of Group A on the plot of $I_{3.3\,\mu{\rm m}}/I_{11.3\,\mu{\rm m}}$ v.s. $I_{7.7\,\mu{\rm m}}/I_{11.3\,\mu{\rm m}}$ is reasonably accounted for by the difference in the minimum size of PAHs.

Therefore, the model calculations quantitatively support the interpretation of the trend seen in the plot of $I_{3.3\,\mu{\rm m}}/I_{11.3\,\mu{\rm m}}$ v.s. $I_{7.7\,\mu{\rm m}}/I_{11.3\,\mu{\rm m}}$. We stress here that an accurate measurement of $I_{3.3\,\mu{\rm m}}/I_{11.3\,\mu{\rm m}}$ ratio should be the key to obtain the average excitation temperature of PAHs, which is determined by the size distribution of PAHs and the hardness of the incident radiation field. The present calculation of Case I and II is made only for representative purposes and the choice of $n_{\rm C}^{\rm min}$ is rather arbitrary. The value of $I_{3.3\,\mu{\rm m}}/I_{11.3\,\mu{\rm m}}$ is sensitive to the specific heat as well as the size distribution of PAHs that we assume in the calculation. The actual values of T_*, $f_{\rm i}$, and $n_{\rm C}^{\rm min}$ inferred from the plot depend on the assumed PAH properties such as the size distribution and the specific heat, which may have non-negligible uncertainties.

3.5 Summary

In this chapter, we present the results of NIR to MIR slit spectroscopic observations of nine diffuse regions in the LMC with the *AKARI*/IRC. Thanks to the unique specifications of *AKARI* in the Phase 2 period, we were able to extract continuous spectra from 2.55 to 13.4 μm of the same slit area, which allows us to investigate the relative intensity of the UIR bands from 2.55 to 13.4 μm emitted from exactly the same region.

The target positions were selected based on the CO mapping data and the *IRAS* colors of $I_{25\,\mu\mathrm{m}}/I_{12\,\mu\mathrm{m}}$ and $I_{60\,\mu\mathrm{m}}/I_{100\,\mu\mathrm{m}}$, which are indicators of star-formation, to cover a wide range of the intensity of the interstellar radiation field. The *AKARI* color of $I_{24\,\mu\mathrm{m}}/I_{11\,\mu\mathrm{m}}$ shows a similar trend to those of the *IRAS* $I_{25\,\mu\mathrm{m}}/I_{12\,\mu\mathrm{m}}$ and $I_{60\,\mu\mathrm{m}}/I_{100\,\mu\mathrm{m}}$ colors, confirming that the selection based on the *IRAS* colors is in fact relevant to the purpose of the present study.

Every obtained spectrum shows a series of the UIR bands at 3.3, 6.2, 7.7, 8.6 and 11.3 μm clearly. Moreover, the ionized gas signatures, such as the hydrogen recombination lines of Brα 4.05 μm, Brβ 2.63 μm, Pfγ 3.75 μm, and Pfβ 4.65 μm and the fine structure lines of [Ar II] 6.98 μm, [Ar III] 8.99 μm, [S IV] 10.51 μm, and [Ne II] 12.81 μm, are detected in some of the spectra. Based on these ionized gas signatures, we classified the nine target positions into two groups: those without the strong ionized gas signatures (Group A) and those with them (Group B). Group A are supposed to be in relatively quiescent radiation field environments, while those of Group B are in harsh radiation field environments powered by young massive stars. This view is consistent with the trends of the *IRAS* and *AKARI* MIR colors.

Group A shows a sequence on the plots of the band ratios of $I_{3.3\,\mu\mathrm{m}}/I_{11.3\,\mu\mathrm{m}}$, $I_{6.2\,\mu\mathrm{m}}/I_{11.3\,\mu\mathrm{m}}$, $I_{7.7\,\mu\mathrm{m}}/I_{11.3\,\mu\mathrm{m}}$, and $I_{8.6\,\mu\mathrm{m}}/I_{11.3\,\mu\mathrm{m}}$ against the *IRAS* and *AKARI* colors, but Group B does not follow the same trend. These results can be interpreted in terms of the facts that (1) in Group A, PAHs are heated to higher excitation temperatures and their ionization fraction increases as the radiation field becomes harder and stronger, whereas (2) in Group B, very small PAHs ($n_{\mathrm{C}} < 100$) are efficiently destroyed, possibly due to electron collisions, and the ionization of PAHs is suppressed by an increase of the electron density inside H II regions. The present observations also show that the interstellar radiation field becomes harder as the intensity increases in Group A based on the UIR band ratios and the IR colors. There is little variation in $I_{6.2\,\mu\mathrm{m}}/I_{7.7\,\mu\mathrm{m}}$ as reported in previous studies, and we find no systematic trend against the colors.

On the plot of $I_{3.3\,\mu\mathrm{m}}/I_{11.3\,\mu\mathrm{m}}$ v.s. $I_{7.7\,\mu\mathrm{m}}/I_{11.3\,\mu\mathrm{m}}$, Groups A and B members are well separated as well as on that of $I_{3.3\,\mu\mathrm{m}}/I_{11.3\,\mu\mathrm{m}}$ v.s. $I_{6.2\,\mu\mathrm{m}}/I_{11.3\,\mu\mathrm{m}}$. These trends can be interpreted in the same way as described above, and simple model calculations support the interpretation quantitatively. Using not only the ratio of $I_{7.7\,\mu\mathrm{m}}/I_{11.3\,\mu\mathrm{m}}$ but also $I_{3.3\,\mu\mathrm{m}}/I_{11.3\,\mu\mathrm{m}}$, which is sensitive to the size distribution and/or the excitation conditions of PAHs, we can estimate the interstellar radiation field conditions more precisely. The diagram of $I_{3.3\,\mu\mathrm{m}}/I_{11.3\,\mu\mathrm{m}}$ v.s. $I_{7.7\,\mu\mathrm{m}}/I_{11.3\,\mu\mathrm{m}}$ is expected to be an useful diagnostic tool for interstellar radiation field

conditions. Further investigation based on a larger amount of observational data of various kinds of objects is needed to confirm the interpretation and ensure the applicability of this diagram to a wide range of objects.

Chapter 4

Detailed analysis of 2–5 μm unidentified infrared bands of galactic H II regions

4.1 Introduction

In this Chapter, we present the observational results of NIR slit spectroscopy of thirty-six galactic H II region or H II region-like objects with the *AKARI*/IRC (Mori et al. 2014).

H II regions are luminous gas clouds ionized by embedded massive O-type or B-type stars. Considering their extreme physical conditions such as intense radiation fields and stellar winds from the central stars, H II regions are a good laboratory for investigating the evolution of materials in the ISM. It can be assumed that destruction and/or processing of dust grains occur in the interior or boundary of H II regions, but the details remain to be explored.

In Chapter 3, we show that the 3.3 μm band plays an important role to investigate the size distribution of PAHs, and it can be a good indicator of interstellar radiation conditions. In addition, the 3.3–3.6 μm region is diagnostically important in identifying the aromatic-aliphatic nature of PAHs. The 3.3 μm band is assigned to a stretching mode of aromatic C-H bonds, whereas the adjacent 3.4–3.6 μm sub-features are thought to be due to vibrational modes of aliphatic C-H bonds (Duley & Williams 1981), or to arise from overtone ($n \times \nu_i$) bands of the 3.3 μm fundamental aromatic C-H stretching mode. It is also known that astronomical spectra exhibit a weak emission feature around 5.25 μm (Allamandola et al. 1989a). Previous studies suggest that this feature is attributed to a mixture of overtone, difference ($\nu_i - \nu_j$), and combination ($\nu_i + \nu_j$) bands of fundamental frequencies of stretching and bending vibrations of aromatic C-H bonds (Allamandola et al. 1989a; Boersma et al. 2009). However, because of its weakness, there is only limited observational data and a detailed observational analysis has not been carried out for the 5.25 μm band.

Here, we present the detailed analysis of 2–5 μm UIR bands of the diffuse emission of galactic H II regions using a large collection of high-quality spectra obtained with the *AKARI*/IRC. The 5.25 μm band appears at the

edge of the spectral range of the prism spectroscopy with *AKARI*/IRC, which enables us to study this minor PAH band for much more samples than previous studies. We first report the detection of this minor PAH band at 5.25 μm with sufficient S/N ratios. The nature and evolution of dust grains in the H II region environment are also discussed based on the variation of the aromatic to aliphatic ratio, $I_{3.4-3.6\,\mu\mathrm{m}}/I_{3.3\,\mu\mathrm{m}}$, and the MIR color, $I_{9\,\mu\mathrm{m}}/I_{18\,\mu\mathrm{m}}$.

§4.2 describes the observations and data reduction. Spectral analysis is presented in §4.3, and its results and discussion are given in §4.4.

4.2 Observations

4.2.1 Near-infrared slit spectroscopy with the AKARI Infrared Camera

The present studies are mainly based on the slit spectroscopic data obtained with the *AKARI*/IRC in the framework of director's time program during the Phase 3 period, during which only NIR channel was in operation. All of the observations were performed by the use of the "Ns" or "Nh" slit ($0.8'$ length $\times$ $5''$ width or $1'$ length $\times$ $3''$ width, respectively) for diffuse sources (see Chapter 2 for more detailed information on the instrument). This director's time program was planned for the purpose of calibration. In the observations, for the the relative calibration of the NIR disperser, grism and prism spectroscopy was done separately for the same slit area in the first and the latter half of a single pointed observation. This procedure provides two kinds of spectra for the same slit area with different wavelength coverages and spectral resolutions (2.5–5.0 μm, $R \sim 100$ for the grism and 1.7–5.4 μm, $R \sim 20$–40 for the prism, see Figure 4.1).

The target sources were selected from galactic ultra-compact (UCH II) and giant H II (GH II) regions catalogued by Crowther & Conti (2003) and Conti & Crowther (2004) according to the visibility of the satellite, except for two unclassified IR sources, G331.386-0.359 and G345.528-0.051. We classify them as H II region-like objects from their spectra showing H II region-like properties. Generally, two pointed observations were performed for each target, whereas some targets were observed only once. We selected sixty-one pointed observations of thirty-six different targets in total that were not severely affected by instrumental artifacts or stray light. The observation logs and target parameters are summarized in Table 4.1. We narrowed the selection further at the spectral analysis stage, by removing those without a sufficient signal-to-noise ratio to quantify the PAH emission features and extinction, and in some cases those without available complementary MIR imaging data (see details below) in the following analysis. The accurate slit position was determined from the *N3* band image taken during each pointed observation, by referring to the positions of point sources in the 2MASS catalog.

4.2.2 Data reduction

The data reduction basically followed the official IDL pipeline for the *AKARI* Phase 3 data (ver.20111121, Ohyama et al. 2007; Onaka et al. 2009). In Phase 3, compared with the Phase 1 and 2, the dark current dramatically increased. The wavelength is fixed for a given detector column in the IRC slit spectroscopy. Even after the standard pipeline process for the Phase 3 data, a systematic pattern sometimes persists in certain wavelengths due to a detector anomaly or dark pattern in the column direction. The grism spectroscopic data are especially sensitive to the fluctuation of those patterns. Therefore, we performed additional dark-subtraction for the grism data. In the *NG* mode, the brink of the image is blocked by the aperture mask and can be used to estimate the residual dark current. We obtained median values of 10 pixels corresponding to a given wavelength

Table 4.1: Observation log and target parameters

Target		d	log$N$	Center position of the slit		Obs.Date	Obs.ID	Obs.AOT[b]	Disperser
Name	Type[a]	[kpc][a]	LyC[a]	l	b				
M8	GH II	2.8	50.19	5.972	-1.172	2008-09-24	5200162.1	IRCZ4 c;Ns	*NG* and *NP*
M8	GH II	2.8	50.19	5.974	-1.176	2008-09-23	5200161.1	IRCZ4 c;Nh	*NG* and *NP*
G8.137+0.228	GH II	13.5	50.47	8.142	0.225	2008-09-23	5200164.1	IRCZ4 c;Ns	*NG* and *NP*
G8.137+0.228	GH II	13.5	50.47	8.143	0.223	2008-09-22	5200163.1	IRCZ4 c;Nh	*NG* and *NP*
W31a	GH II	4.5	50.66	10.163	-0.358	2008-09-25	5200166.1	IRCZ4 c;Ns	*NG* and *NP*
W31a	GH II	4.5	50.66	10.165	-0.362	2008-09-24	5200165.1	IRCZ4 c;Nh	*NG* and *NP*
W31b	GH II	15.0	50.90	10.324	-0.158	2008-09-24	5200167.1	IRCZ4 c;Nh	*NG* and *NP*
M17b	GH II	2.4	51.22	15.027	-0.693	2008-09-28	5200172.1	IRCZ4 c;Ns	*NG* and *NP*
M17b	GH II	2.4	51.22	15.031	-0.696	2008-09-28	5200171.1	IRCZ4 c;Nh	*NG* and *NP*
M17a	GH II	2.4	51.22	15.048	-0.677	2008-09-27	5200169.1	IRCZ4 c;Nh	*NG* and *NP*
W42	GH II	11.5	50.93	25.384	-0.179	2008-10-02	5200294.2	IRCZ4 c;Nh	*NG* and *NP*
W42	GH II	11.5	50.93	25.385	-0.180	2008-10-02	5200294.1	IRCZ4 c;Nh	*NG* and *NP*
G29.944-0.042	GH II	6.2	50.33	29.958	-0.017	2008-10-04	5200295.2	IRCZ4 c;Nh	*NG* and *NP*
G29.944-0.042	GH II	6.2	50.33	29.960	-0.017	2008-10-04	5200295.1	IRCZ4 c;Nh	*NG* and *NP*
W49A	GH II	11.8	51.21	43.175	0.004	2008-10-13	5200299.2	IRCZ4 c;Nh	*NG* and *NP*
W49A	GH II	11.8	51.21	43.176	0.003	2008-10-12	5200299.1	IRCZ4 c;Nh	*NG* and *NP*
G48.596+0.042	GH II	9.8	50.14	48.610	0.027	2008-10-17	5200300.1	IRCZ4 c;Nh	*NG* and *NP*
G48.596+0.042	GH II	9.8	50.14	48.611	0.028	2008-10-17	5200300.2	IRCZ4 c;Nh	*NG* and *NP*
W51	GH II	5.5	50.03	48.915	-0.286	2008-10-18	5200301.2	IRCZ4 c;Nh	*NG* and *NP*
W51	GH II	5.5	50.03	48.916	-0.286	2008-10-17	5200301.1	IRCZ4 c;Nh	*NG* and *NP*
W58A	GH II	8.6	50.06	70.289	1.602	2009-05-02	5200767.1	IRCZ4 c;Nh	*NG* and *NP*
G70.293+1.600	UCH II	8.6	49.29	70.295	1.602	2008-11-06	5200337.1	IRCZ4 c;Nh	*NG* and *NP*
W58A	GH II	8.6	50.06	70.295	1.602	2009-11-06	5201198.1	IRCZ4 c;Nh	*NG* and *NP*
G75.783+0.343	UCH II	4.1	46.78	75.765	0.342	2009-05-11	5200772.1	IRCZ4 c;Nh	*NG* and *NP*
G76.383-0.621	UCH II	1.0	45.06	76.379	-0.619	2008-11-15	5200344.1	IRCZ4 c;Ns	*NG* and *NP*
G76.383-0.621	UCH II	1.0	45.06	76.385	-0.622	2008-11-15	5200343.1	IRCZ4 c;Nh	*NG* and *NP*
G78.438+2.659	UCH II	3.3	46.83	78.437	2.659	2009-05-13	5200776.1	IRCZ4 c;Nh	*NG* and *NP*
G78.438+2.659	UCH II	3.3	46.83	78.438	2.657	2009-05-13	5200777.1	IRCZ4 c;Ns	*NG* and *NP*
DR7	GH II	8.3	50.15	79.302	1.305	2009-05-17	5200769.1	IRCZ4 c;Nh	*NG* and *NP*
DR7	GH II	8.3	50.15	79.304	1.304	2009-05-18	5200770.1	IRCZ4 c;Ns	*NG* and *NP*
G81.679+0.537	UCH II	2.0	47.52	81.682	0.542	2008-11-22	5200347.1	IRCZ4 c;Nh	*NG* and *NP*
G111.282-0.663	UCH II	2.5	46.68	111.282	-0.661	2009-01-18	5200433.1	IRCZ4 c;Ns	*NG* and *NP*
G111.282-0.663	UCH II	2.5	46.68	111.286	-0.660	2009-01-16	5200432.1	IRCZ4 c;Nh	*NG* and *NP*
G133.947+1.064	UCH II	3.0	47.92	133.950	1.064	2009-08-20	5200959.1	IRCZ4 c;Ns	*NG* and *NP*
RCW42	GH II	6.4	50.36	274.004	-1.146	2008-12-15	5200452.1	IRCZ4 c;Nh	*NG* and *NP*
RCW42	GH II	6.4	50.36	274.008	-1.146	2008-12-15	5200453.1	IRCZ4 c;Ns	*NG* and *NP*
G282.023-1.180	GH II	5.9	50.32	282.022	-1.182	2009-01-01	5200436.1	IRCZ4 c;Nh	*NG* and *NP*
G282.023-1.180	GH II	5.9	50.32	282.025	-1.183	2009-01-02	5200437.1	IRCZ4 c;Ns	*NG* and *NP*
RCW49	GH II	4.7	50.96	284.299	-0.346	2009-01-04	5200438.1	IRCZ4 c;Nh	*NG* and *NP*
RCW49	GH II	4.7	50.96	284.303	-0.347	2009-01-04	5200439.1	IRCZ4 c;Ns	*NG* and *NP*
NGC3372	GH II	2.5	50.11	287.377	-0.628	2009-01-10	5200440.1	IRCZ4 c;Nh	*NG* and *NP*
NGC3372	GH II	2.5	50.11	287.381	-0.631	2009-01-10	5200441.1	IRCZ4 c;Ns	*NG* and *NP*
G289.066-0.357	GH II	7.9	50.05	289.064	-0.358	2009-01-13	5200442.1	IRCZ4 c;Nh	*NG* and *NP*
G289.066-0.357	GH II	7.9	50.05	289.068	-0.359	2009-01-13	5200443.1	IRCZ4 c;Ns	*NG* and *NP*
NGC3576	GH II	3.1	50.28	291.282	-0.713	2009-01-17	5200444.1	IRCZ4 c;Nh	*NG* and *NP*
NGC3576	GH II	3.1	50.28	291.286	-0.715	2009-01-17	5200445.1	IRCZ4 c;Ns	*NG* and *NP*
NGC3603	GH II	7.9	51.50	291.608	-0.529	2009-01-17	5200446.1	IRCZ4 c;Nh	*NG* and *NP*
NGC3603	GH II	7.9	51.50	291.611	-0.530	2009-01-17	5200447.1	IRCZ4 c;Ns	*NG* and *NP*
G305.359+0.194	GH II	3.5	50.13	305.353	0.197	2009-08-09	5200932.2	IRCZ4 c;Ns	*NG* and *NP*
G305.359+0.194	GH II	3.5	50.13	305.354	0.196	2009-08-09	5200932.1	IRCZ4 c;Ns	*NG* and *NP*
G319.158-0.398	GH II	11.5	50.30	319.167	-0.422	2009-08-25	5200933.1	IRCZ4 c;Nh	*NG* and *NP*
G319.392-0.009	GH II	11.5	50.17	319.400	-0.011	2009-08-26	5200936.2	IRCZ4 c;Ns	*NG* and *NP*
G319.392-0.009	GH II	11.5	50.17	319.402	-0.011	2009-08-26	5200936.1	IRCZ4 c;Ns	*NG* and *NP*
G330.868-0.365	GH II	10.8	50.56	330.888	-0.372	2008-09-02	5200109.1	IRCZ4 c;Nh	*NG* and *NP*
G331.386-0.359	UNKNOWN	–	–	331.390	-0.360	2008-09-03	5200113.1	IRCZ4 c;Nh	*NG* and *NP*
G333.122-0.446	GH II	3.5	50.08	333.133	-0.427	2008-09-04	5200121.1	IRCZ4 c;Nh	*NG* and *NP*
G338.398+0.164	GH II	13.1	50.90	338.358	0.154	2009-09-07	5200942.1	IRCZ4 c;Nh	*NG* and *NP*
G338.398+0.164	GH II	13.1	50.90	338.360	0.155	2009-09-07	5200942.2	IRCZ4 c;Nh	*NG* and *NP*
G338.400-0.201	GH II	15.7	50.24	338.409	-0.202	2009-09-07	5200943.2	IRCZ4 c;Nh	*NG* and *NP*
G345.528-0.051	UNKNOWN	–	–	345.528	-0.049	2008-09-11	5200134.1	IRCZ4 c;Ns	*NG* and *NP*
G345.528-0.051	UNKNOWN	–	–	345.530	-0.053	2008-09-11	5200133.1	IRCZ4 c;Nh	*NG* and *NP*

[a] From Crowther & Conti (2003); Conti & Crowther (2004).

[b] From Onaka et al. (2007b).

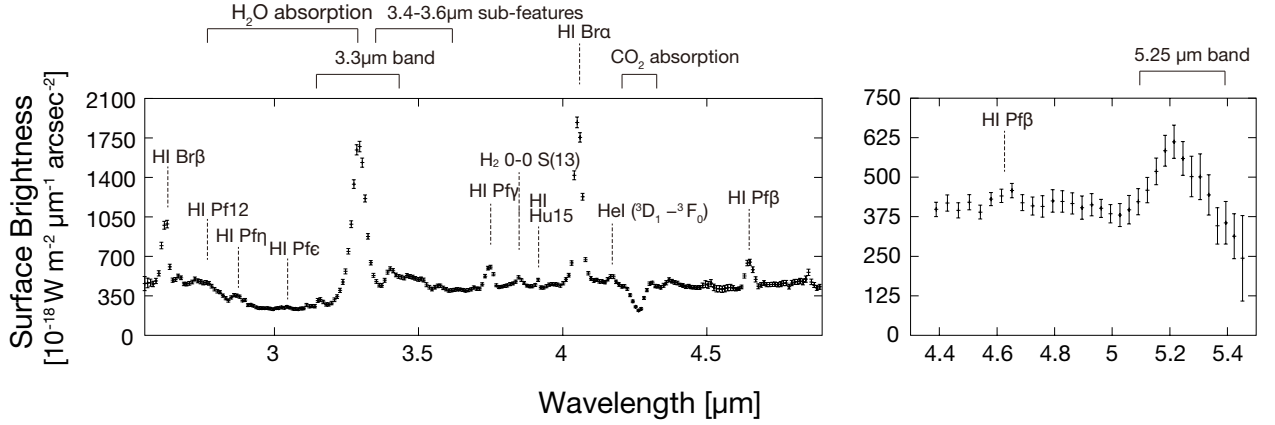

Figure 4.1: Typical example of the spectra obtained by the present observations. They are taken from the position "-04" of W31a (ID: 5200165.1) by the use of the "Nh" slit. The left panel indicates the spectra taken with the grism ($R \sim 100$), and the right panel that of the prism ($R \sim 20$–40).

in this region, and subtracted them from the spectrum.

The spectral data generally show a spatial variation within the entire slit area. The FWHM of the point-spread function of the IRC is approximately 3.2 pixels ($\sim$4.6″) at the NIR wavelengths during the Phase 3 period (Onaka et al. 2010). We extracted spectra taken with the grism and the prism respectively from the same slit area with the length of 6 pixels ($\sim$9″) one by one along the slit direction, avoiding those affected by point-like sources. As a result, we obtained several sets of grism and prism spectra from each pointed observation (see Appendix C). We extracted the spectra from 232 lines of sight in total. Even though the telescope was pointed towards the same position on the sky, due to the different optical alignments between the *NG* and the *NP* modes, prism spectral images were systematically shifted from grism ones by about 4 pixels along the slit direction. When we created a pair of grism and prism spectra of the same position, this position shift was taken into consideration. Figure 4.1 gives an example of the obtained spectra. In the short wavelength region, the spectral resolution of the prism is too low to discuss features quantitatively. Furthermore, saturation frequently occurs in the prism spectra because of its extremely high sensitivity particularly in this wavelength range. For these reasons, we truncate the prism spectra, and use only a 4.35–5.4 μm wavelength region in the following analysis. Appendix C exhibits all of the resultant spectra together with the individual *S9W* band images taken by the *AKARI* MIR All-Sky Survey (see details below), in which the location of the slit and each spectra-extracted region are depicted with colored boxes. The present reduced spectral data are open to the public on the JAXA archive at the following URL: `http://www.ir.isas.jaxa.jp/AKARI/Archive/Catalogues/IRC_GALHII_spec/` as "AKARI Near-infrared Spectral Atlas of Galactic H II regions".

4.2.3 Ancillary mid-infrared imaging data

We secondarily utilized the diffuse data obtained in the *AKARI* MIR All-Sky Survey (Ishihara et al. 2010). The *AKARI* MIR All-Sky Survey was carried out by the IRC at two MIR wide band filters, *S9W* and *L18W*. In the

NIR regime, the effect of the zodiacal light is negligible, but its intensity increases dramatically by a factor of approximately one hundred in units of Jy at MIR wavelengths. We therefore subtracted the medium value of a relatively dark area within the same frame from the processed images as the background, most of which is expected to arise from the zodiacal emission, and performed aperture-photometry within a $5''$ radius circle centered on each spectrum-extracted region. From the nature of the present targets, the background signals that we subtracted are considerably small relative to the source ones in most cases. The pixels where saturation occurs due to the presence of bright astronomical sources were automatically masked through the data reduction process. Some of the present target objects (e.g. M17a) contain such masked regions, which were excluded from the analysis involving the MIR imaging data.

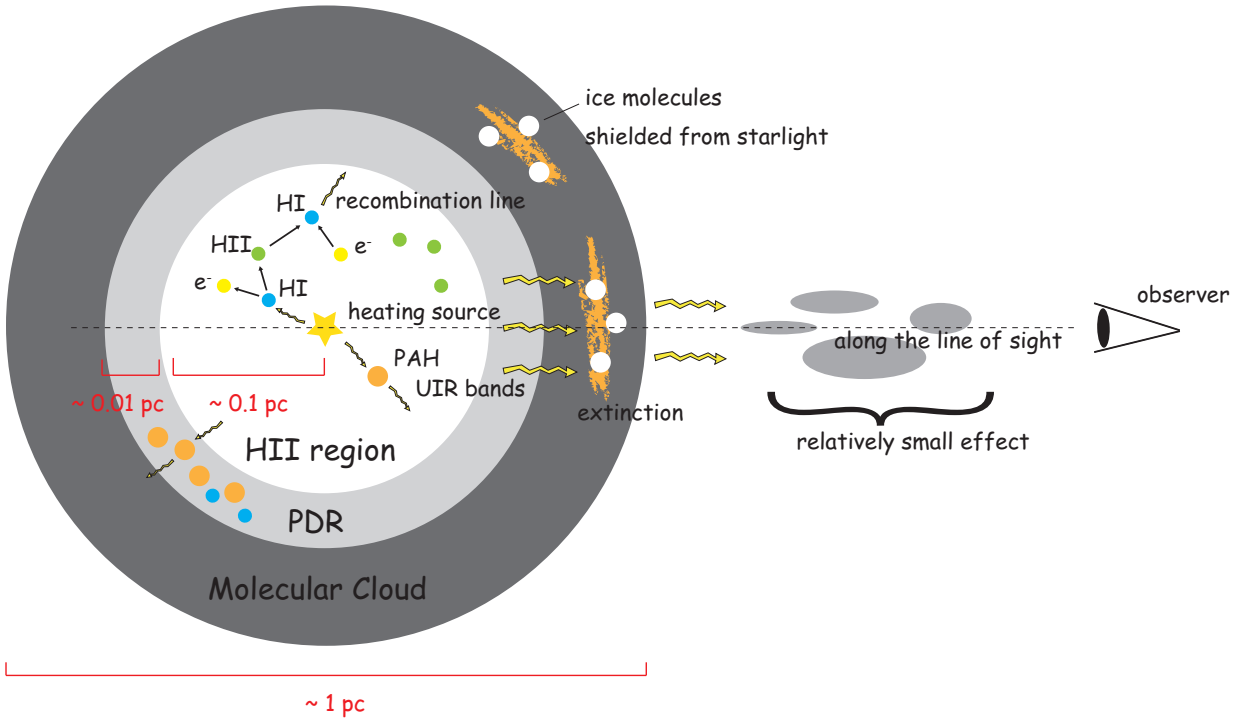

Figure 4.2: Illustration of the assumed configuration of a H II region and its surroundings along the line of sight.

4.3 Spectral analysis

As shown in Figure 4.1, the obtained spectra are rich in ISM features, reflecting the complex geometry of the sources. A number of hydrogen and helium recombination lines (e.g. Brβ at 2.63 μm, and Brα at 4.05 μm) signify ionized gas, and the grism spectra clearly show the distinct 3.3 μm PAH emission band and the adjacent weak sub-features around 3.4–3.6 μm. Intriguingly, a broad emission feature can be seen in the unique coverage of the prism spectra of 5.0–5.4 μm. The central wavelength was estimated as 5.22 μm in the present spectra. It has been suggested that interstellar PAHs give a faint emission feature around this area (e.g. Allamandola et al. 1989a; Boersma et al. 2009). Boersma et al. (2009) reported that the central wavelength of this PAH emission feature is 5.25 μm. This value differs from that measured from the present dataset by about 1 pixel ($\sim$0.03 μm), but the discrepancy is still within the uncertainty of the wavelength calibration particularly because of the edge of the spectrum. Hydrogen recombination line Huδ at 5.13 μm is also a possible source of this feature. However, we can recognize that a line around at 5.13 μm is perched on the tail of the feature in some spectra like those of RCW42 and RCW49, and Huδ is clearly separated from the 5.22 μm feature. In addition to Huδ, several hydrogen and helium recombination lines fall in the range of 5.0–5.4 μm, but they are negligibly small when compared to Huδ. Therefore, we identify the observed feature as the PAH 5.25 μm band, although we cannot completely rule out the possibility of some contamination. The uncertainty in the absolute flux calibration accompanied by the wavelength uncertainty is less than 5%, and is within the observational error. In some cases, clear absorption features associated with H_2O and CO_2 ices also appear at around 3.05 and 4.27 μm. These ice absorption features will be investigated separately, and are not discussed further here. Furthermore,

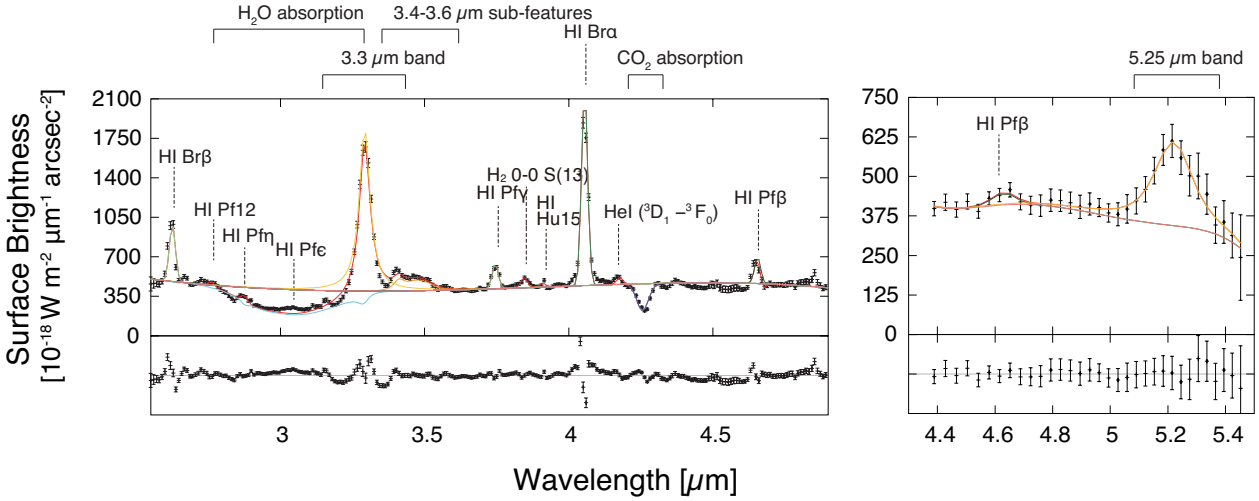

Figure 4.3: Fitting results for the spectra shown in Figure 4.1. The salmon lines designate the continuum component of a quintic function. The major emission line features like Brβ at 2.63 μm, Pfγ 3.75 μm, Brα 4.05 μm, and Pfβ 4.65 μm (green lines), the PAH emission bands (yellow lines), and the ice absorption features (blue lines) are respectively overlaid on the best-fit model spectra (red lines). As for the the grism spectrum, the wavelength region from 2.9 to 3.1 μm is out of the spectral fitting (see details in §4.3.1). The lower panels indicate the residual spectra of each plot.

Table 4.2: Gaussian profile parameters for ice features

Band	$\lambda_{k'_g}$ [μm]	$\gamma_{k'_g}$ [μm] for "Ns" slit	$\gamma_{k'_g}$ [μm] for "Nh" slit
CO_2 Ice	4.26	0.060	0.048
CO Ice	4.67	0.031	0.025

there is no apparent signature of PADs at approximately 4.3–4.8 μm (e.g. Allamandola et al. 1989b; Peeters et al. 2004a). The aromatic and aliphatic C-D stretching bands are known to appear in this wavelength range. The detailed analysis and discussion on these PAD features are presented in Onaka et al. (2014); Doney et al. (2016) and Chapter 5. In Chapter 5, we introduce laboratory work on deuterated hydrocarbon materials and discuss the possibility of application of these experimental results to observations.

Taking these distinctive spectral features into account, we used a least–squares method for the spectral fitting on the following supposition to investigate the observed features quantitatively. We assumed that the emission features such as the hydrogen and helium recombination lines and the PAH emission features come entirely from H II region–PDR complexes excited by embedded stars, and that those emissions are attenuated mostly by adjacent clouds, which contain and shield the ices from starlight. The schematic diagram of this assumed configuration is presented in Figure 4.2.

4.3.1 Fitting for the grism spectra

First, we discuss the analysis of spectra taken with the grism. The ice absorption features can be regarded as a "foreground-screen". Except for the broad absorption feature around 3.05 μm associated with H_2O ice, the CO and CO_2 ice absorption features cannot be completely resolved with the spectral resolution of the *AKARI*/IRC

Table 4.3: Lorentzian and Gaussian profile parameters for UIR bands

λ_{k_l} [μm]	γ_{k_l} [μm] for "Ns" slit	γ_{k_l} [μm] for "Nh" slit
3.29	0.048	0.045
3.41	0.044	0.043
λ_{k_g} [μm]	γ_{k_g} [μm] for "Ns" slit	γ_{k_g} [μm] for "Nh" slit
3.48	0.113	0.100

Table 4.4: Gaussian profile parameters for emission lines

Line	λ_{k_g} [μm]	γ_{k_g} [μm] for "Ns" slit	γ_{k_g} [μm] for "Nh" sllit
HI Hu15	3.91	0.031	0.025
HI Hu13	4.18	0.031	0.025
HI Hu12	4.38	0.031	0.025
HI Pf12	2.76	0.031	0.025
HI Pfη	2.88	0.031	0.025
HI Pfγ	3.75	0.031	0.025
HI Pfβ	4.65	0.031	0.025
HI Brβ	2.63	0.031	0.025
HI Brα	4.05	0.031	0.025
HeI ($^3D_1 - ^3F_0$)	4.30	0.031	0.025
H_2 0-0 S(13)	3.85	0.031	0.025

slit spectroscopy. We fitted the laboratory spectrum of the pure H_2O ice at 10 K to the observed spectra, while the CO and CO_2 ice absorption features were modeled with Gaussian functions with negative signs. Then, the function we fitted to the observed spectra is given by

$$F_\lambda(\lambda) = \left[\sum_{k=0}^{5} a_k \lambda^k + \sum_{k_l=1}^{2} b_{k_l} f_{\rm l}(\lambda;\lambda_{k_l};\gamma_{k_l}) + \sum_{k_g=1}^{12} c_{k_g} f_{\rm g}(\lambda;\lambda_{k_g};\gamma_{k_g})\right] \cdot \exp(-d\ln 10\, A_{\rm H_2O}(\lambda)) - \sum_{k'_g=1}^{2} e_{k'_g} f_{\rm g}(\lambda;\lambda_{k'_g};\gamma_{k'_g}), \quad (4.1)$$

where $f_{\rm l}(\lambda;\lambda_0;\gamma)$ and $f_{\rm g}(\lambda;\lambda_0;\gamma)$ denote Lorentzian and Gaussian functions with the central wavelength λ_0 and the FWHM γ respectively. $A_{\rm H_2O}(\lambda)$ denotes the absorbance of the H_2O ice. Here, we employed the laboratory data, which were retrieved from the Leiden atomic and molecular database (Ehrenfreund et al. 1996). The second term represents the CO and CO_2 absorption features. The FWHM $\gamma_{k'_g}$ and the center of the wavelength $\lambda_{k'_g}$ were fixed to the best-fit values, which were estimated from the spectra with good signal-to-noise ratios. Due to the different slit width (5″ for the "Ns" slit and 3″ for the "Nh" slit), the spectral resolution is slightly different between the spectra taken with "Ns" slit and those with "Nh" slit, and thus the best-fit values were derived for the "Ns" slit and "Nh" slit, respectively (See Tables 4.2). The terms in the first brackets of Eq. (1) represent emission features, which are made up of three components, a continuum, PAH, and line emission features. The continuum were modeled with a polynomial function of the 5th order and constrained to be non-negative. We expressed both the PAH 3.3 μm and the adjacent 3.4 μm sub-feature with a Lorentzian function, whereas the sub-features at around 3.5 μm were altogether modeled by one Gaussian function centered at 3.48 μm, even though they are supposed to consist of multiple components. It is because the spectral resolution achieved by the *AKARI*/IRC is not sufficient to resolve each of faint features around the 3.5 μm. We attempted

other combinations of Gaussians and Lorentzians, but the adopted combination provided the best fit. The center of the wavelength and the FWHM of these three components were fixed to the best-fit values estimated for the spectra obtained with the *AKARI*/IRC (See Tables 4.3). The emission lines were modeled with Gaussian profiles with the FWHM γ_{k_g} fixed to match with the spectral resolution, 0.031 μm for "Ns" and 0.025 μm for "Nh" (See Table 4.4). In the fitting, only a_k, b_{k_l}, c_{k_g}, d, and $e_{k'_g}$ were free parameters. The fitting was non-linear and thus we used the Levenberg–Marquardt method (Press et al. 2002). We note that the wavelength region of 2.9–3.1 μm was not used in the fitting, since this region is at the bottom of the H_2O absorption feature and is easily contaminated by weak foreground emissions. The left panel of Figure 4.3 shows an example of the fitting for the grism spectra.

4.3.2 Fitting for the prism spectra

In the prism spectroscopy, the spectral dispersion varies with wavelength. Taking into the account of this non-uniform spectral dispersion in the prism mode, we succeed in reproducing the prism spectrum from the grism spectrum by a simulation (see Appendix B for details). On the basis of this analytical result, we simulated the spectral profile in a spectrum taken with the prism mode, $f_{k_f}(\lambda)$, for each fitting component. As the fitting components, three emission features were selected: Pfβ at 4.65 μm, Huδ at 5.13 μm, and the 5.25 μm band, which are clearly seen in most of the resultant spectra taken with the prism. Then, we fitted the spectra with the function

$$F_\lambda(\lambda) = \sum_{k=0}^{5} a_k \lambda^k + \sum_{k_f=1}^{3} b_{k_f} \cdot f_{k_f}(\lambda), \tag{4.2}$$

where the first term represents the continuum, and the $f_{k_f}(\lambda)$ in the second term is the modeled function of each fitting component. In the formulation of the $f_{k_f}(\lambda)$, we assumed that Pfβ and Huδ lines have a Gaussian profile and the 5.25 μm band has a Lorentzian profile in grism spectra. The FWHM of the 5.25 μm band was set to the literature value reported by Boersma et al. (2009), 0.12 μm, and the central wavelength was slightly modified to match with the best-fit value for the *AKARI*/IRC prism spectroscopy, 5.22 μm. An example of the fits is given by the right panel of Figure 4.3. As described above, the wavelength calibration in the prism mode is no better than $\sim$0.03 μm in this spectral range, but the assumed spectral profile fits the observed spectrum fairly well.

4.3.3 Estimate of the extinction

We adopted the dust model of "Milky Way, R_V=3.1" of Weingartner & Draine (2001) as the extinction curve, and estimated the value of a visual extinction A_V from the observed intensity ratio of Brβ to Brα in the assumption of the Case B condition of $T_\mathrm{e} = 10^4\,\mathrm{K}$ and $n_\mathrm{e} = 10^4\,\mathrm{cm}^{-3}$ (Storey & Hummer 1995) and the

foreground-screen extinction (see Figure 4.2). It is remarked that the line and band intensities derived from the fitting are corrected for the extinction. The A_V value ranges widely from 0 to 40 mag. In several regions, the effect of the extinction cannot be ignored. In addition to the extinction correction, we also corrected for a contribution from the unresolved emission line Pfδ at 3.30 μm to the UIR 3.3 μm band. According to the Case B condition, we assumed that the intensity of Pfδ is equal to 9.3% of the extinction-corrected intensity of Brα, and subtracted it from the extinction-corrected intensity of the 3.3 μm band.

4.4 Discussion

In most resultant spectra, as well as the 3.3 μm band, both the 3.4–3.6 μm sub-features and 5.25 μm band were detected with sufficient signal-to-noise ratios. The 3.3 μm band has been enthusiastically studied for various astronomical objects, and is generally accepted as a fundamental C-H stretching band of astronomical PAHs; nevertheless less is known about the 3.4–3.6 μm sub-features and 5.25 μm band. In particular, there are only a few detailed observational studies on the 5.25 μm band due to its weakness and position, which is often located at the edge or gap of the detector spectral coverage. Here, the legacy of *AKARI* gives us a great opportunity to investigate these minor bands together with the 3.3 μm band based on a larger collection of spectra of galactic H II regions than ever before. In this section, we present analysis results, and discuss the processing of carbonaceous grains in H II regions.

4.4.1 The 5.25 μm band

Based on the results of their laboratory experiments and quantum-chemical calculations, previous studies indicated that the astronomical 5.25 μm band could be a blend of overtone, difference, and combination bands of the fundamental C-H stretching and bending vibration modes (Allamandola et al. 1989a; Boersma et al. 2009). Boersma et al. (2009) also suggested that C-C modes of large ionized PAHs contribute to those two bands. From the point of view of observations, Boersma et al. (2009) showed that the 5.25 μm band strength is strongly correlated with the 11.3 μm band strength, which supports their close connection with C-H vibration modes. However, their observational study was based on only four spectra obtained by the *ISO*/SWS for HD44179 (post-AGB star), NGC7027 (planetary nebula), and two positions in the Orion Bar (H II regions). A larger collection of astronomical spectra is important to make a firm conclusion.

In order to consider the nature of the 5.25 μm band, we investigated their relative variation to the 3.3 μm band and the 3.4–3.6 μm sub-features (the summation of the 3.41 and 3.48 μm components). Figures 4.4 (a) and (b) show the relative strength of the 5.25 μm band with respect to the *AKARI S9W* band surface brightness against those of the 3.3 μm band and the 3.4–3.6 μm sub-features respectively. There is a tight correlation of the 5.25 μm band both with the 3.3 μm band and the 3.4–3.6 μm sub-features (the weighted correlation coefficient r is 0.92 and 0.88 respectively). As mentioned above, the 3.3 μm band is assigned to an aromatic C-H stretching mode, and the 3.4–3.6 μm sub-features to aliphatic C-H vibrational modes (Duley & Williams 1981), or overtone of the fundamental aromatic C-H stretching mode. The present result supports the idea that the 5.25 μm band is a member of the family of PAH emission bands, and is compatible with the theoretical prediction that it has a close relation to C-H vibration modes. Given that the emission feature at a short wavelength like the 3.3 μm band requires high excitation, it is compatible with the hypothesis that the overtone bands of fundamental C-H vibration modes contribute to the 5.25 μm band. A slightly higher correlation is found with the 3.3 μm

Table 4.5: Linear fit parameters for $I_{5.25\,\mu\mathrm{m}}/I_{9\,\mu\mathrm{m}}$ with $I_{3.3\,\mu\mathrm{m}}/I_{9\,\mu\mathrm{m}}$[a]

Objects	$A_{\mathrm{intercept}}$	B_{slope}
UCH II +GH II +UNKNOWN	0.00007±0.00007	0.22±0.01
UCH II	0.00015±0.00012	0.24±0.01
GH II	0.00005±0.00008	0.22±0.01

[a] See text.

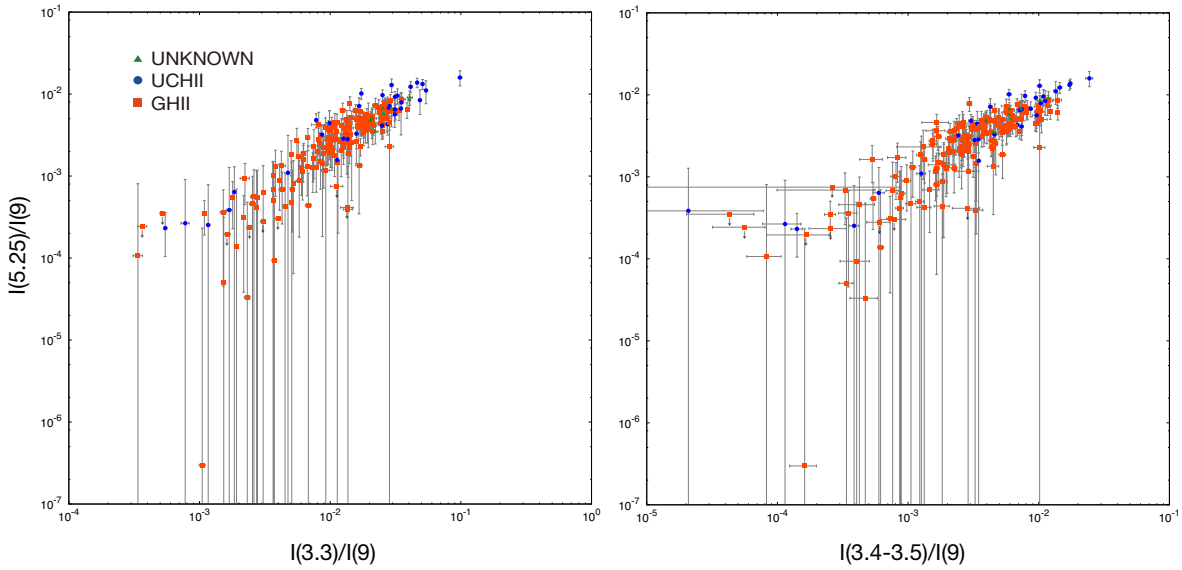

Figure 4.4: Plots of the ratio of the 5.25 μm band to the *AKARI*/IRC *S9W* band surface brightness versus that of **(a)** the 3.3 μm band and **(b)** the 3.4–3.6 μm sub-features. The downward arrows indicate upper limits, where no apparent sign of the 5.25 μm band is seen.

band than with the 3.4–3.6 μm sub-features, suggesting that the 5.25 μm band may have stronger connection to aromatic ones. Since the 3.4–3.6 μm sub-features correlates with the 3.3 μm band to some extent, the correlation between the 3.4–3.6 μm sub-features and the 5.25 μm band may be a secondary relation. However, the difference between those two correlations is not significant, and thus we cannot draw a clear conclusion on this point from the present data.

We fitted a linear function, $y = A_{\mathrm{intercept}} + B_{\mathrm{slope}} \cdot x$, where y is the relative strength of the 5.25 μm band to the 9 μm surface brightness and x is that of the 3.3 μm band for all the data points and for those classified into UCH II and GH II regions separately, using the IDL routine "FITEXY" (Press et al. 2002). The fitting results are summarized in Table 4.5. In all cases, the intercept $A_{\mathrm{intercept}}$ is very small, and the regression lines pass through the origin within uncertainty. The slope B_{slope} does not differ significantly between the UCH II and H II regions, and is in agreement with the intensity ratio of the 5.25 μm band to the 3.3 μm band of HD44179, NGC7027, and two positions in the Orion Bar reported by Boersma et al. (2009), which ranges from 0.16 to 0.38 within a factor of two. These results suggest that the relative intensity of the 5.25 μm band to the 3.3 μm band is rather constant over a wide range of galactic objects regardless their evolutionary stage.

4.4.2 The 3.4–3.6 μm sub-features

It is widely known that the 3.3 μm PAH band is commonly accompanied by adjacent satellite features at 3.41, 3.51, and 3.56 μm and a broad plateau extending to 3.6 μm for various kinds of astronomical objects (e.g. Geballe et al. 1985; Joblin et al. 1996a), yet the origin of these satellite features has not been clearly identified. Aliphatic hydrocarbon materials have a fundamental C-H stretching mode at 3.4 μm (Pendleton & Allamandola 2002). Hydrogenated PAHs also cause the 3.4 μm band. Additional H atoms to peripheral C atoms of PAHs convert aromatic rings to aliphatic rings, which newly create aliphatic C-H stretching bands especially near 3.4 μm and 3.5 μm (Bernstein et al. 1996). Aliphatic side-groups at the periphery of PAHs like methyl (-CH_3), methylene (-CH_2-), and ethyl (-CH_2CH_3) also give rise to the satellite features around 3.4–3.5 μm as aliphatic C-H stretching modes (e.g. Duley & Williams 1981). On the other hand, overtone bands of the aromatic C-H stretching mode also appear in that spectral range due to the anharmonicity (at 3.41, 3.47, 3.5, and 3.56 μm, Barker et al. 1987). Joblin et al. (1996a) reported the 3 μm spectrum variation within the reflection nebulae NGC 1333 SVS3 and NGC 2023, suggesting that the observed 3.4 μm band is too intense to originate from overtone bands of the aromatic C-H stretching mode alone, and that the relative variation of the 3.4 μm band with respect to the 3.3 μm band can be explained by photochemical erosion of aliphatic side-groups attached to PAHs due to the strong far-ultraviolet (FUV) radiation field. Some other studies also suggested that the variation of the 3.4–3.6 μm sub-features relative to the 3.3 μm band reflects the processing of interstellar hydrocarbon materials due to thermal annealing, but they were discussed only for a limited number of astronomical objects including H II regions, planetary nebulae, and reflection nebulae (e.g., Goto et al. 2003; Boulanger et al. 2011).

In the present study, the relative intensity of the 3.4–3.6 μm sub-features to the 3.3 μm band, $I_{3.4-3.6\,\mu\mathrm{m}}/I_{3.3\,\mu\mathrm{m}}$, lies in a range of relatively small values, 0.0–0.5, which implies that the aliphatic structure is a small part of the band carriers at least for the present target sources (e.g. Li & Draine 2012), however, exhibits a small, but systematic variation against the intensity ratio of the 3.7 μm continuum intensity to the 3.3 μm band, $I_{\mathrm{cont},3.7\,\mu\mathrm{m}}/I_{3.3\,\mu\mathrm{m}}$ (see Figure 4.5). The 3.7 μm continuum intensity, $I_{\mathrm{cont},3.7\,\mu\mathrm{m}}$, is the integrated intensity over a 3.65–3.71 μm range. Hydrogen free-free emission and free-bound and helium free-free emission were estimated from the intensity of Brα and were subtracted from the observed continuum. Sellgren (1984) indicated the presence of the continuum emission with a high color temperature of $\sim$1000 K in the NIR spectra of reflection nebulae. Based on observations of the Orion Nebulae with the Wide Field Cryogenic Telescope-II, Haraguchi et al. (2012) suggested that after subtraction of the free-free emission from the 3.7 μm continuum there remains significant residual component, and that its relative strength to the 3.3 μm band emission reflects the ionization degree of PAHs. As suggested by Haraguchi et al. (2012), we assume that the ratio of $I_{\mathrm{cont},3.7\,\mu\mathrm{m}}/I_{3.3\,\mu\mathrm{m}}$ mirrors the ionization degree of PAHs. The PAH ionization degree is controlled by a balance between photo-ionization and recombination with ambient electrons. Among the present target regions, the variation of the UV radiation field is expected to be the most contributing factor in the difference of the PAH

ionization degree. The ratio of the 3.7 μm continuum intensity to the 3.3 μm band is thus a good indicator of the strength of radiation field of the region where PAHs emit rather than the ratio of $I_{\mathrm{Br}\alpha}/I_{3.3\,\mu\mathrm{m}}$ (see §4.4.3).

The aliphatic fraction of the band emitters is thought to be a major factor to influence the observed intensity ratio of $I_{3.4-3.6\,\mu\mathrm{m}}/I_{3.3\,\mu\mathrm{m}}$. Aliphatic C-H bonds are less resilient than aromatic ones and they need less energy to break. The laboratory experiments revealed that irradiation of UV light and heating drive hydrocarbon solid materials to evolve to aromatic-rich materials (e.g. Iida et al. 1985; Smith 1984; Sakata et al. 1990). Recently Jones (2012a,b,c) and Jones et al. (2013) presented a theoretical model for the evolution of amorphous hydrocarbon materials, suggesting that UV-photolysis leads to the ultimate transition towards aromatic-dominated materials especially for small grains ($a \lesssim 20$ nm). Given that the grains in this size range dominate the 3.3–3.6 μm band emission (e.g. Schutte et al. 1993; Draine & Li 2007), their prediction can be applicable to our study. The observed ratio of $I_{3.4-3.6\,\mu\mathrm{m}}/I_{3.3\,\mu\mathrm{m}}$ decreases with the increase of the ratio of $I_{\mathrm{cont},3.7\,\mu\mathrm{m}}/I_{3.3\,\mu\mathrm{m}}$, which indicates the strength of interstellar radiation field. This trend is consistent with the scenario that aliphatic C-H bonds in the band emitters are efficiently destroyed prior to aromatic ones in ionized gas and/or its boundary with the evolution of the UV radiation field. If a photo-thermal process is the main cause of the decrease of the 3.4–3.6 μm sub-features relative to the 3.3 μm band, we can investigate the evolutionary history of hydrocarbon materials in interstellar environments from the intensity ratio of $I_{3.4-3.6\,\mu\mathrm{m}}/I_{3.3\,\mu\mathrm{m}}$. Kaneda et al. (2012) and Yamagishi et al. (2012) reported the enhancement of the 3.4–3.6 μm sub-features relative to the 3.3 μm band in the CO molecular loop near the galactic center and in the halo of M82. They concluded that this enhancement arises from shattering of carbonaceous grains driven by shock winds (Jones et al. 1996). In contrast, the present study indicates no such enhancement in the ionized gas-dominated regions. Therefore, it can be inferred that shattering is not an effective process in the interior and the periphery of H II regions, which is consistent with the model prediction of Micelotta et al. (2010a).

4.4.3 Variation of the mid-infrared color

The *AKARI S9W* band filter covers a wavelength range of 6.7–11.6 μm, which includes the prominent PAH emission band features at 6.2, 7.7, 8.6, and 11.3 μm. Therefore, it can be conjectured that the *S9W* band intensity mostly originates in these PAH emission features (e.g. Ishihara et al. 2007; Kaneda et al. 2012). On the other hand, the origin of the *L18W* band intensity is still ambiguous. In the report of *AKARI* imaging observations of the reflection nebulae IC 4954 and IC 4955 region, Ishihara et al. (2007) suggested that the continuum emission originating from stochastic heating of VSGs dominates spectra in the wavelength range of the *L18W* band filter. However, this assumption does not always hold good in the case of H II regions, the target objects of this study. In H II regions, the intensity of radiation field reaches 10^4–10^5 times of that in the solar vicinity (e.g. Tielens et al. 1993; Berné et al. 2009; Salgado et al. 2012). In such a harsh environment, the equilibrium temperature of BGs becomes higher and thermal emission can be dominant even at short wavelengths around 18 μm.

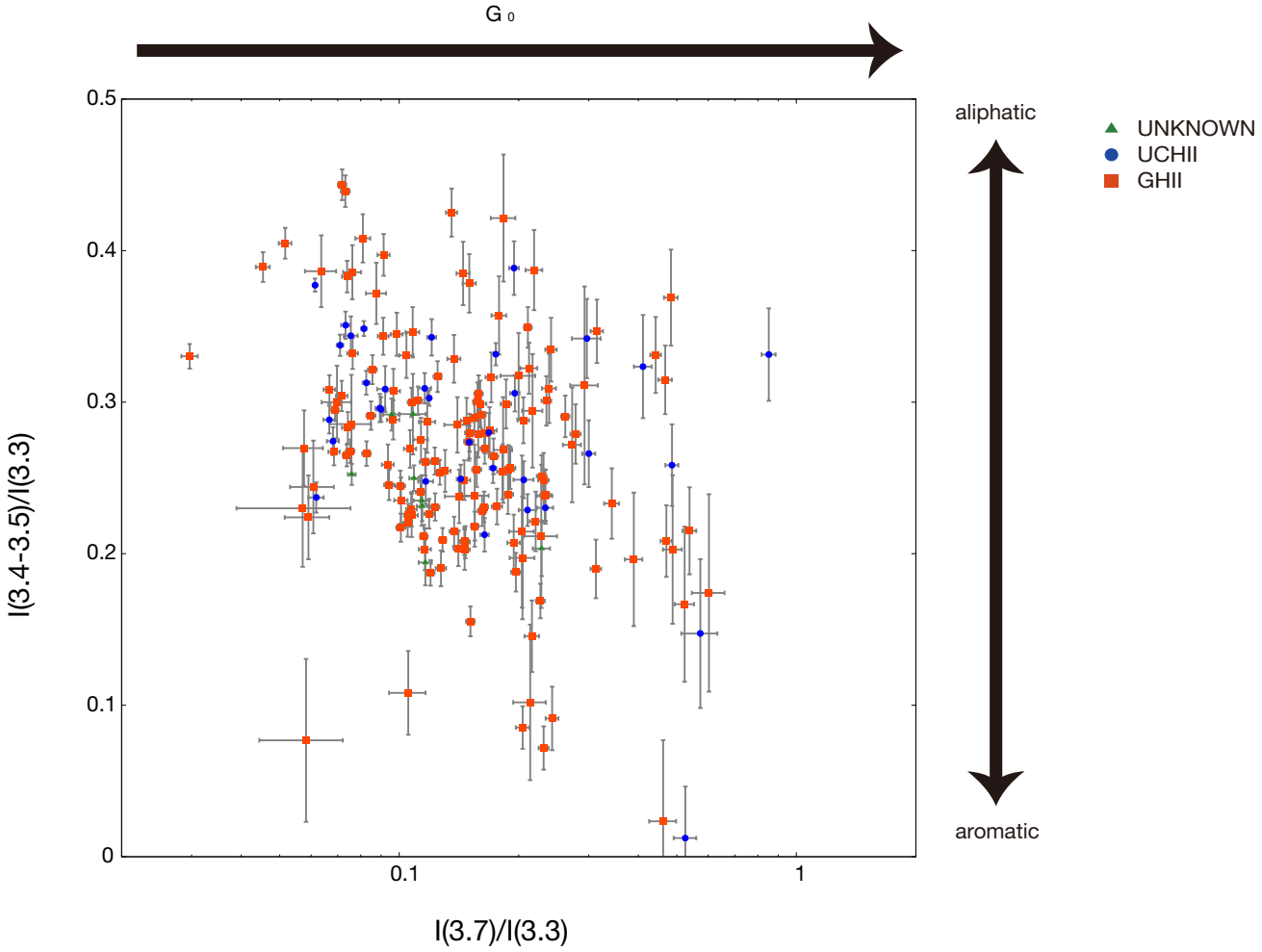

Figure 4.5: Diagram of the relative intensity ratio of the 3.4–3.6 μm sub-features to the 3.3 μm band, $I_{3.4-3.6\,\mu\mathrm{m}}/I_{3.3\,\mu\mathrm{m}}$, versus that of the 3.7 μm continuum intensity to the 3.3 μm band, $I_{\mathrm{cont},3.7\,\mu\mathrm{m}}/I_{3.3\,\mu\mathrm{m}}$.

As shown in Figure 4.6, the MIR color of *AKARI* 9 μm to 18 μm band steeply declines against the ratio of $I_{\mathrm{Br}\alpha}/I_{3.3\,\mu\mathrm{m}}$ especially for GH II regions. The ratio of $I_{\mathrm{Br}\alpha}/I_{3.3\,\mu\mathrm{m}}$ is considered as a good indicator of the fraction of the ionized gas along the line of sight. The present result suggests that the MIR excess around 18 μm becomes stronger relative to the PAH 9 μm emission with the transition from PDRs to ionized-gas dominated regions. The observed trend can be explained by PAH destruction and either VSG or BG replenishment inside the ionized medium, which are proposed by several authors as a possible interpretation of *Herschel* and *Spitzer* multi-wavelength observations (e.g. Paradis et al. 2011; Paladini et al. 2012). On the other hand, it is expected that the temperature of BGs is raised with the increase of incident radiation field from PDRs to ionized-gas, which can also contribute to the observed trend. The present result may reflect the variation in the incident radiation field between PDRs and ionized gas rather than that of dust abundance. These two effects cannot be distinguished from the present dataset and we cannot draw a clear conclusion at the moment. In comparison with the GH II regions, the UCH II regions are distributed over a different region in Figure 4.6, in the relatively left side of the diagram. This might result from the different geometric structures between them, that is, larger contamination from their surroundings in the UCH II sources.

AKARI MIR survey covers more than 96% of the whole sky. The wide scope of the *AKARI* MIR survey will be very helpful to investigate the dust processing in the ISM.

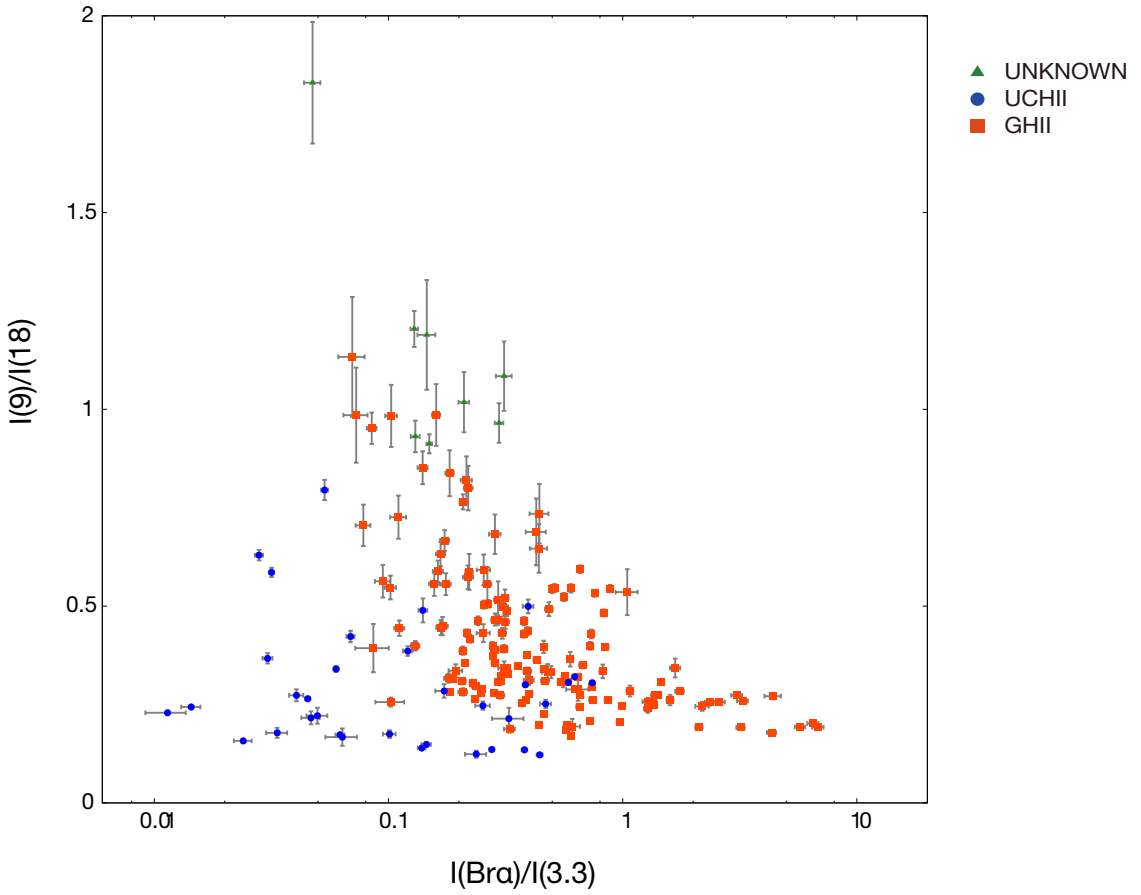

Figure 4.6: Diagram of the MIR color of the *AKARI*/IRC *S9W* to *L18W* band, $I_{9\,\mu\mathrm{m}}/I_{18\,\mu\mathrm{m}}$, against the relative intensity of the hydrogen recombination line Brα at 4.05 μm to the 3.3 μm band, $I_{\mathrm{Br}\alpha}/I_{3.3\,\mu\mathrm{m}}$.

4.5 Summary

We analyzed the PAH emission features in the NIR spectra of the diffuse regions observed from thirty-six galactic H II region or H II region-like objects. The observations were performed with the *AKARI*/IRC in the framework of director's time program during the Phase 3 period. The targets include seven UCH II and twenty-seven GH II regions, which were selected from the catalogue compiled by Crowther & Conti (2003) and Conti & Crowther (2004), plus two H II region-like IR sources. By virtue of the special calibration mode, we extracted spectra taken with the grism and prism (2.5–5.0 μm, $R \sim 100$ and 1.7–5.4 μm, $R \sim 20$–40) at the same place on the sky from 232 lines of sight. The reduced data are released as "AKARI Near-infrared Spectral Atlas of Galactic H II regions" in the following address: `http://www.ir.isas.jaxa.jp/AKARI/Archive/Catalogues/IRC_GALHII_spec/`.

In addition to the 3.3–3.6 μm PAH band complex, the spectra exhibit a variety of ISM features such as helium and hydrogen recombination lines. Some spectra also show the clear absorption features of H_2O and CO ices at 3.05 μm and 4.27 μm. No spectrum shows 4.3–4.8 μm PAD features significantly. See also Doney et al. (2016).

In the unique wavelength coverage of the prism spectroscopic mode, the emission band appears at 5.22 μm. We identify this feature as the PAH 5.25 μm band. The 5.25 μm band strongly correlates with both the 3.3 μm band and the 3.4–3.6 μm sub-features, which proves its close relationship to the C-H vibration modes of PAHs. The relative intensity of the 5.25 μm band to the 3.3 μm band does not vary significantly between different kinds of astronomical objects in our Galaxy. Similar to the 3.3 μm band, the 5.25 μm band can be a good indicator of PAH size distribution, when compared with the PAH emission features involving C-H vibrations at longer wavelengths such as the 11.3 μm band.

The intensity ratio of the 3.4–3.6 μm sub-features to the 3.3μm band decreases as the intensity ratio of the 3.7 μm continuum to the 3.3 μm band increases. Among the present targets, the intensity ratio of the 3.7 μm continuum to the 3.3 μm band is considered to be influenced by the interstellar radiation field most. This result is the first clear evidence for erosion of the aliphatic structure of the band carriers inside or at the boundary of the ionized domain, which supports the latest model of carbonaceous dust (Jones et al. 2013).

We also found that the 9 μm to 18 μm color falls rapidly against the ratio of $I_{\mathrm{Br}\alpha}/I_{3.3\,\mu\mathrm{m}}$. The ratio of $I_{\mathrm{Br}\alpha}/I_{3.3\,\mu\mathrm{m}}$ indicates the fraction of the ionized gas along the line of sight. The result can be nicely interpreted in terms of the model of PAH destruction and VSG or BG reproduction inside the ionized medium, but can also be accounted for by the variation in the interstellar radiation field between PDRs and ionized gas.

Chapter 5

Experimental study on deuterated hydrocarbon materials in the interstellar medium

5.1 Introduction

In this chapter, we present an experimental study on deuterated hydrocarbon materials inspired by recent observations of *AKARI* (Onaka et al. 2014).

Deuterium (D) was created by the Big Bang, and it was gradually reduced by nucleosynthesis inside stars during the chemical evolution of the universe (e.g., Epstein et al. 1976). This process is called "astration". The deuterium abundance in the present universe therefore directly relates to the history of cosmic nucleosynthesis. However, recent observations at UV wavelengths have revealed that the D/H ratio of gas in the solar system varies regionally from 5 to 22 ppm. This dispersion cannot be explained only by the difference in astration between regions (Linsky et al. 2006). These observations also showed that the D/H ratio correlates with the depletion of refractory metal elements such as iron and silicon and the H_2 rotational temperature, suggesting the depletion of deuterium onto dust grains, which was first proposed by Jura (1982). One of the possible candidates that harbor missing deuterium in the ISM is PAHs. Draine (2006) estimated from the observed scatter of the D/H ratio of gas that the D/H ratio in interstellar PAHs can be at most approximately 0.3 if all the missing deuterium is locked up in PAHs.

We can investigate the incorporation of deuterium into PAHs using emission features associated with D-involved vibration modes of PADs. Bauschlicher et al. (1997) and Hudgins et al. (2004) showed that aromatic C-H stretching, aliphatic C-H stretching, C-H in-plane bending, and C-H out-of-plane bending modes are respectively shifted from 3000–3100, 2860–2940,1100–1400, and 700–930 cm^{-1} (3.3–3.2, 3.5–3.4,9.1–7.1, and14.0–10.8 μm) to 2250–2325, 2080–2170,830–1050, and 560–740 cm^{-1} (4.5–4.3, 4.8–4.6,12.0–9.5, and

17.9–13.5 μm) by deuteration based on theoretical calculations (see Table 5.1). Among these D-involved features, NIR features at 2080–2325 cm^{-1} (4.8–4.3 μm) associated with aromatic and aliphatic C-D stretching modes are expected to be good tracers of PADs in the ISM because of their robustness and lack of competitive features in their surroundings.

Peeters et al. (2004a) reported the detection of C-D stretching features at 4.3–4.8 μm in M17 and the Orion Bar based on *ISO*/SWS spectroscopic observations. From the relative intensity of C-D stretching features to C-H ones at 3.2–3.5 μm, they estimated the D/H ratio of PAHs in the ISM as approximately 30%. This value is consistent with the prediction by Draine (2006), suggesting that PAHs could be a major carrier of deuterium in the ISM. On the other hand, NIR spectra of galactic objects, including the same targets as Peeters et al. (2004a) taken by the *AKARI*/IRC with higher sensitivity, do not show the apparent signature of PAD features (Onaka et al. 2014). From this result, the D/H ratio of PAHs is estimated as at most approximately 3%. Doney et al. (2016) also searched for the PAD features at 4.3–4.8 μm in the NIR spectra of fifty-three H II regions obtained with the *AKARI*/IRC, including the dataset of AKARI Near-infrared Spectral Atlas of Galactic H II regions presented in Chapter 4. Among them, only six sources showed the possible PAD features. These latest *AKARI* observations pointed out the possibility that the large-scale depletion of deuterium by PAHs as suggested in Peeters et al. (2004a) is not common in the ISM.

These estimates depend on the ratio of the cross-sections between PAH and PAD features. To correctly estimate the relative abundance of PADs from the observations, we should evaluate the cross-sections of PAH and PAD features accurately. Bauschlicher et al. (1997) suggested that the integrated intensity of the cross-section of PAHs is diminished by a factor of 1.75 due to perdeuteration. However, the relative intensities of C-D features to C-H ones have not been experimentally examined yet for partly deuterated hydrocarbon materials. In addition, because the UIR bands at NIR wavelengths are dominated by emission from very small PAHs ($n_{\mathrm{C}} < 100$, see details in Chapter 3), the 4.3–4.8 μm C-D stretching features cannot trace the depletion of deuterium by large PAHs. To acquire a complete picture of the depletion of deuterium by PAHs in the ISM, investigation at MIR wavelengths is also important. We therefore synthesized deuterated hydrocarbon materials in the laboratory using the method for the synthesis of quenched carbonaceous composites (QCCs), which was originally reported by Sakata et al. (1983). We investigated the ratio of the cross-sections between PAH and PAD features and searched for the possible PAD tracer at MIR wavelengths. We describe the experimental details in §5.2. Results and discussion are presented in §5.3. With respect to carbon, Wada et al. (2003) investigated ^{13}C isotope effects on the IR spectra of QCCs. Here, we employ a similar technique for hydrogen.

Table 5.1: Characteristic positions of C-H and C-D modes

	C-H bond		C-D bond	
Mode	ν [cm^{-1}]	λ [μm]	ν [cm^{-1}]	λ [μm]
aromatic stretching[a]	3000–3100	3.3–3.2	2250–2325	4.5–4.3
aliphatic stretching[a]	2860–2940	3.5–3.4	2080–2170	4.8–4.6
in-plane bending[b]	1100–1400	9.1–7.1	830–1050	12.0–9.5
out-of-plane bending[a]	700–930	14.0–10.8	560–740	17.9–13.5

[a]From Bauschlicher et al. (1997).
[b]From Hudgins et al. (2004).

5.2 Experimental

5.2.1 Synthesis of carbonaceous materials

We synthesized carbonaceous materials from five different isotopic compositions of gas: methane (CH_4), perdeuterated methane (CD_4) gas, and a mixture of CH_4 and CD_4 gas with three different mixture ratios (see below), and we measured the IR absorption spectra and hydrogen isotope ratios. An overview of the experiment is illustrated in Figure 5.1.

D-containing hydrocarbon deposits were synthesized in the same way as that of the filmy quenched carbonaceous composites (f-QCCs) described in Sakata et al. (1992, 1994) and Wada et al. (2009). QCCs are hydrocarbon composites that are experimentally synthesized by quenching plasma methane gas. They exhibit similar spectra to the UIR bands and the 220 nm bump at IR and UV wavelengths, respectively. They are likely an interesting laboratory analogue to interstellar dust and contain PAH-like materials (e.g., Sakata et al. 1983, 1984, 1990). We used the same apparatus as that used in QCC studies. It is composed of a fused quartz tube, vacuum chamber, and 24.5 GHz magnetron [see Sakata (1980) for more details]. In the present experiment, mixtures of CH_4 and CD_4 gas, whose compositions were adjusted before the experiment, were used as the starting gas instead of 100% CH_4. We introduced 4 Torr gas into the fused quartz tube and exposed the gas to the magnetic field of the magnetron to generate a plasmic gas. The input energy of the microwave was approximately 300 W. Through an orifice between the fused quartz tube and the vacuum chamber, the plasmic gas was injected onto potassium bromide (KBr) and silicon (Si) plates installed in the vacuum chamber side by side. The initial pressure of the chamber was pumped down to less than 10^{-4} torr. During the injection of the plasma, a yellow-brown thin film formed on the plates by the condensation of carbonaceous materials. The injection was continued for 5 min. After the 5-min injection, the film thickness was approximately 2 μm. We prepared starting gas mixtures whose CD_4 fractions had been measured accurately in advance as 0.0, 19.7, 38.3, 79.4, and 100%. Hereafter, we refer to the materials synthesized from those gas mixtures as deut-QCC(0), deut-QCC(20), deut-QCC(40), deut-QCC(80), and deut-QCC(100), respectively.

5.2.2 Fourier transform infrared spectroscopy measurement

We measured the 400–3500 cm^{-1} (25–2.8 μm) IR transmission spectra of deut-QCC(00), deut-QCC(20), deut-QCC(40), deut-QCC(80), and deut-QCC(100) with a resolution of 2 cm^{-1} by the Fourier transform infrared spectroscopy (FT-IR) spectrometer IFS 125 series of Bruker Optics Inc. The spectroscopy was carried out for an area approximately 5 mm^2 of the sample and the plate together. The KBr plates were used for the IR spectrum measurement because of their good transmission in the IR region. We measured the transmission spectrum of the empty plate before the deposition of the material to use as the reference. Figure 5.2 shows the absorbance spectrum of each material. The transmission spectra were converted into absorbance spectra after

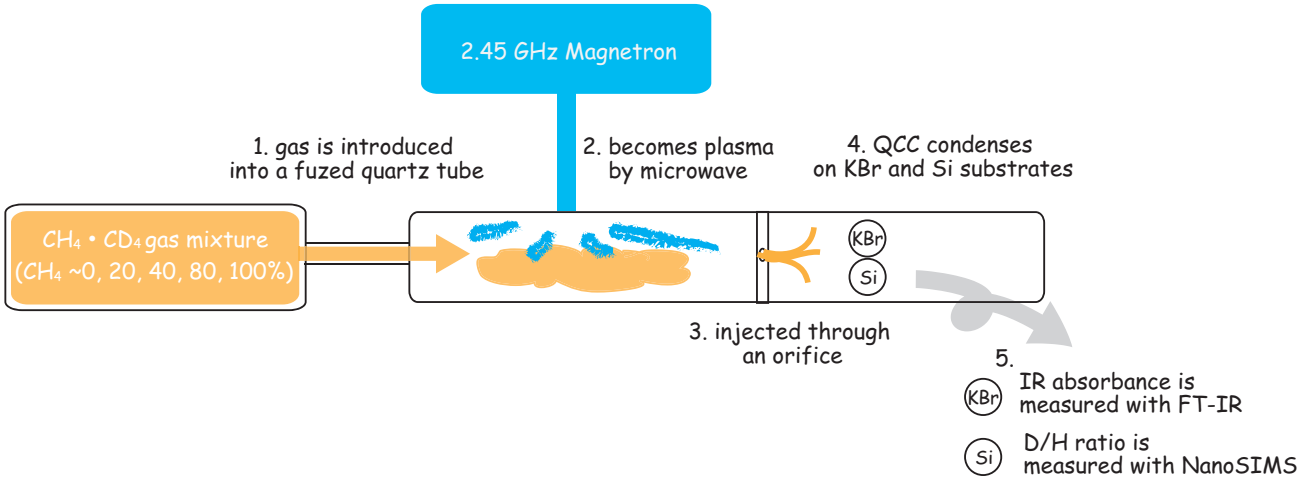

Figure 5.1: Schematic view of experiment.

being divided by the reference spectra. All the absorbance spectra are normalized in the same way by being divided by the integrated intensity of the band feature peaking at 1610 cm^{-1} (6.2 μm), because the 1610 cm^{-1} (6.2 μm) band is attributed to C-C bond vibrations and thus is supposed to be unaffected by deuteration. The sharp line that appears at approximately 750 cm^{-1} (13.3 μm) is an artifact and we do not discuss the spectral range of 700–800 cm^{-1} (14.2–12 μm) in the following sections.

5.2.3 Nano-scale secondary ion mass spectrometer measurement

Because the synthesized materials did not necessarily have the same absolute hydrogen isotope ratios as the starting gas mixtures, we measured the D/H ratios of deut-QCC(20), deut-QCC(40), and deut-QCC(80) with the nano-scale secondary ion mass spectrometer (NanoSIMS). The measurements were performed with the Cameca NanoSIMS50 ion-microprobe at the Atmosphere and Ocean Research Institute, University of Tokyo, Japan. For the NanoSIMS measurement, we used the Si plates. We also used coronene ($C_{24}H_{12}$), which has a known D/H ratio (δD vs VSMOW = -45.7%), for the calibration. The radius and thickness of the plate were 5 mm and 0.7 mm, respectively. In one time measurement, the abundances of hydrogen and deuterium were measured for a 5 $\mu\mathrm{m}^2$ region of the surface. We performed the measurement at several spots per plate to look for areas that gave good signals. The blank signal level was estimated by measuring the blank substrate. After subtraction of the blank signal, we calculated the mean and standard deviation of the D/H ratios in a set of these measurements and used them as the D/H ratio and its uncertainty, respectively, for the sample. The measurements of the coronene and the empty plate were made under the same conditions as the samples. The results of the NanoSIMS measurements are summarized in Table 5.2. The table shows that although deut-QCC(20) shows almost the same D/H ratio as the starting gas, the ratios of deut-QCC(40) and deut-QCC(80) are smaller than the D/H ratios of the starting gas mixtures, suggesting that deuterium is taken into the deposits less effectively than hydrogen when the D/H ratio of the gas is high.

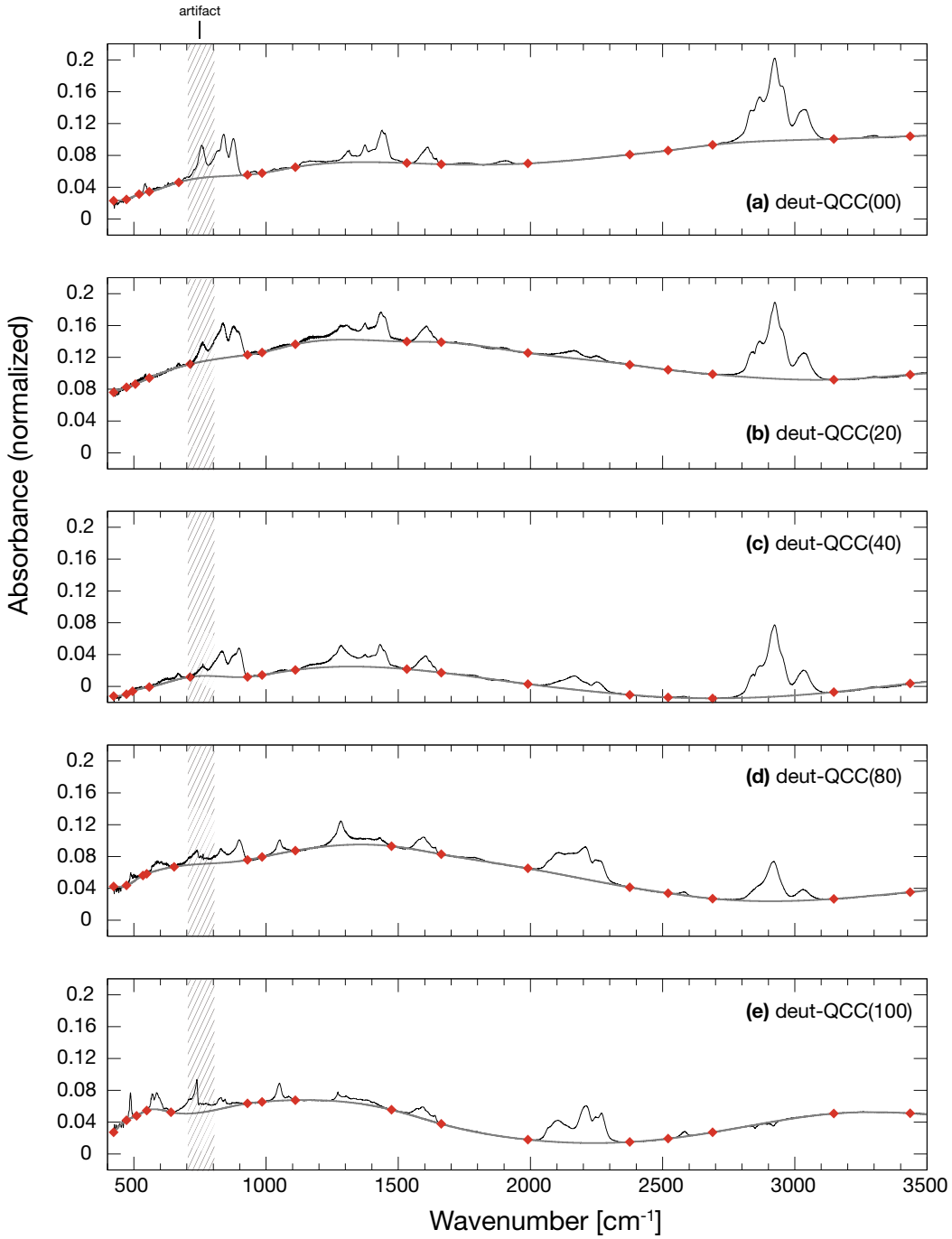

Figure 5.2: Absorbance spectra of **(a)** deut-QCC(00), **(b)** deut-QCC(20), **(c)** deut-QCC(40), **(d)** deut-QCC(80), and **(e)** deut-QCC(100). The spectra are normalized by the integrated intensity of the 1610 cm^{-1} (6.2 μm) band (see text). The grey lines indicate continua determined by the spline method (see details in text). The red diamonds denote pivot points of the spline. The hatched area designates the spectral range of 700–800 cm^{-1} (14.2–12 μm), which is contaminated by the artifact at approximately 750 cm^{-1} (13.3 μm).

Table 5.2: D/H ratios of synthesized materials

Material	Source gas	D/H ratio of source gas	D/H ratio measured by NanoSIMS
deut-QCC(20)	mixture of methane and deuterated methane with $f(\mathrm{CD_4}) = 19.7\%$	0.25	0.24±0.02
deut-QCC(40)	mixture of methane and deuterated methane with $f(\mathrm{CD_4}) = 38.8\%$	0.63	0.60±0.04
deut-QCC(80)	mixture of methane and deuterated methane with $f(\mathrm{CD_4}) = 79.4\%$	3.85	3.2±0.2

Table 5.3: Band assignments for neutral coronene (Buragohain & Pathak 2015)

ν [cm^{-1}]	λ [μm]	Intensity [D^2/u/Å^2]	Mode
128	77.9	0.151	C-C-C out-of-plane bending
374	26.7	0.0890	C-C-C in-plane bending
374	26.7	0.0890	C-C-C in-plane bending
551	18.1	0.922	C-C-C out-of-plane bending + C-H out-of-plane bending
762	13.1	0.150	C-C-C in-plane bending
762	13.1	0.150	C-C-C in-plane bending
850	11.7	3.483	C-H out-of-plane bending
1119	8.93	0.215	C-H in-plane bending
1119	8.93	0.215	C-H in-plane bending
1195	8.36	0.0146	C-C stretching + C-H in-plane bending
1195	8.36	0.0146	C-C stretching + C-H in-plane bending
1297	7.70	0.550	C-C stretching + C-H in-plane bending
1297	7.70	0.550	C-C stretching + C-H in-plane bending
1382	7.23	0.0104	C-C stretching + C-H in-plane bending
1382	7.23	0.0104	C-C stretching + C-H in-plane bending
1485	6.73	0.0614	C-C stretching + C-H in-plane bending
1485	6.73	0.0614	C-C stretching + C-H in-plane bending
1605	6.22	0.252	C-C stretching
1605	6.22	0.252	C-C stretching
3040	3.28	0.133	C-H stretching
3040	3.28	0.133	C-H stretching
3059	3.26	2.55	C-H stretching
3059	3.26	2.55	C-H stretching

5.3 Results and discussion

As shown in Figure 5.2, the IR spectra of the synthesized material exhibit multiple band features lying on the continuum. Their positions and relative intensities vary according to the D/H ratio of the material step by step. In order to investigate the variations in detail, we subtracted the continuum component using the spline fit and extracted the band features. In the spline fit, the pivot points were selected arbitrarily for each spectrum. The NIR and MIR spectra after subtraction of the continuum are shown in Figures 5.3 and 5.4, together with the results of density-functional theory (DFT) calculations of neutral coronene and perdeuterated coronene (Buragohain & Pathak 2015) for the reference. The details of the calculation are described in Buragohain et al. (2015). These theoretical spectra were smoothed with the FWHM of 60 cm^{-1} and normalized by being divided by the 1610 cm^{-1} (6.2 μm) band feature.

5.3.1 2000–3500 cm^{-1} (2.8–5 μm) near-infrared region

As shown in Table 5.1, the aromatic and aliphatic C-H (D) stretching vibration modes fall within the 2000–3500 cm^{-1} (5–2.8 μm) NIR wavelength region. Figures 5.3 (a)–(e) show the 2000–3500 cm^{-1} (5–2.8 μm) NIR spectra of deut-QCC(00), deut-QCC(20), deut-QCC(40), deut-QCC(80), and deut-QCC(100), respectively. With the increase of the D/H ratios of the synthesized material, $R_{\rm mat}$, the band complex appearing at 2860–3100 cm^{-1} (3.5–3.2 μm) becomes weaker, whereas new features appear at 2080–2325 cm^{-1} (4.8–4.3 μm). This transition can be attributed to the replacement of C-H stretching features by C-D ones due to deuteration. Regardless of $R_{\rm mat}$, aliphatic components dominate over aromatic ones in the the spectra, which is a characteristic of QCCs.

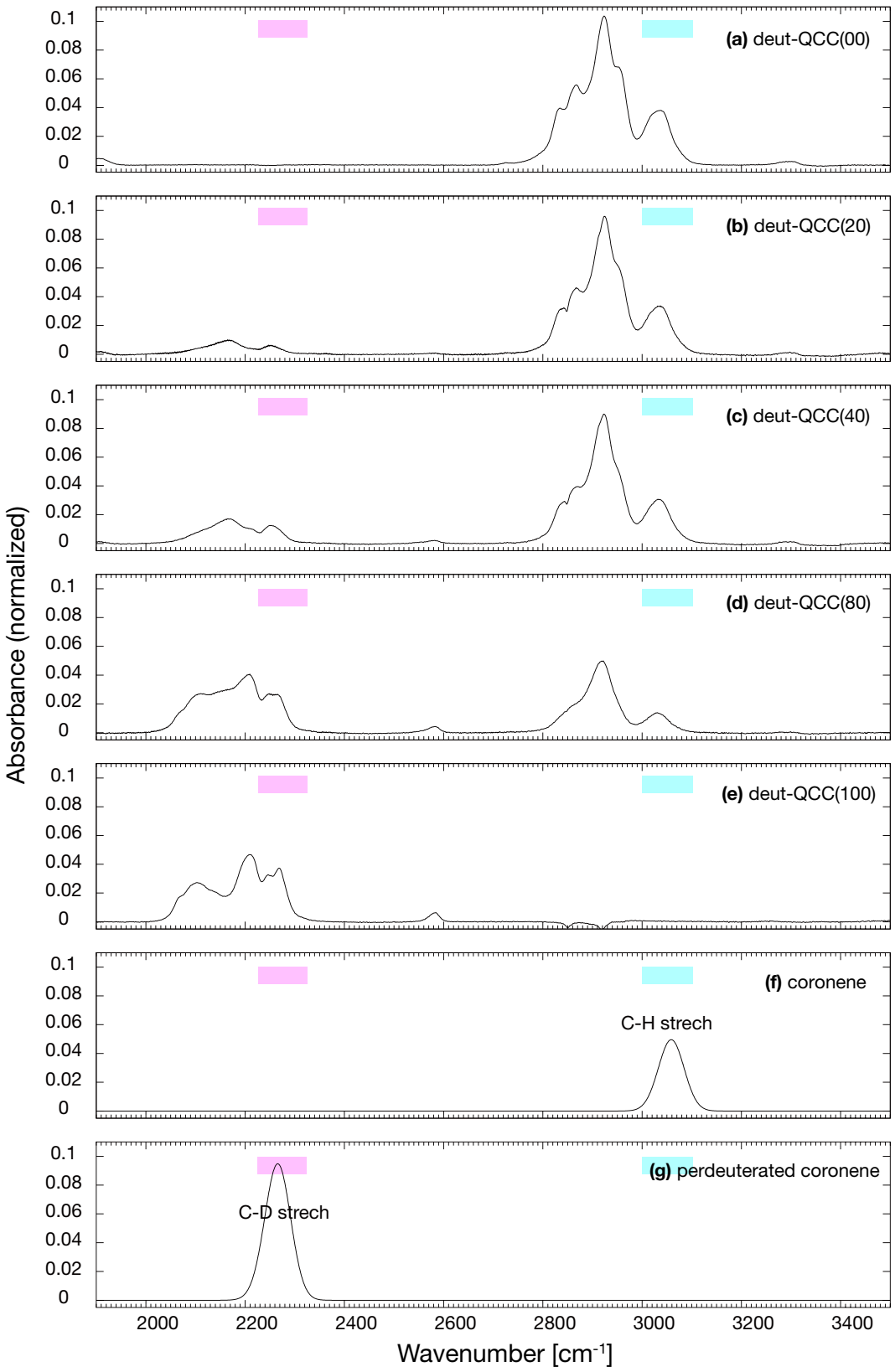

Figure 5.3: 2000–3500 cm^{-1} (2.8–5 μm) NIR spectra of **(a)** deut-QCC(00), **(b)** deut-QCC(20), **(c)** deut-QCC(40), **(d)** deut-QCC(80), and **(e)** deut-QCC(100) after the subtraction of continuum together with the spectra of **(f)** coronene and **(g)** perdeterated coronene calculated by the use of DFT (Buragohain & Pathak 2015). The spectra were normalized by the integrated intensity of the 1610 cm^{-1} (6.2 μm) band (see text). The blue and red boxes designate the regions where C-H and C-D involved features appear, respectively (Bauschlicher et al. 1997; Hudgins et al. 2004, see Table 5.1 for detailed information). In the spectra of coronene and perdeuterated coronene, major band assignments are indicated. For detailed information, see Tables 5.3 and 5.4.

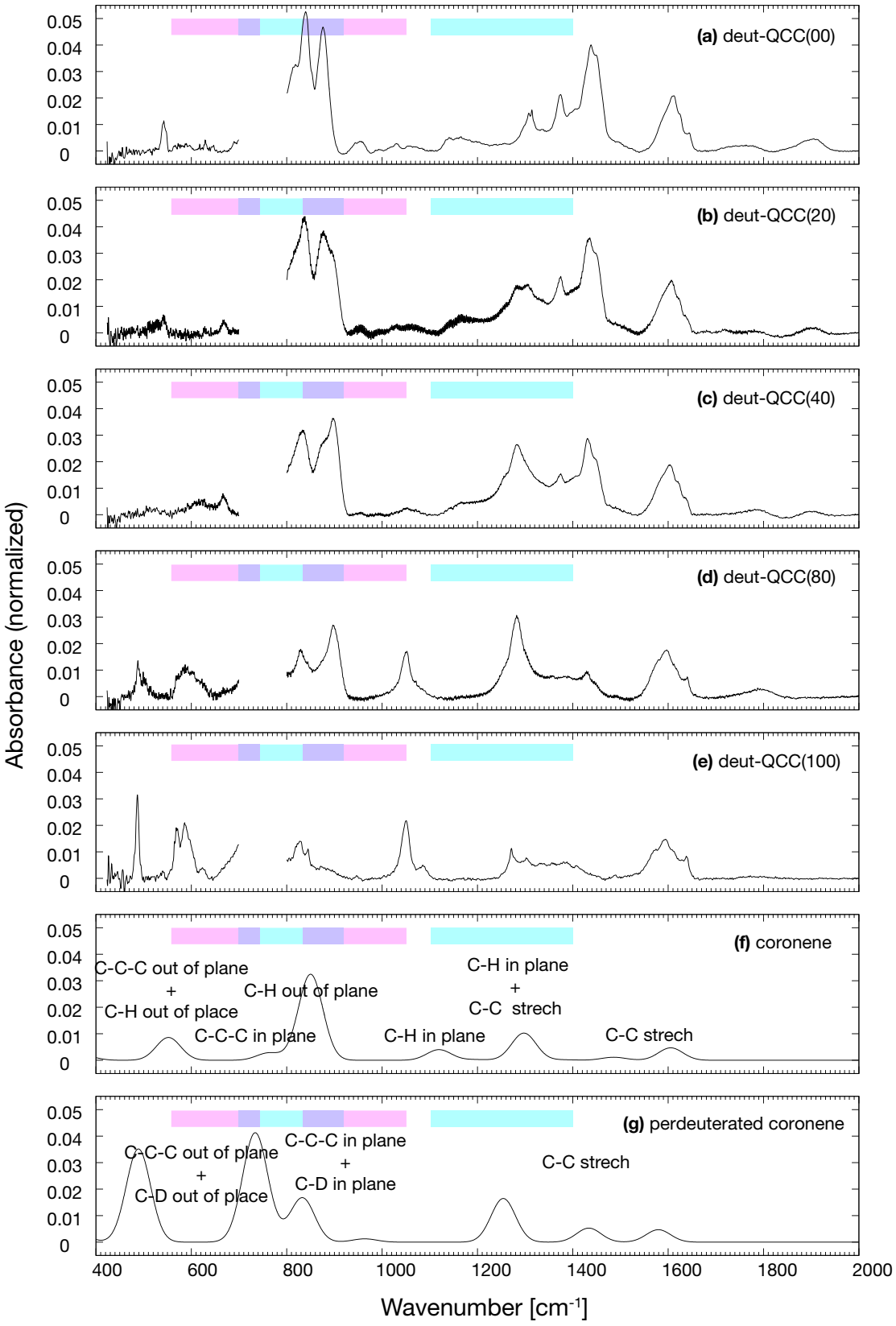

Figure 5.4: 400–2000 cm^{-1} (5–25 μm) MIR spectra of **(a)** deut-QCC(00), **(b)** deut-QCC(20), **(c)** deut-QCC(40), **(d)** deut-QCC(80), and **(e)** deut-QCC(100) after the subtraction of continuum together with the spectra of **(f)** coronene and **(g)** perdeuterated coronene calculated by the use of DFT (Buragohain & Pathak 2015). The spectra were normalized by the integrated intensity of the 1610 cm^{-1} (6.2 μm) band (see text). The symbols are the same as in Figure 5.3.

Table 5.4: Band assignments for perdeuterated coronene (Buragohain & Pathak 2015)

ν [cm^{-1}]	λ [μm]	Intensity [D^2/u/Å^2]	Mode
120	82.7	0.147	C-C-C out-of-plane bending
353	28.2	0.0821	C-C-C in-plane bending
353	28.2	0.0821	C-C-C in-plane bending
489	20.4	1.14	C-C-C out-of-plane bending + C-D out-of-plane bending
717	13.9	0.0846	C-C-C in-plane bending + C-D in-plane bending
717	13.9	0.0846	C-C-C in-plane bending + C-D in-plane bending
735	13.5	1.18	C-C-C out-of-plane bending + C-D out-of-plane bending
771	12.9	0.0232	C-C-C in-plane bending + C-D in-plane bending
771	12.9	0.0232	C-C-C in-plane bending + C-D in-plane bending
832	12.0	0.270	C-C-C in-plane bending + C-D in-plane bending
832	12.0	0.270	C-C-C in-plane bending + C-D in-plane bending
963	10.3	0.0203	C-C-C in-plane bending + C-D in-plane bending
963	10.3	0.0203	C-C-C in-plane bending + C-D in-plane bending
1254	7.97	0.267	C-C stretching
1254	7.97	0.267	C-C stretching
1433	6.97	0.0858	C-C stretching
1433	6.97	0.0858	C-C stretching
1579	6.33	0.0762	C-C stretching
1579	6.33	0.0762	C-C stretching
2241	4.46	0.0949	C-D stretching
2241	4.46	0.0949	C-D stretching
2266	4.41	1.47	C-D stretching
2266	4.41	1.47	C-D stretching

In order to evaluate the ratio of the cross-sections between PAH and PAD features, we fitted the spectra of deut-QCC(20), deut-QCC(40), deut-QCC(80) and derived the relative intensities of the C-D to C-H features. The fitting was done for the 2770–3110 cm^{-1} (3.6–3.2 μm) and 2000–2350 cm^{-1} (5–4.3 μm) spectral ranges, which are associated with the C-H and C-D stretching modes, respectively. We separately fitted the spectra in these spectral ranges to a combination of five or six Gaussian functions whose central wavelengths, FWHMs, and integrated intensities were set as free parameters, using the Levenberg-Marquardt method (Press et al. 2002).

We present the results of fitting in Figure 5.5 and Table 5.5. We sum up the integrated intensities of features appearing at 2000–2250, 2250–2350, 2770–3000, and 3000–3110 cm^{-1} (5–4.4, 4.4–4.3, 3.6–3.3, and 3.3–3.2 μm, respectively), and regard them as the respective total integrated intensities of C-D aliphatic, C-D aromatic, C-H aliphatic, and C-H aromatic features, denoted as $I_{\rm CD\,alipha}$, $I_{\rm CD\,aroma}$, $I_{\rm CH\,alipha}$, and $I_{\rm CH\,aroma}$, respectively. Table 5.6 shows the relative intensities of aromatic and aliphatic C-D to C-H features, $R_{\rm int,alipha}$=$I_{\rm CD\,alipha}$/$I_{\rm CH\,alipha}$ and $R_{\rm int,aroma}$=$I_{\rm CD\,aroma}$/$I_{\rm CH\,aroma}$, respectively. In Figure 5.6, we plot these values, together with the D/H ratios of the synthesized materials measured by NanoSIMS, $R_{\rm mat}$, for deut-QCC(20), deut-QCC(40), and deut-QCC(80). Assuming that the efficiency of the incorporation of deuterium does not vary between aromatic and aliphatic structures, the ratios of $R_{\rm int,alipha}$ and $R_{\rm int,aroma}$ to $R_{\rm mat}$ are equal to the ratios of the cross-sections, $R_{\rm cs,alipha}$ and $R_{\rm cs,aroma}$, respectively. The weighted averages of $R_{\rm cs,alipha}$ and $R_{\rm cs,aroma}$, $< R_{\rm cs,alipha} >$ and $< R_{\rm cs,aroma} >$, are 0.38 and 0.56, respectively. In terms of aromatic components, the value of $< R_{\rm cs,aroma} >$ is almost consistent with the value reported by Bauschlicher et al. (1997), 1/1.75 (=0.57). Because aliphatic features dominate over aromatic ones in the present sample and because the intensity ratio for the aromatic features is in agreement with theoretical calculations, the D/H ratio in the

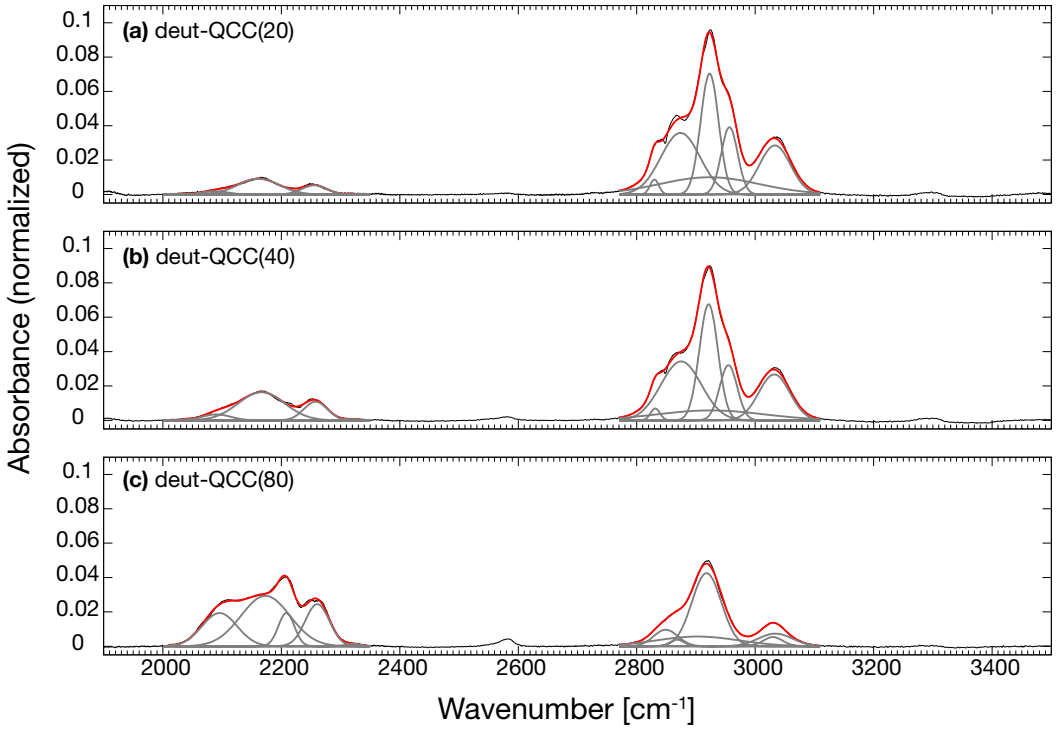

Figure 5.5: Fitting results of 2000–3500 cm^{-1} (2.8–5 μm) NIR spectra of **(a)** deut-QCC(20), **(b)** deut-QCC(40), and **(c)** deut-QCC(80). Best-fit model spectra (red lines) are overlaid on the absorbance spectra (black lines). The gray lines designate individual Gaussian components.

aromatic component should not be much different from the results of the NanoSIMS measurements, which are the summation of both aromatic and aliphatic components. Therefore, the D/H ratio of the aliphatic component can also be considered to be the same as that of the aromatic component. This evidence supports the above assumption that the efficiency of the incorporation of deuterium does not vary between aromatic and aliphatic structures. Previous investigations did not take into account the difference between $R_{\mathrm{cs,aroma}}$ and $R_{\mathrm{cs,alipha}}$ (e.g., Onaka et al. 2014). Therefore, the D/H ratio in interstellar PAHs derived from the aliphatic features could be underestimated at most by a factor of 1.5. Because the factor is not large, however, this will not change the conclusion that very small PAHs ($n_{\mathrm{C}} < 100$) are not a major reservoir for interstellar deuterium (Onaka et al. 2014; Doney et al. 2016). The present experiment clearly rules out the possibility that the cross-sections of the 2080–2325 cm^{-1} (4.8–4.3 μm) PAD features are much smaller than those of the 2860-3100 cm^{-1} (3.5–3.2 μm) PAH features to account for the observed very small excess emission of 4.4-4.6 μm. It is also suggested that decomposing aromatic and aliphatic components is important to correctly estimate the depletion of deuterium onto PAHs in the ISM.

5.3.2 400–2000 cm^{-1} (25–5 μm) mid-infrared region

In addition to C-H(D) in-plane and out-of-plane bending modes (Table 5.1), C-C stretching, C-C-C in-plane bending, C-C-C out-of-plane bending, and mixtures of these vibration modes appear at the 400–2000 cm^{-1} (25–5 μm) MIR wavelength region. Figures 5.4 (a)–(e) display the 400–2000 cm^{-1} (25–5 μm) MIR spectra of

Table 5.5: Fitting results

Material	Fitting region [cm^{-1}]	Center wavenumber [cm^{-1}]	FWHM [cm^{-1}]	Relative integrated intensity
deut-QCC(20)	2770–3110	2829.90 ± 0.07	17.57 ± 0.16	0.16180 ± 0.00197
		2873.85 ± 0.26	78.08 ± 0.36	2.97723 ± 0.03427
		2923.05 ± 0.12	35.81 ± 0.25	2.68236 ± 0.02900
		2956.56 ± 0.20	32.89 ± 0.31	1.36983 ± 0.02874
		2922.65 ± 0.37	197.86 ± 1.36	2.10485 ± 0.05444
		3033.33 ± 0.11	61.72 ± 0.18	1.87417 ± 0.01260
	2000–2350	2033.99 ± 0.05	23.18 ± 0.06	0.01140 ± 0.00007
		2087.71 ± 0.17	51.82 ± 0.26	0.10340 ± 0.00111
		2161.48 ± 0.06	81.28 ± 0.17	0.79423 ± 0.00138
		2255.66 ± 0.04	49.00 ± 0.06	0.27831 ± 0.00045
		2317.05 ± 0.02	18.54 ± 0.03	0.01061 ± 0.00003
deut-QCC(40)	2770–3110	2831.25 ± 0.09	18.78 ± 0.20	0.13780 ± 0.00212
		2874.99 ± 0.35	80.53 ± 0.47	2.93862 ± 0.04116
		2921.38 ± 0.15	37.01 ± 0.30	2.66150 ± 0.03789
		2954.84 ± 0.29	34.84 ± 0.41	1.19043 ± 0.03375
		2924.99 ± 0.53	212.33 ± 3.05	1.30551 ± 0.05675
		3032.20 ± 0.11	61.52 ± 0.19	1.74895 ± 0.01370
	2000–2350	2016.17 ± 0.02	7.20 ± 0.04	0.00215 ± 0.00002
		2036.10 ± 0.07	22.86 ± 0.19	0.01290 ± 0.00018
		2090.27 ± 0.24	56.35 ± 0.36	0.20710 ± 0.00359
		2166.44 ± 0.09	91.83 ± 0.31	1.60507 ± 0.00471
		2257.83 ± 0.04	46.53 ± 0.08	0.53685 ± 0.00150
		2318.18 ± 0.09	38.57 ± 0.12	0.02823 ± 0.00014
deut-QCC(80)	2770–3110	2848.95 ± 0.85	48.19 ± 0.85	0.49325 ± 0.02479
		2868.20 ± 0.27	27.79 ± 1.33	0.11260 ± 0.01866
		2902.86 ± 0.98	163.68 ± 1.70	0.98612 ± 0.02239
		2917.92 ± 0.05	58.39 ± 0.19	2.64352 ± 0.01505
		3029.98 ± 0.16	38.86 ± 0.36	0.22117 ± 0.00620
		3033.97 ± 0.33	68.10 ± 0.43	0.53281 ± 0.00945
	2000–2350	2015.15 ± 0.02	6.86 ± 0.05	0.00337 ± 0.00003
		2095.72 ± 0.33	69.82 ± 0.22	1.43589 ± 0.03534
		2173.19 ± 0.54	97.14 ± 2.62	3.03458 ± 0.09483
		2208.50 ± 0.09	31.77 ± 0.46	0.65514 ± 0.02868
		2260.69 ± 0.26	47.90 ± 0.34	1.24933 ± 0.03280
		2321.44 ± 0.08	31.97 ± 0.09	0.04643 ± 0.00034

Table 5.6: Relative intensity ratios

Material	$I_{\mathrm{CD\,alipha}}/I_{\mathrm{CH\,alipha}}$	$I_{\mathrm{CD\,aroma}}/I_{\mathrm{CH\,aroma}}$
deut-QCC(20)	0.098 ± 0.002	0.154 ± 0.001
deut-QCC(40)	0.222 ± 0.005	0.323 ± 0.003
deut-QCC(80)	1.21 ± 0.04	1.72 ± 0.06

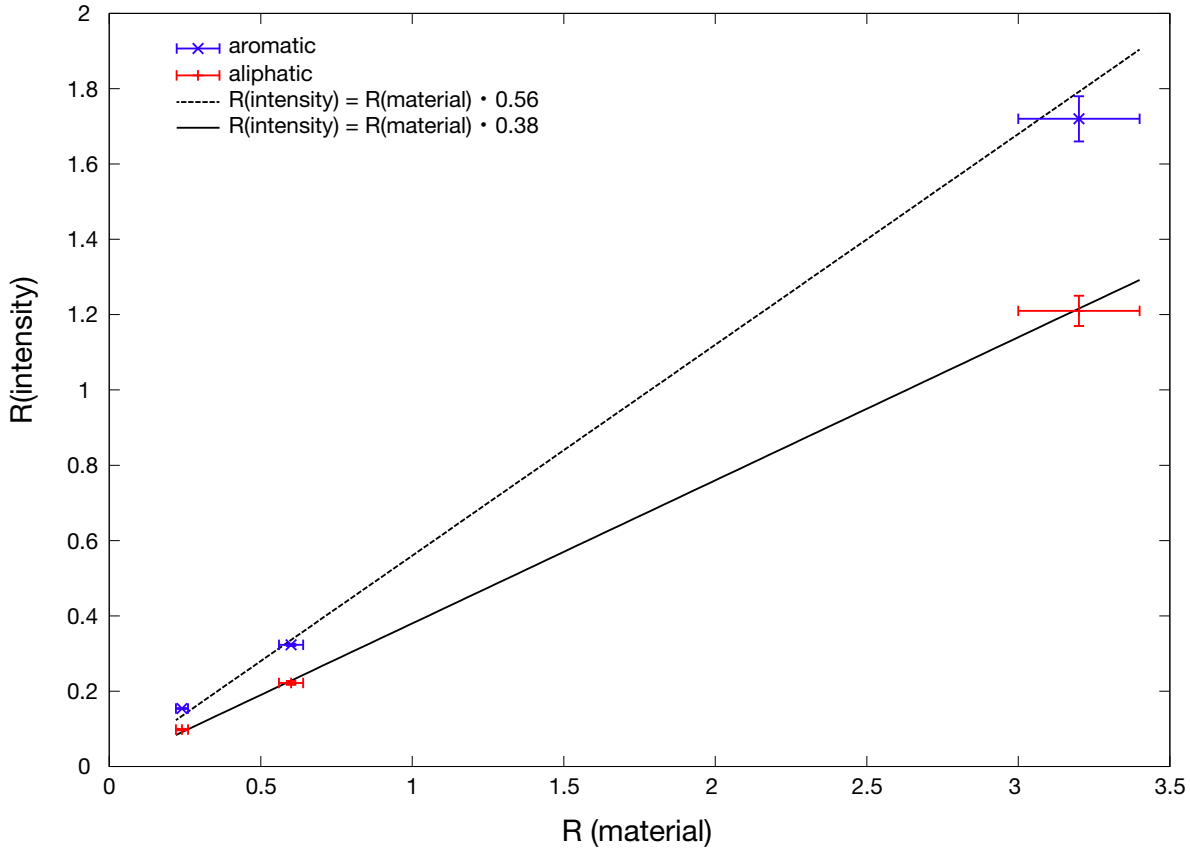

Figure 5.6: D/H ratios of the synthesized material v.s. intensity ratios of aliphatic and aromatic C-D stretching features to those of C-H.

deut-QCC(00), deut-QCC(20), deut-QCC(40), deut-QCC(80), and deut-QCC(100), respectively. All materials exhibit similar band features at approximately 1200–1700 cm^{-1} (8.3–5.9 μm). These features can be attributed mostly to C-C stretching vibration modes except for C-H in-plane modes at approximately 12000 cm^{-1}. On the other hand, with the increase of R_{mat}, band complexes appearing at 800–900 cm^{-1} (12.5–11.1 μm) and 1200–1500 (8.3–6.7 μm) grow fainter, whereas new features emerge at 550–650 cm^{-1} (18.2–15.4 μm) and 1000–1100 cm^{-1} (10–9.1 μm). These changes are considered to result from the replacement of C-H by C-D features due to deuteration. The features at 800–900 cm^{-1} (12.5–11.1 μm), 1200–1500 (8.3–6.7 μm), 550–650 cm^{-1} (18.2–15.4 μm), and 1000–1100 cm^{-1} (10–9.1 μm) can be linked to C-H in-plane bending, C-H out-of-plane bending, C-D in-plane bending, and C-D out-of-plane bending vibration modes, respectively. However, as pointed out by Bauschlicher et al. (1997), in this spectral range a variety of vibration modes such as C-C-C in-plane bending gather together, making it difficult to use these features as a PAD tracer at MIR wavelengths. In addition to these changes, we found that in the spectra of deut-QCC(80) and and deut-QCC(100), a sharp feature newly appears at 490 cm^{-1} (20.4 μm) in exchange for a feature at 540 cm^{-1} (18.5 μm), which can be clearly seen in the spectra of deut-QCC(00) and deut-QCC(20). A similar change is recognized in the simulated spectra of coronene and perdeuterated coronene [see Figures 5.4 (f) and (g)]. This is caused by the shift of the mixture mode of C-C-C out-of-plane bending and C-H out-of-plane bending vibration due to deuteration (see Tables

5.3 and 5.4). If QCCs have comparable structures to coronene, the observed transition of the sharp feature from 540 cm^{-1} (18.5 μm) to 490 cm^{-1} (20.4 μm) in the spectra of deuterated QCCs can be attributed to the shift of the same vibration mode. The 490 cm^{-1} (20.4 μm) feature is expected to be a useful tracer of PADs, especially large ones, which cannot be traced by NIR spectroscopy because there are no other competitive features and it appears at MIR wavelengths. Combined with the C-D stretching features at NIR wavelengths, the 490 cm^{-1} (20.4 μm) feature will play an important role in the investigation of depletion of deuterium by PAHs in the ISM. However, since the peak position of the mixture mode of C-C-C out-of-plane bending and C-H out-of-plane bending vibration shifts by approximately $\pm$0.3 μm according to the structures of PAHs (Buragohain & Pathak 2015), careful discussion is required at the stage of application to observational studies.

5.4 Summary

We present an experimental study of deuterated hydrocarbon materials. We generated deuterated hydrocarbon materials, deut-QCC(0), deut-QCC(20), deut-QCC(40), deut-QCC(80), and deut-QCC(100), from a mixture of CH_4 and CD_4 gas with five different CD_4 fractions: 0, 19.7, 38.3, 79.4, and 100 %. The synthesis of materials was done in a similar way to that of f-QCCs. The 2–25 μm IR absorption spectra of the synthesized materials were measured by the FT-IR. The hydrogen isotope ratios of deut-QCC(20), deut-QCC(40), and deut-QCC(80) were determined by the NanoSIMS, which shows that when the source gas becomes D-rich, deuterium is incorporated into the deposits less efficiently than hydrogen.

With increasing D-fraction, the band complexes at 2860–3100, 1200–1500, and 800–900 cm^{-1} (3.5–3.2, 8.3–6.7, and 12.5–11.1 μm) are weakened, whereas new features emerge at 2080–2325, 1000–1100, and 550–650 cm^{-1} (4.8–4.3, 10–9.1, and 18.2–15.4 μm). This trend can be well accounted for by the replacement of C-H features by C-D features. Among these C-D features, the aromatic and aliphatic C-D stretching features at 4.3–4.8 μm are considered to be a good PAD tracer because of their strength and the lack of other competitors in their surroundings.

From the relative intensities of C-D to C-H features and the hydrogen isotope ratios, we evaluated the ratio of the cross-sections between PAH and PAD stretching features. Deuteration weakens the cross-section of aromatic C-H stretching features by a factor of 0.56, which is consistent with the value reported by Bauschlicher et al. (1997). On the other hand, aliphatic C-H stretching features become smaller by a factor of 0.38 due to deuteration, suggesting the possibility that we have underestimated the D/H ratio in PAHs at most by a factor of 1.5. However, the difference is not so large. This result rules out the possibility that the cross-section of the 4 μm PAD feature is much lower than that of the 3 μm PAH feature as an interpretation for the low upper limit on the D/H ratio in PAHs constrained by the *AKARI* observations.

We also found that when the D-fraction increases, a new feature appears at 20.4 μm in replacement of the 18.5 μm feature. Based on comparison with the results of DFT calculation of coronene and perdeuterated coronene, we surmise that the 20.4 μm feature originates from a combination of the C-C-C out-of-plane and the C-D out-of-plane vibration modes, and can be a good PAD tracer for large carriers.

The present results show that it is crucial to resolve the aliphatic and aromatic stretching features at NIR wavelengths for correct estimate of the D/H ratio in PAHs and that we can investigate deuteration of large PAHs from the 20.4 μm feature. The 20.4 μm feature seems to be weaker than the NIR features, and no detection has so far been reported in *Spitzer*/IRS observations. The *James Webb Space Telescope* (*JWST*) will have significantly better sensitivity at IR wavelengths to 28 μm and higher spectral resolution in the 1–5 μm NIR regime. It will offer us a special opportunity to look for the PAD 20.4 μm feature and to get better constraint on the D/H ratio in PAHs.

Chapter 6

Summary

In this thesis, we investigated spectroscopic properties of interstellar PAHs to discuss their physical properties as well as their processing in the ISM based on the observations with *AKARI*.

In Chapter 3, from simultaneous spectroscopy at 2–5 μm NIR and 5–13 μm MIR wavelengths using the *Ns* slit in the *AKARI* Phase 2 period, we investigated the relative intensity of the UIR bands from 2.55 to 13.4 μm emitted from exactly the same region. The targets are nine diffuse regions in the LMC, which were selected based on the CO mapping data and the *IRAS* colors of $I_{25\,\mu\mathrm{m}}/I_{12\,\mu\mathrm{m}}$ and $I_{60\,\mu\mathrm{m}}/I_{100\,\mu\mathrm{m}}$. From the spectral features such as Brα at 4.05 μm, which originate from ionized gas, we divided the targets into two groups: those in relatively quiescent radiation field environments (Group A) and those in harsh radiation field environments powered by young massive stars (Group B). Group A members show the positive correlations between the band ratios of $I_{3.3\,\mu\mathrm{m}}/I_{11.3\,\mu\mathrm{m}}$, $I_{6.2\,\mu\mathrm{m}}/I_{11.3\,\mu\mathrm{m}}$, $I_{7.7\,\mu\mathrm{m}}/I_{11.3\,\mu\mathrm{m}}$, and $I_{8.6\,\mu\mathrm{m}}/I_{11.3\,\mu\mathrm{m}}$ and the *IRAS* and *AKARI* colors, but Group B members do not follow the sequence, which can be explained in terms of the fact that in Group A PAHs are more highly excited and ionized with the increase of interstellar radiation field, whereas in Group B the excitation of PAHs is reduced due to the paucity of very small PAHs ($n_{\mathrm{C}} < 100$) and the recombination of ionized PAHs with electrons is promoted by an increase of the electron density inside H II regions. This view is compatible with the efficient destruction of very small PAHs ($n_{\mathrm{C}} < 100$) by electron collisions in a hot plasma suggested by Micelotta et al. (2010a). This result suggests that by adding the 3.3 μm band to the analysis, we can diagnose the interstellar radiation field conditions more precisely from the UIR bands, in particular in the diagram of $I_{3.3\,\mu\mathrm{m}}/I_{11.3\,\mu\mathrm{m}}$ v.s. $I_{7.7\,\mu\mathrm{m}}/I_{11.3\,\mu\mathrm{m}}$.

In Chapter 4, we investigated the UIR bands appearing between 2.0–5.4 μm in detail based on a large quantity of high-quality spectra of galactic H II regions. The data were taken in the framework of director's time program during the *AKARI* Phase 3 period, and grism and prism spectroscopy were performed for the same slit area with the special calibration mode. The targets include seven UCH II and twenty-seven GH II regions, which were selected from the catalogue compiled by Crowther & Conti (2003) and Conti & Crowther (2004), plus two IR sources which show H II region-like spectra. Thanks to the unique wavelength coverage of the prism

spectroscopy, we identify the PAH 5.25 μm at the edge of the prism spectra. This band has a good correlation with both the 3.3 μm band and the 3.4–3.6 μm sub-features, which confirms its close relationship to the C-H vibration modes of PAHs. As well as the 3.3 μm band, combined with the longer-wavelength bands such as the 11.3 μm band, the 5.25 μm could be a useful probe for the size distribution of PAHs. We also found that the relative intensity of the 3.4–3.6 μm sub-features to the 3.3μm band decreases with the ratio of of the 3.7 μm continuum to the 3.3 μm band. The ratio of the 3.7 μm continuum to the 3.3 μm band is thought to indicate the strength of interstellar radiation field. This is the first investigation of the 3.3–3.6 μm band complex based on a large quantity of high-quality spectra of various galactic H II regions. It gives the first clear evidence for PAH erosion in ionized medium. Besides, the 9 μm to 18 μm color shows a sharp decline against the ratio of $I_{\mathrm{Br}\alpha}/I_{3.3\,\mu\mathrm{m}}$. This trend is compatible with the idea that inside the ionized medium VSGs and BGs are reproduced, whereas PAHs are destroyed. Alternatively, the variation in the interstellar radiation field between PDRs and ionized gas also accounts for the result.

Chapter 5 show the laboratory work on deuterated hydrocarbon materials motivated by the latest *AKARI* results. We synthesized deuterated hydrocarbon materials from a mixture of CH_4 and CD_4 gas with five different mixture rates, and investigated the spectral variation due to the deuteration using the NanoSIMS and FT-IR. The synthesis was done in the same way as that of f-QCCs. The deuteration weakens the cross-sections of aromatic and aliphatic C-H stretching features by a factor of 0.56 and 0.37, respectively, which reinforces our interpretation for the *AKARI* observations that very small PAHs ($n_{\mathrm{C}} < 100$) are not the major carrier of the missing deuterium in the ISM. Besides, we found that D-rich materials show a new feature at 20.4 μm, which can be associated with a combination of the C-C-C out-of-plane and the C-D out-of-plane vibration mode. This feature is expected to be helpful for understanding the deuteration of large PAHs.

The present study demonstrates the power of NIR spectroscopy for the understanding of the ISM physics. It provides us significant information on the size distribution, chemical structure, hydrogen isotope ratio of PAHs, and accordingly the host environments in the nearby and far universe. In particular, we revealed that the size distribution and chemical structure vary inside or at the boundary of H II regions unambiguously for the first time. However, it should be noted that what we have observed represents only a small part of the PAH evolution in the universe. Further investigation is necessary to draw a whole picture of the PAH evolution and to use PAHs as a diagnostic tool for interstellar environments. To achieve that, the NIR spectroscopy is undoubtedly indispensable.

Appendix A

Model calculation

The present model calculation basically followed Schutte et al. (1993) with the recent model parameters provided by Draine & Li (2001) and Draine & Li (2007) (see also Boersma et al. 2010; Bauschlicher et al. 2010). The emission intensity due to an IR active fundamental vibrational transition, i, from level (v-1) to level v, in a j-type PAH molecule with a total internal vibrational energy E is given by

$$I(j, E, i, v) = h\nu_i v A^{1,0}_{j,i} \frac{\rho_{j,r}(E - vh\nu_i)}{\rho_j(E)}, \tag{A.1}$$

where h is the Plank constant, v is the vibrational quantum number, ν_i is the frequency of the emitting mode, $A^{1,0}_{j,i}$ is the Einstein coefficient of the $1 \rightarrow 0$ transition, $\rho_j(E)$ is the total density of vibrational states at total energy E, i.e., the number of ways the energy E can be distributed over all available states, and $\rho_{j,r}(E - vh\nu_i)$ is the density of vibrational states for all modes except the emitting mode at a vibrational energy $E - vh\nu_i$. For the Einstein coefficient of the $1 \rightarrow 0$ transition, $A^{1,0}_{j,i}$ is given by

$$A^{1,0}_{j,i} = \frac{8\pi c}{\lambda_i^4} \sigma_{j,int,i}, \tag{A.2}$$

where λ_i is the wavelength of the emitting mode, $\sigma_{j,int,i}$ is the cross-section of the i-th mode integrated over the wavelength. We adopted the values described in Table 1 of Draine & Li (2007) as $\sigma_{j,int,i}$ for each type of PAH molecules. Here we calculated the model spectra with various parameters to semi-quantitatively compare with the observations and thus adopted a simple thermal approximation. The validity of the thermal approximation has been studied to a large extent and it is shown that the presence of the size distribution alleviates the difference and the effect on the relative band intensities is small enough for the present study (Allamandola et al. 1989b; Schutte et al. 1993; Draine & Li 2001).

In the thermal approximation, the emitted intensity of a j-type molecule with internal energy E in the i-th

mode, from level v to level (v-1), is described by

$$I(j, E, i, v) = h\nu_i v A^{1,0}_{j,i} \exp(-vh\nu_i/kT_j(E))[1 - \exp(-h\nu_i/kT_j(E))]^{-1}, \tag{A.3}$$

where $T_j(E)$ is the vibrational excitation temperature of a j-type molecule with E and where k is the Boltzmann constant. The sum of equation (A.3) from $v = 1$ to $v = \infty$, i.e., the total emitted intensity in the i-th mode, is given by

$$I(j, E, i) = h\nu_i A^{1,0}_{j,i}[\exp(h\nu_i/kT_j(E)) - 1]^{-1}. \tag{A.4}$$

In this approximation, the energy-temperature relation for a j-type molecule is given by

$$E(T_j) = \sum_{i=1}^{s} h\nu_i[\exp(h\nu_i/kT_j) - 1]^{-1}, \tag{A.5}$$

where s is the number of vibrational modes of a j-type molecule equal to 3 times of atoms minus 6, i.e., $3n_{\rm atom} - 6$. We derived this relationship, using equations (2)–(8) in Draine & Li (2001) for each type of PAH molecules.

The total energy emitted in the i-th mode following the absorption of a UV/visual photon of frequency of ν, $f(j, \nu, i)$ is given by

$$f(j, \nu, i) = \int_0^{h\nu} \frac{I(j, E, i)}{I(j, E)} dE, \tag{A.6}$$

where $I(j, E, i)/I(j, E)$ is the fraction of the total IR intensity emitted by a j-type molecule with the internal energy E in the i-th mode. Hence, the total emitted intensity in the i-th mode of a j-type molecule exposed by a star, whose spectrum is approximated with a blackbody, $P(j, T_*, i)$ is given by

$$P(j, T_*, i) = \int_0^{\infty} \frac{\sigma_{j,\nu} B_\nu(T_*)}{h\nu} f(j, v, i) d\nu, \tag{A.7}$$

where $\sigma_{j,\nu}$ is the UV/visual absorption cross-section of a j-type molecule, as which we adopted the values described in equations (17)–(20) in Schutte et al. (1993). Then, the flux in the i-th mode from a certain size distribution of interstellar PAHs, exposed to a star with T_*, is given by

$$F(T_*, i) = \sum_j n_{\rm PAH}(j) P(j, T_*, i), \tag{A.8}$$

where $n_{\rm PAH}(j)$ is the number density of the j-type PAH molecule.

In order to evaluate the effect of depletion of very small PAHs quantitively, we calculated the ratio of $F(T_*, i)$ relative to the $F(T_*, i')$, the model ratio of the emitted intensity in the i-th mode relative to that in the

i'-th mode in two cases; Case I and Case II (see text). In both cases, we assumed that the number density of interstellar PAHs is given by a power-law distribution with the size, i.e., the number of carbon atoms contained by PAH molecules, $n_{\rm C}$. If the number of PAH molecules per interstellar H atoms with a radius a between $a+da$ is proportional to $a^{-\alpha}$ and $n_{\rm C} \propto a^{\gamma}$, the number of PAH molecules per interstellar H atoms with a number of carbon atoms $n_{\rm C}$ between $n_{\rm C} + dn_{\rm C}$ is given by

$$\frac{dN_{PAH}}{N_H} \propto n_{\rm C}^{\frac{1-\alpha-\gamma}{\gamma}} dn_{\rm C}. \tag{A.9}$$

We adopted α=3.5 and γ=3 as assumed in Schutte et al. (1993). Then the number density is given by

$$n_{PAH}(j) \propto n_{\rm C}^{-1.833}. \tag{A.10}$$

Allamandola et al. (1989b) suggested that smaller PAHs with $n_{\rm C} < 20$ are photolytically unstable. The minimum size of PAHs was set to $n_{\rm C}$=20 in Case I, whereas we varied the minimum size of PAHs from $n_{\rm C}$=20 to $n_{\rm C}$=100 in Case II. In both cases, the maximum sizes of PAH molecules was fixed at 4000. Draine & Li (2007) suggested that larger PAHs with $n_{\rm C} > 4000$ do not contribute to the UIR bands at 3–11 μm. We ran the model twice with the cross-sections for neutral PAHs and ionic PAHs provided by Draine & Li (2007), respectively, and calculated the ratio of $F(T_*, i)$ from a summation of the spectra of both components by varying the ionization fraction.

Appendix B

Comparison of the grism and prism spectra

To make quantitative comparison of the spectra taken with the *NG* and *NP* modes, we developed software to simulate a spectrum taken with the the prism from that a spectrum taken with the the grism. In the simulation, we took into account that the spectral dispersion in the prism mode changes with the wavelength. We dispersed the photons detected in a spectral element in the grism spectrum into a spectral element of the prism spectrum taking account of the slit width. While the slit is located at the same position on the sky, the location on the array differs between the *NG* and *NP* modes due to the different optical alignment. We corrected for the position shift along the slit direction between the *NG* and *NP* modes and extracted the spectra at the same position (see also §4.2.2). To minimize a possible shift remaining, we compared spectra of regions that did not show particular spatial structures. Figure B.1 (a) shows the prism and simulated spectra of W49A (ID: 5200299.1) as an example of the comparison and Figure B.1 (b) plots the corresponding spectrum taken with the grism for reference. The simulated spectrum shown by the dashed line is in good agreement with the spectrum taken with the prism (solid line). Note that the grism spectrum does not provide the data needed for the both ends of the simulated spectrum and thus the deviations at the ends come partly from the insufficient data for the simulation. The band emission in the simulated spectrum reproduces that seen in the prism spectrum fairly well, confirming that the relative calibration between the prism and grism spectra is within the given uncertainty and assuring that the software simulates the prism spectrum reliably. There is a small systematic difference in the continuum level and the simulated spectrum is slightly brighter than the actual prism spectrum particularly around 4.7–4.9 μm. It may come from the residual in the dark current correction, but does not affect the band profile.

Based upon the above result, we fitted the prism spectra with the simulated spectral profiles of each component (see details in §4.3.2). By this technique, we estimated the intensity of the hydrogen recombination line Pfβ at 4.65 μm from the prism spectra, which is in good agreement with the results of the spectral fitting to the grism spectra (see Figure B.2). This fact establishes the validity of our fitting method, and also confirms the accuracy of the absolute flux calibration of the *AKARI*/IRC at NIR wavelengths.

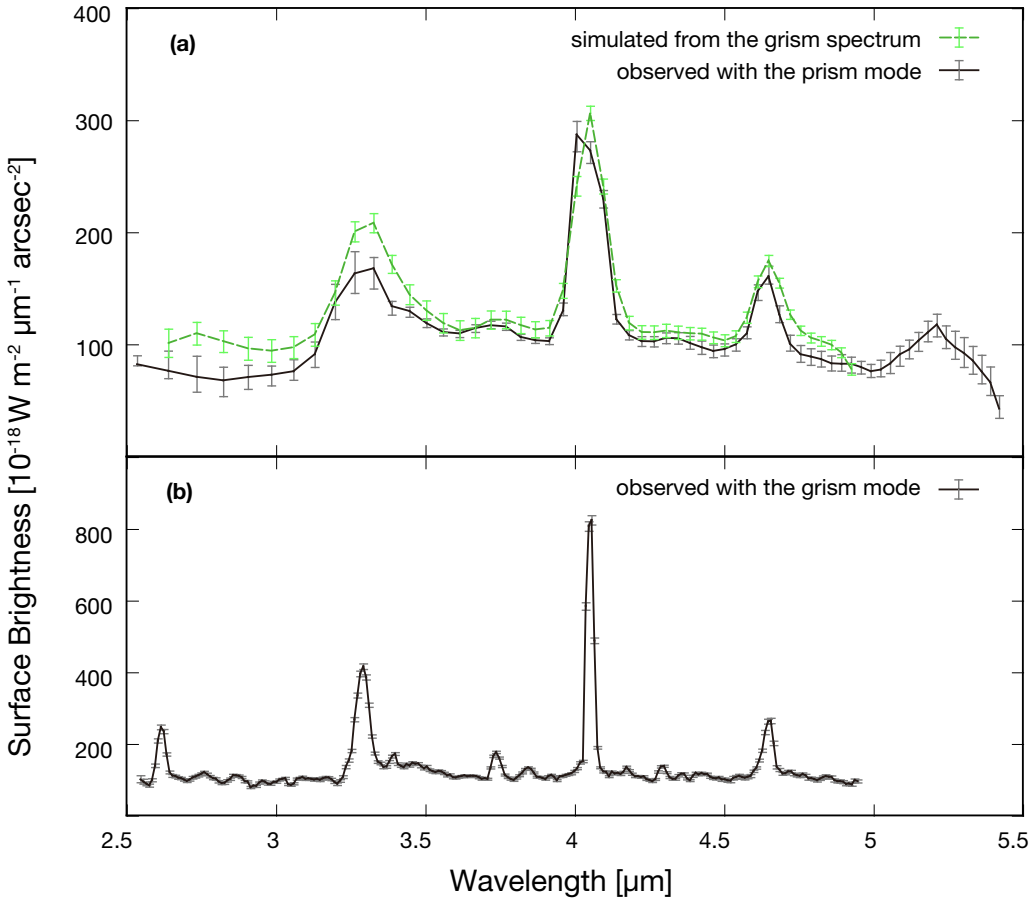

Figure B.1: **(a)** Example of the comparison of the prism spectrum (black solid line) and the simulated spectrum (green dashed line). The corresponding grism spectrum is shown in the lower panel **(b)**. The spectra are those taken towards W49A (ID: 5200299.1).

See Ohyama et al. (2007) and Baba et al. (2015) for details of wavelength calibration of *AKARI*/IRC slit spectroscopy.

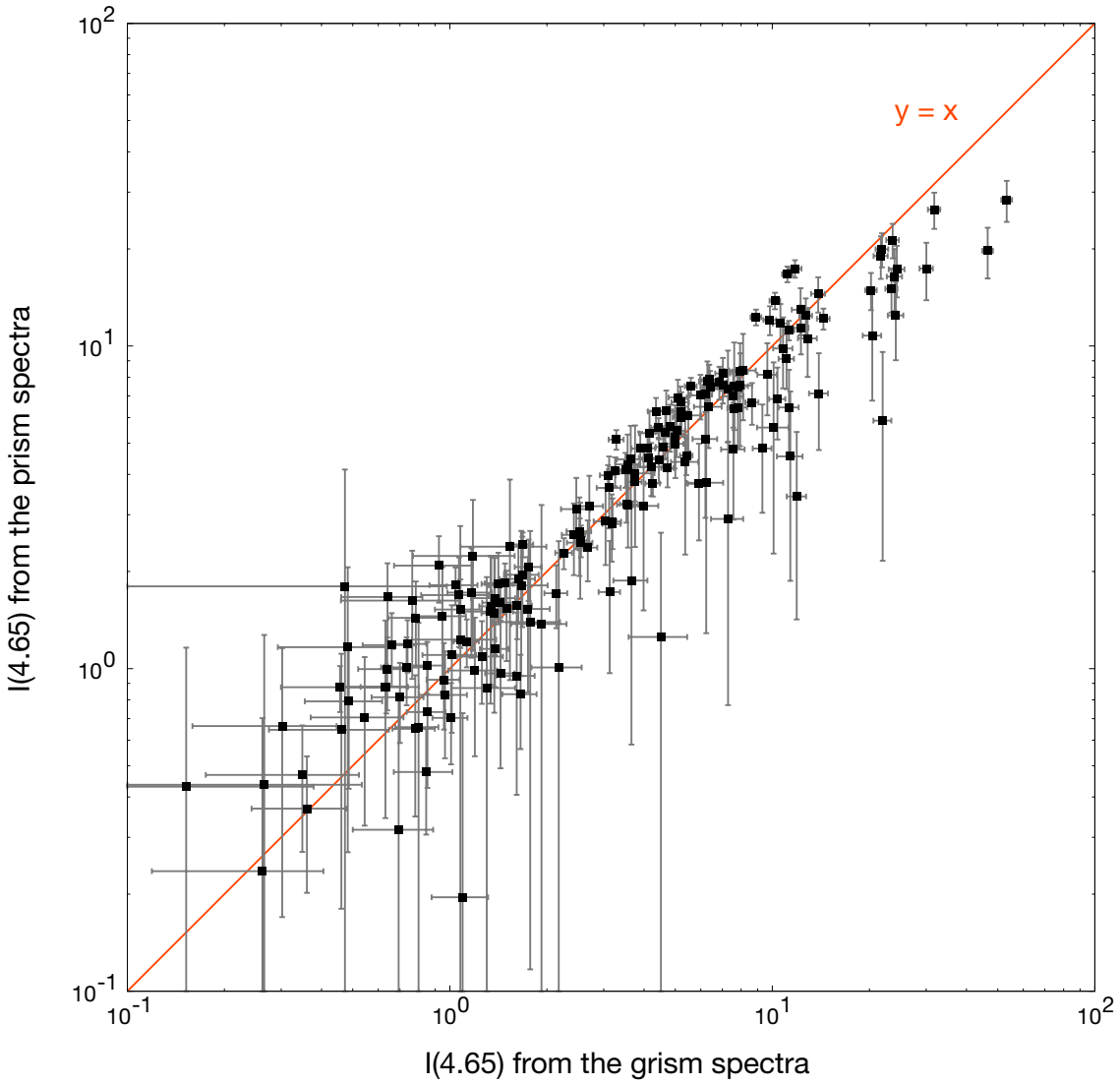

Figure B.2: Plot of the intensity of the hydrogen recombination line Pfβ at 4.65 μm measured from the prism spectra by the spectral fitting described in §4.3.2, against that of the grism spectra. We exclude those which exhibit a serious effect of saturation around the peak of Pfβ from the plot.

Appendix C

Gallery of the grism and prism spectra and S9W images of galactic H II regions

Figure C.1 summarizes the *AKARI*/IRC NIR grism and prism spectra and *S9W* band images of the galactic H II regions presented in Chapter 4.

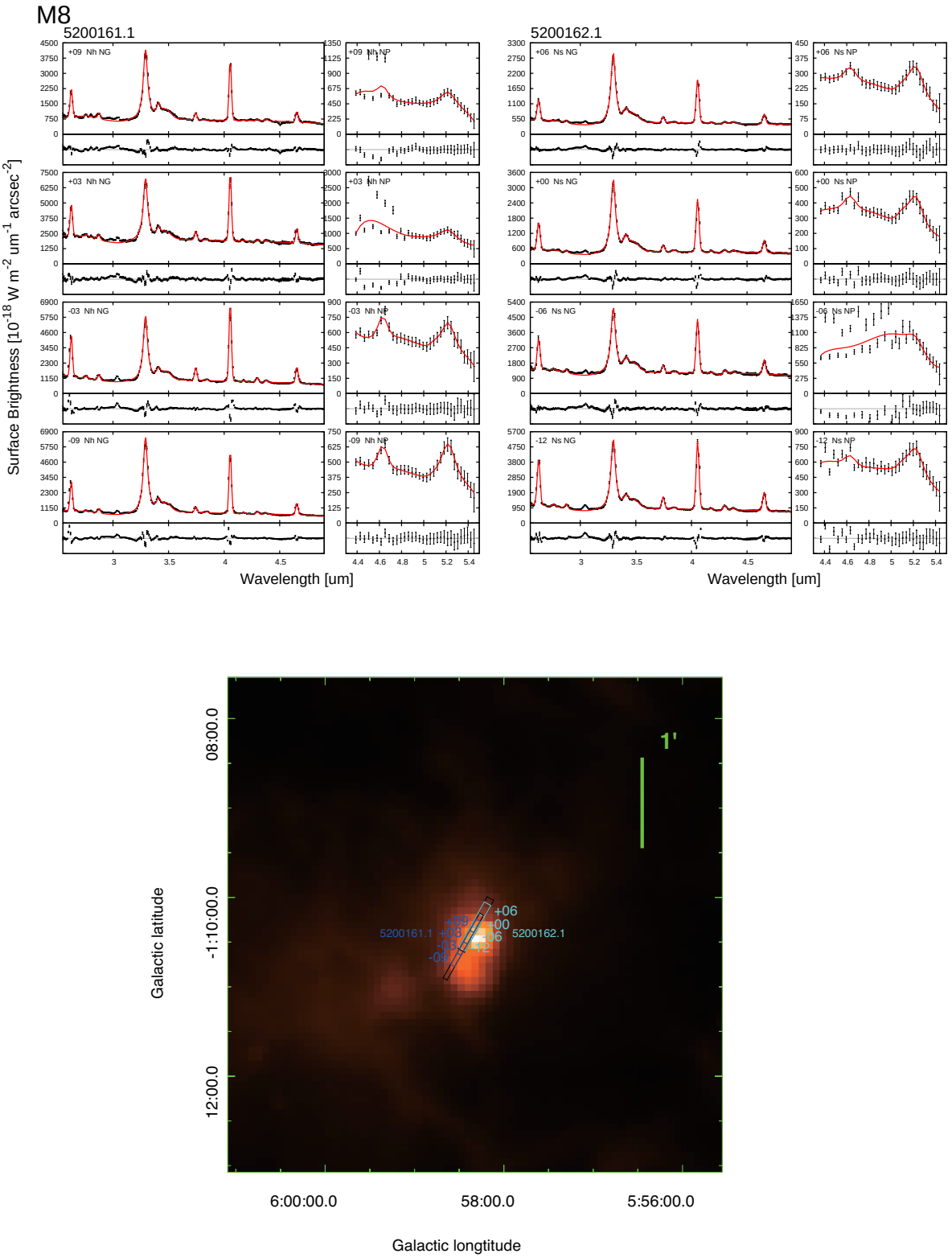

Figure C.1: List of the *AKARI*/IRC NIR grism and prism spectra and *S9W* band images of the galactic H II regions presented in Chapter 4. *(Lower)* The *S9W* band image of the target. In the spectra analysis, we extracted a spectrum from the length of 6 pixels one by one. On the *S9W* image each position is designated by a blue box with a corresponding position number within a slit area indicated by a black box. *(Upper)* The best-fit model for each spectrum is designated by the red solid line, overlain on the observed one. The lower panel at each plot demonstrates the residual spectrum of the best-fit. The grism spectra are displayed in the left panels, while the prism spectra in the right panels. For each pointed observation, the pointing ID is labeled at the upper left of the figures. The position number inside the slit, the kind of the slit ("Ns" or "Nh"), and the kind of the NIR disperser ("NG"; the grism or "NP"; the prism) are described at the upper left inside each plot. The region from which we extracted the spectra are indicated by blue boxes with the position number on the *S9W* images.

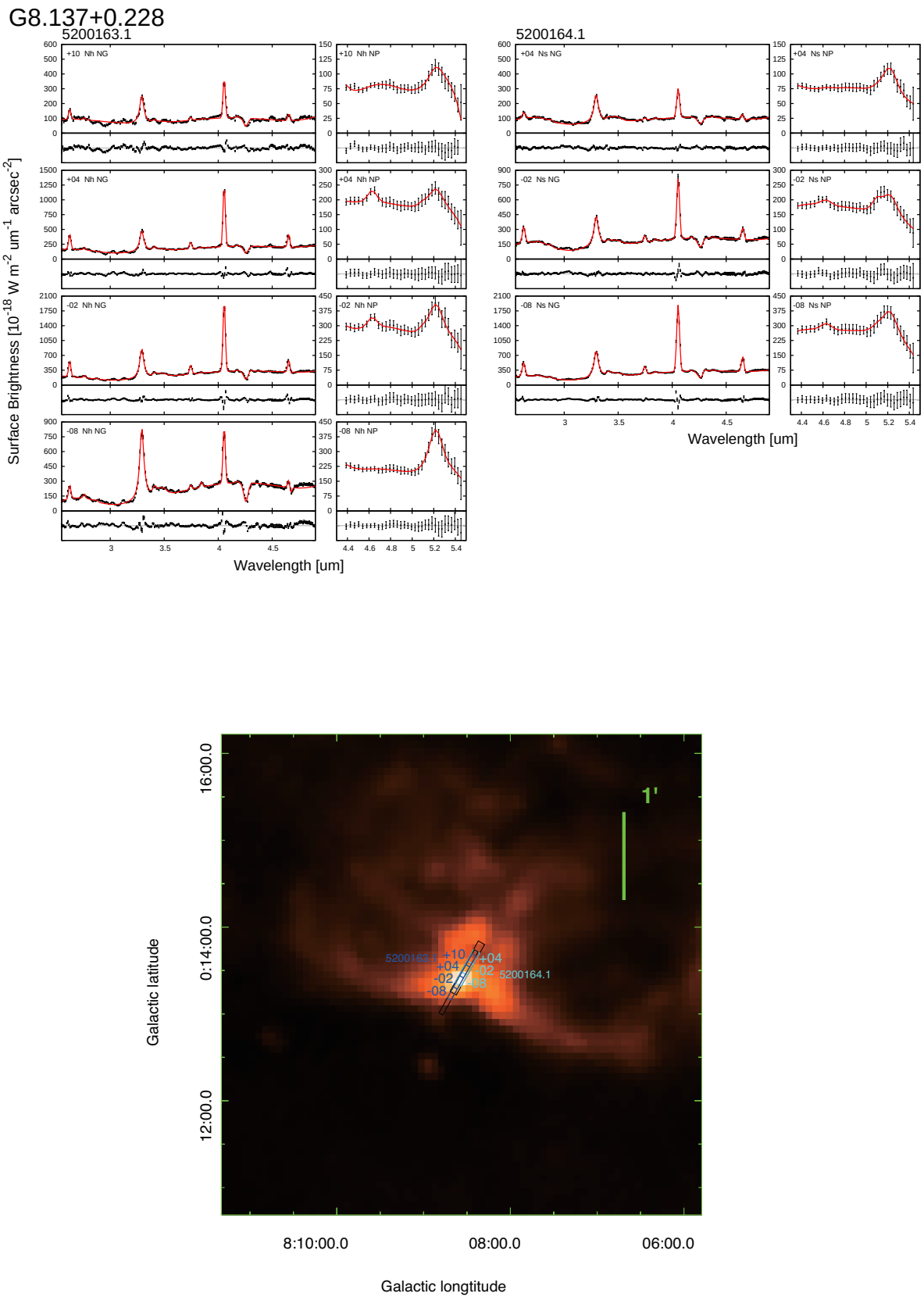

Figure C.1: *Continued.*

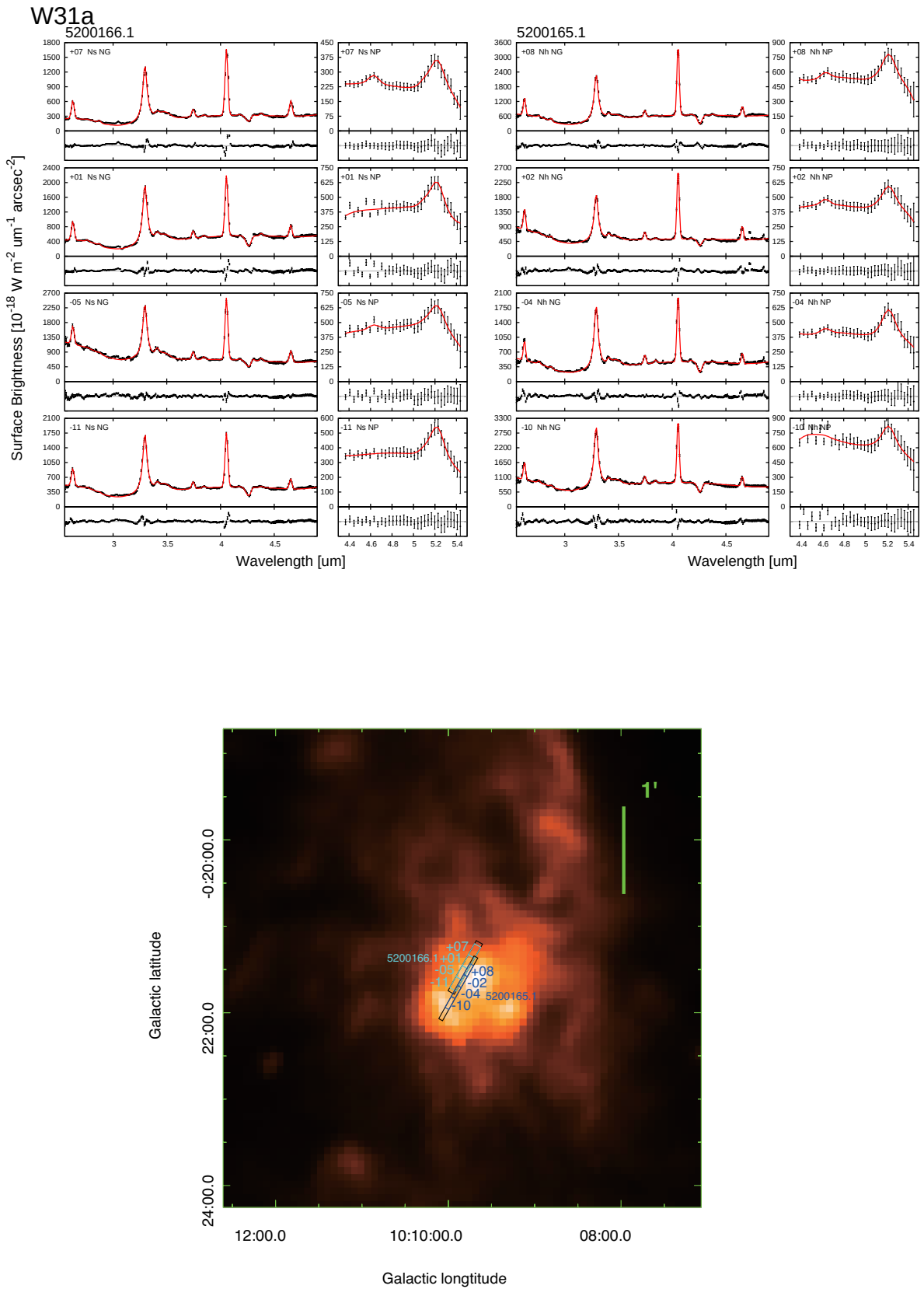

Figure C.1: *Continued.*

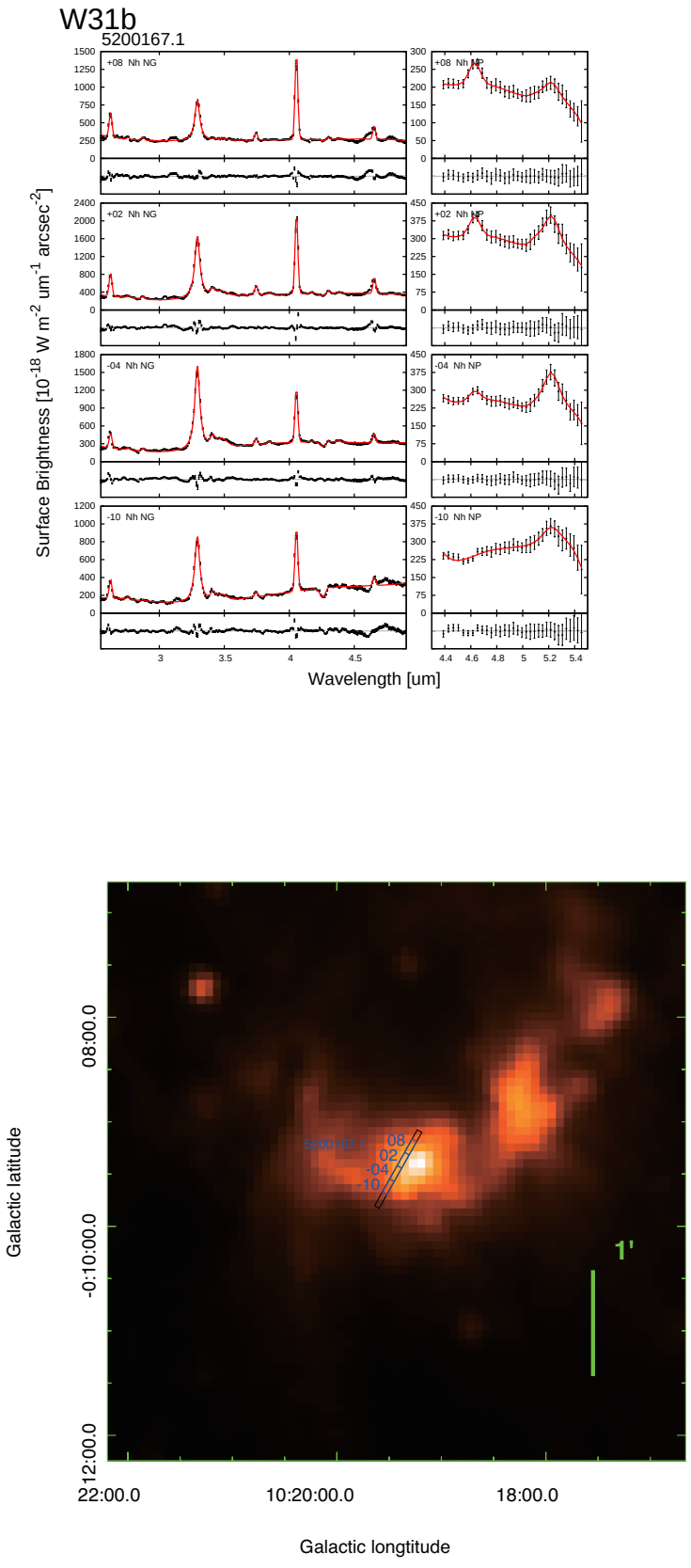

Figure C.1: *Continued.*

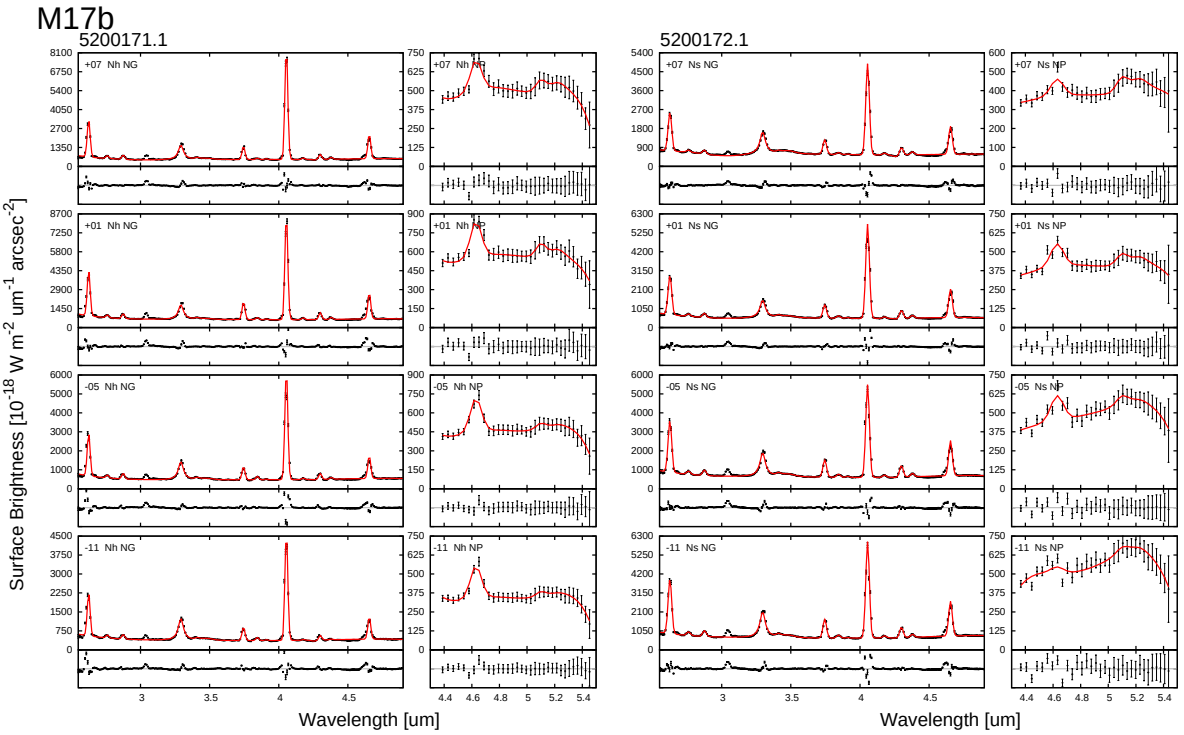

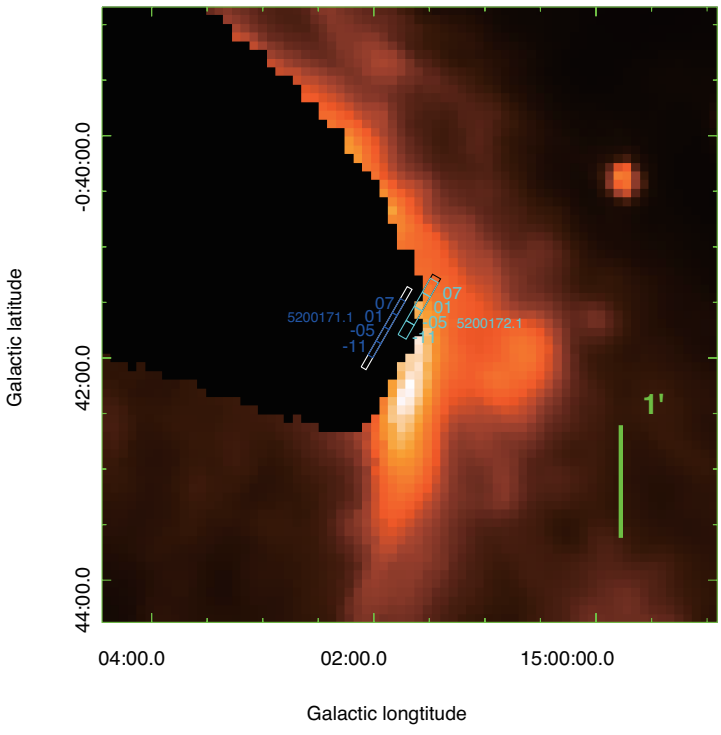

Figure C.1: *Continued.*

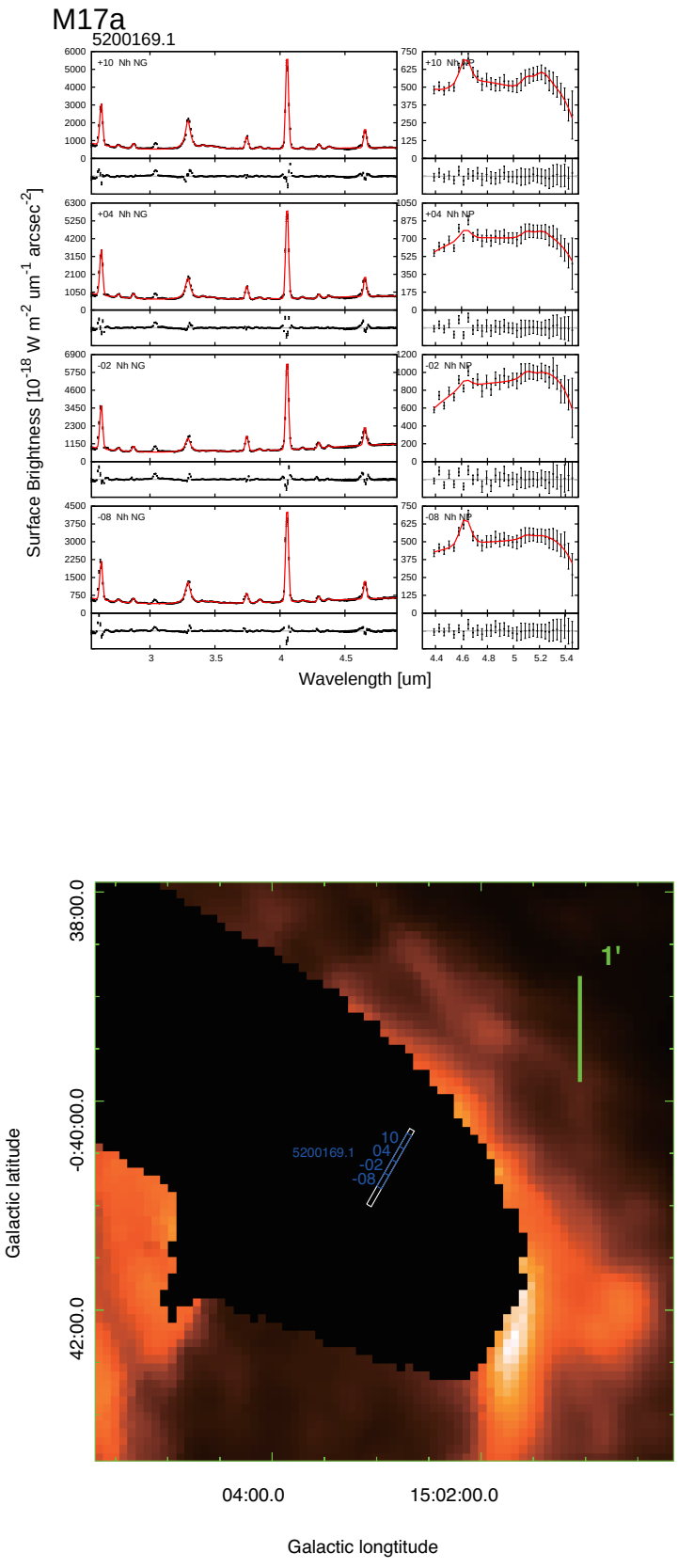

Figure C.1: *Continued.*

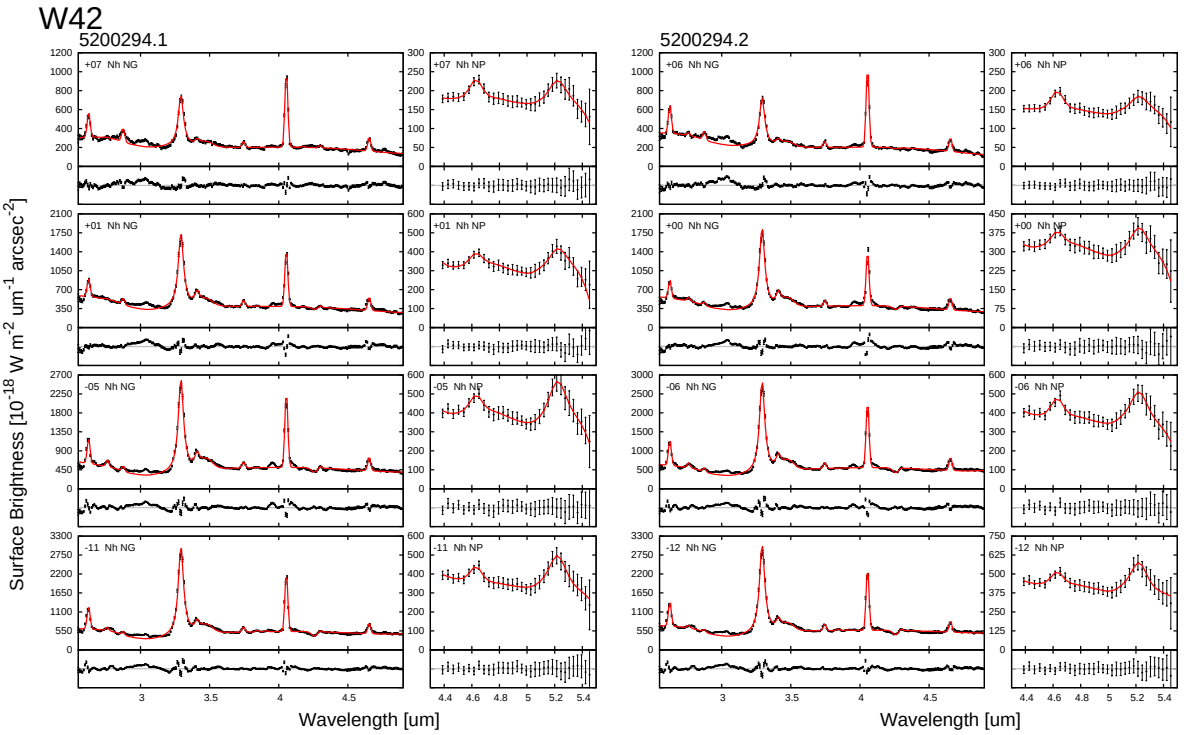

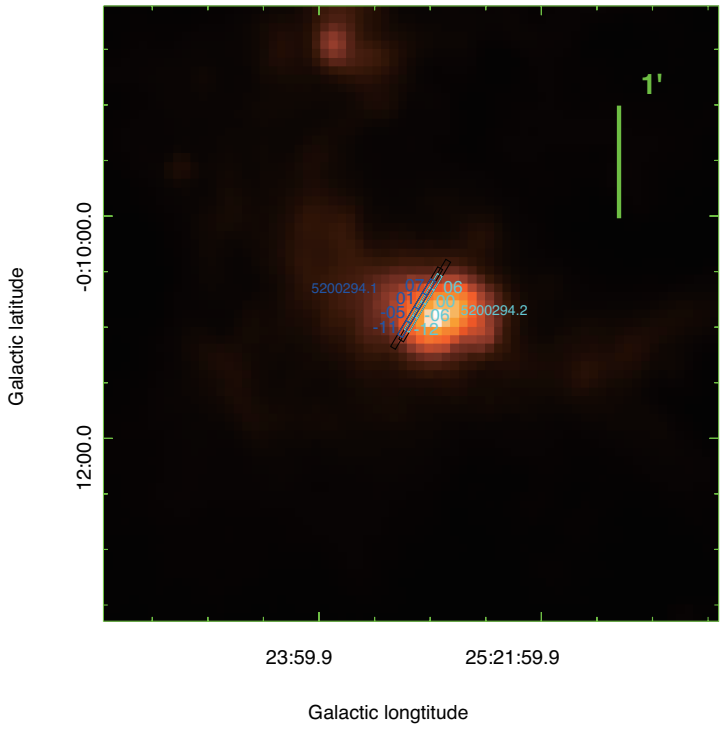

Figure C.1: *Continued.*

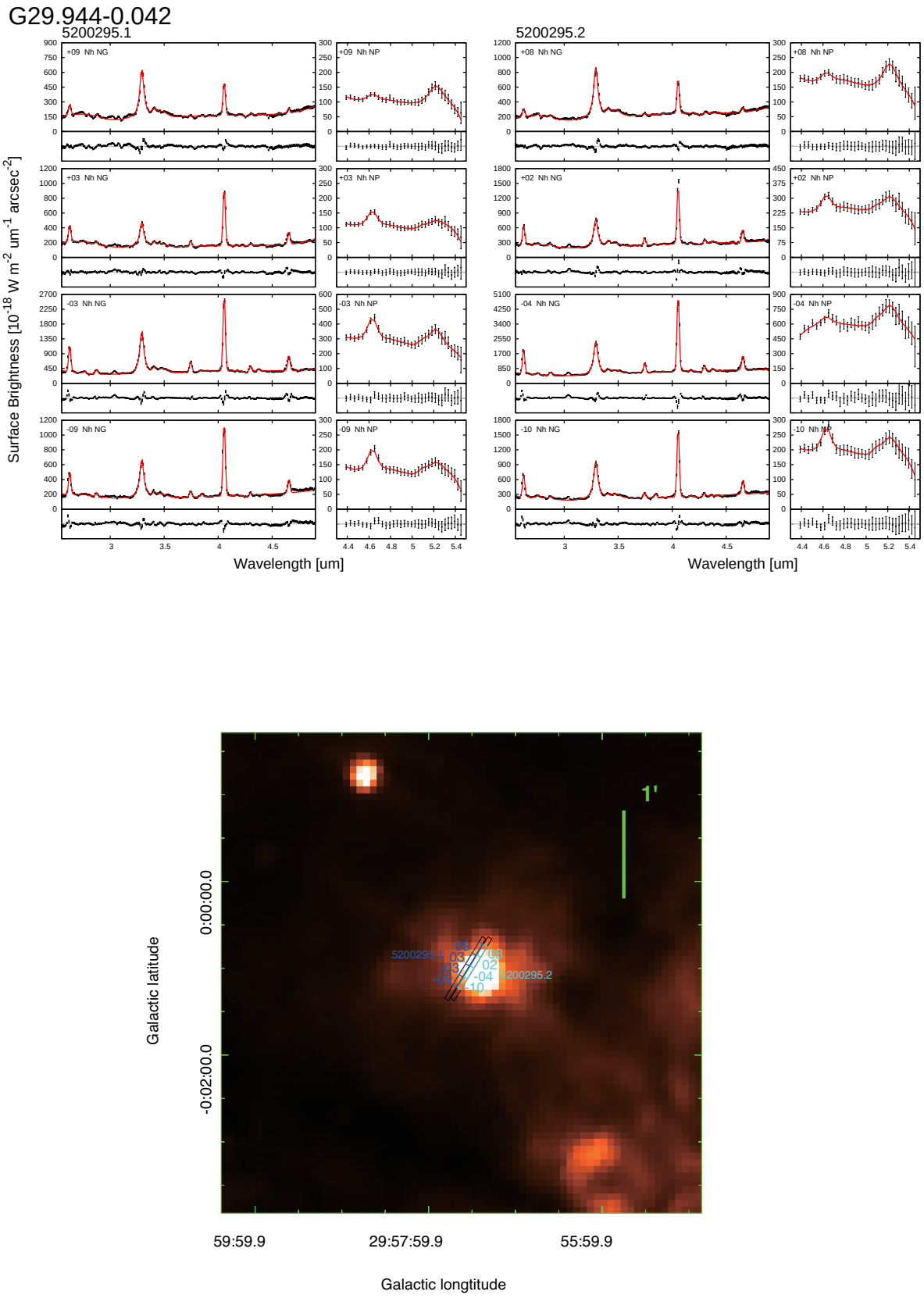

Figure C.1: *Continued.*

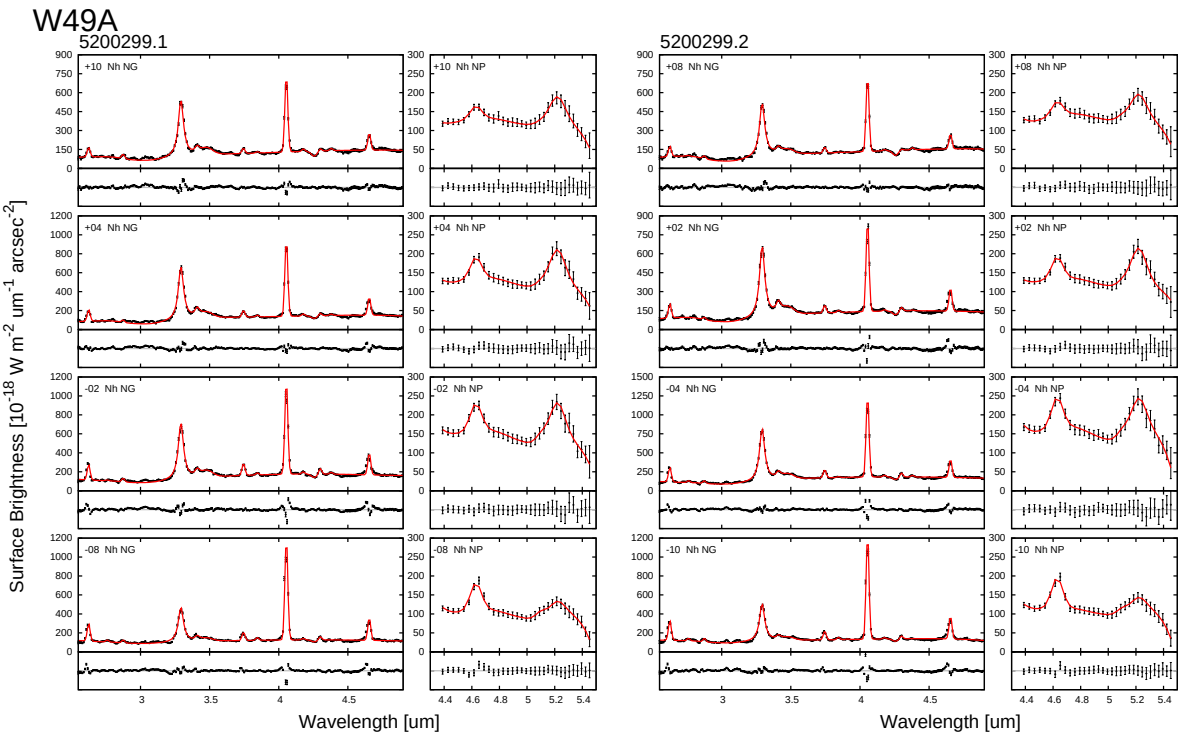

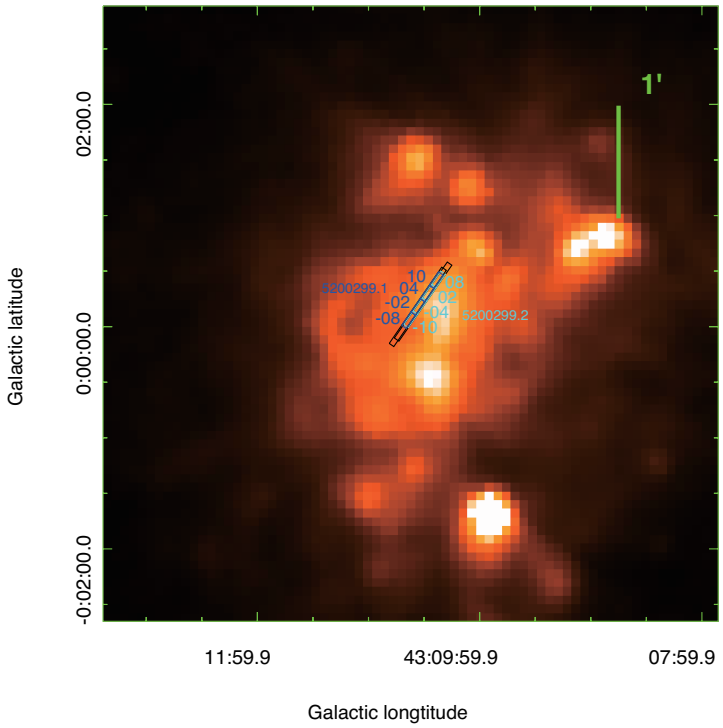

Figure C.1: *Continued.*

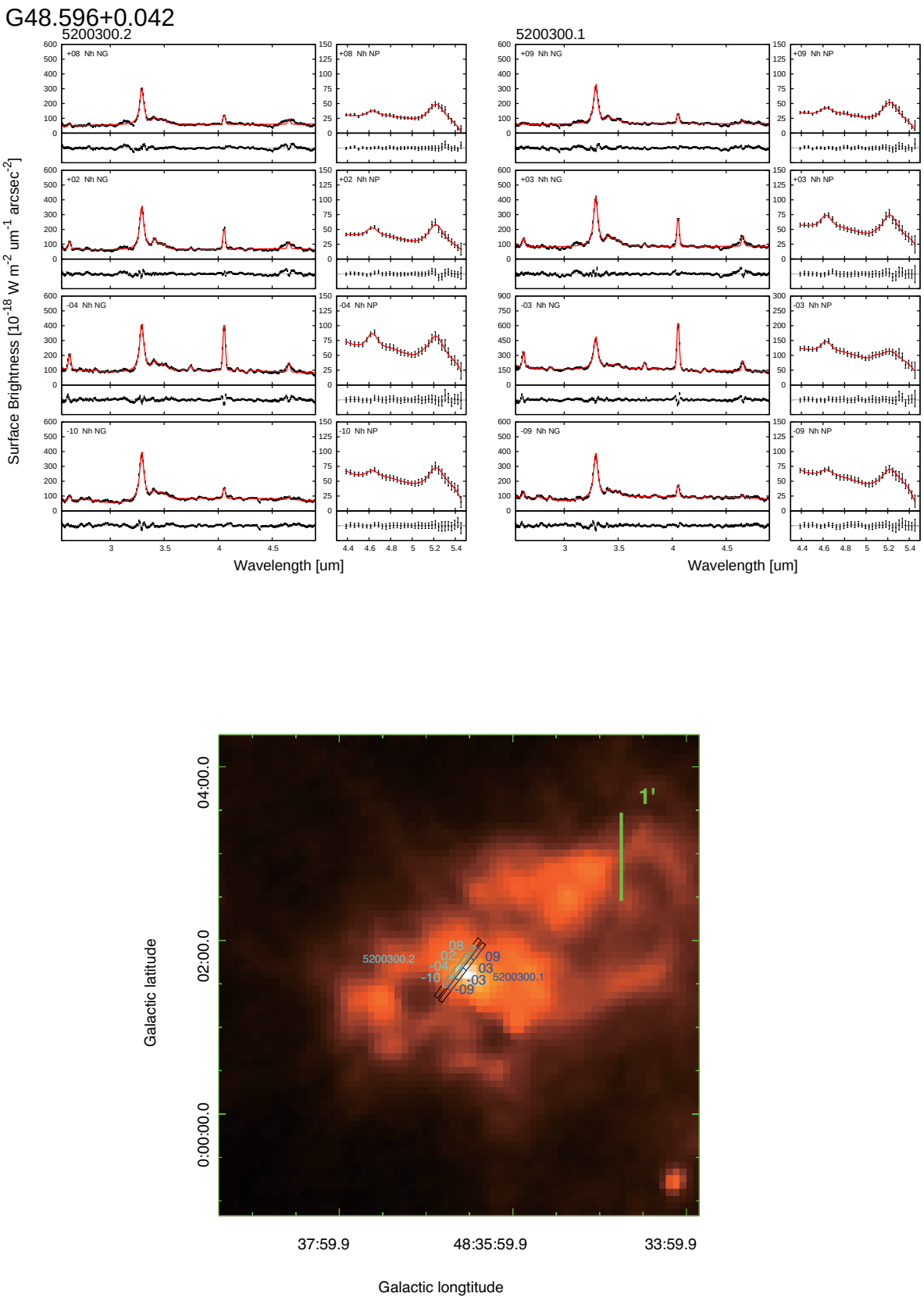

Figure C.1: *Continued.*

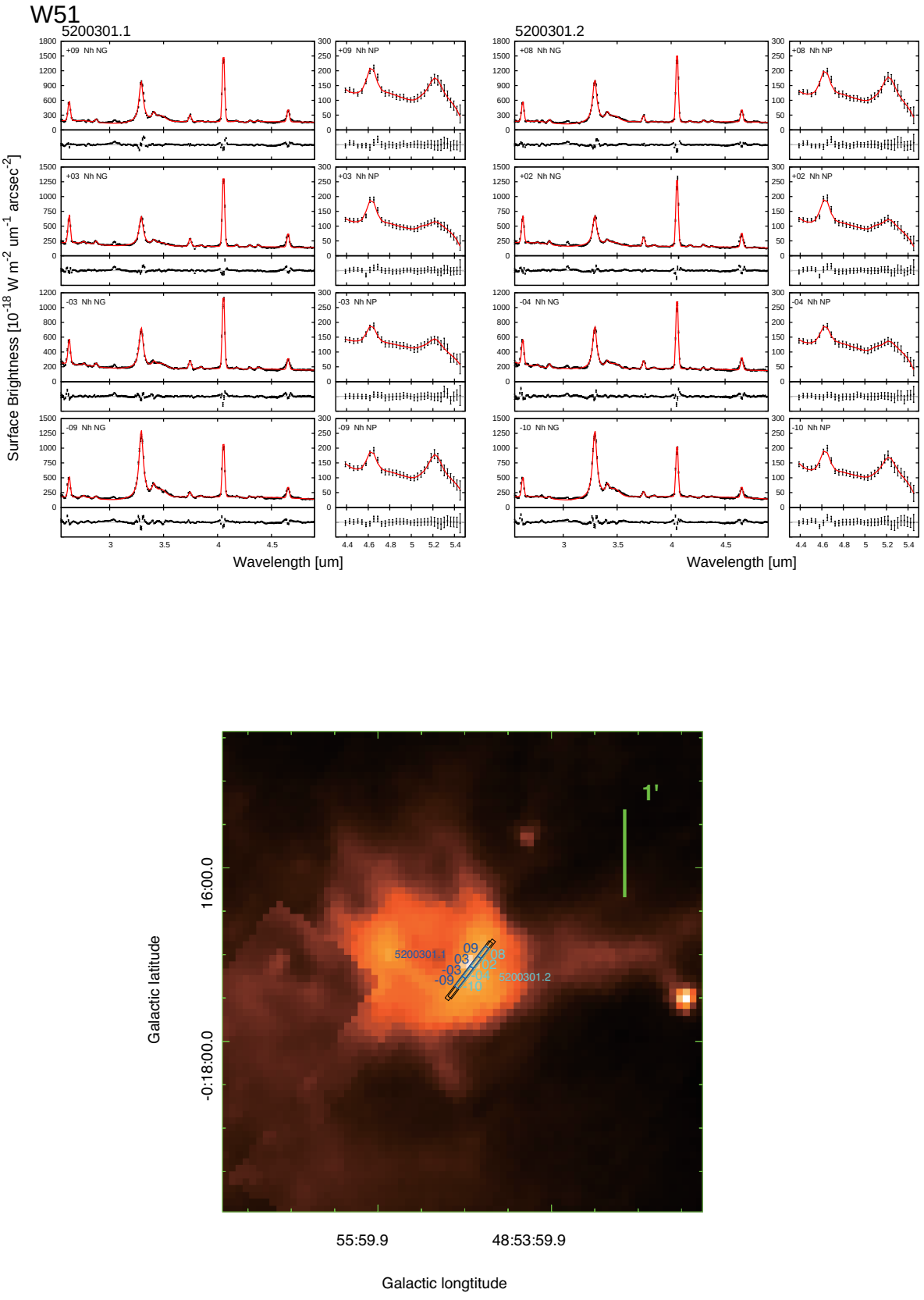

Figure C.1: *Continued.*

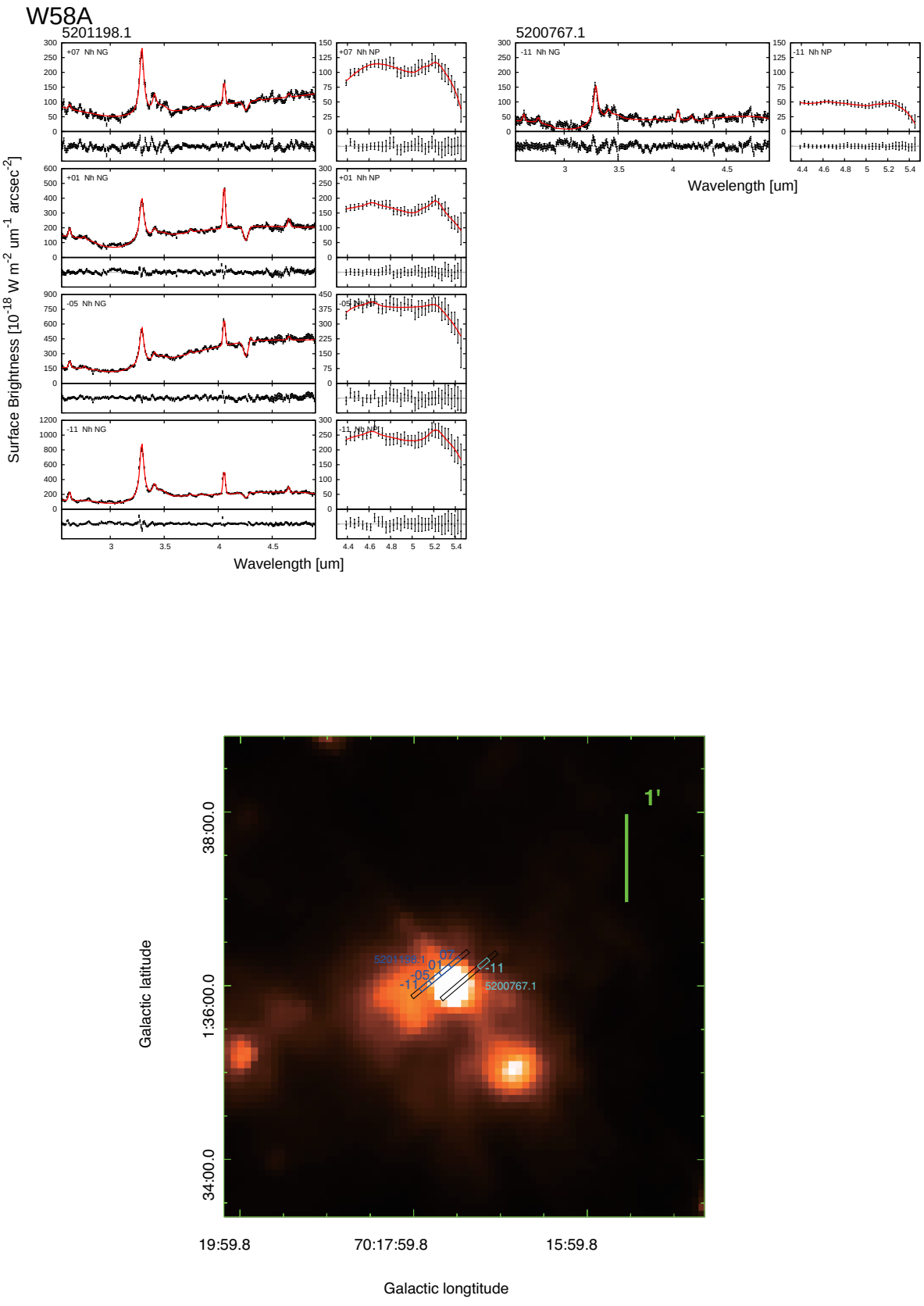

Figure C.1: *Continued.*

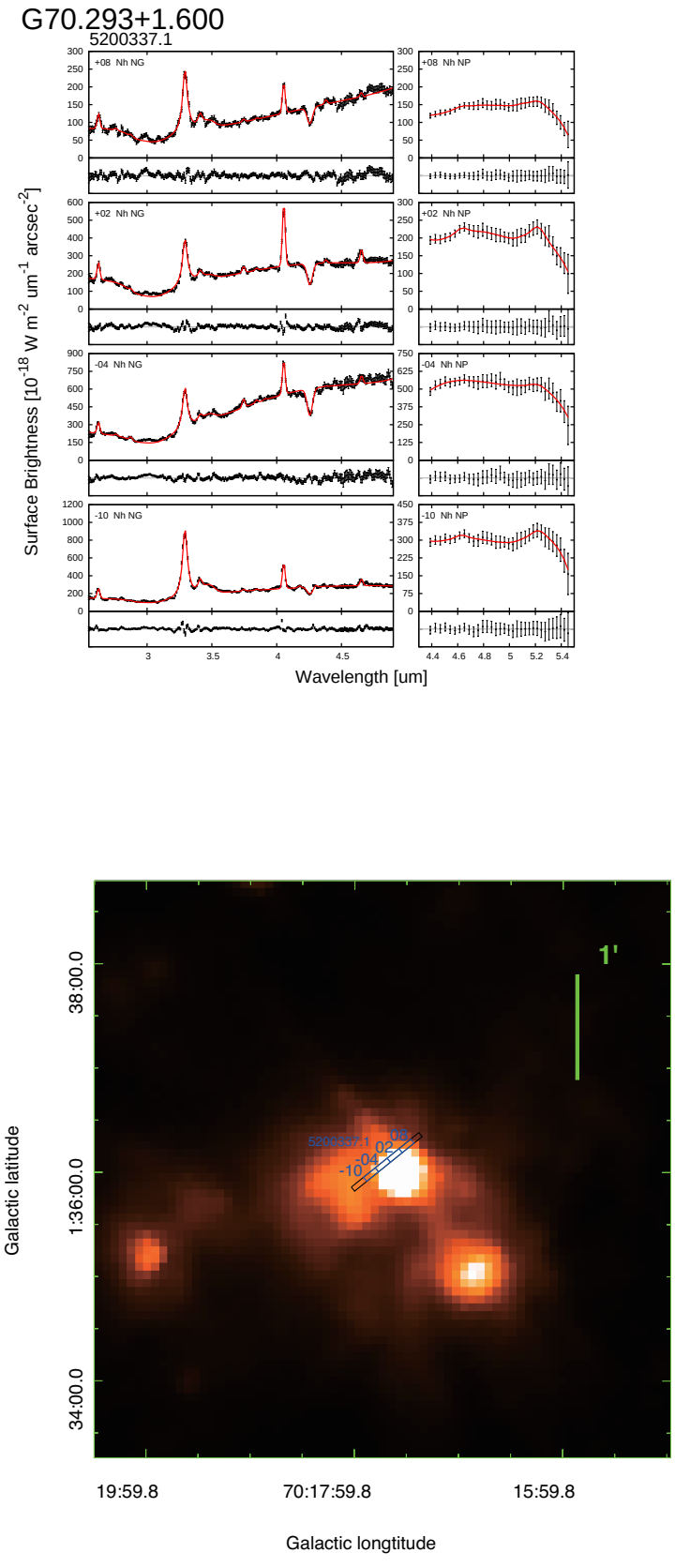

Figure C.1: *Continued.*

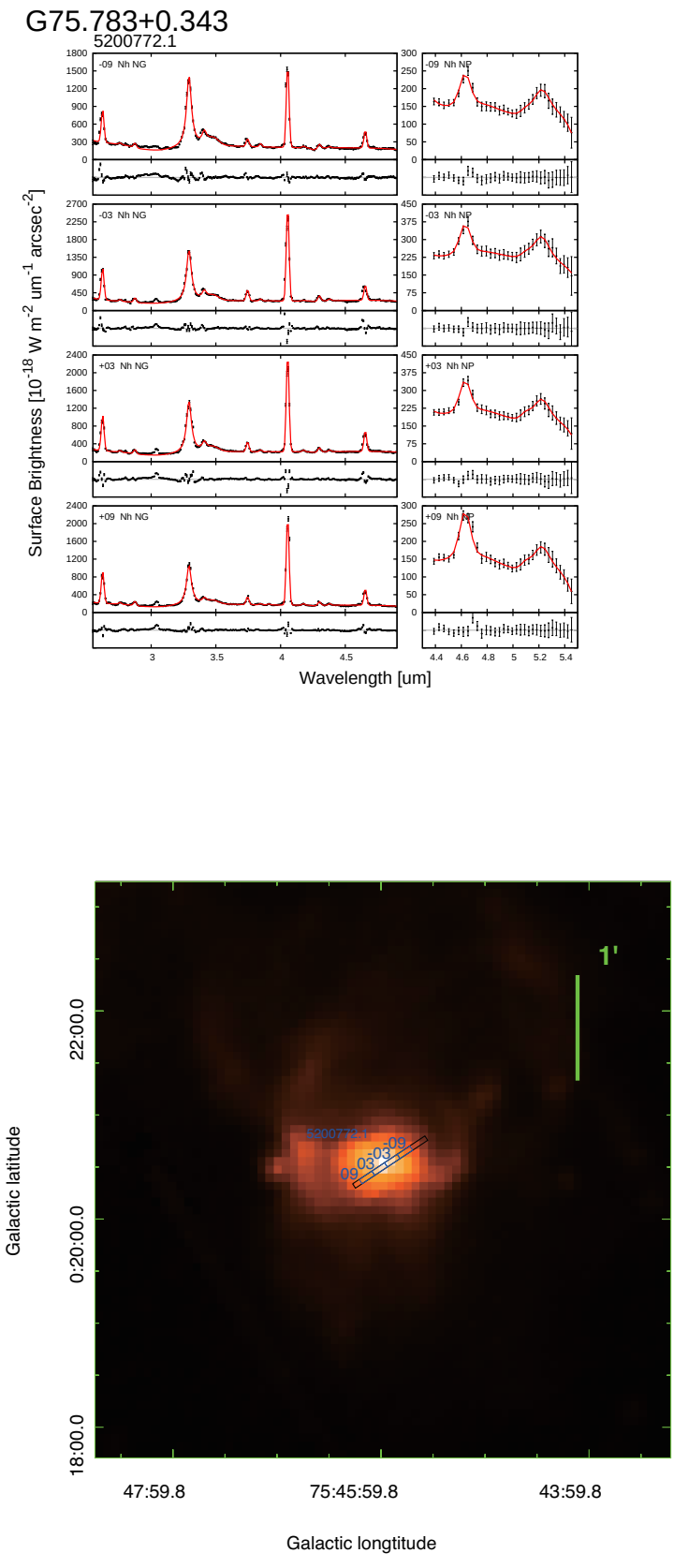

Figure C.1: *Continued.*

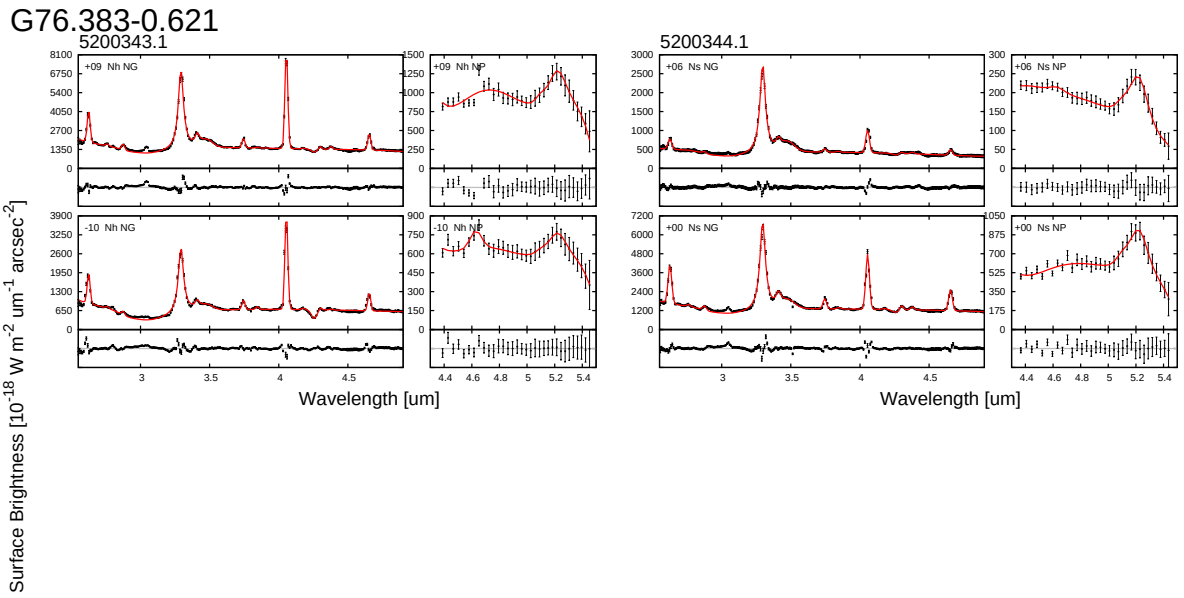

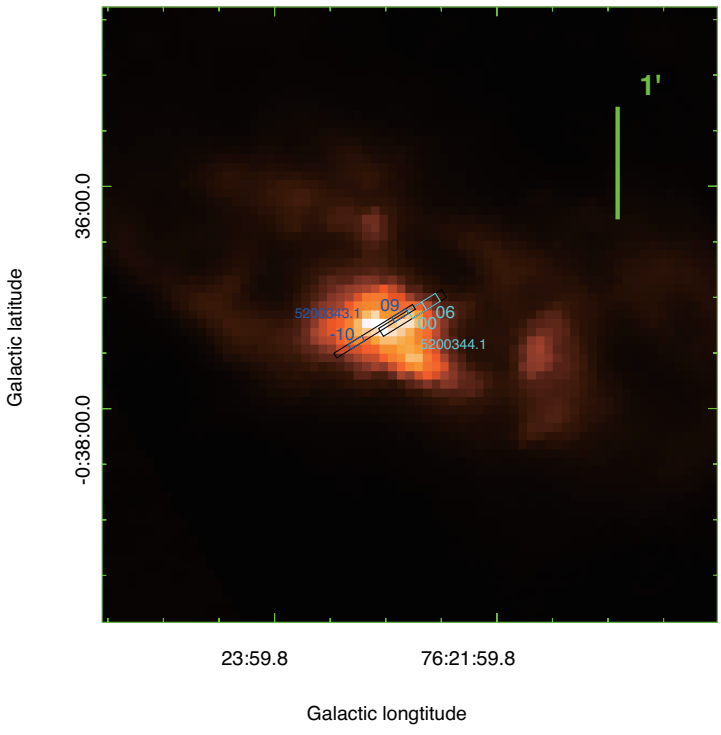

Figure C.1: *Continued.*

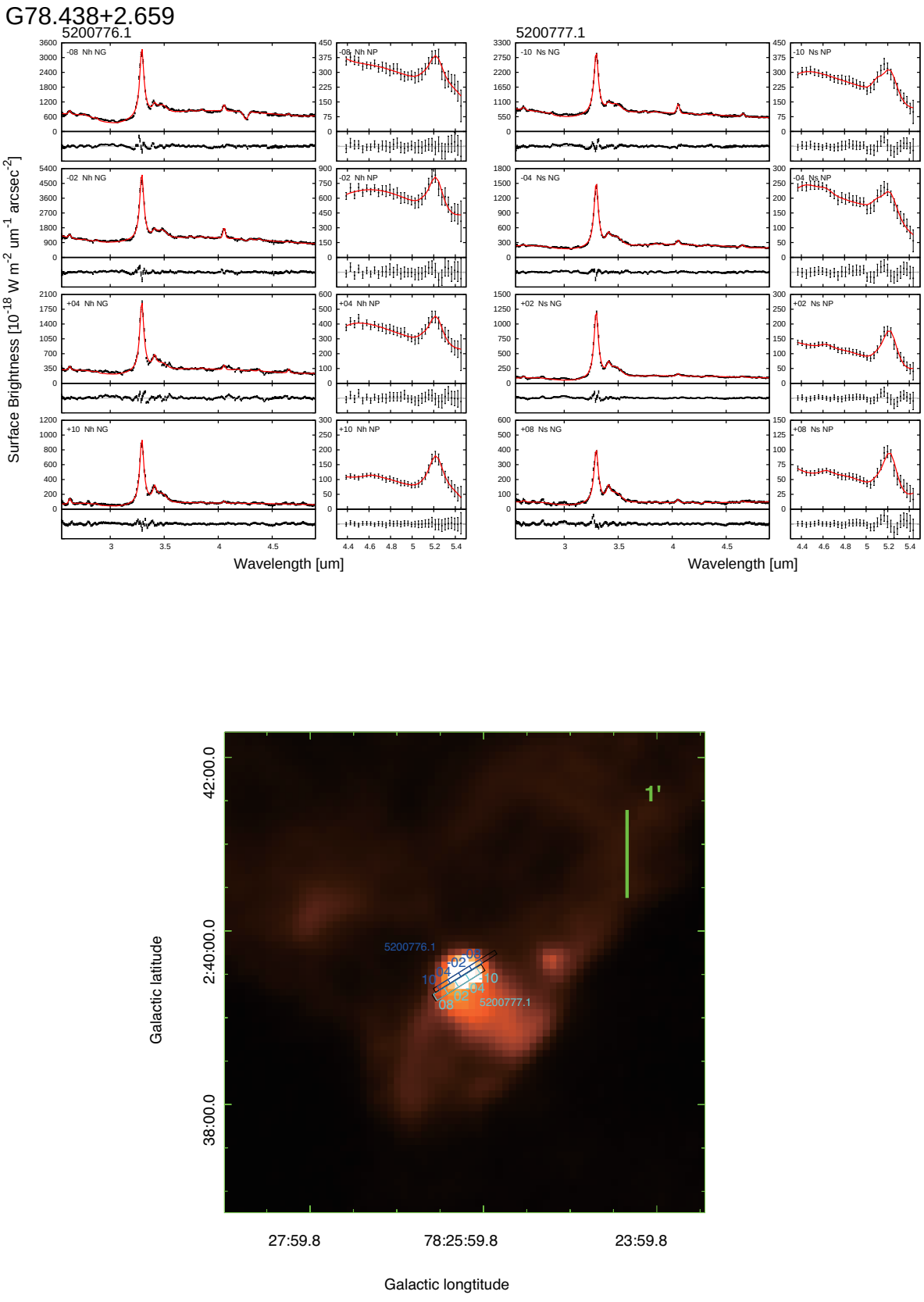

Figure C.1: *Continued.*

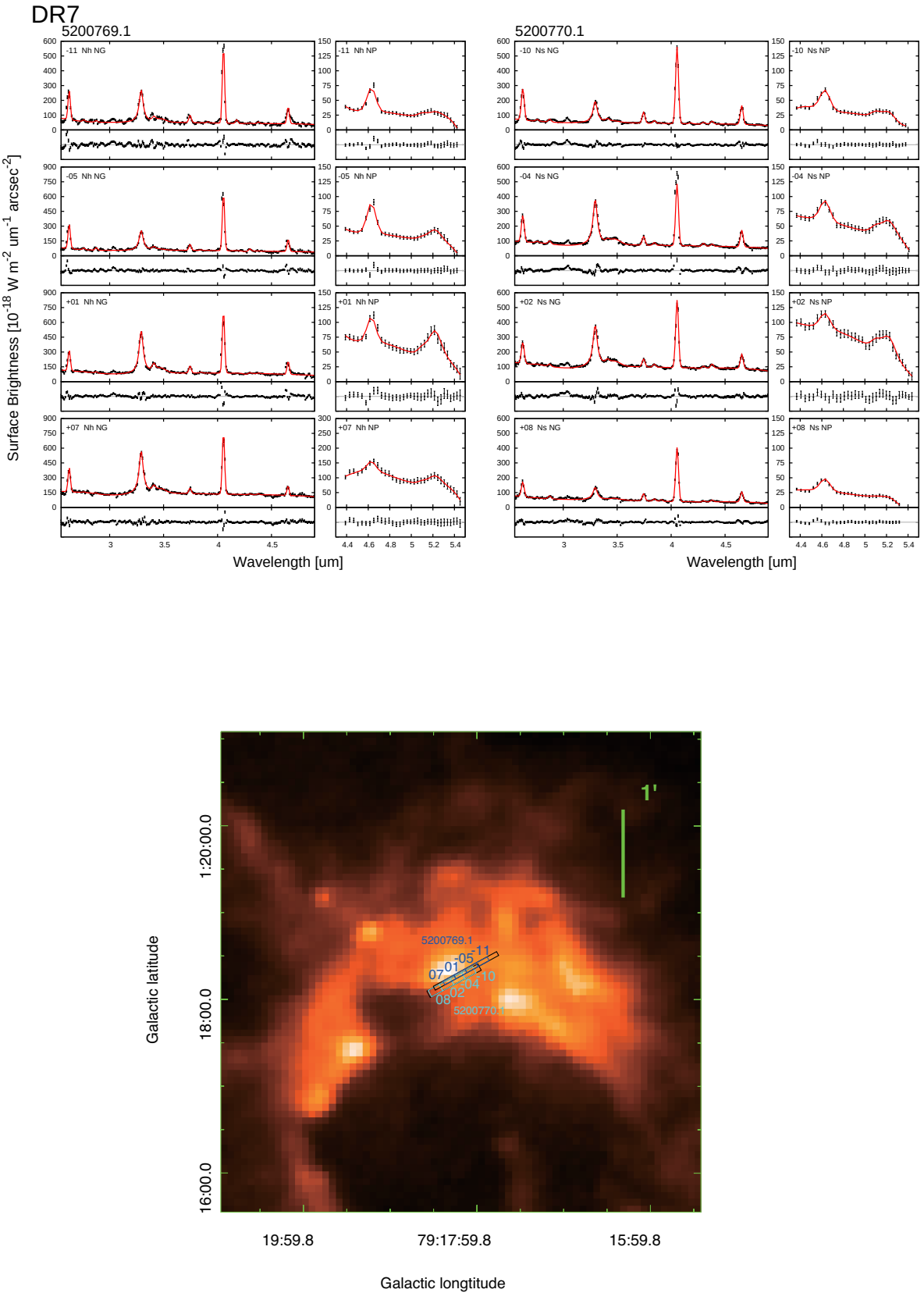

Figure C.1: *Continued.*

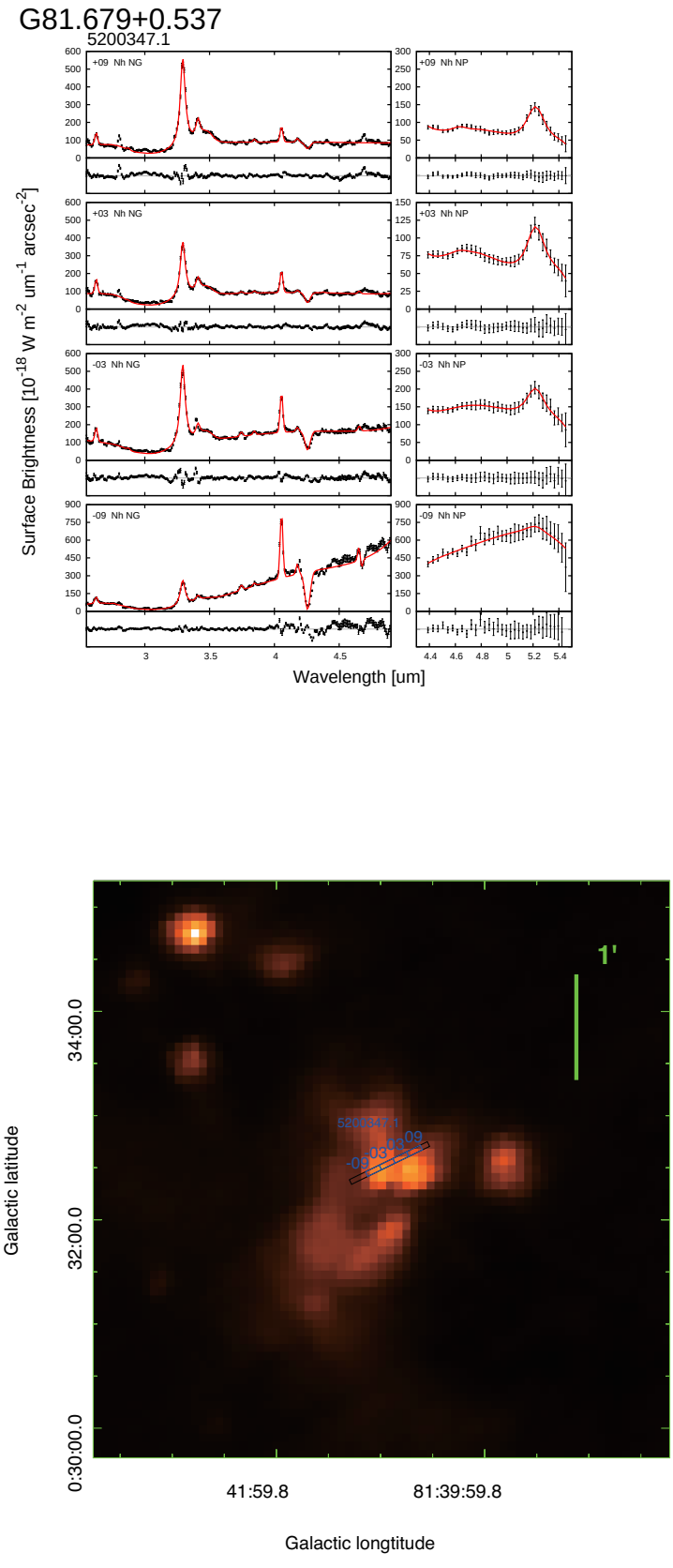

Figure C.1: *Continued.*

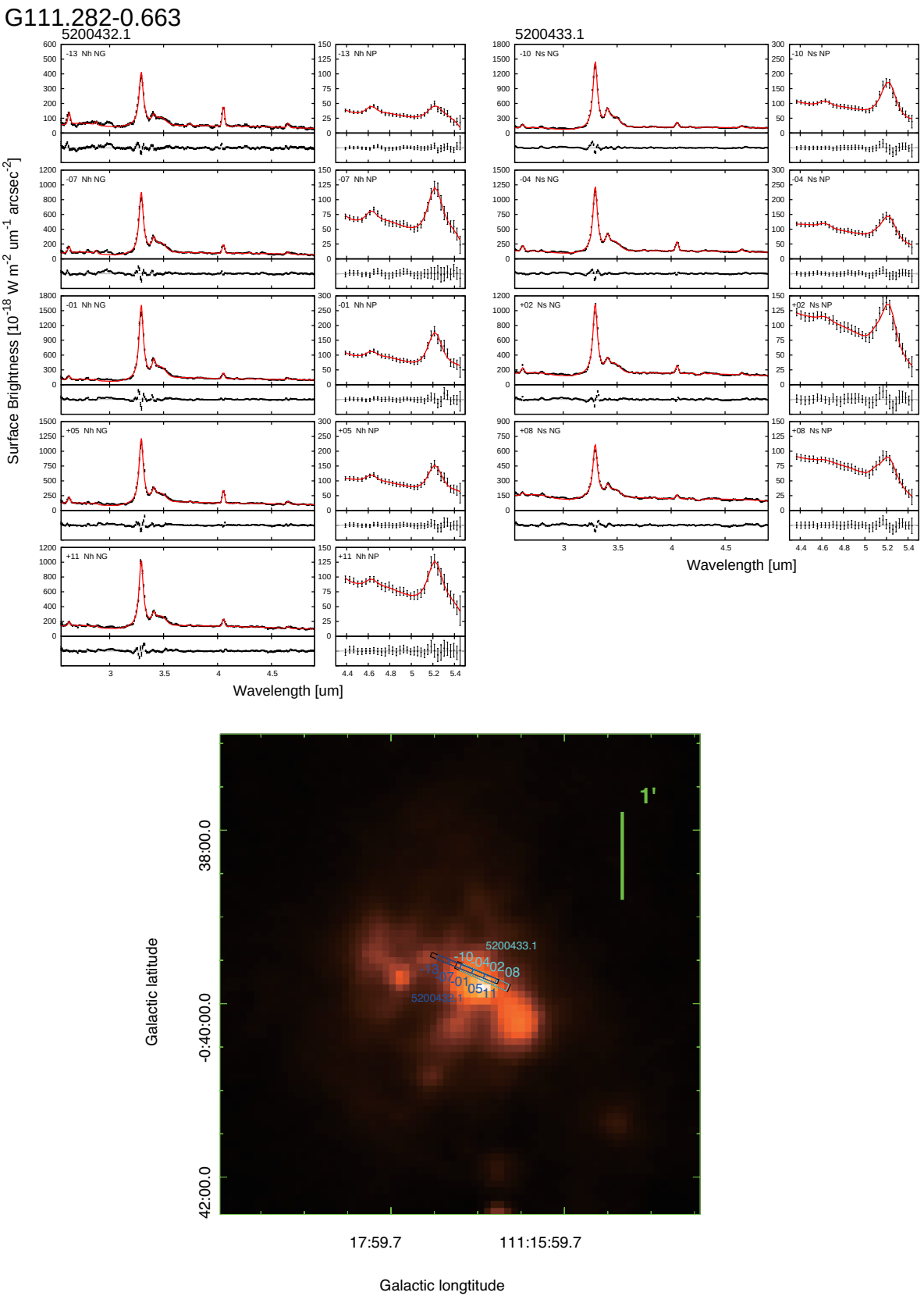

Figure C.1: *Continued.*

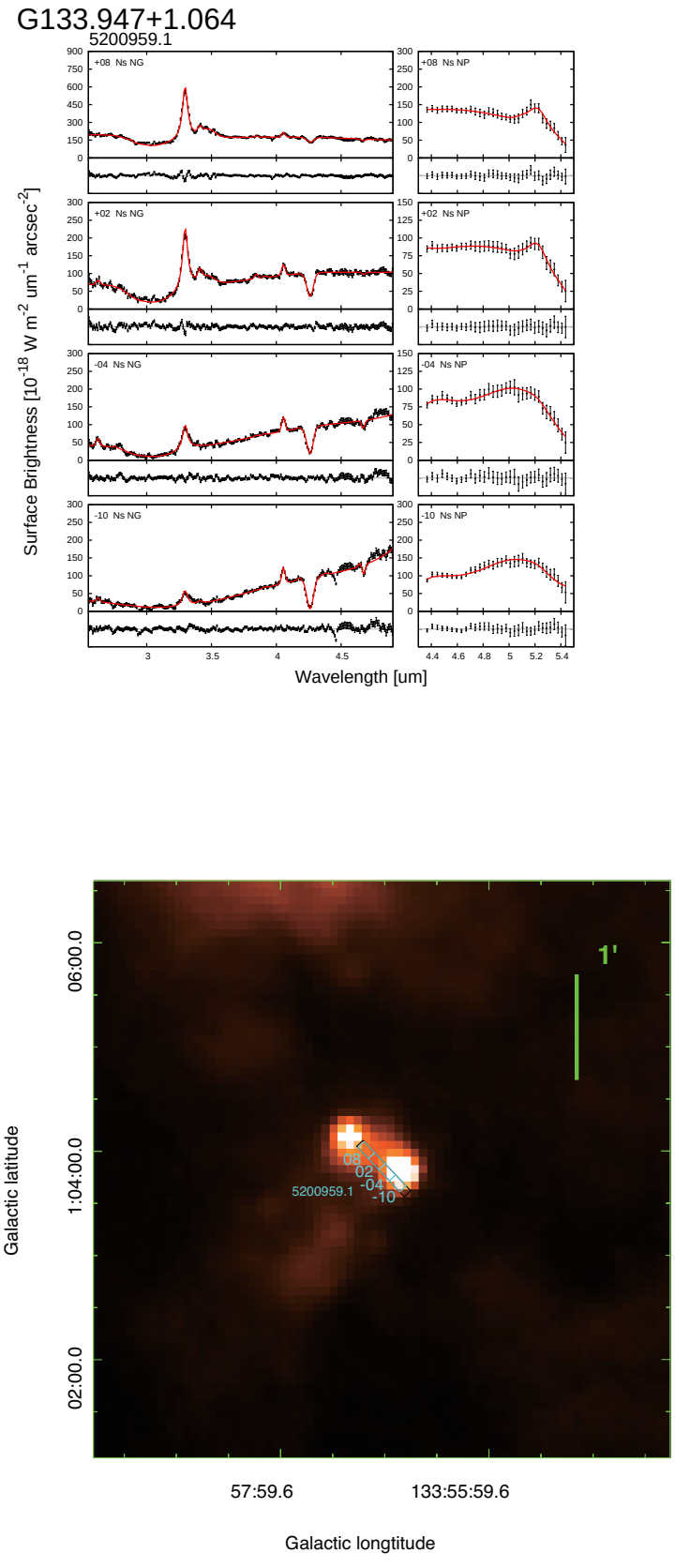

Figure C.1: *Continued.*

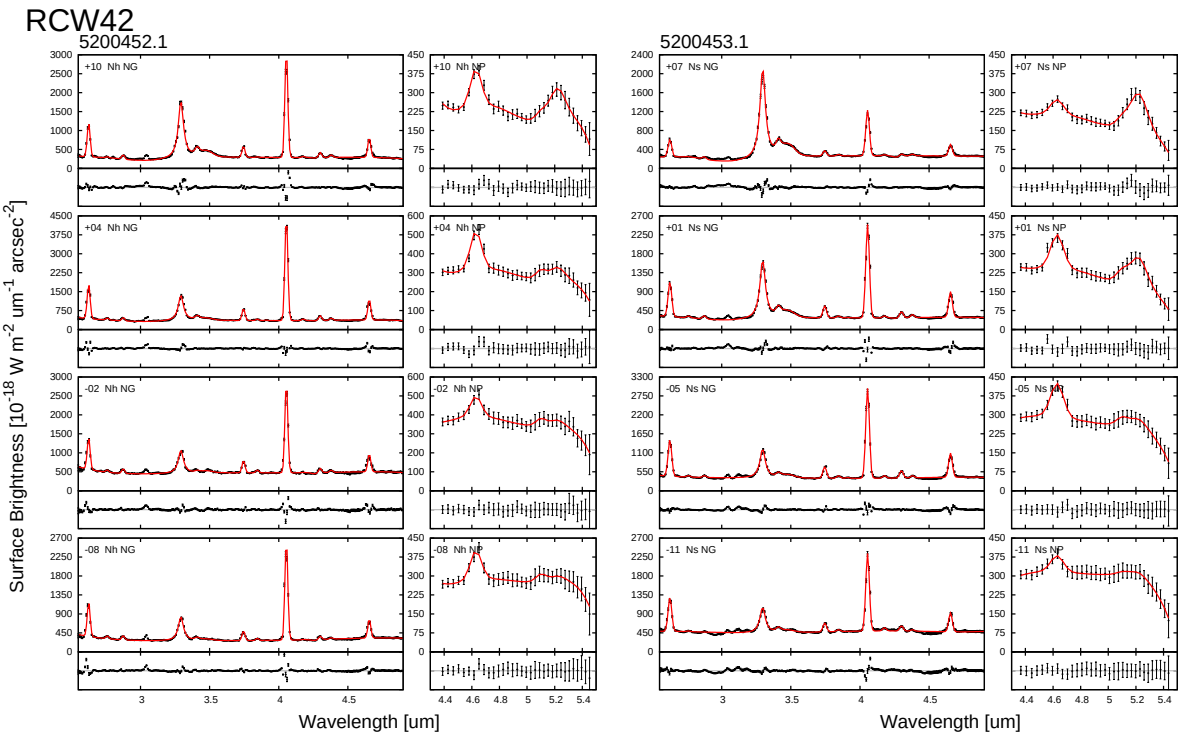

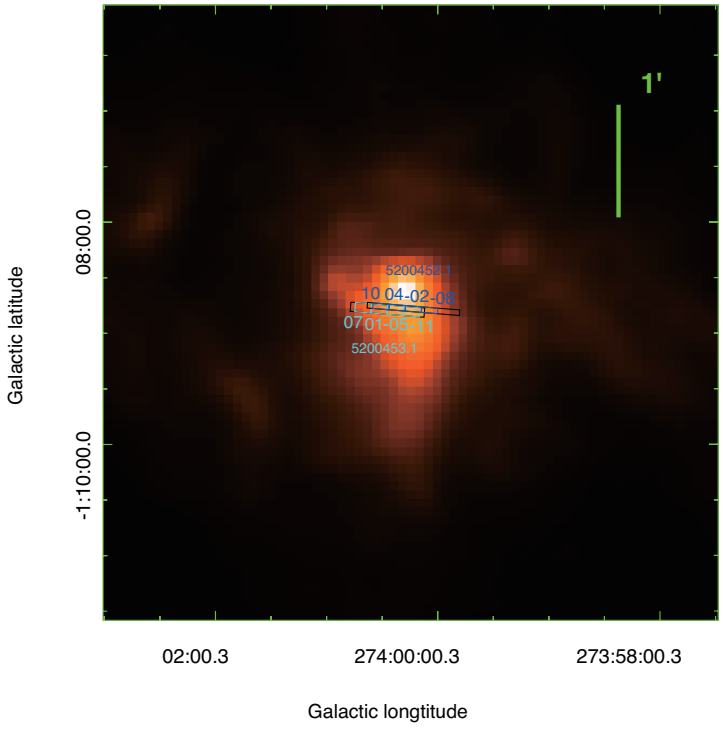

Figure C.1: *Continued.*

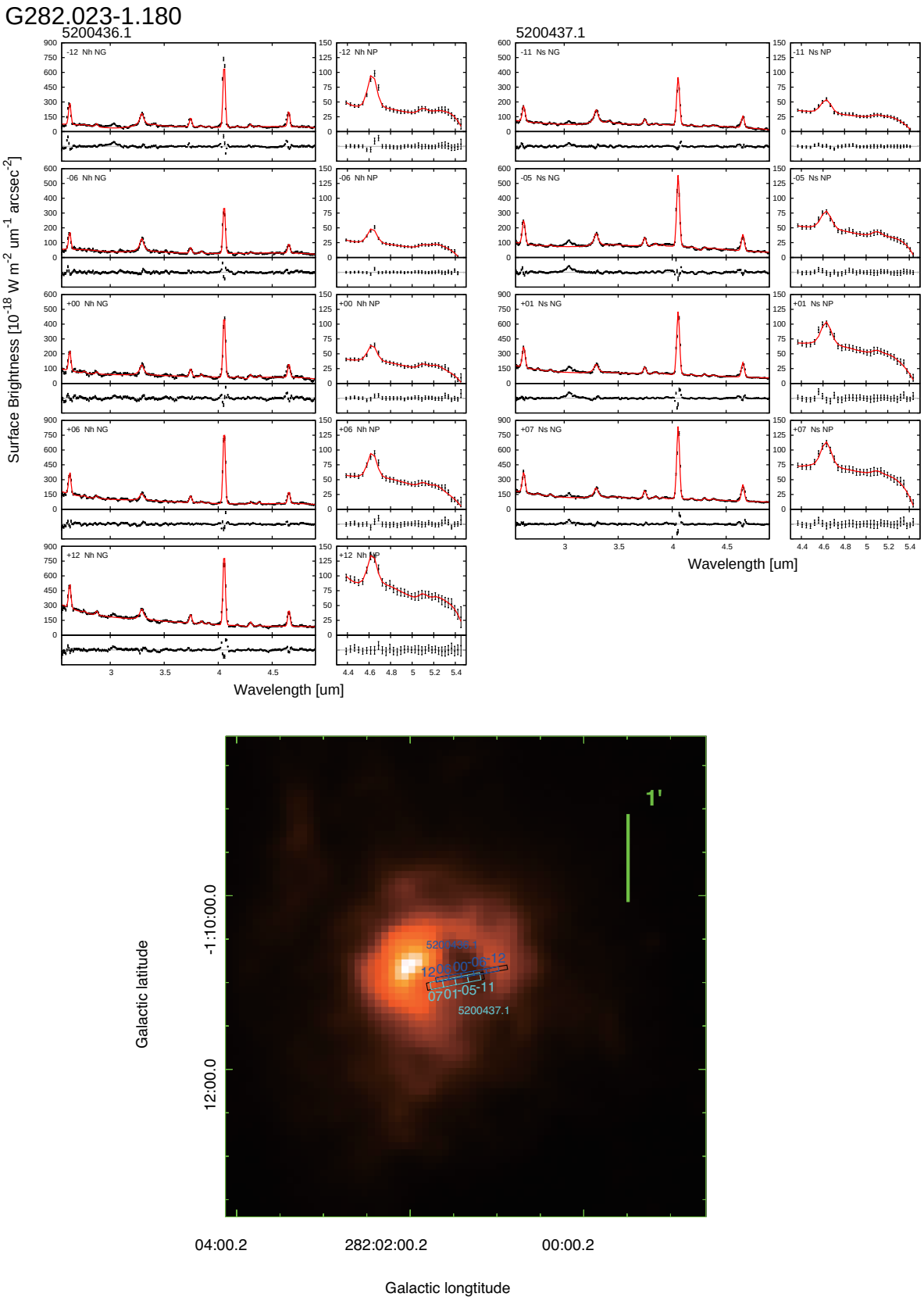

Figure C.1: *Continued.*

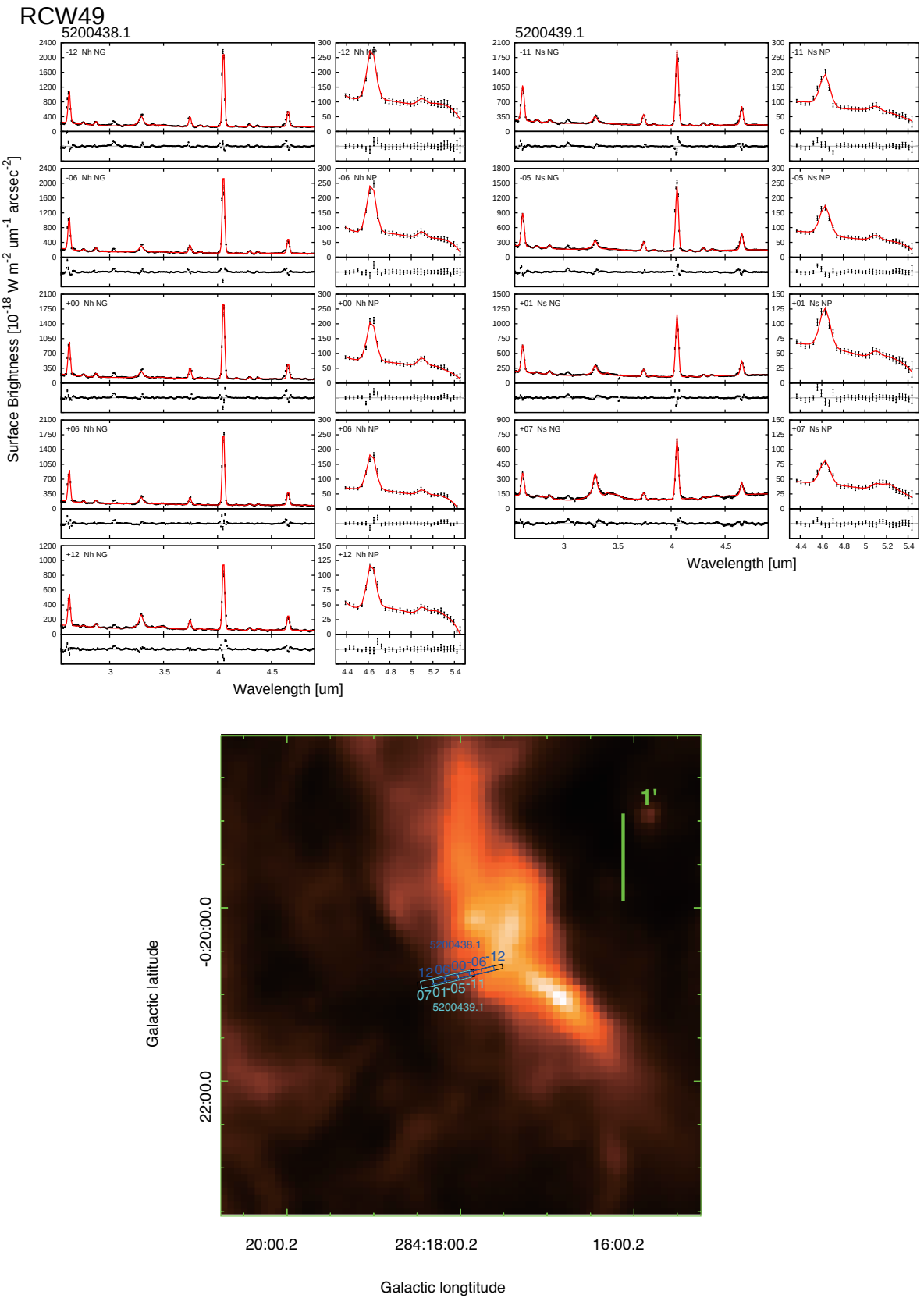

Figure C.1: *Continued.*

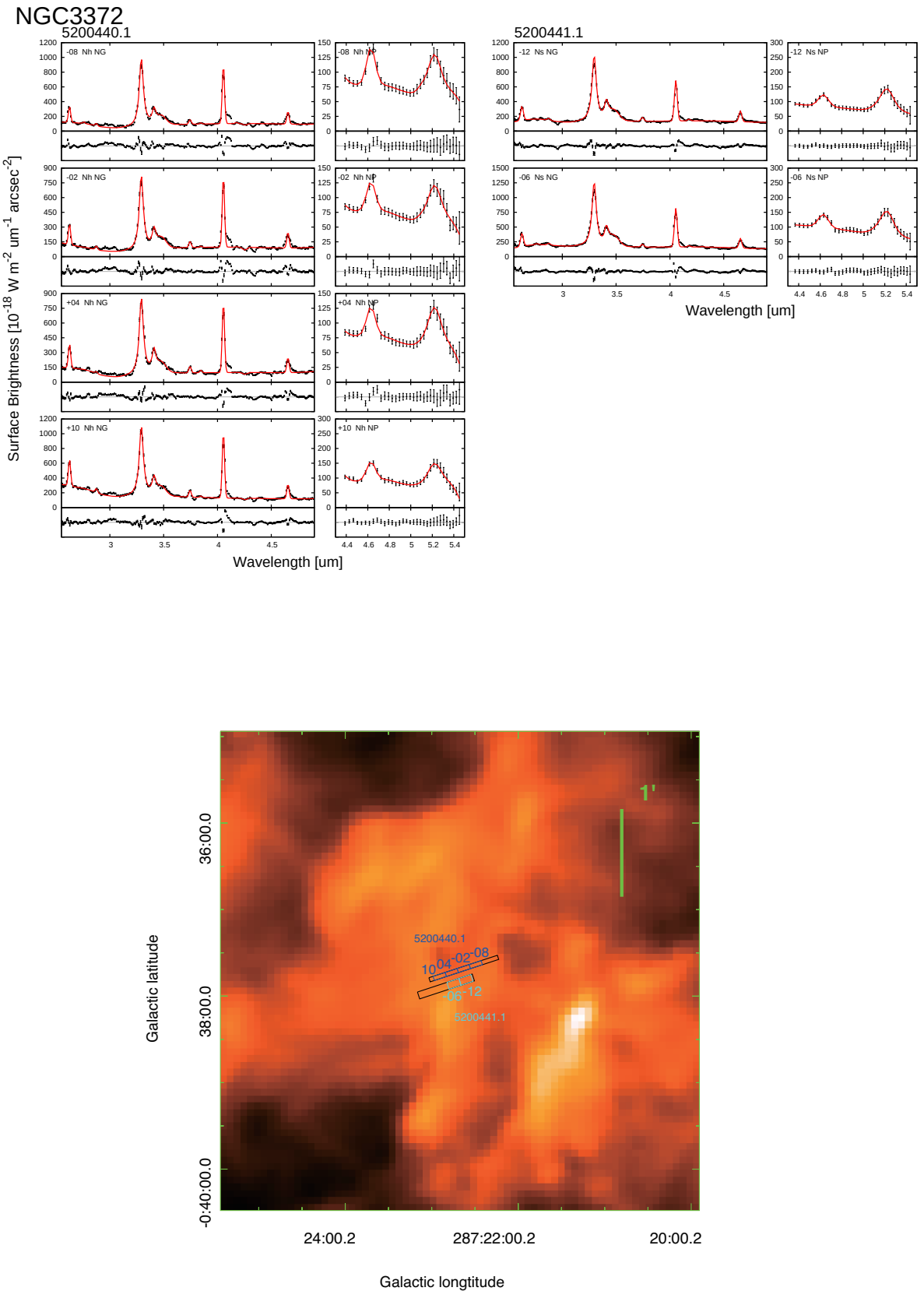

Figure C.1: *Continued.*

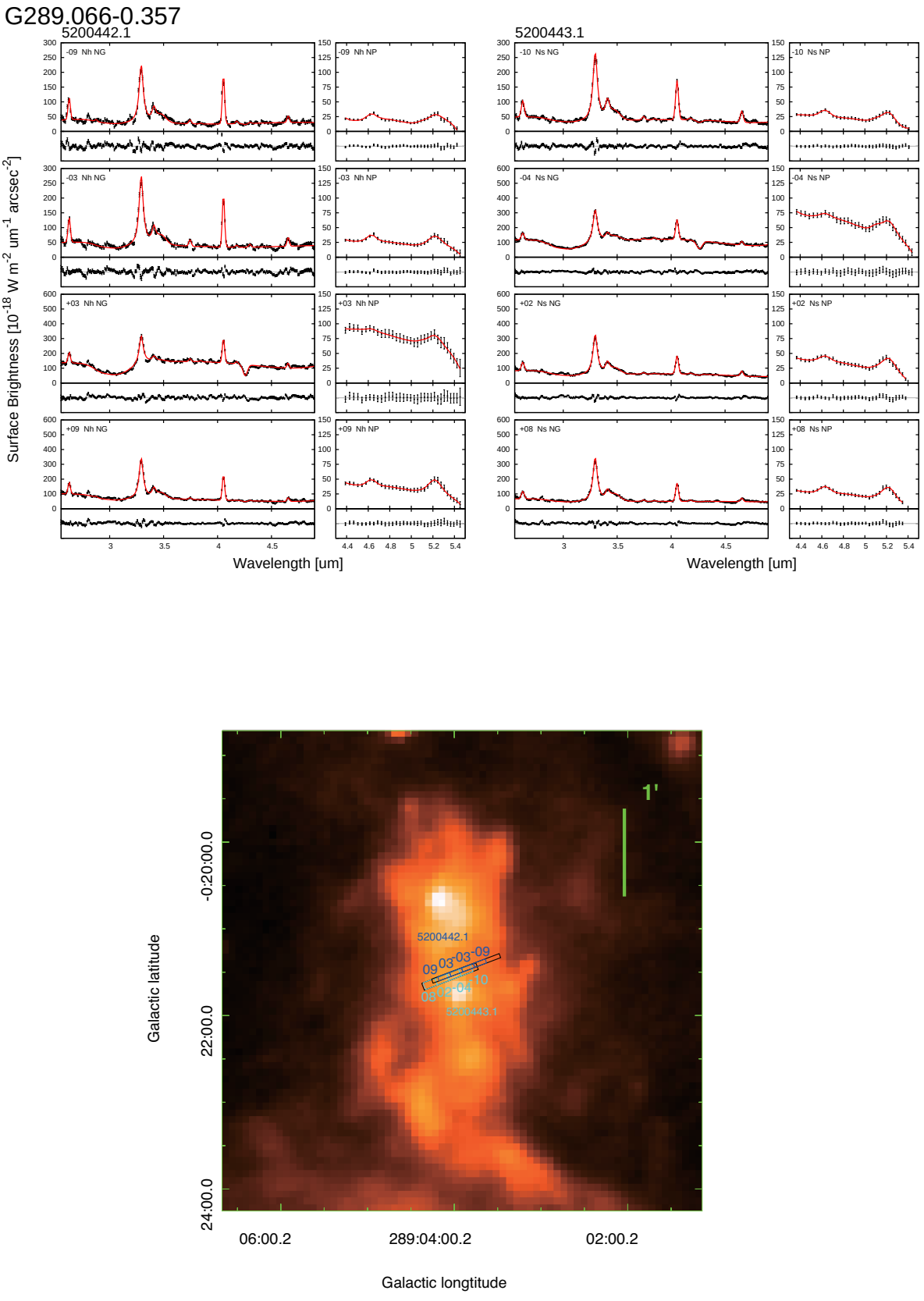

Figure C.1: *Continued.*

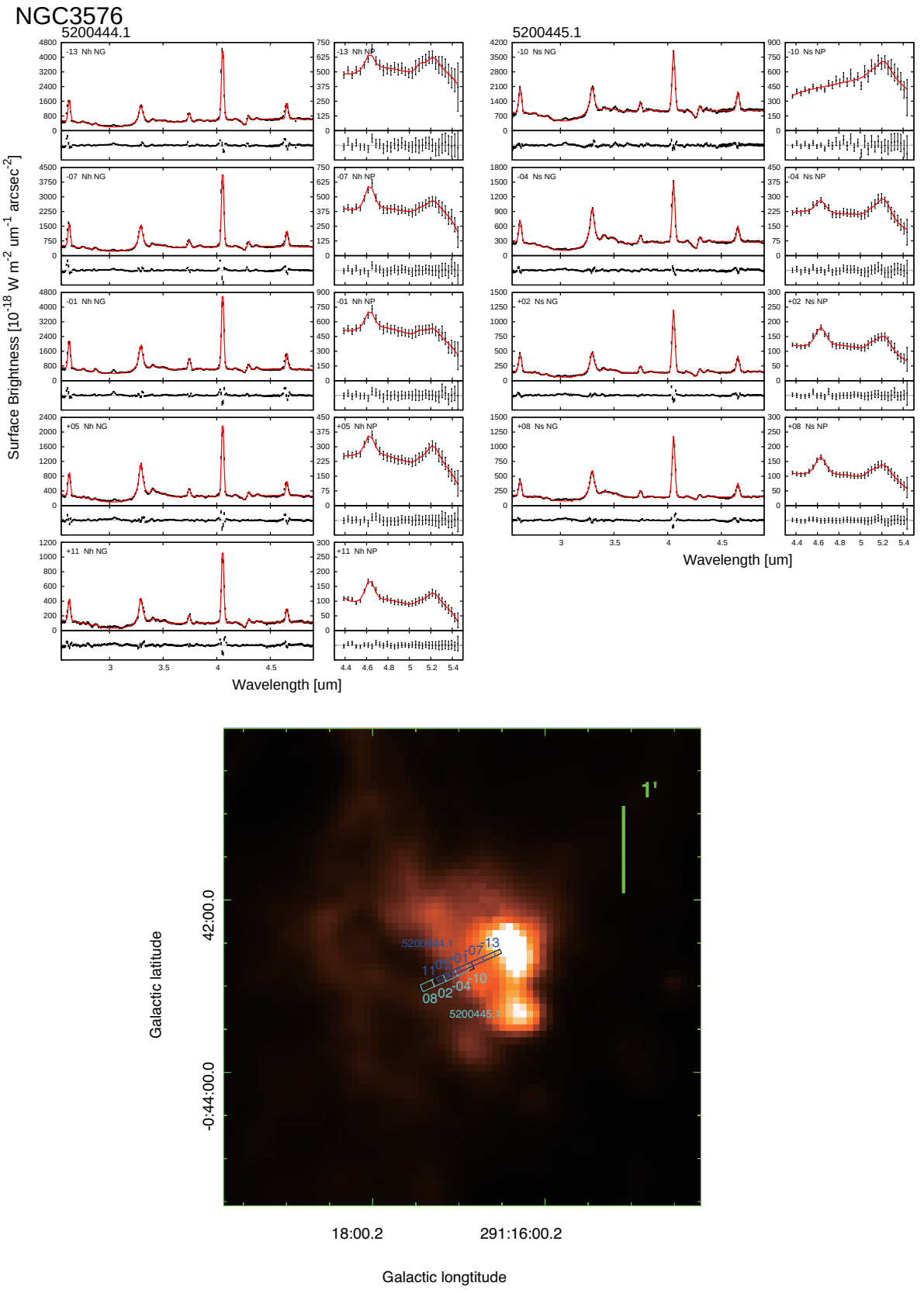

Figure C.1: *Continued.*

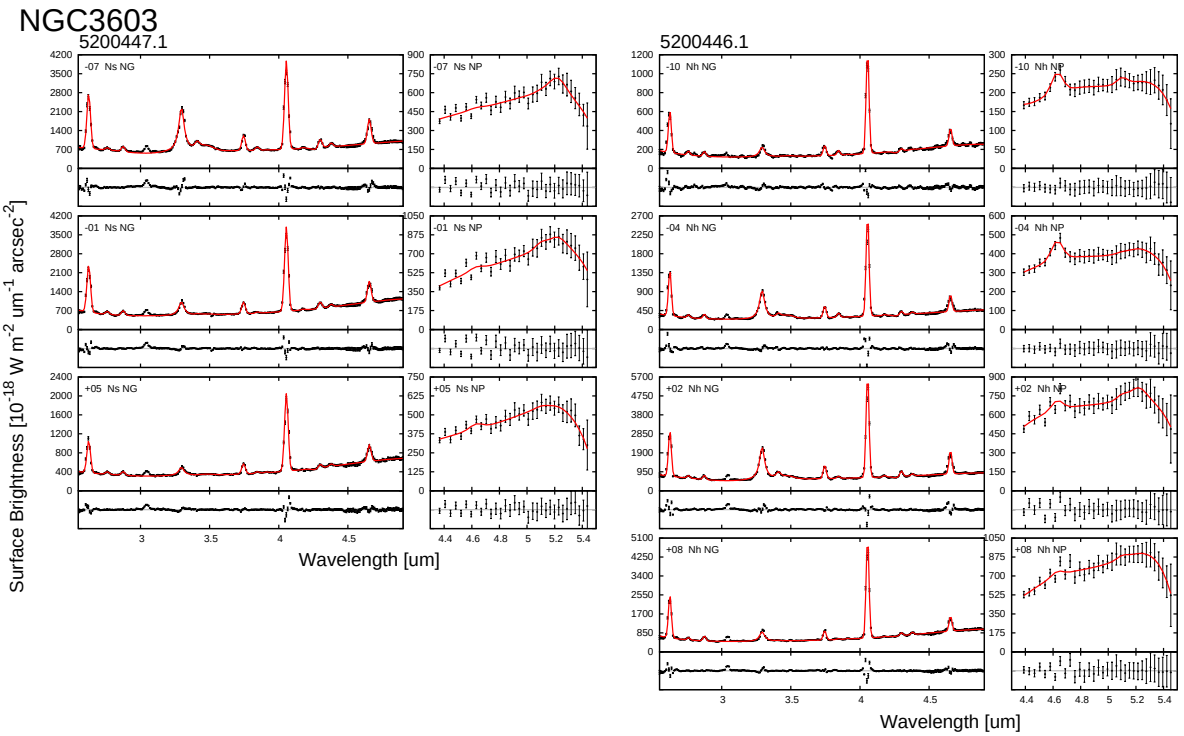

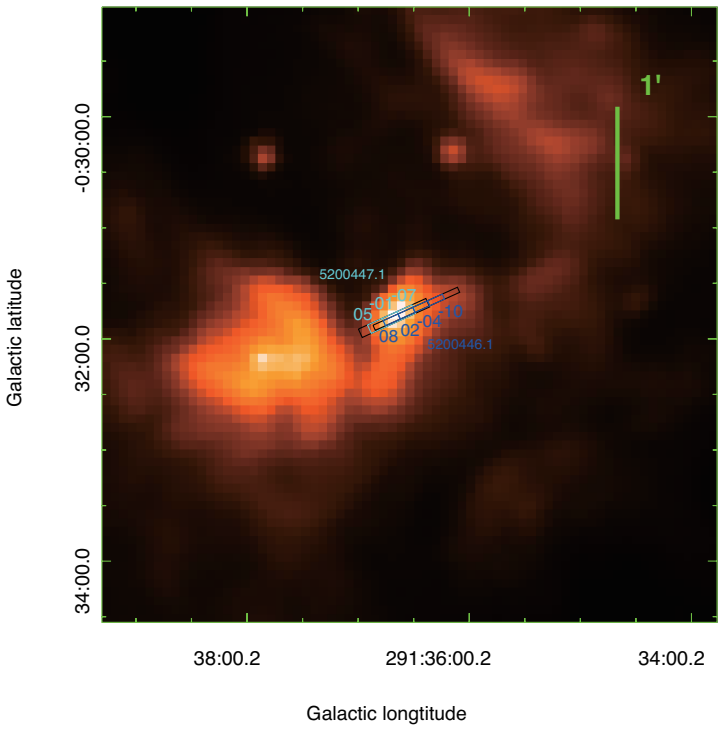

Figure C.1: *Continued.*

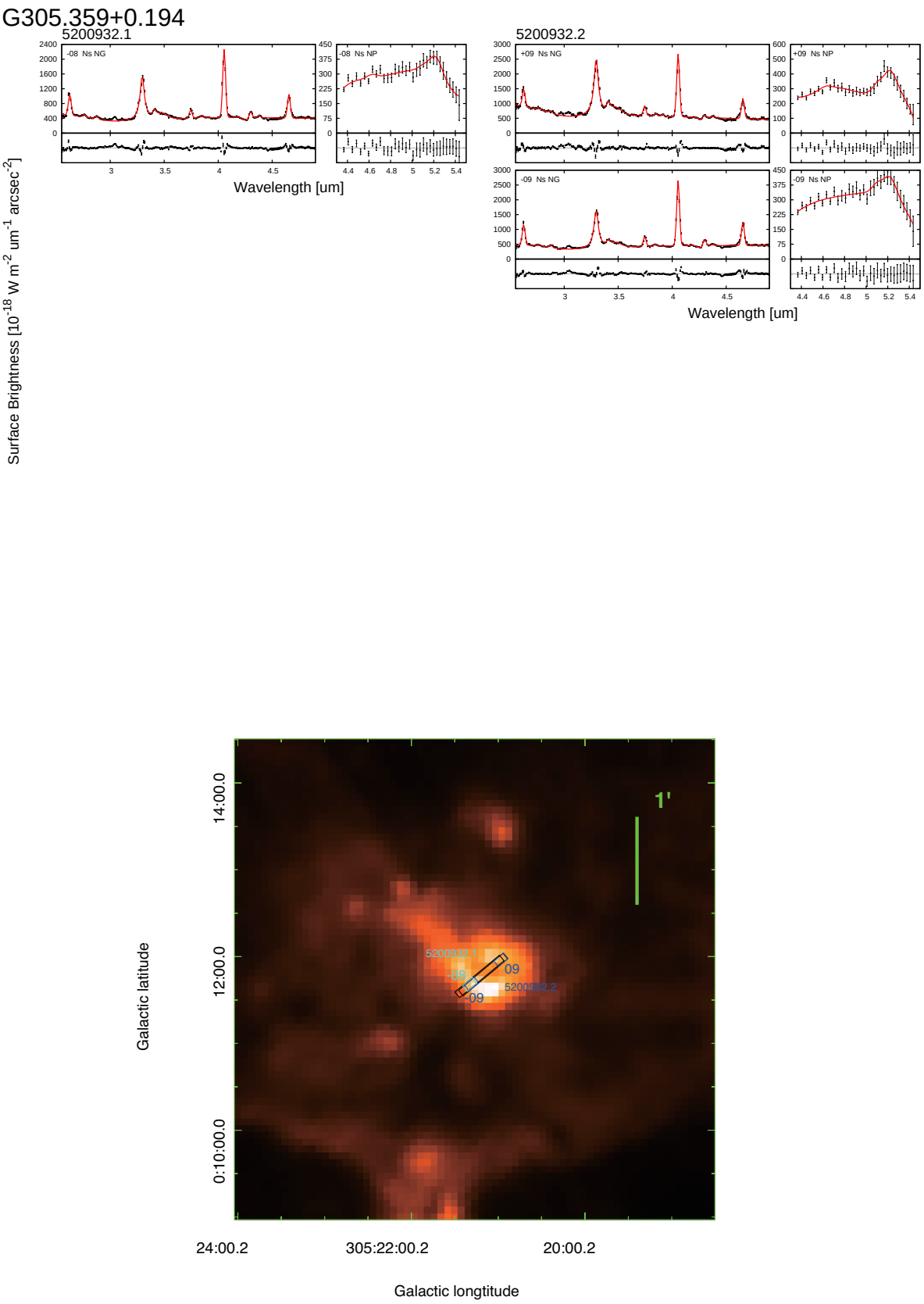

Figure C.1: *Continued.*

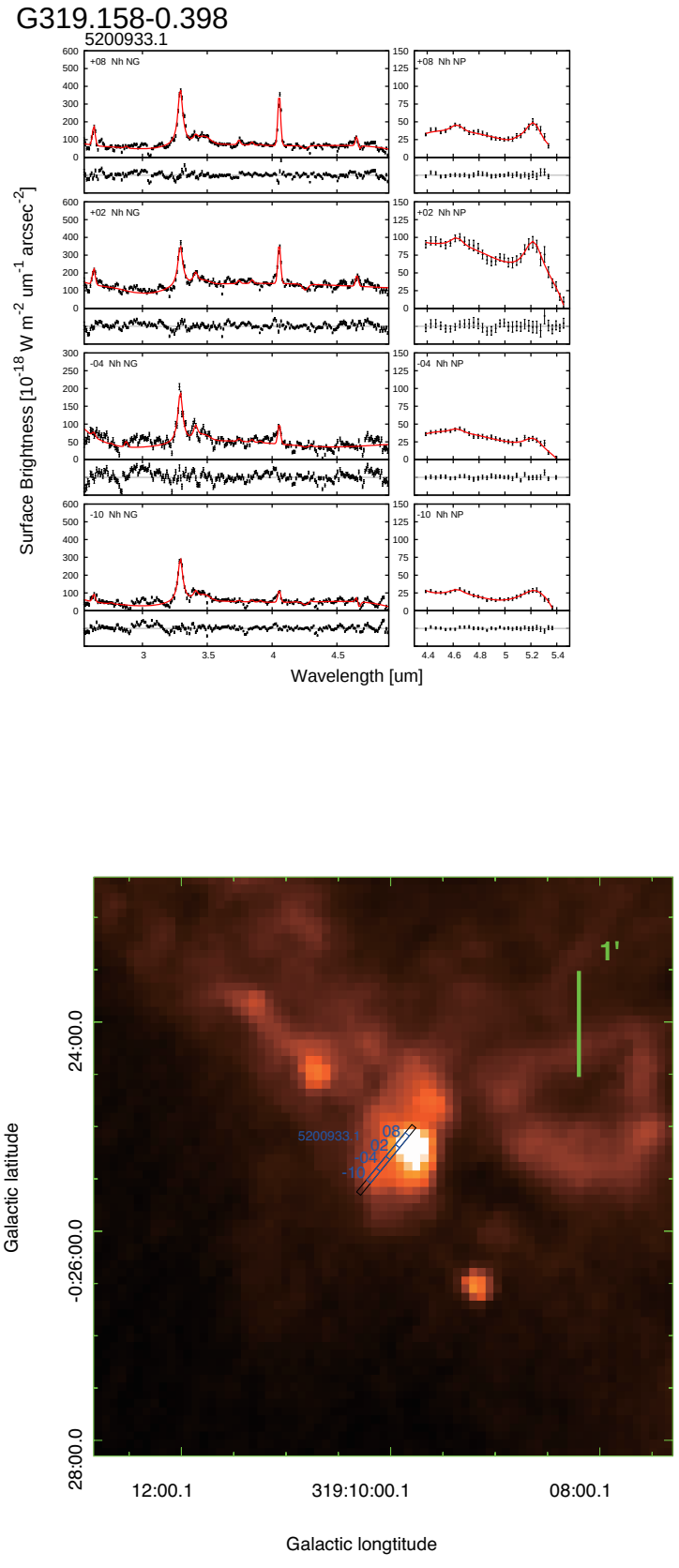

Figure C.1: *Continued.*

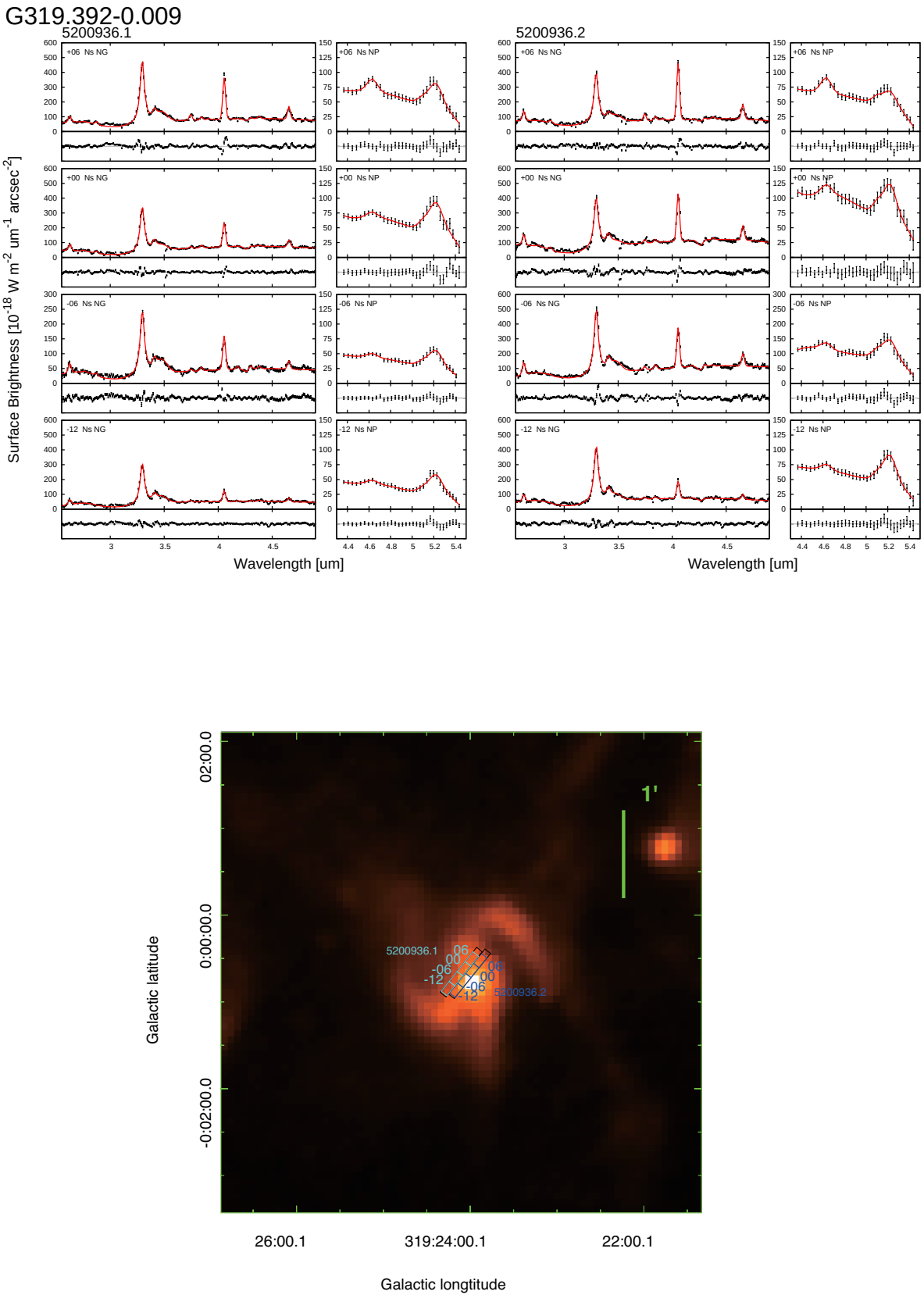

Figure C.1: *Continued.*

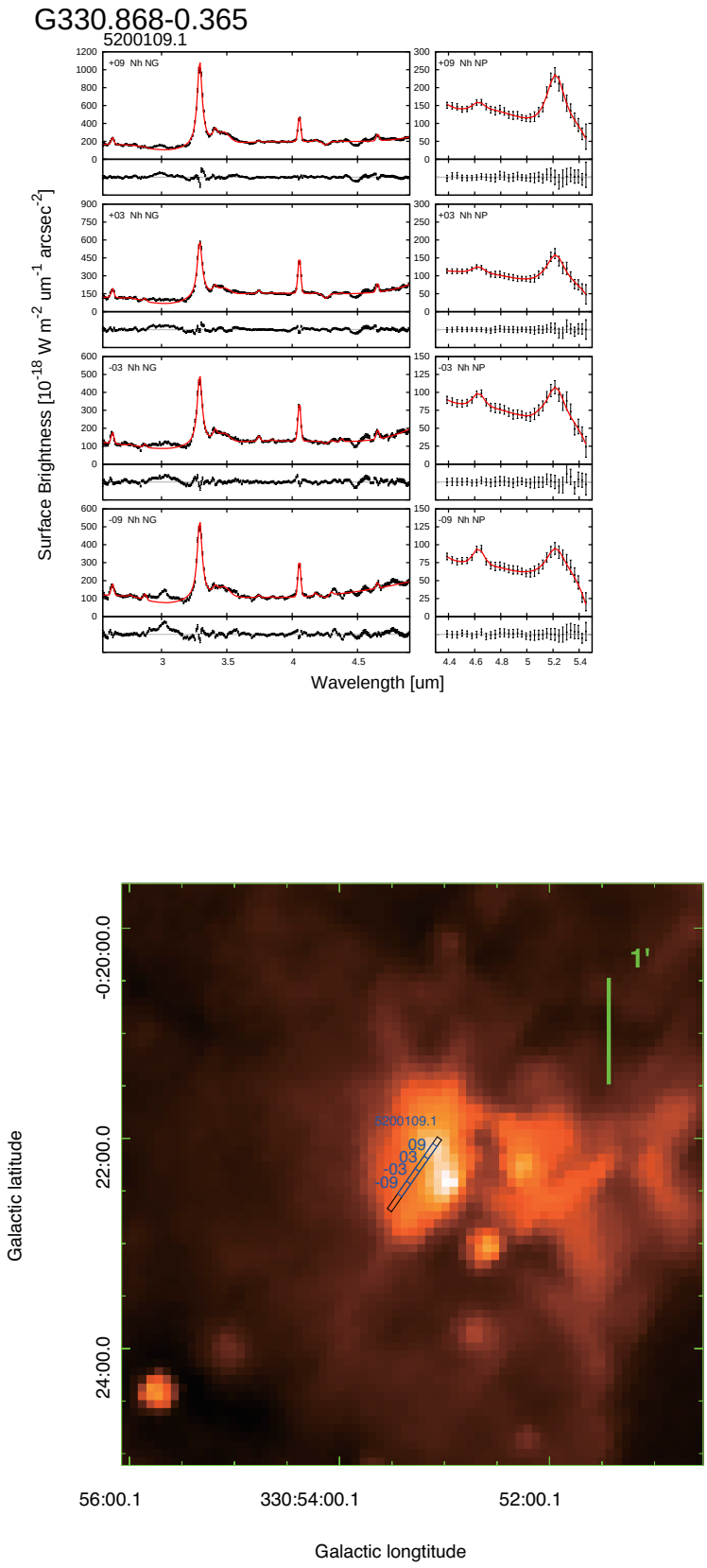

Figure C.1: *Continued.*

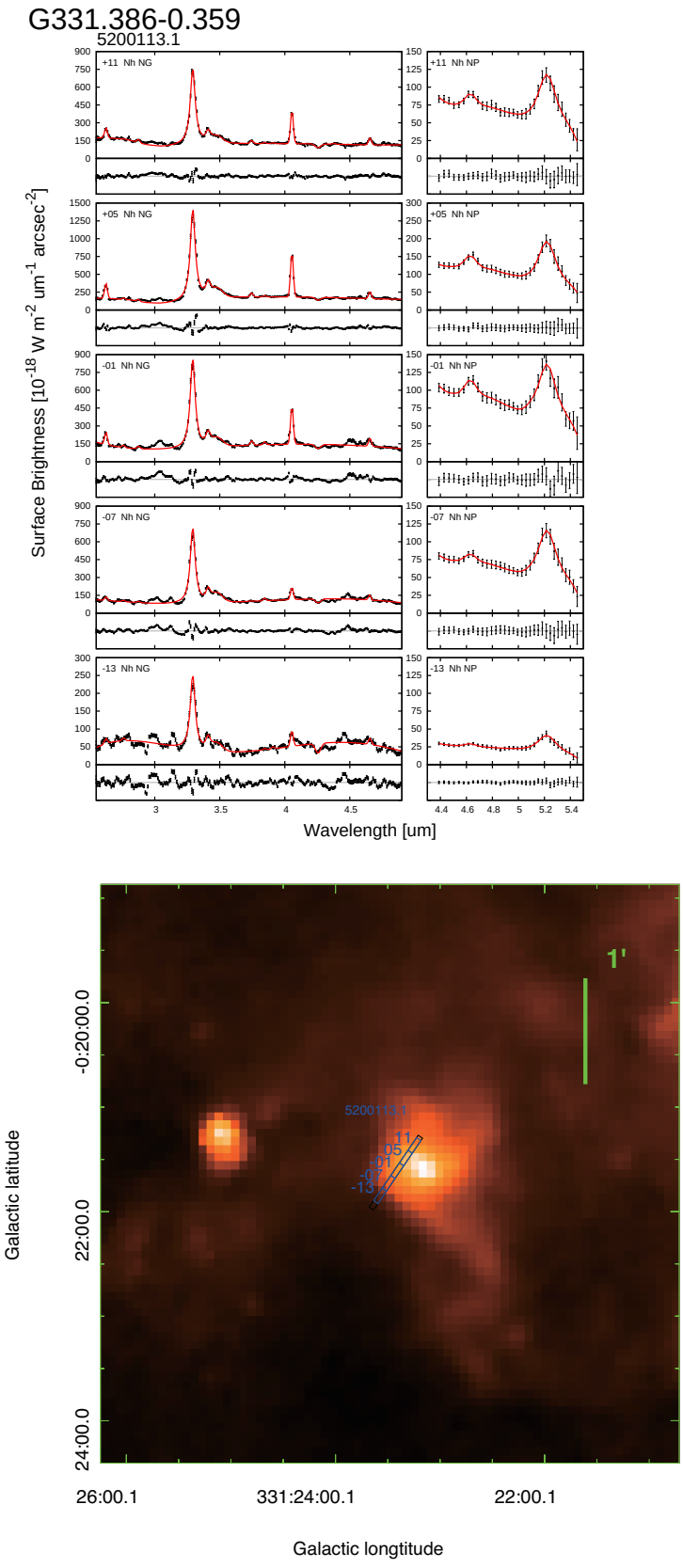

Figure C.1: *Continued.*

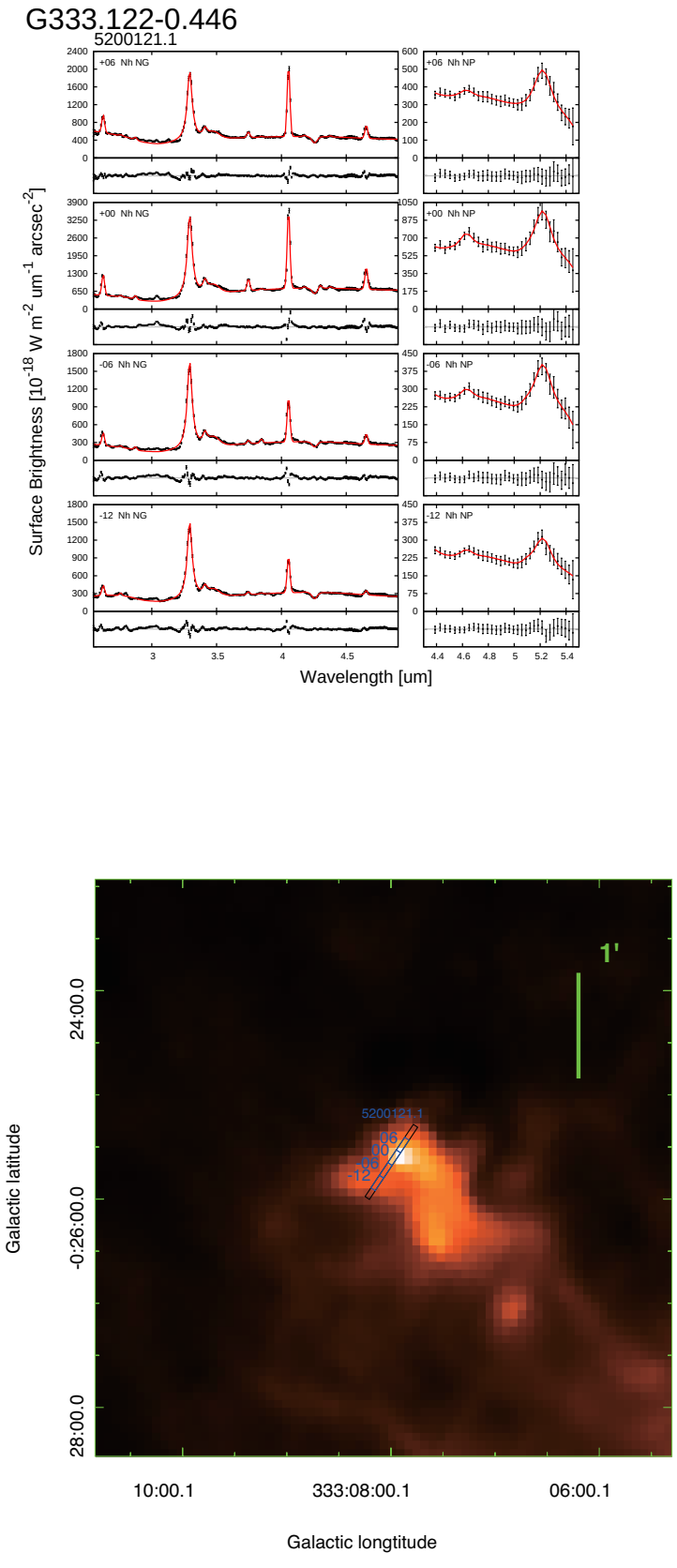

Figure C.1: *Continued.*

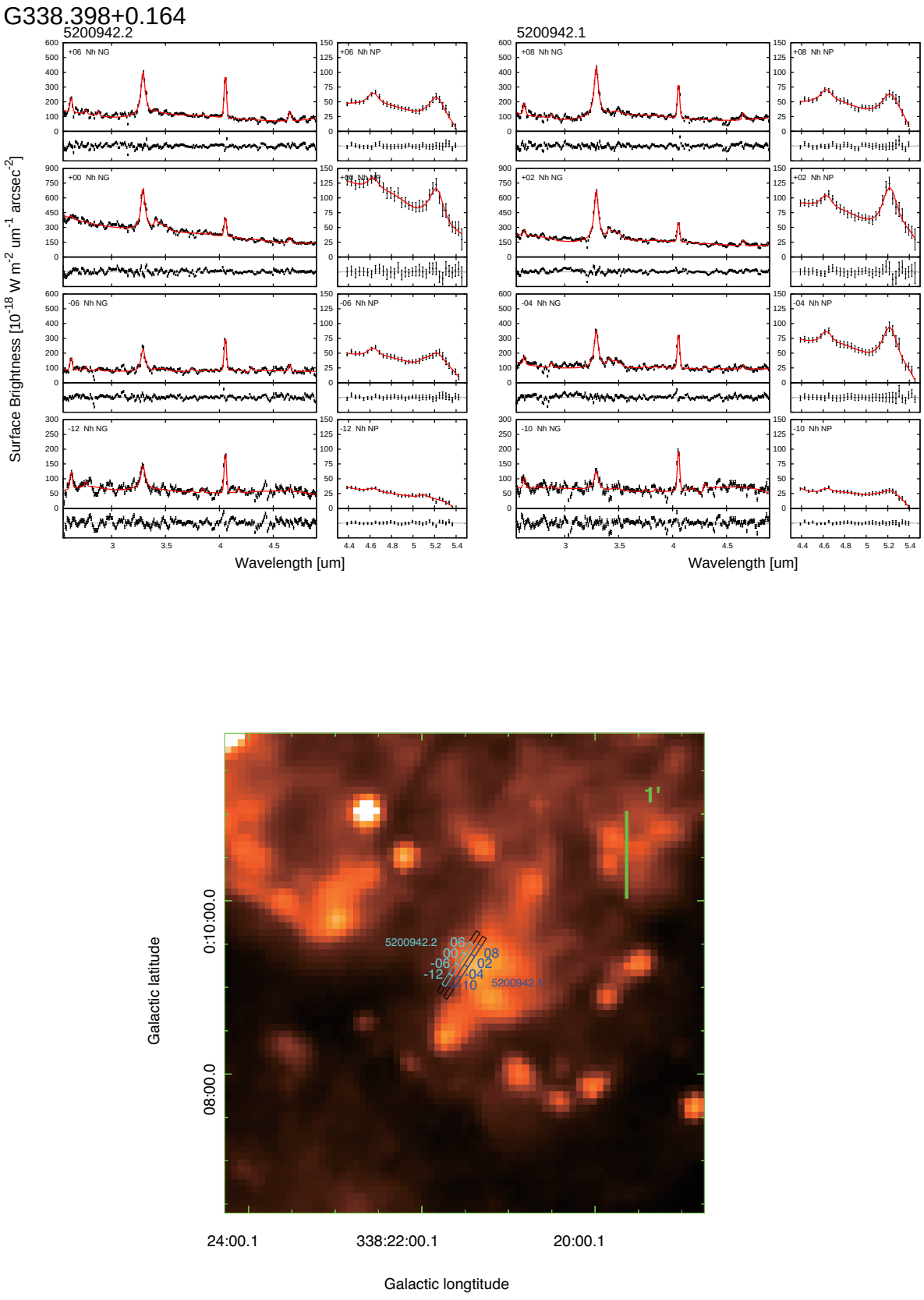

Figure C.1: *Continued.*

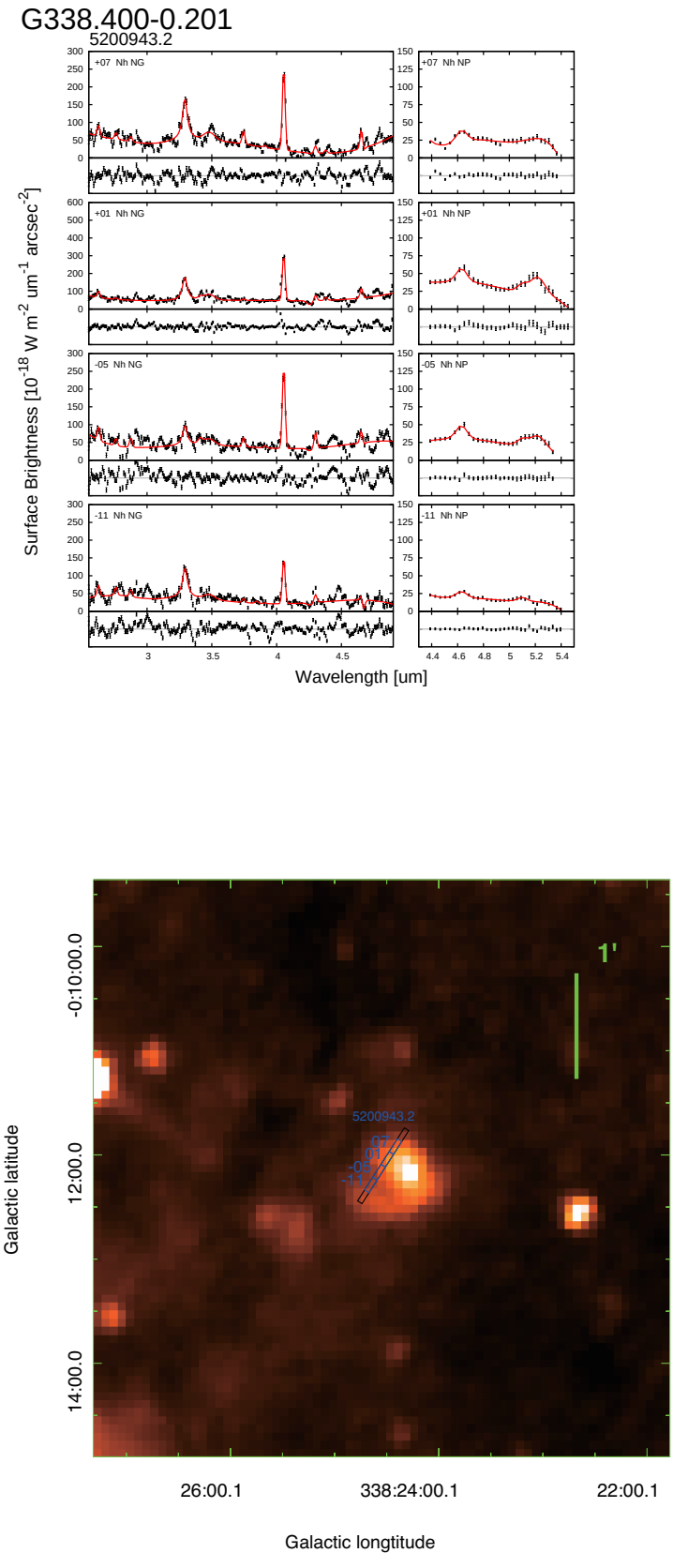

Figure C.1: *Continued.*

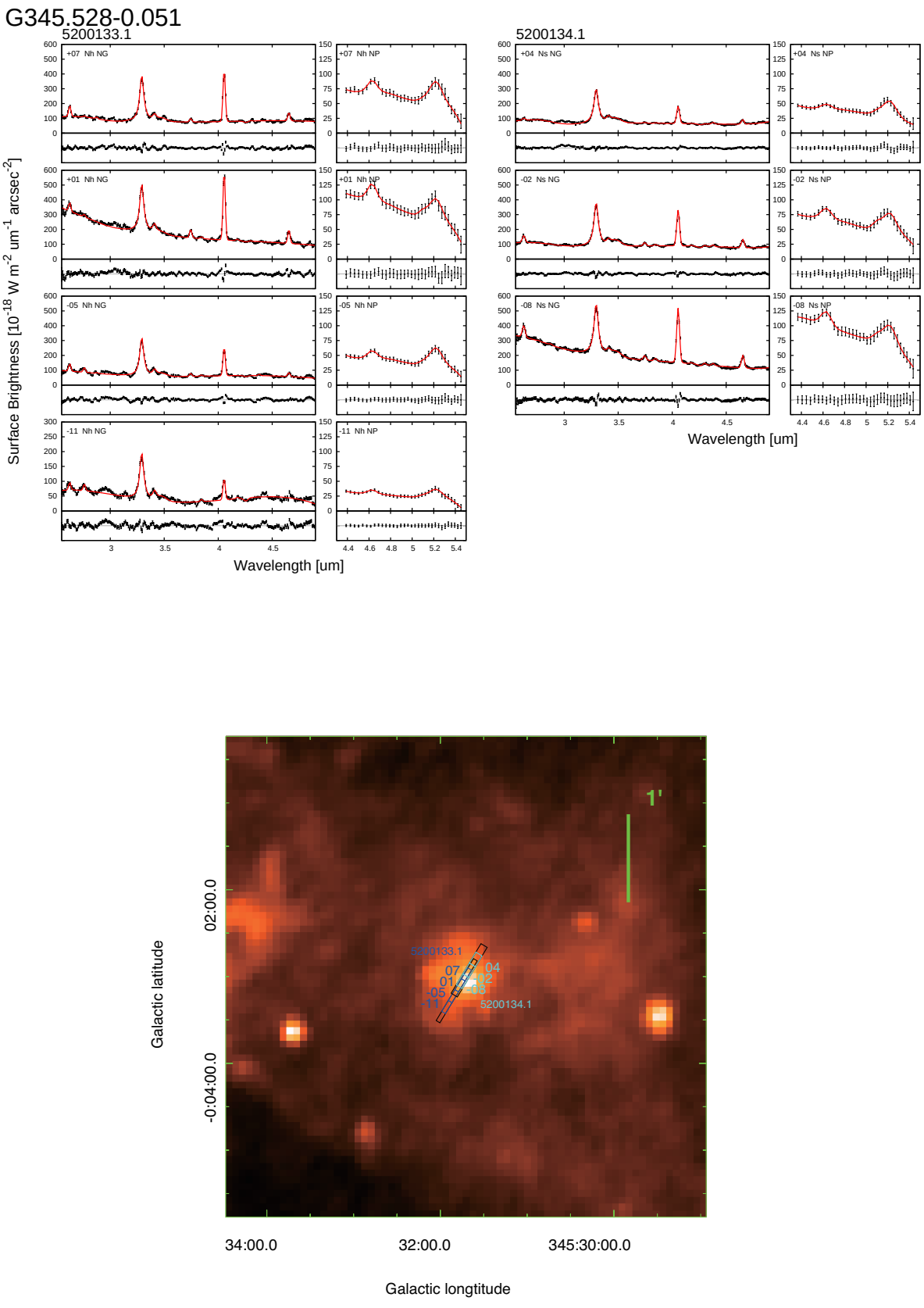

Figure C.1: *Continued.*

Acknowledgments

This work is based on observations with *AKARI*, a JAXA project with the participation of ESA. I am deeply grateful to all the members of the *AKARI* project and the members of the Interstellar and Nearby Galaxy team for their help and continuous encouragements. The ISSA data were obtained from the NASA Astrophysics Data Center (ADC). The MSX data were taken from the NASA/IPAC Infrared Science Archive. I would like to express my gratitude to K. Dobashi for providing for us with the extinction data of the LMC. Additionally, I want to thank Y. Ita for providing for us with the LMC survey program data by *AKARI*. I thank A. Kawamura and Y. Fukui for providing for us with the LMC 12CO survey data at 2.7 mm taken by the NANTEN millimeter-wave telescope of Nagoya University. This work is supported in part by a Grant-in-Aid for Scientific Research from the Japan Society of Promotion of Science (JSPS).

My deepest appreciation goes to Prof. Onaka whose supports were of inestimable value for my study. I would also like to thank all the members of Onaka laboratory and my co-investigators whose comments and suggestions made enormous contribution to my work. I would also like to express my gratitude to my family for their moral support and warm encouragements.

References

Allain, T., Leach, S., & Sedlmayr, E. 1996a, A&A, 305, 602

—. 1996b, A&A, 305, 616

Allamandola, L. J., Bregman, J. D., Sandford, S. A., Tielens, A. G. G. M., Witteborn, F. C., Wooden, D. H., & Rank, D. 1989a, ApJ, 345, L59

Allamandola, L. J., Hudgins, D. M., & Sandford, S. A. 1999, ApJ, 511, L115

Allamandola, L. J., Tielens, A. G. G. M., & Barker, J. R. 1989b, ApJS, 71, 733

Allen, C. W. 1973, Astrophysical quantities 3rd ed. (Athlone press: London)

Baba, S., et al. 2015, submitted to PASJ

Bakes, E. L. O., & Tielens, A. G. G. M. 1994, ApJ, 427, 822

Bakes, E. L. O., Tielens, A. G. G. M., & Bauschlicher, Jr., C. W. 2001, ApJ, 556, 501

Barker, J. R., Allamandola, L. J., & Tielens, A. G. G. M. 1987, ApJ, 315, L61

Bauschlicher, C. W., Langhoff, J. S. R., Sandford, S. A., & Hudgins, D. M. 1997, J. Phys. Chem., 101, 2414

Bauschlicher, Jr., C. W., et al. 2010, ApJS, 189, 341

Bell, A. C., et al. 2015, ArXiv e-prints

Berné, O., Fuente, A., Goicoechea, J. R., Pilleri, P., González-García, M., & Joblin, C. 2009, ApJ, 706, L160

Bernstein, M. P., Sandford, S. A., & Allamandola, L. J. 1996, ApJ, 472, L127

Bica, E., Claria, J. J., Dottori, H., Santos, Jr., J. F. C., & Piatti, A. E. 1996, ApJS, 102, 57

Boersma, C., Bauschlicher, C. W., Allamandola, L. J., Ricca, A., Peeters, E., & Tielens, A. G. G. M. 2010, A&A, 511, A32+

Boersma, C., Mattioda, A. L., Bauschlicher, Jr., C. W., Peeters, E., Tielens, A. G. G. M., & Allamandola, L. J. 2009, ApJ, 690, 1208

Boogert, A. C. A., Schutte, W. A., Helmich, F. P., Tielens, A. G. G. M., & Wooden, D. H. 1997, A&A, 317, 929

Boulanger, F., Baud, B., & van Albada, G. D. 1985, A&A, 144, L9

Boulanger, F., Beichman, C., Desert, F. X., Helou, G., Perault, M., & Ryter, C. 1988, ApJ, 332, 328

Boulanger, F., Onaka, T., Pilleri, P., & Joblin, C. 2011, in EAS Publications Series, Vol. 46, EAS Publications Series, ed. C. Joblin & A. G. G. M. Tielens, 399–405

Bregman, J., & Temi, P. 2005, ApJ, 621, 831

Buch, V. 1989, ApJ, 343, 208

Buragohain, M., & Pathak, A. 2015, private communication

Buragohain, M., Pathak, A., Sarre, P., Onaka, T., & Sakon, I. 2015, ArXiv e-prints

Cami, J., Bernard-Salas, J., Peeters, E., & Malek, S. E. 2010, Science, 329, 1180

Chiar, J. E., Tielens, A. G. G. M., Adamson, A. J., & Ricca, A. 2013, ApJ, 770, 78

Compiègne, M., et al. 2011, A&A, 525, A103

Conti, P. S., & Crowther, P. A. 2004, MNRAS, 355, 899

Crowther, P. A., & Conti, P. S. 2003, MNRAS, 343, 143

Dale, D. A., et al. 2006, ApJ, 646, 161

Dartois, E., & Muñoz-Caro, G. M. 2007, A&A, 476, 1235

Dartois, E., Muñoz Caro, G. M., Deboffle, D., & d'Hendecourt, L. 2004, A&A, 423, L33

de Graauw, T., et al. 1996, A&A, 315, L49

DeFrees, D. J., Miller, M. D., Talbi, D., Pauzat, F., & Ellinger, Y. 1993, ApJ, 408, 530

D'Hendecourt, L. B., & Allamandola, L. J. 1986, A&AS, 64, 453

Dobashi, K., Bernard, J.-P., Hughes, A., Paradis, D., Reach, W. T., & Kawamura, A. 2008, A&A, 484, 205

Doi, Y., et al. 2015, PASJ, 67, 50

Doney, K. D., Candian, A., Mori, I. T., Onaka, T., & Tielens, A. G. G. M. 2016, A&A, 586, A65

Draine, B. T. 2006, in Astronomical Society of the Pacific Conference Series, Vol. 348, Astrophysics in the Far Ultraviolet: Five Years of Discovery with FUSE, ed. G. Sonneborn, H. W. Moos, & B.-G. Andersson, 58

Draine, B. T., & Lazarian, A. 1998, ApJ, 494, L19

Draine, B. T., & Li, A. 2001, ApJ, 551, 807

—. 2007, ApJ, 657, 810

Duley, W. W., & Williams, D. A. 1981, MNRAS, 196, 269

Dwek, E., & Scalo, J. M. 1980, ApJ, 239, 193

Ehrenfreund, P., Boogert, A. C. A., Gerakines, P. A., Jansen, D. J., Schutte, W. A., Tielens, A. G. G. M., & van Dishoeck, E. F. 1996, A&A, 315, L341

Epstein, R. I., Lattimer, J. M., & Schramm, D. N. 1976, Nature, 263, 198

Fazio, G. G., et al. 2004, ApJS, 154, 10

Feast, M. 1999, PASP, 111, 775

Fukui, Y., et al. 2008, ApJS, 178, 56

Galliano, F., Madden, S. C., Tielens, A. G. G. M., Peeters, E., & Jones, A. P. 2008, ApJ, 679, 310

Geballe, T. R., Lacy, J. H., Persson, S. E., McGregor, P. J., & Soifer, B. T. 1985, ApJ, 292, 500

Gerakines, P. A., Schutte, W. A., Greenberg, J. M., & van Dishoeck, E. F. 1995, A&A, 296, 810

Gibb, E. L., Whittet, D. C. B., Boogert, A. C. A., & Tielens, A. G. G. M. 2004, ApJS, 151, 35

Gillett, F. C., Forrest, W. J., & Merrill, K. M. 1973, ApJ, 183, 87

Goto, M., et al. 2003, ApJ, 589, 419

—. 2009, ApJ, 693, 610

Habing, H. J. 1968, Bull. Astron. Inst. Netherlands, 19, 421

Hammonds, M. 2015, private communication

Hammonds, M., Mori, I. T., Usui, F., & Onaka, T. 2015, Planet. Space Sci., 116, 73

Haraguchi, K., Nagayama, T., Kurita, M., Kino, M., & Sato, S. 2012, PASJ, 64, 127

Hensley, B. S., Draine, B. T., & Meisner, A. M. 2015, ArXiv e-prints

Hony, S., & SAGE-Spec Team. 2011, IAU Symposium, 280, poster 45, session 2

Hora, J. L., et al. 2000, in Society of Photo-Optical Instrumentation Engineers (SPIE) Conference Series, Vol. 4131, Infrared Spaceborne Remote Sensing VIII, ed. M. Strojnik & B. F. Andresen, 13–25

Hora, J. L., et al. 2003a, in ESA Special Publication, Vol. 481, The Calibration Legacy of the ISO Mission, ed. L. Metcalfe, A. Salama, S. B. Peschke, & M. F. Kessler, 73

Hora, J. L., et al. 2003b, in Society of Photo-Optical Instrumentation Engineers (SPIE) Conference Series, Vol. 4850, IR Space Telescopes and Instruments, ed. J. C. Mather, 83–97

Hora, J. L., et al. 2004, in Society of Photo-Optical Instrumentation Engineers (SPIE) Conference Series, Vol. 5487, Optical, Infrared, and Millimeter Space Telescopes, ed. J. C. Mather, 77–92

Houck, J. R., et al. 2004, ApJS, 154, 18

Hudgins, D. M., Bauschlicher, Jr., C. W., & Allamandola, L. J. 2005, ApJ, 632, 316

Hudgins, D. M., Bauschlicher, Jr., C. W., & Sandford, S. A. 2004, ApJ, 614, 770

Hudgins, D. M., Sandford, S. A., Allamandola, L. J., & Tielens, A. G. G. M. 1993, ApJS, 86, 713

Iida, S., Ohtaki, T., & Seki, T. 1985, in AIP Conference Proceedings, Vol. 120, Optical Effects in Amorphous Semiconductors, 258

Ishihara, D., et al. 2007, PASJ, 59, 443

—. 2010, A&A, 514, A1

Ita, Y., et al. 2008, PASJ, 60, 435

Joblin, C., Tielens, A. G. G. M., Allamandola, L. J., & Geballe, T. R. 1996a, ApJ, 458, 610

Joblin, C., Tielens, A. G. G. M., Geballe, T. R., & Wooden, D. H. 1996b, ApJ, 460, L119+

Jones, A. P. 2004, in Astronomical Society of the Pacific Conference Series, Vol. 309, Astrophysics of Dust, ed. A. N. Witt, G. C. Clayton, & B. T. Draine, 347

Jones, A. P. 2012a, A&A, 540, A1

—. 2012b, A&A, 540, A2

—. 2012c, A&A, 542, A98

Jones, A. P., Fanciullo, L., Köhler, M., Verstraete, L., Guillet, V., Bocchio, M., & Ysard, N. 2013, A&A, 558, A62

Jones, A. P., Tielens, A. G. G. M., & Hollenbach, D. J. 1996, ApJ, 469, 740

Jourdain de Muizon, M., D'Hendecourt, L. B., & Geballe, T. R. 1990, A&A, 227, 526

Jura, M. 1982, in NASA Conference Publication, Vol. 2238, NASA Conference Publication, ed. Y. Kondo, 54–60

Kaneda, H., Koo, B. C., Onaka, T., & Takahashi, H. 2009, Advances in Space Research, 44, 1038

Kaneda, H., Onaka, T., Sakon, I., Kitayama, T., Okada, Y., & Suzuki, T. 2008, ApJ, 684, 270

Kaneda, H., et al. 2012, PASJ, 64, 25

Kato, D., et al. 2012, AJ, 144, 179

Kawada, M., et al. 2007, PASJ, 59, 389

Keller, S. C., & Wood, P. R. 2006, ApJ, 642, 834

Kerkhof, O., Schutte, W. A., & Ehrenfreund, P. 1999, A&A, 346, 990

Kroto, H. W., Heath, J. R., Obrien, S. C., Curl, R. F., & Smalley, R. E. 1985, Nature, 318, 162

Kwok, S., & Zhang, Y. 2011, Nature, 479, 80

Lee, H.-G., Moon, D.-S., Koo, B.-C., Onaka, T., Jeong, W.-S., Shinn, J.-H., & Sakon, I. 2011, ApJ, 740, 31

Li, A., & Draine, B. T. 2012, ApJ, 760, L35

Linsky, J. L., et al. 2006, ApJ, 647, 1106

Lutz, D., Valiante, E., Sturm, E., Genzel, R., Tacconi, L. J., Lehnert, M. D., Sternberg, A., & Baker, A. J. 2005, ApJ, 625, L83

Mattila, K., Lemke, D., Haikala, L. K., Laureijs, R. J., Leger, A., Lehtinen, K., Leinert, C., & Mezger, P. G. 1996, A&A, 315, L353

Meixner, M., et al. 2006, AJ, 132, 2268

Micelotta, E. R., Jones, A. P., & Tielens, A. G. G. M. 2010a, A&A, 510, A37+

—. 2010b, A&A, 510, A36+

—. 2011, A&A, 526, A52+

Miville-Deschênes, M.-A., Lagache, G., & Puget, J.-L. 2002, A&A, 393, 749

Mizuno, N., et al. 2001, PASJ, 53, 971

Mori, T. I., Onaka, T., Sakon, I., Ishihara, D., Shimonishi, T., Ohsawa, R., & Bell, A. C. 2014, ApJ, 784, 53

Mori, T. I., Sakon, I., Onaka, T., Kaneda, H., Umehata, H., & Ohsawa, R. 2012, ApJ, 744, 68

Murakami, H., et al. 2007, PASJ, 59, 369

Nakagawa, T., et al. 2007, PASJ, 59, S377

Nakajima, Y., et al. 2005, AJ, 129, 776

Nikolaev, S., Drake, A. J., Keller, S. C., Cook, K. H., Dalal, N., Griest, K., Welch, D. L., & Kanbur, S. M. 2004, ApJ, 601, 260

Ohyama, Y., et al. 2007, PASJ, 59, 411

Olsen, K. A. G., & Salyk, C. 2002, AJ, 124, 2045

Onaka, T. 2012, in Proc. of IAU Symposium, Vol. 292, Molecular Gas, Dust, and Star Formation in Galaxies in press

Onaka, T., Lorente, R., Ita, Y., Ohyama, Y., Tanabè, T., & Pearson, C. 2009, IRC Data Users's Manual for Phase 3 ver 1.1

Onaka, T., Matsumoto, H., Sakon, I., & Kaneda, H. 2010, A&A, 514, A15+

Onaka, T., Mori, T. I., Sakon, I., Ohsawa, R., Kaneda, H., Okada, Y., & Tanaka, M. 2014, ApJ, 780, 114

Onaka, T., Tokura, D., Sakon, I., Tajiri, Y. Y., Takagi, T., & Shibai, H. 2007a, ApJ, 654, 844

Onaka, T., Yamamura, I., Tanabe, T., Roellig, T. L., & Yuen, L. 1996, PASJ, 48, L59

Onaka, T., et al. 2007b, PASJ, 59, 401

Paladini, R., et al. 2012, ApJ, 760, 149

Papoular, R., Conrad, J., Giuliano, M., Kister, J., & Mille, G. 1989, A&A, 217, 204

Paradis, D., et al. 2009, AJ, 138, 196

—. 2011, AJ, 141, 43

Peeters, E., Allamandola, L. J., Bauschlicher, Jr., C. W., Hudgins, D. M., Sandford, S. A., & Tielens, A. G. G. M. 2004a, ApJ, 604, 252

Peeters, E., Allamandola, L. J., Hudgins, D. M., Hony, S., & Tielens, A. G. G. M. 2004b, in Astronomical Society of the Pacific Conference Series, Vol. 309, Astrophysics of Dust, ed. A. N. Witt, G. C. Clayton, & B. T. Draine, 141

Peeters, E., Hony, S., Van Kerckhoven, C., Tielens, A. G. G. M., Allamandola, L. J., Hudgins, D. M., & Bauschlicher, C. W. 2002, A&A, 390, 1089

Pendleton, Y. J., & Allamandola, L. J. 2002, ApJS, 138, 75

Pipher, J. L., et al. 2004, Proc. of SPIE, 5487, 234

Press, W. H., Teukolsky, S. A., Vetterling, W. T., & Flannery, B. P. 2002, Numerical recipes in C++ : the art of scientific computing

Puget, J. L., & Leger, A. 1989, ARA&A, 27, 161

Rho, J., Onaka, T., Cami, J., & Reach, W. T. 2012, ApJ, 747, L6

Riechers, D. A., et al. 2014, ApJ, 786, 31

Sadjadi, S., Zhang, Y., & Kwok, S. 2015, ApJ, 801, 34

Sajina, A., Yan, L., Armus, L., Choi, P., Fadda, D., Helou, G., & Spoon, H. 2007, ApJ, 664, 713

Sakata, A. 1980, in IAU Symposium, Vol. 87, Interstellar Molecules, ed. B. H. Andrew, 325–328

Sakata, A., Wada, S., Narisawa, T., Asano, Y., Iijima, Y., Onaka, T., & Tokunaga, A. T. 1992, ApJ, 393, L83

Sakata, A., Wada, S., Okutsu, Y., Shintani, H., & Nakada, Y. 1983, Nature, 301, 493

Sakata, A., Wada, S., Onaka, T., & Tokunaga, A. T. 1990, ApJ, 353, 543

Sakata, A., Wada, S., Tanabe, T., & Onaka, T. 1984, ApJ, 287, L51

Sakata, A., Wada, S., Tokunaga, A. T., Narisawa, T., Nakagawa, H., & Ono, H. 1994, ApJ, 430, 311

Sakon, I., Onaka, T., Ishihara, D., Ootsubo, T., Yamamura, I., Tanabé, T., & Roellig, T. L. 2004, ApJ, 609, 203

Sakon, I., et al. 2006, ApJ, 651, 174

—. 2007, PASJ, 59, 483

—. 2008, Proc. of SPIE, 7010, 70102Y

Sales, D. A., Pastoriza, M. G., & Riffel, R. 2010, ApJ, 725, 605

Salgado, F., et al. 2012, ApJ, 749, L21

Schutte, W. A., & Greenberg, J. M. 1997, A&A, 317, L43

Schutte, W. A., Tielens, A. G. G. M., & Allamandola, L. J. 1993, ApJ, 415, 397

Sellgren, K. 1984, ApJ, 277, 623

Sellgren, K., Werner, M. W., Ingalls, J. G., Smith, J. D. T., Carleton, T. M., & Joblin, C. 2010, ApJ, 722, L54

Seok, J. Y., Koo, B.-C., & Onaka, T. 2012, ApJ, 744, 160

Shimonishi, T., Onaka, T., Kato, D., Sakon, I., Ita, Y., Kawamura, A., & Kaneda, H. 2010, A&A, 514, A12

Sloan, G. C., Kraemer, K. E., Price, S. D., & Shipman, R. F. 2003, ApJS, 147, 379

Sloan, G. C., et al. 2005, ApJ, 632, 956

Smith, F. W. 1984, J. Appl. Phys., 55, 764

Smith, J. D. T., et al. 2007, ApJ, 656, 770

Storey, P. J., & Hummer, D. G. 1995, MNRAS, 272, 41

Szczepanski, J., & Vala, M. 1993, ApJ, 414, 646

Tielens, A. G. G. M. 2005, The Physics and Chemistry of the Interstellar Medium

—. 2008, ARA&A, 46, 289

Tielens, A. G. G. M., Meixner, M. M., van der Werf, P. P., Bregman, J., Tauber, J. A., Stutzki, J., & Rank, D. 1993, Science, 262, 86

van der Marel, R. P., & Cioni, M.-R. L. 2001, AJ, 122, 1807

Van Kerckhoven, C., Tielens, A. G. G. M., & Waelkens, C. 2002, A&A, 384, 568

Vermeij, R., Peeters, E., Tielens, A. G. G. M., & van der Hulst, J. M. 2002, A&A, 382, 1042

Wada, S., Mizutani, Y., Narisawa, T., & Tokunaga, A. T. 2009, ApJ, 690, 111

Wada, S., Onaka, T., Yamamura, I., Murata, Y., & Tokunaga, A. T. 2003, A&A, 407, 551

Weingartner, J. C., & Draine, B. T. 2001, ApJ, 548, 296

Yamagishi, M., Kaneda, H., Ishihara, D., Kondo, T., Onaka, T., Suzuki, T., & Minh, Y. C. 2012, A&A, 541, A10